


FEBEX II Project  
Final report on  
thermo-hydro-mechanical  
laboratory tests





# FEBEX II Project Final report on thermo-hydro-mechanical laboratory tests

Antonio Lloret, Enrique Romero

*CIMNE*

María Victoria Villar

*CIEMAT*

enresa



ENRESA  
Dirección de Ciencia y Tecnología  
Emilio Vargas nº 7  
28043 Madrid - España  
Tfno.: 915 668 100  
Fax: 915 668 169  
[www.enresa.es](http://www.enresa.es)

*Diseño y producción: TransEdit*  
*Imprime: GRAFISTAFF, S.L.*  
*ISSN: 1134-380X*  
*D.L.: M-54173-2004*  
*Enero de 2005*

*This report has been drawn up within the context of the FEBEX project.  
Its contents represents only the opinion of the authors, which do not necessarily coincide  
with those of the other participants in the said project.*

*In addition to the authors included in the cover, the following researchers of CIEMAT and CIMNE have participated actively in the works included in this report:*

CIEMAT:

*Campos, R.*

*Marín, P.L.: Section 3.3.2*

*Mingarro, M.: Section 3.3.1*

*Cózar, J.S.: Section 3.3.1*

CIMNE:

*Castellanos, J.E.: Sections 3.2.2 and 3.2.3.2*

*Daucousse, D.: Section 3.2.1.1*

*Di Mariano, A. : Sections 3.1.2, 3.1.4.2 and 3.2.2.1*

*Gens, A.: Section 3.1.1*

*Hoffmann, C. : Section 3.2.2.1*

*Musso, G. : Section 3.2.3.2*

*Sánchez, M.: Sections 3.1.1.2 and 3.1.4*

*Suriol, J.: Section 3.2.2*

This page blank



# Table of contents



Table of contents



RESUMEN . . . . .	1
ABSTRACT . . . . .	5
1. INTRODUCTION. . . . .	9
2. MATERIAL. . . . .	13
3. METHODS AND RESULTS . . . . .	19
3.1 Continuation of the tests initiated during FEBEX I . . . . .	21
3.1.1 Analisis of suction controlled oedometer tests . . . . .	21
3.1.1.1 Summary of suction controlled odometer tests results . . . . .	21
3.1.1.2 Model results . . . . .	27
3.1.2 Retention curves at constant volume . . . . .	33
3.1.3 Suction and temperature controlled oedometer tests . . . . .	39
3.1.4 Infiltration tests in different conditions, interpreted by full modelling analysis . . . . .	45
3.1.4.1 Tests in 60-cm long cells. . . . .	46
3.1.4.2 New tests in ceramic cell. . . . .	54
3.2 New thermo-hydro-mechanical tests . . . . .	59
3.2.1 Temperature influence on the hydro-mechanical properties of the clay . . . . .	59
3.2.1.1 Retention curves . . . . .	60
3.2.1.2 Swelling capacity . . . . .	62
3.2.1.3 Swelling pressure and permeability . . . . .	67
3.2.1.4 Oedometric tests . . . . .	70
3.2.2 Study of the microstructure . . . . .	72
3.2.2.1 Mercury intrusion porosimetry . . . . .	72
3.2.2.2 Observations in the environmental scanning electron microscope (ESEM) . . . . .	84
3.2.3 Influence of solutes in the THM behaviour of the clay . . . . .	91

3.2.3.1 Preliminary oedometric tests with high salinity solutions . . . . .	91
3.2.3.2 Tests using NaCl and CaCl <sub>2</sub> solutions . . . . .	92
3.2.3.3 Tests with low concentration solutions . . . . .	102
3.3 New test performed up to the dismantling . . . . .	104
3.3.1 Permeability tests. . . . .	106
3.3.2 Infiltration tests. . . . .	109
3.3.3 Study of the repercussion of the hydraulic gradient . . . . .	113
3.3.4 Suction and temperature oedometric tests. . . . .	116
4. CONCLUSIONS . . . . .	125
5. REFERENCES . . . . .	131
APPENDIX A. Tables with the results of tests . . . . .	135
APPENDIX B. Thermo-hydro-mechanical model used for the analysis of the infiltration tests. . . . .	147
B.1 Balance equations . . . . .	149
B.2 Constitutive equations: Thermo-hydraulic model . . . . .	149
B.3 Constitutive equations: Mechanical model. . . . .	150
APPENDIX C. Observations in environmental scanning electron microscope . . . . .	153



# Resumen



Resumen

Se presentan los resultados del estudio termo-hidro-mecánico de la bentonita FEBEX realizado durante FEBEX II. El programa de laboratorio ha incluido la continuación de algunos ensayos comenzados durante FEBEX I, en concreto ensayos destinados a la calibración de modelos, la adquisición de parámetros mediante retroanálisis y la mejora del conocimiento del comportamiento de arcillas expansivas. El programa de ensayos ha explorado también nuevas áreas, como la influencia sobre el comportamiento de la arcilla de los cambios de microestructura de la bentonita, de la temperatura y de la concentración de solutos. Además, hacia el final del segundo año de proyecto, se propusieron varios ensayos con el objeto de comprender la inesperada tendencia en la hidratación del ensayo en maqueta.

Se ha determinado el efecto de la temperatura en las curvas de retención obtenidas en condiciones de confinamiento y de volumen libre; así mismo se han medido la presión de hinchamiento, la conductividad hidráulica y las deformaciones de hinchamiento y consolidación en función de la temperatura. Se han desarrollado varias técnicas experimentales y equipos para el estudio de los cambios originados por la temperatura en la bentonita no saturada, cubriéndose un amplio rango de succiones. En el rango de temperaturas estudiado, la bentonita FEBEX mantiene su alta capacidad de retención de agua y de sellado y su baja permeabilidad, lo que prueba su idoneidad hasta 80 °C como material de sellado en almacenamientos de residuos radiactivos de alta actividad desde el punto de vista hidro-mecánico. La extrapolación de los resultados a temperaturas mayores parece indicar que estas propiedades se mantienen dentro de límites aceptables al menos hasta 100 °C.

La porosimetría por intrusión de mercurio y la microscopía electrónica de barrido ambiental han aportado resultados prometedores para la caracterización de la microestructura de la bentonita y para el estudio de los mecanismos que condicionan los cambios en la distribución de tamaño de poros en arcillas expansivas. El uso de técnicas de imagen digital ha permitido verificar que, en el nivel microestructural en el que prevalecen los procesos químicos, las deformaciones son casi reversibles, como consideran los modelos elasto-plásticos de doble estructura.

Se han medido las deformaciones por hinchamiento tras saturación con diferentes tipos de agua (desionizada, granítica y salina) en función de la densidad

seca y la sobrecarga. Se ha investigado también el efecto de la salinidad en la rigidez y permeabilidad de la bentonita. La capacidad de hinchamiento de la arcilla se reduce drásticamente cuando se satura con agua de elevada concentración salina, llegándose a producir consolidación osmótica. Las deformaciones por hinchamiento medidas al saturar la arcilla con soluciones de diferente concentración son similares a las medidas en ensayos con succión controlada en los que la succión aplicada es igual a la succión osmótica de las soluciones salinas. La conductividad hidráulica de la bentonita aumenta con la concentración salina del permeante, sobre todo para densidad bajas.

Los ensayos de infiltración han mostrado que la permeabilidad al gas de la bentonita seca es muy alta. En estos ensayos, la toma de agua es mayor cuando la infiltración se realiza a temperatura de laboratorio, puesto que las zonas calientes de las muestras ensayadas bajo gradiente térmico permanecen desecadas durante largos periodos de tiempo. La combinación de la información aportada por ensayos de infiltración y por su análisis numérico THMQ acoplado ha demostrado gran utilidad para la comprensión del comportamiento de la bentonita FEBEX en las condiciones del almacenamiento.

Resumiendo, el comportamiento de la arcilla puede explicarse en su mayoría si se tiene en cuenta su doble estructura, puesto que las interacciones entre los dos niveles estructurales son responsables de los principales rasgos de su comportamiento mecánico. La utilización de un marco elasto-plástico que incorpora de forma simplificada la interacción entre los niveles micro y macroestructurales ha permitido una comprensión más profunda del comportamiento de la bentonita compactada y de los mecanismos básicos que lo controlan. Por otra parte, las transferencias entre el agua adsorbida en el interior de los agregados –de densidad mayor que el agua libre– y el agua libre inter-agregado, podría explicar la mayoría de los efectos observados como consecuencia de la temperatura.

Es necesario seguir estudiando aspectos como el flujo de agua bajo pequeños gradientes hidráulicos, el efecto de los gradientes térmicos y osmóticos en dicho flujo, y la influencia de las tensiones de corte en el comportamiento mecánico. Por último, es fundamental relacionar el conocimiento sobre aspectos físico-químicos de la microestructura de la arcilla con el comportamiento macroscópico de la bentonita compactada.





# Abstract



Abstract



The results of the thermo-hydro-mechanical (THM) study of the FEBEX bentonite performed during FEBEX II are presented. The laboratory test program continued in part with the works carried out during FEBEX I, particularly in activities related to tests aimed to the calibration of the models, the acquisition of parameters by back-analysis and the improvement of the knowledge on the behaviour of expansive clays. But the program has also included tests on new areas: investigations about the influence of the microstructure changes in bentonite, of temperature and of the solute concentration on the behaviour of clay. Besides, several tests were proposed in order to understand the unexpected behaviour observed in the "mock-up" test, towards the end of year 2.

Temperature effects on water retention curves in confined and unconfined conditions were determined, and swelling pressure, hydraulic conductivity and swelling and consolidation strains as a function of temperature were successfully measured. Different experimental techniques and equipments were developed to study thermal induced changes under partially saturated states, covering a wide range of suctions. FEBEX bentonite remains suitable as a sealing material in HLW repositories (from the hydro-mechanical point of view) for temperatures of up to 80 °C, as it keeps its high water retention capacity, low permeability and self-healing ability. The extrapolation of results points out to the preservation of properties for at least up to 100 °C.

Mercury intrusion porosimetry and environmental scanning electron microscopy provided promising results in order to characterise the bentonite microstructure and to give information about the mechanisms influencing pore size distribution changes on high active clays. The use of digital imaging techniques allowed verifying that at micro-scale level, where chemical phenomena prevail, strains are almost reversible as it is considered in the two-level elasto-plastic models.

The swelling strains of clay upon saturation with different kinds of water (deionised, granitic and saline with different salts and concentrations) were measured as a function of initial dry density and overload. The effects of salinity on bentonite stiffness

and permeability were also investigated. The swelling capacity of clay, saturated with highly saline water, reduces drastically, osmotic consolidation being even observed. The swelling strains measured when the samples were soaked with different saline concentrations are similar to the strains measured in suction controlled oedometer tests, in which it is applied a final suction equal to the osmotic suction of the saline solutions. The hydraulic conductivity of bentonite increases with saline concentration of the permeant, especially in the case of low densities.

The infiltration tests have shown that the gas permeability of dry bentonite is very high. The water intake is higher for the sample tested under room temperature, since the hot zones of the sample tested under thermal gradient remain desiccated for a long time. It has been proven that the combination of infiltration tests and coupled THMC numerical analysis can help to a better understanding of the FEBEX bentonite behaviour under repository conditions.

In summary, the behaviour of the clay may be mostly explained taking into account its double structure. The interactions between the two structural levels are responsible of the main features of the mechanical aspects of this behaviour. A deeper insight of the behaviour of compacted bentonite, and of the basic mechanisms controlling it, has been achieved using an elasto-plastic framework that incorporates the interplay between microstructural and macrostructural fabric levels in a simplified manner. On the other hand, temperature induced transfers between intra-aggregate adsorbed water –of density higher than that of free water– and inter-aggregate free water could explain most of the features related with the temperature observed.

However, more research effort must be dedicated to study certain aspects such as the water flow under low hydraulic gradients, the effect of osmotic and temperature gradients on this flow and the effects of deviatoric stresses on the mechanical behaviour, and, more generally, to relate the actual knowledge about the physico-chemical aspects of clay microstructure to the macroscopic behaviour of compacted bentonite.



# 1. Introduction

## 1. Introduction

The aim of FEBEX (Full-scale Engineered Barriers Experiment) is to study the behaviour of components in the near-field for a high-level radioactive waste (HLW) repository in crystalline rock. The experimental work consists of three main parts:

- an “in situ” test, under natural conditions and at full scale,
- a “mock-up” test, at almost full scale, and
- a series of laboratory tests to complement the information from the two large-scale tests.

The project is based on the Spanish reference concept for disposal of radioactive waste in crystalline rock (AGP Granito): the waste canisters are placed horizontally in drifts and surrounded by a clay barrier constructed from highly-compacted bentonite blocks (ENRESA 1995).

The engineered barriers (waste, canister and clay barrier) are key elements in the final disposal concept for HLW. The clay barrier has the multiple purpose of providing mechanical stability for the canister, by absorbing stress and deformations, of sealing discontinuities in the adjacent rock and retarding the arrival of groundwater at the canister and of retaining/retarding the migration of the radionuclides released, once failure of the canister and lixiviation of the spent fuel have occurred.

The behaviour of a HLW repository is determined, to a large extent, by the characteristics of the design and construction of the engineered barriers, and especially by the changes that may occur in the mechanical, hydraulic, and geochemical properties, as a result of the combined effects of heat generated by the radioactive decay and of the water and solutes contributed by the surrounding rock. Therefore, in FEBEX I, it was considered of as a main issue that the processes taking place in the near-field be understood and quantified, for the evaluation of long-term behaviour. As a consequence, the program of laboratory tests was designed to study and comprehend the processes that take place in the clay barrier under simple and controlled conditions and to develop the governing equations. These laboratory tests enabled to isolate the different processes, making their interpretation easier, and they provided fundamental data concerning the parameters to be used in the THM and THG models. The laboratory tests served also to support the checking of the predictive capacities of the THM and THG numerical models.

FEBEX I showed that the THM and THG models are very sensible to small variations in some of the parameters that represent the properties of the materi-

als. It became also clear that such parameters are not constant, but they may vary as a result of the changing conditions in the clay buffer.

For these reasons, the FEBEX II project includes also a wide laboratory tests programme, which should focus on those aspects not sufficiently covered during FEBEX I, and in the new processes and scenarios that are being considered in this second phase of the project. This information will help in the interpretation of the results obtained in the “Mock-up” and “In situ” tests. Specifically, the objective of the THM tests to be performed during FEBEX II is to cover those aspects considered most significant or less known on the basis of the previous work concerning the two large-scale experiments. Sensitivity analyses have underlined the fact that the critical parameters are those included in the retention curves of the granite and bentonite, and the permeability to water of the bentonite for different states of saturation (relative permeability). Although considerable effort was made to determine these parameters through the tests performed within the framework of the FEBEX I project, the fact is that little information is currently available on the variation of these parameters with temperature and with the changes occurring in the clay microstructure during the swelling process.

Furthermore, it was not possible to complete some of the activities proposed in the THM experimental Work Plan within the periods foreseen of the FEBEX I project. These activities relate fundamentally to tests aimed to the calibration of the models, the acquisition of parameters by back-analysis and the improvement of the knowledge on the behaviour of expansive clays. This type of tests requires the improvement of the available testing techniques and the development of prototypes of new equipment, which, due to their complexity, often leads to delays. As a result, the FEBEX II tests programme also includes those tasks not finished within the framework of FEBEX I, but that might lead to significant progress in the understanding of the behaviour of the clay or the knowledge of the most significant parameters.

The design of the tests is based on the experience gained during FEBEX I, and also completes some experiments not fully developed during FEBEX I. It is proposed that in the new tests, emphasis be directed towards the study of the THM behaviour of the bentonite from the microstructural point of view, and towards the effect of changes in the chemical composition of the dissolved salts on the mechanical behaviour of the soil. The specific objectives can be summarised as:

- Reduction of the uncertainties revealed by sensitivity analysis in relation to predictions of the barrier system behaviour, including more accurate investigation of the parameters defining the retention curves of bentonite and the permeability to water of the bentonite under different saturation conditions (relative permeability) and temperatures.
- Knowledge of the THM behaviour of the bentonite from the microstructural point of view and of the effect of changes in the chemical composition of dissolved salts.
- Finally, the conclusion of the phase I testing programme for the following aspects: parameter acquisition by back-analysis, calibration of models through the performance of *ad hoc* tests and improvement of the knowledge on the behaviour of expansive clays.

Two laboratories participate in this Task, as the tests proposed are experimentally difficult and time-consuming. Most of the work will be shared and repetition will be avoided, except when the importance of the parameters to determine or the technical difficulty recommends it.

## 2. Material

## 2. Material



The tests were performed in a bentonite coming from the Cortijo de Archidona deposit (Almería, Spain) which was selected by ENRESA as suitable material for the backfilling and sealing of HLW repositories. It is the same clay material used in the FEBEX Project to manufacture the blocks of the mock-up (Madrid, Spain) and the “in situ” (Grimsel Test Site, Switzerland) tests. The processing at the factory consisted in disaggregation and gently grinding, drying at 60 °C and sieving by 5 mm.

The physico-chemical properties of the FEBEX bentonite, as well as its most relevant thermo-hydro-mechanical and geochemical characteristics obtained during FEBEX I are summarised in the final report of the project (ENRESA 2000) and are shown in detail in ENRESA (1998), CIEMAT (1999), UPC (1999), Villar (2000, 2002), Lloret *et al.* 2002 and Fernández (2003). Several laboratories participated in these characterisation tasks. A summary of the results obtained is gathered below.

The mineralogical composition of the FEBEX bentonite was analysed by X-ray diffraction (XRD). The montmorillonite content is higher than 90 percent ( $92 \pm 3$  %). The smectitic phases are actually made up of a smectite-illite mixed layer, with 10-15 percent of illite layers. Besides, the bentonite contains variable quantities of quartz ( $2 \pm 1$  %), plagioclase ( $2 \pm 1$  %), K-felspar, calcite and opal-CT (cristobalite-trydimite,  $2 \pm 1$  %). By weight from dense concentrates and SEM observation, the following miner-

als have been identified: mica (biotite, sericite, muscovite), chlorite, non-differentiated silicates (Al, K, Fe, Mg, Mn), augite-diopside, hypersthene, hornblende, oxides (ilmenite, rutile, magnetite, Fe-oxides), phosphates (apatite, xenotime, monacite) and other non differentiated minerals of titanium and rare earth. Their contribution to bentonite composition is around 0.8 percent.

The mineralogical composition was also observed and quantified by optical microscopy study of thin sections. The textural heterogeneity itself is the main feature that can be described in the sample. The FEBEX bentonite is mainly composed of clay aggregates whose aspect ranges between dark isotropic low crystalline size ones to those presenting preferred orientation and relatively large (sub-micrometric) crystals. The remaining elements of the texture are glassy materials, volcanic rock fragments and individual accessory minerals (quartz and feldspars). Calcite is usually present as espartitic crystals replacing feldspars, but it has been observed also as isolated micritic cements.

Table I shows the average content values of the exchangeable cations along with the cation exchange capacity (CEC), as determined by different methods and laboratories.

The chemical composition of an aqueous extract of bentonite/water ratio (b/w) of 1/4 is presented in Table II. The content of chlorides and sulphates is worthy of mention.

**Table I**  
Average values of exchangeable cations and cation exchange complex (CEC) as determined by different methods (meq/100g).

	CSIC-Zaidin <sup>1</sup>	CIEMAT <sup>1</sup>	CIEMAT <sup>2</sup>
Ca <sup>2+</sup>	43 ± 5	42 ± 3	35 ± 2
Mg <sup>2+</sup>	32 ± 3	32 ± 2	31 ± 3
Na <sup>+</sup>	24 ± 4	25 ± 2	27 ± 0
K <sup>+</sup>	2.1 ± 0.2	2.5 ± 0.3	2.6 ± 0.4
Sum of exchangeable cations	101 ± 4		96 ± 0
CEC <sup>3</sup>		102 ± 4	

<sup>1</sup> Determined by displacement by 1M NH<sub>4</sub>AcO at pH 7 after washing of soluble salts (ENRESA 2000), the values are recalculated to give a sum of cations equal to CEC;

<sup>2</sup> Determined by displacement by 0.5M CsNO<sub>3</sub> at pH 7 (Fernández 2003);

<sup>3</sup> Determined by NaAcO/NH<sub>4</sub>AcO pH=8.2 (ENRESA 2000)

**Table II**  
Solubilised elements in the 1/4 bentonite/water aqueous extract as determined by two laboratories. Concentrations are related to the dry mass of clay (mmol/100 g, dried at 110°C).

	pH	Cl <sup>-</sup>	SO <sub>4</sub> <sup>2-</sup>	HCO <sub>3</sub> <sup>-</sup>	Na <sup>+</sup>	K <sup>+</sup>	Mg <sup>2+</sup>	Ca <sup>2+</sup>	Sr <sup>2+</sup>	Fe <sup>3+</sup>	SiO <sub>2</sub>
CIEMAT <sup>1</sup>	8.73	1.979	0.979	1.184	5.017	0.073	0.055	0.050	0.0004	0.0017	0.145
UAM <sup>2</sup>	7.93	2.03	1.84	1.56	6.04	0.062	0.146	0.067	0.0006	0.0013	

<sup>1</sup> Fernández 2003. Sr<sup>2+</sup> and Fe<sup>3+</sup> were found in concentrations lower than 10<sup>3</sup> mmol/100g.

<sup>2</sup> ENRESA 2000. As, V, Br, Sr, Ti, Mn, Fe, Ni, Cu, Zn and Y in concentrations lower than 10<sup>3</sup> mmol/100g.

The liquid limit of the bentonite is 102±4 percent, the specific gravity 2.70±0.04, and 67±3 percent of particles are smaller than 2 μm. The hygroscopic water content in equilibrium with the laboratory atmosphere (relative humidity 50±10 %, temperature 21±3 °C, total suction about 100 MPa) is 13.7±1.3 percent. The value obtained for the external specific surface using nitrogen adsorption technique (BET method) is 32±3 m<sup>2</sup>/g and the total specific surface obtained using the Keeling hygroscopicity method is about 725 m<sup>2</sup>/g. The analysis of the mercury intrusion data reveals that the intra-aggregate pores (smaller than 0.006 μm) represent the 73-78 percent of total pore volume when the bentonite is compacted at a dry density of 1.7 g/cm<sup>3</sup> (Villar 2000, 2002).

The saturated permeability to deionised water ( $k_w$ , m/s) of samples of untreated FEBEX bentonite compacted at different dry densities is exponentially related to dry density ( $\rho_d$ , g/cm<sup>3</sup>). A distinction may be made between two different empirical fittings depending on the density interval (Villar 2000, 2002):

- for dry densities of less than 1.47 g/cm<sup>3</sup>:

$$\log k_w = -6.00 \rho_d - 4.09 \quad (r^2 = 0.97, 8 \text{ points}) \quad [1]$$

- for dry densities in excess of 1.47 g/cm<sup>3</sup>:

$$\log k_w = -2.96 \rho_d - 8.57 \quad (r^2 = 0.70, 26 \text{ points}) \quad [2]$$

The determinations were done at room temperature. The variation in the experimental values with respect to these fittings is smaller for low densities than it is for higher values, with an average –in absolute values– of 30 percent.

The swelling pressure ( $P_s$ , MPa) of FEBEX samples compacted with their hygroscopic water content and flooded with deionised water up to saturation at

room temperature can be related to dry density ( $\rho_d$ , g/cm<sup>3</sup>) through the following equation (Villar 2000, 2002):

$$\ln P_s = 6.77 \rho_d - 9.07 \quad (r^2 = 0.88, 52 \text{ measurements}) \quad [3]$$

In this case, the difference between experimental values and this fitting is, on average, 25 percent. This dispersion, which is wider for higher dry densities, is due both to the natural variability of bentonite and to the measurement method used, which does not allow high degrees of accuracy.

The retention curve of the bentonite (or soil water characteristic curve, SWCC) was determined in samples compacted to different dry densities under different temperatures (Villar *et al.* 2002, Villar & Lloret, in press). The volume of the samples remained constant during the determinations, since they were confined in constant volume cells. To impose the different relative humidities the cells were placed in desiccators with sulphuric acid solutions of various concentrations. The data from these laboratory determinations are shown in Figure 1.

In unconfined conditions, the relationship between suction ( $s$ , MPa) and water content ( $w$ , %) changes, taking into account the initial dry density ( $\rho_{d0}$ , g/cm<sup>3</sup>), may be fitted to the following equation:

$$w = (45.1 \rho_{d0} - 39.2) - (18.8 \rho_{d0} - 20.34) \log s$$

On the other hand, the thermal conductivity ( $\lambda$ , W/mK) of the compacted bentonite at laboratory temperature is related to the degree of saturation ( $S_r$ ) through the following expression:

$$\lambda = \frac{A_1 - A_2}{1 + e^{\frac{(S_r - x_0)}{\lambda_0}}} + A_2 \quad [5]$$

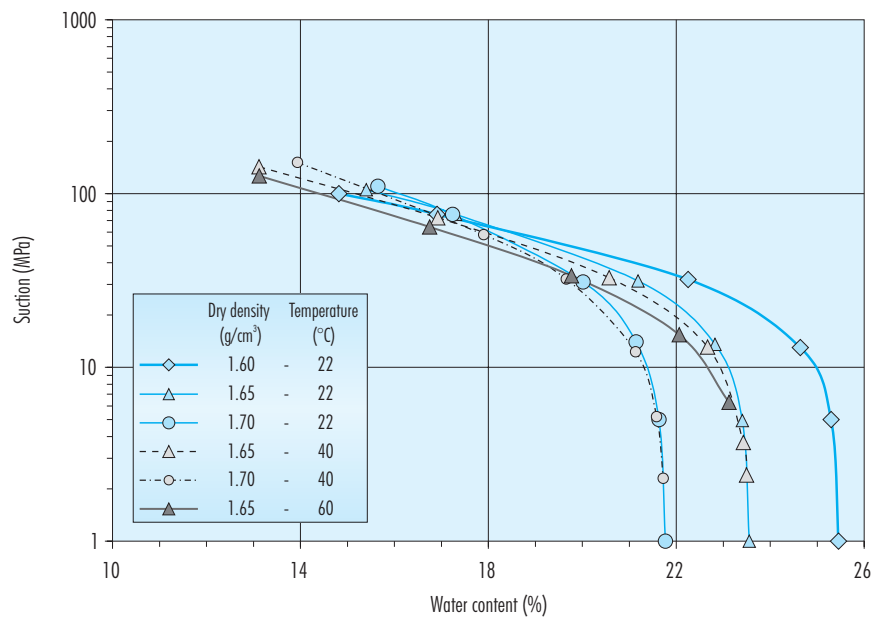


Figure 1: Water retention curves at different temperatures and for different bentonite densities.

where  $A_1$  represents the value of  $\lambda$  for  $S_r=0$ ,  $A_2$  the value of  $\lambda$  for  $S_r=1$ ,  $x_0$  the degree of saturation for which thermal conductivity is the average of the two extreme values and  $dx$  is a parameter. This equation was chosen because it accurately represents the behaviour of conductivity versus water content (degree of saturation), which are directly related but not in a linear fashion (Villar 2000, 2002). The fitting obtained, with an  $r^2$  of 0.923, gives the following values for each parameter:

$$A_1 = 0.57 \pm 0.02$$

$$A_2 = 1.28 \pm 0.03$$

$$x_0 = 0.65 \pm 0.01$$

$$dx = 0.100 \pm 0.016$$

Some isothermal infiltration tests and heat flow tests at constant overall water content were performed during FEBEX I project and they were backanalysed using CODEBRIGHT (Lloret *et al.* 2002). It is possible to fit the experimental data using a cubic law for the relative permeability ( $k_r = S_r^3$ ) and a value of 0.8 for the tortuosity factor ( $\tau$ ).



## 3. Methods and results

### 3. Methods and results

### 3.1 Continuation of the tests initiated during FEBEX I

This task is a continuation of some of the tests carried out during FEBEX I for the determination of the THM properties and parameters of the bentonite. These activities relate mainly to tests aimed to the calibration of the models, the acquisition of parameters by back-analysis and the improvement of the knowledge on the behaviour of expansive clays. Improved and new testing techniques, and in some cases different test conditions, are being used.

#### 3.1.1 Analysis of suction controlled oedometer tests

During FEBEX I an extensive programme of suction controlled oedometer tests was performed and their results were taken into account in the numerical modelling performed during this phase of the project (Lloret *et al.* 2002). Nevertheless, in this Section some of the most characteristic results will be newly examined using a new elasto-plastic constitutive model that incorporates the mechanical effects of the double structure of highly compacted expansive clays (Lloret *et al.* 2003). This model is described in Sánchez *et al.* (2001) and Sánchez (2004).

##### 3.1.1.1 Summary of suction controlled oedometer tests results

Table III presents the initial conditions and the stress paths of five tests performed at CIEMAT in which a

combination of loading paths at constant suction and suction change paths at constant load were applied (Villar 2000, 2002). The various load or suction changes were applied in stages as shown in Figure 2. In order to use a logarithmic scale a constant value of 0.1 MPa was added to all suction values plotted in this Figure. The same convention was used in the rest of the section. All tests start at an applied vertical stress of 0.1 MPa and at a compaction suction of about 125 MPa. Then, a variation of suction is applied under constant load, except for one specimen in which suction was kept unchanged. Afterwards the load was increased also under constant suction, which was then followed by wetting until saturation (zero suction) is reached. Maximum vertical stresses under saturated conditions were either 5 MPa or 9 MPa, depending on the test.

Figure 3a shows the variation of void ratio during the initial stage of suction modifications and subsequent loading. The starting points for the loading stages are very different because of the large dependence of volumetric strains on suction applied at low loads. On loading, the stiffness of the bentonite (*i.e.* the slope of the void ratio vs. vertical stress line plotted in semi-logarithmic scale) reduces slightly as the suction applied during loading increases. However, the most noticeable effect of suction is the shifting of the point at which there is a change in the slope of these lines, indicated by a vertical arrow in Figure 3a. In the framework of elasto-plasticity this change is interpreted as the crossing of a yield surface and the load at which it takes place can be considered as an apparent preconsolidation pressure. Figure 3b shows the dependence of this pre-

Table III

Stress paths of the tests in which a combination of loading paths at constant suction and suction change paths at constant load were applied. Tests performed at CIEMAT (Villar 2000, 2002).

Test	Initial conditions		Path ( $\sigma_v$ (MPa) s (MPa))									
	$\rho_d$ (g/cm <sup>3</sup> )	w (%)	I		II		III		IV		V	
			$\sigma_v$	s	$\sigma_v$	s	$\sigma_v$	s	$\sigma_v$	s	$\sigma_v$	s
S1	1.72	13.0	0.1	138	0.1	550	5.1	460	5.1	0	0.1	0
S2	1.68	13.7	0.1	126	—	—	9.1	127	9.1	0	0.1	0
S3	1.69	14.2	0.1	121	0.1	14	9.0	14	9.0	0	0.1	0
S4	1.71	12.9	0.1	119	0.1	3.7	8.4	4.1	8.4	0	0.1	0
S5	1.72	13.2	0.1	138	0.1	520	0.1	0	5.0	0	0.01	0

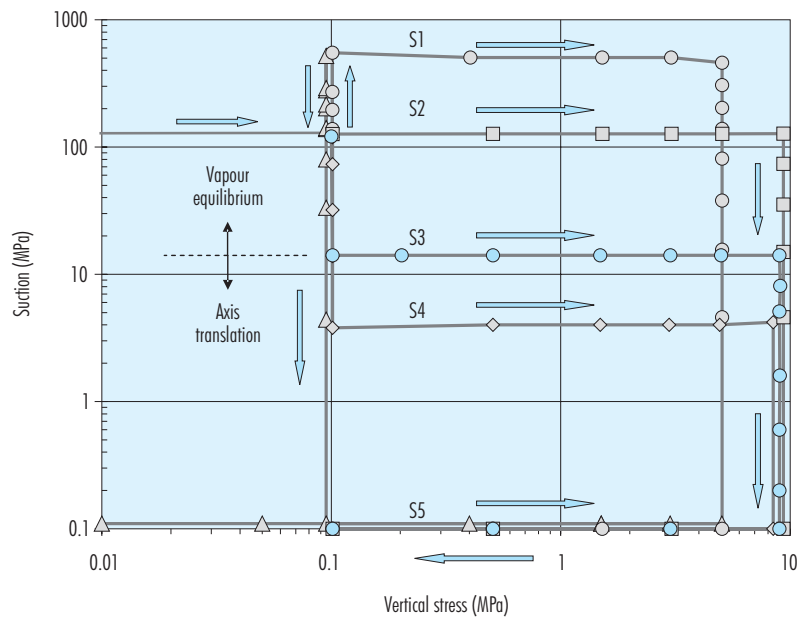


Figure 2: Generalized stress paths followed by tests S1 to S5.

consolidation pressure on suction. Large preconsolidation pressure reductions are apparent at low suction values. According to the conceptual model of Gens & Alonso (1992), the reduction of the yield point is due to the irreversible macrostructural strains induced by microstructural deformations that have occurred during the swelling to low suction values. Yielding was not reached in tests S1 and S2, and in the plot of Figure 3b it is assumed that the preconsolidation stress corresponds approximately to the vertical stress value reached during static compaction, about 18 MPa.

The variations of void ratio during the stages at which the vertical stress is maintained constant and suction is varied are presented in Figure 4a. Large void ratio changes are observed in the specimens where wetting takes place at 0.1 MPa, whereas in the samples where wetting takes place at 5.1 MPa and, especially, at 9 MPa load, the volume changes are quite small. Figure 4b summarises this information in terms of the slope of the swelling line (in a semi-logarithmic plot) with the applied vertical stress during wetting. The effects of applied load are very noticeable.

One of the samples (S5) was subjected to drying to 500 MPa suction before being wetted to a suction of 0.1 MPa. The measured void ratio changes are

plotted in Figure 5. It can be seen that the drying produces very small volumetric strains. However, when wetting is continued towards smaller suction values a large increase of swelling strains is observed signalling a significant change of behaviour. The comparison of the results of this test with those of test S4, which did not undergo this initial drying/wetting cycle (Figure 5), suggests that such a suction cycle does not have any noticeable effects on subsequent behaviour.

An important feature of behaviour concerns the possible stress path dependency or independency of the material under generalised stress including suction. In unsaturated non-expansive soils, it is often found that the behaviour is stress path independent if the trajectories only include loading and wetting (suction reduction) stages (Alonso *et al.* 1987). However, Gens & Alonso (1992) argued that, in expansive soils, there would be irreversible macrostructural rearrangements caused by the swelling of the microstructure when wetting the samples. This interaction would be higher when applied stresses are low. As a consequence, this macrostructural changes could result in stress path dependency of volume changes even in the cases where only wetting paths are involved. This issue was examined in this experimental programme.



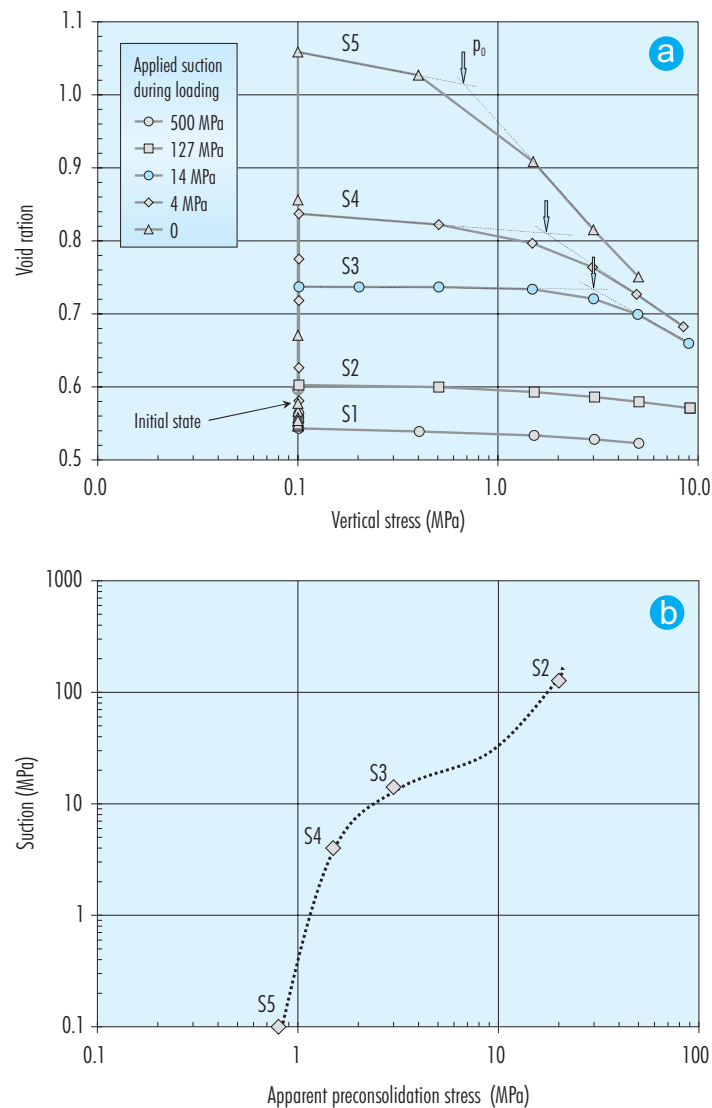


Figure 3: a) Variation of void ratio during the initial stage of suction variation and subsequent loading. Tests S1 to S5. b) Relationship between the apparent preconsolidation stress and applied suction identified in the loading stages of tests S3, S4 and S5. The preconsolidation stress of samples S1 and S2 are assumed to be approximately equal to the static compaction stress.

Figure 6a shows void ratio variation for two specimens that share the initial and final stress points but have followed different stress paths. It can be noted that the final state is different, so there is a measure of stress path dependency. As observed in other cases (Brackley 1973, Justo *et al.* 1984), the final void ratio of the sample wetted under low stresses is higher. The disruption of the macrostructure would be more severe in this case because of the larger swelling

strains developed during wetting, inducing large macrostructural volume changes that cannot be recovered upon subsequent loading. Figure 6b shows a similar plot for another three specimens with the same initial and final points where, again, it can be noted that the final void ratio values do not coincide. As before, the sample that was wetted at the lower applied vertical stress (4 MPa) reaches the highest final void ratio.

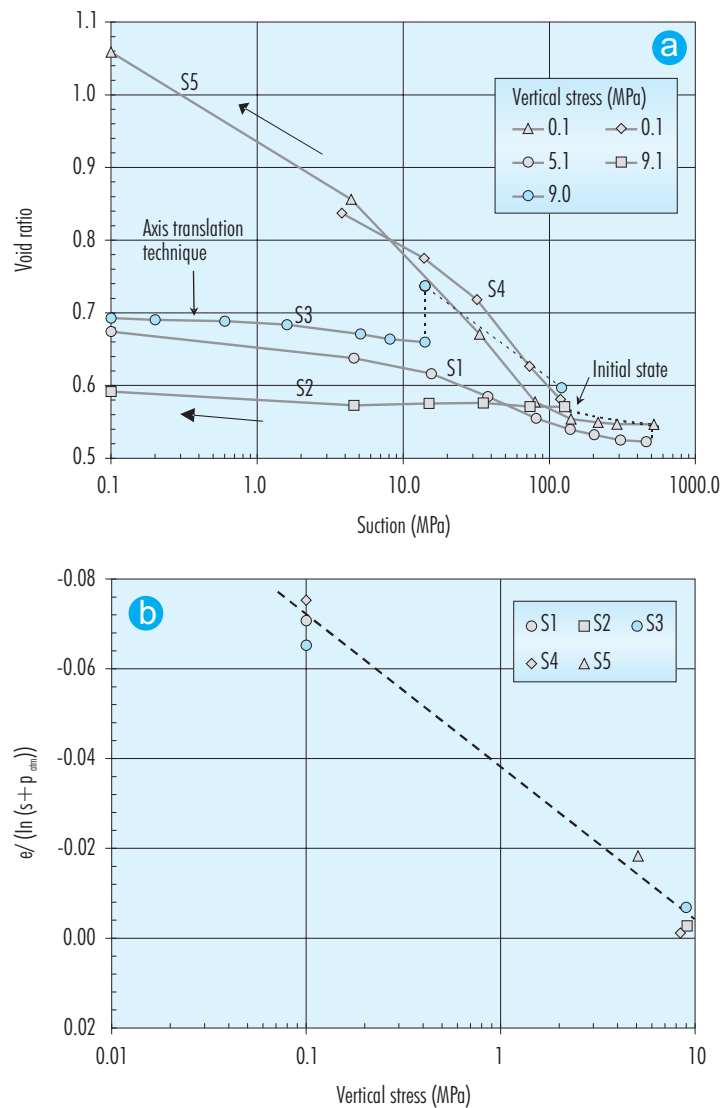


Figure 4: a) Variation of void ratio during the stages at which vertical stress is maintained constant and suction varied. Tests S1 to S5. b) Influence of applied vertical stress on the slope of the swelling line measured on wetting. Tests S1 to S5.

The main features of the swelling pressure tests performed in the UPC laboratory are presented in [Table IV](#) (Pintado 2002). Initially a suction change is applied to three of the samples in order to achieve a range of initial conditions for the next testing stage.

During the swelling pressure phase a condition of no volume change is prescribed and suction was reduced in stages under controlled conditions. In this way it is possible to follow the stress path, in terms

of suction vs. vertical stress throughout the tests, as shown in [Figure 7](#).

The examination of these stress paths provides important information on the stress-strain characteristics of the bentonite in this type of tests (that corresponds to a number of relevant field situations) but, also, on the underlying causes of the observed behaviour. Three zones can be distinguished ([Figure 7](#)). The first one corresponds to the stage of high

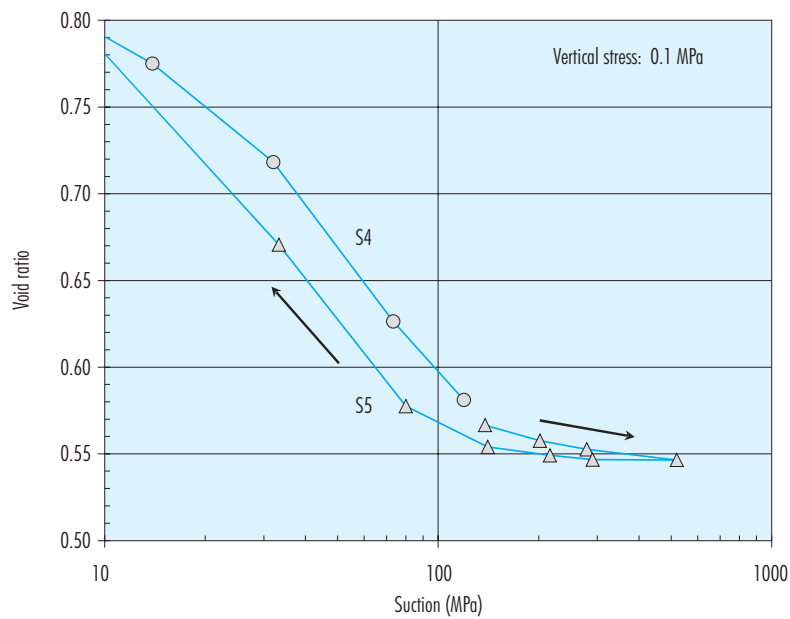


Figure 5: Variation of void ratio with suction of test S5 during an initial drying/swelling cycle and subsequent wetting. The results of test S4 are included for comparison.

Table IV  
Main features of the swelling pressure tests performed at the UPC laboratory (Pintado 2002).

Test	Initial conditions		Path before swelling pressure test ( $\sigma_v$ (MPa), $s$ (MPa))				Dry density before swelling pressure test
	$\rho_d$ (g/cm <sup>3</sup> )	$w$ (%)	I		II		$\rho_d$ (g/cm <sup>3</sup> )
			$\sigma_v$	$s$	$\sigma_v$	$s$	
SP1	1.62	14.6	0.11	128	0.11	424	1.65
SP2	1.63	13.2	0.15	146	-	-	1.63
SP3	1.62	14.6	0.16	128	0.16	70	1.57
SP4	1.63	14.2	0.15	128	0.15	39	1.50

suction and low applied loads. In this region the vertical stress remains below the preconsolidation stress (in elasto-plastic terms, the stress state has not reached the yield locus) and the stress path is defined by the increase of load required to compensate the small swelling strains due to suction reduction.

Once the preconsolidation pressure (yield locus) is reached, the second zone is entered and a drastic change of slope ensues. If the load is sufficiently high, collapse of the macrostructure occurs and the value of vertical stress tends to reduce to compensate the collapse compressive strains. Naturally, the

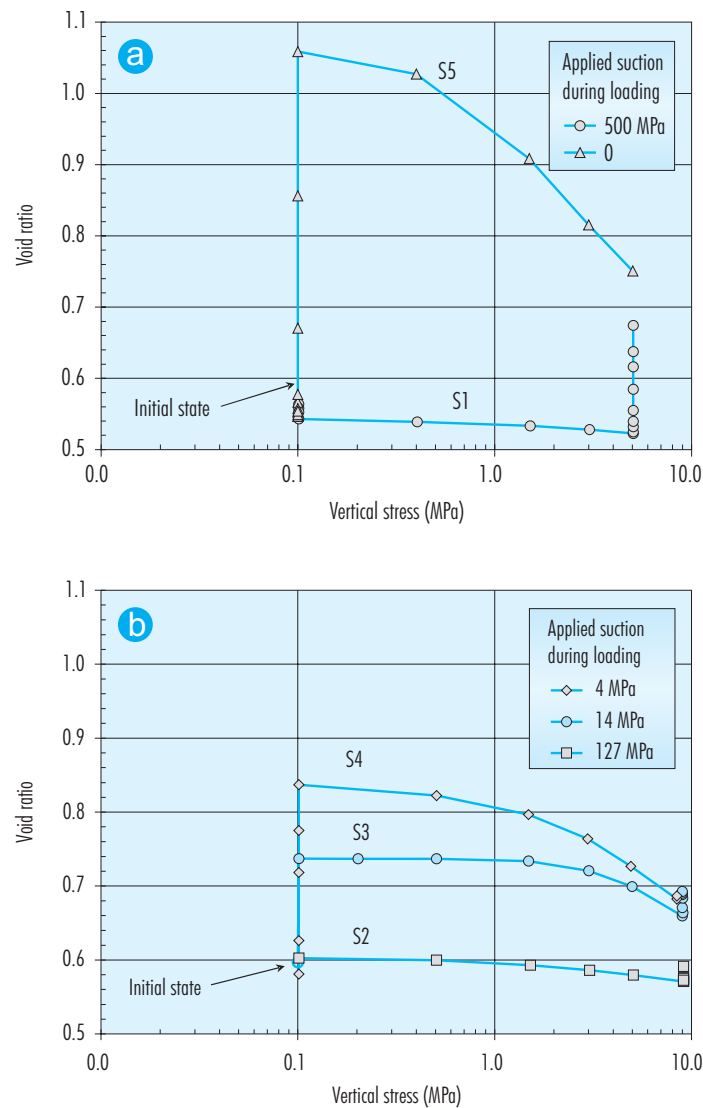


Figure 6: Variation of void ratio observed in tests with the same initial and final stress states. a) Tests S1 and S5. b) Tests S2, S3 and S4.

microstructural swelling strains also contribute to the compensation of collapse deformation but, at this stage, they may not be large enough to offset the reduction of vertical stress.

The points indicating the preconsolidation stress identified in the suction reduction tests under constant stress have been added to Figure 7 for reference. In fact, a close coincidence of yield points from the two type of tests should not be expected because of the different stress paths followed, which lead to different magnitudes of irreversible strains and, therefore,

to somewhat different yield surfaces. Generally, in the constant load tests, the larger swelling strains should lead to smaller sizes of yield loci.

Finally, zone III corresponds to the region of low suctions where microstructural swelling strains exhibit their largest magnitude. Now microstructural strains overcome any possible collapse strains and the vertical stress must rise again to compensate for the large swelling strains. It is interesting to note that, even the rather complex behaviour displayed by the compacted bentonite during the swelling

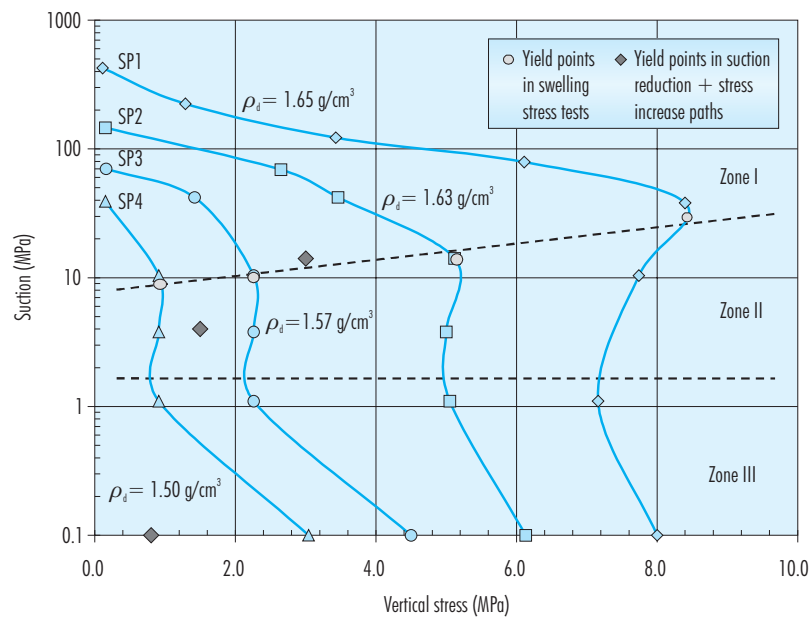


Figure 7: Generalised stress paths observed in the swelling pressure tests.

pressure tests can be readily explained in the context of a conceptual framework that considers the interaction between microstructure and macrostructure.

The dependence of swelling pressure with compacted dry density were examined by a large number of tests performed in conventional oedometers without suction control where the wetting is applied in a single step. The results of the swelling pressure tests performed in suction-controlled equipment have been added to the Figure 8, where it can be observed that they agree closely with the independently-determined trend. It is reassuring that no spurious effects due to the equipment appear to affect the results of the swelling pressure tests.

### 3.1.1.2 Model results

The model used in the analysis of the tests is based on the conceptual approach contained in Gens & Alonso (1992) and on the mathematical formulation presented in Alonso *et al.* (1999). It is graphically summarised in Figure 9a. The behaviour of the macrostructure is defined in terms of the Barcelona Basic Model, BBM, (Alonso *et al.* 1990), represented in the Figure by the LC yield curve. The behaviour of the microstructure is considered always

reversible and logarithmically dependent on the classical effective stress  $p+s$ , where  $p$  is the mean net stress and  $s$ , the suction (total suction in this case). When the stress state crosses either the SI (suction increase) or SD (suction decrease) yield locus, the microstructural strains induce irreversible plastic strains on the macrostructure that result in the movement of the LC yield surface. Important components of the model are the interaction functions that control the magnitude of the macrostructural plastic strain caused by microstructural strains. Figure 9b shows generic interaction functions indicating the physical phenomena underlying each of the branches. The shape of the  $f_D$  interaction curve implies that when the stress point is far from the LC (*i.e.* values of  $p/p_0$  much less than one) the interaction during wetting is very strong. This corresponds to the fact that, in that situation, the macrostructure is in a dense state, far from the collapsible behaviour implied by the LC curve. Therefore, the expansion of the microstructure causes large disruptions and significant irrecoverable strains. As the state of the soil moves towards the LC, the specimen becomes less dense (relative to the applied stress) and the strength of the interaction reduces accordingly. Indeed, the interaction may change sign if the ex-

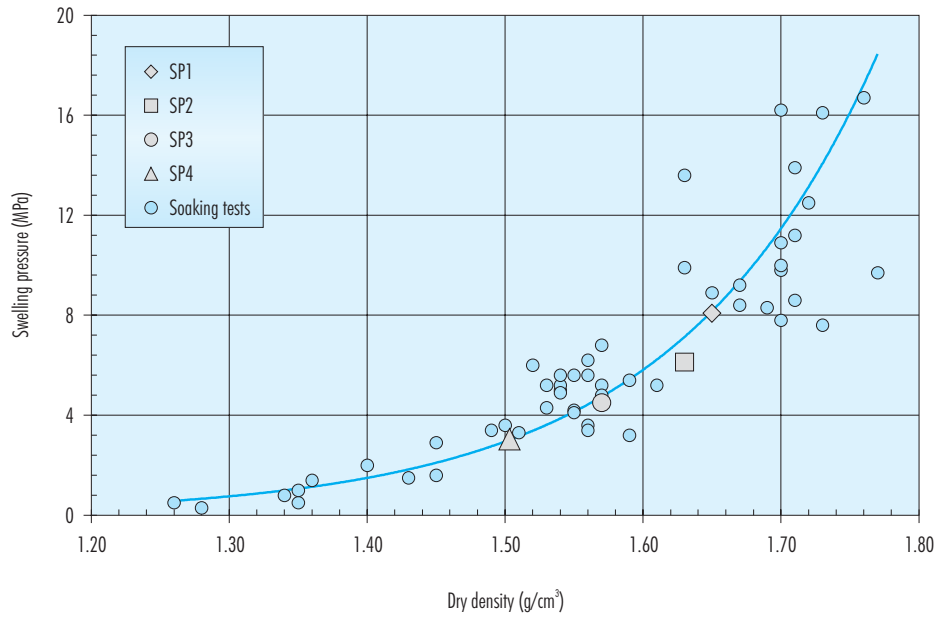


Figure 8: Dependence on swelling pressure on compaction dry density as determined in conventional oedometers. The swelling pressures measured in the suction-controlled oedometers agree well with the general trend.

pansion of the aggregates leads to an invasion of the macropores with a consequent reduction of the macrostructural void ratio. Opposite consideration apply to the  $f_i$  interaction curve. Additional information on the model is given elsewhere (e.g. Gens & Alonso 1992, Alonso *et al.* 1999, Sánchez *et al.* 2001). The relevant equations for the model are the following:

LC yield surface:

$$p_0 = p_c \left( \frac{p_0^*}{p_c} \right)^{\frac{\lambda(0)-\kappa}{\lambda(s)-\kappa}} \quad \text{and} \quad \lambda(s) = \lambda(0)[r + (1-r)e^{-\beta s}] \quad [6]$$

Hardening law

$$\frac{dp_0^*}{p_0^*} = \frac{(1+e_M)d\varepsilon_v}{\lambda(0)-\kappa} \quad [7]$$

Elastic macrostructural behaviour (reversible)

$$d\varepsilon_{vM}^e = \frac{dp}{K_t} + \frac{ds}{K_s} \quad \text{with} \quad K_t = \frac{(1+e_M)p}{\kappa} \quad \text{and} \quad K_s = \frac{(1+e_M)(s+p_{atm})}{\kappa_s} \quad [8]$$

Microstructural behaviour (reversible)

$$d\varepsilon_{vM}^e = \frac{dp}{K_m} \quad \text{with} \quad K_m = \frac{e^{-\alpha_m p}}{\beta_m} \quad [9]$$

Interaction micro-macro

$$d\varepsilon_{vM}^p = f_D d\varepsilon_{vM}^e \quad \text{when SD is activated} \quad [10]$$

$$d\varepsilon_{vM}^p = f_I d\varepsilon_{vM}^e \quad \text{when SI is activated} \quad [11]$$

An important advantage of this model is that it allows taking into account the two levels of structure actually existing in the material tested, so that the variables associated with each level can be followed throughout the test and a more detailed examination of the patterns of behaviour can be made. It should be strongly stressed that the aim of this modelling exercise is not to test the predictive capability of the model. In fact, the parameters have been chosen specifically to give a good representation of the experimental observations. The objective is to use the constitutive model as a consistent tool to gain a better and more founded understanding of the behaviour of the soil and of the mechanisms that underlie it.

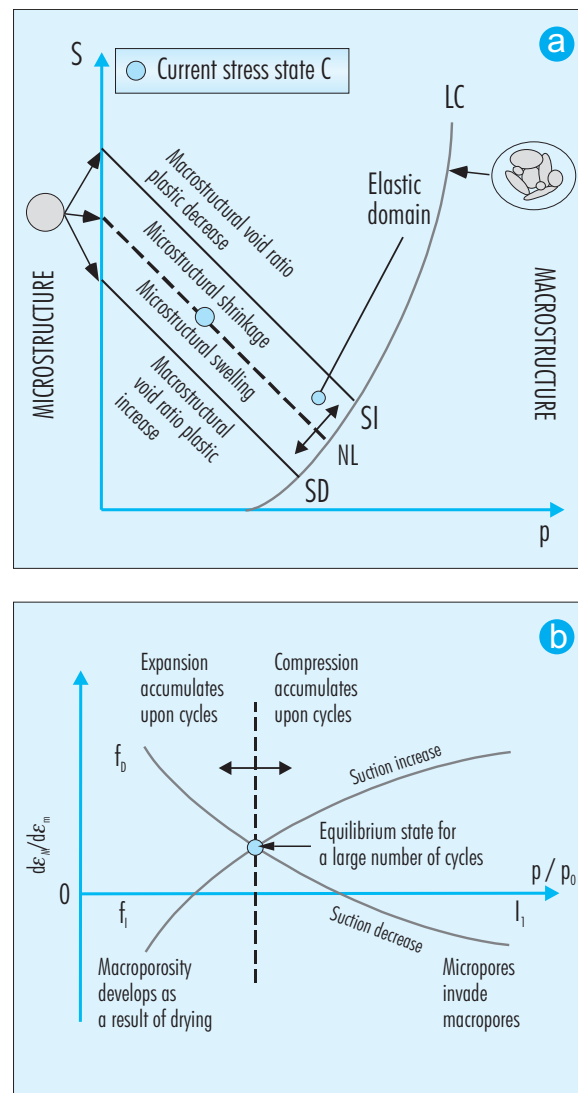


Figure 9: a) Graphical summary of the double structure elasto-plastic model for expansive soils. b) Generic interaction functions that indicated the intensity of the interaction between the two structural levels.

The model is used one-dimensionally, substituting applied vertical stress for mean net stress. Therefore,  $p$  denotes, in this case, net vertical stress. SI and SD surfaces coincide, so that there is always some degree of interaction between micro and macro levels.

The parameters used in the modelling are shown in Table V. The results of tests S1 and S5 have been used to determine them. Elastic macrostructural parameters have been obtained from the sections of the tests that are inside the LC yield curve. The value

of the slope of the saturated consolidation line,  $\lambda(0)$ , was based on the loading stage of S5 test. The parameters of the interaction curves have been adjusted to yield the correct amount of stress path dependency and the parameters for the microstructural behaviour have been derived from the swelling stages of tests S1 and S5. Finally the parameters controlling the shape of the LC yield surface have been evaluated from the experimental results plotted in Figure 3b, which shows the variation of the apparent preconsolidation stress with suction.

**Table V**  
Parameters used to define the elasto-plastic constitutive law used in modelling.

Parameters defining the Barcelona Basic Model (BBM) for macrostructural behaviour			
$\kappa$	0.005	$\kappa_s$	0.001
$\lambda_0$	0.080	$p_c$	0.50 MPa
$r$	0.90	$\beta$	1.0
Parameters defining the law for microstructural behaviour			
$\alpha_m$	$2.1e-02 \text{ MPa}^{-1}$	$\beta_m$	$2.3e-03 \text{ MPa}^{-1}$
Interaction functions			
$f_i = 1 + 0.9 \tanh(20(p/p_0) - 0.25)$		$f_0 = 0.8 - 1.1 \tanh(20(p/p_0) - 0.25)$	

The initial values of the microstructural and macrostructural void ratio are 0.45 and 0.11, respectively, in accordance with the observations on the soil fabric. The static compaction stress (18 MPa) gives the initial position of the LC yield surface. With the expression used to define the LC curve (equation), the hardening parameter  $p_0^*$  has an initial value of 12 MPa.

The model is first applied to the analysis of tests S1 and S5. They share the same initial and final generalised stress states, but their trajectories are very different (Figure 10). In test S1 the specimen is loaded under a high 550 MPa suction up to a 5.1 MPa vertical load and then is wetted reducing the suction to 0 in stages. In contrast, test S5 is first wetted at a low applied vertical stress value of 0.1 MPa and afterward the sample, already saturated, is loaded to a vertical stress of 5.0 MPa. These two tests, therefore, provide the opportunity to examine the behaviour over a wide range of stress paths. Figure 10a shows the computed variation of void ratio over the stress paths followed by the two tests, together with the experimental results. It can be observed that major features of behaviour are correctly reproduced including:

- Large swelling strains when the material is wetted at low stresses (Path B-D, Test S5)
- Smaller, but still significant, swelling strains when the soil is wetted under a 5 MPa vertical stress (Path C-E, Test S1)
- Change of the slope of the compression line during loading indicating yield in test S5 (Path

D-E). No yield is apparent during the loading at high suction of specimen S1 (Path B-C).

- Final void ratio (point E) is different in the two samples, there is a measure of stress path dependency, at least regarding volumetric strains.

Good reproduction of behaviour is also achieved when considering the experimental results in terms of void ratio vs. suction variation (Figure 10b), although some departures are observed at intermediate stages of the swelling of test S5.

Summarising, the model allows offering a good simulation of the observed results and, with the set of parameters adopted, even the quantitative agreement is quite close. Accepting then that the constitutive law is a reasonable representation of the real behaviour, it is interesting to explore the further information that can be obtained from the model so that the behaviour mechanisms underlying the mechanical behaviour of the soil can be better understood.

Figure 11a shows the evolution of the microstructural and macrostructural void ratio computed for Test S5. During the swelling stage (path B-D), the microstructural strains are relatively large and they cause even larger irreversible strains in the macrostructure because of the large coupling between the two structural levels that exist at low stresses. During the subsequent loading (path D-E) under saturated conditions the deformation of the macrostructure is significant, although it is not due to microstructural strains, which are now quite small. This part of the test is basically controlled by the behaviour of the



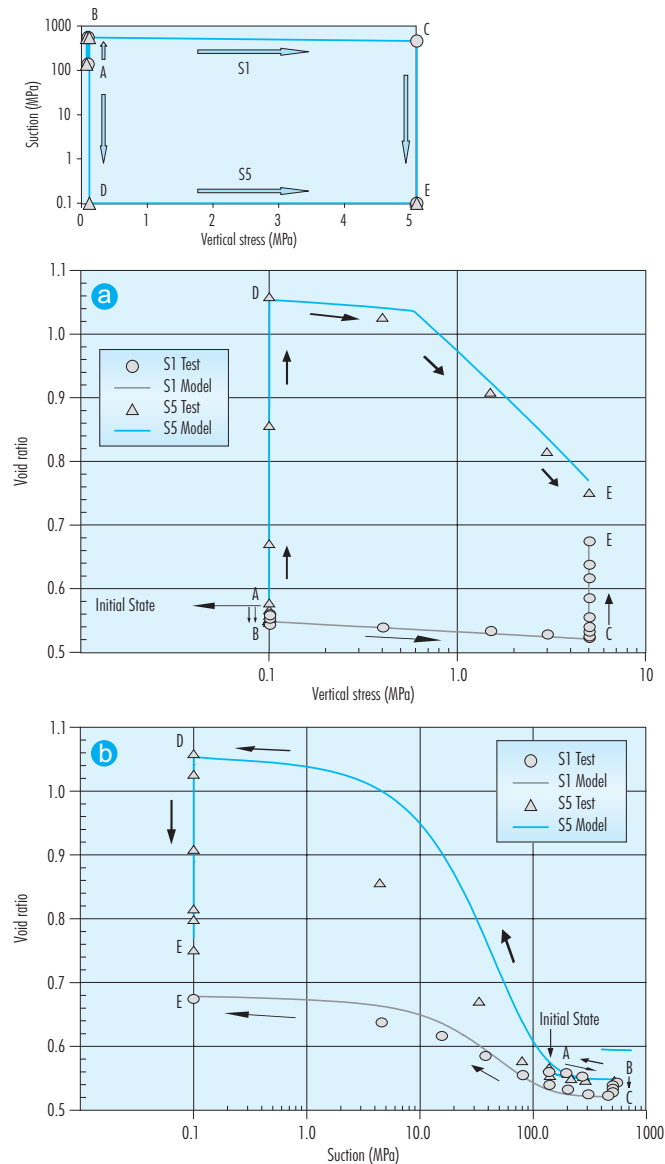


Figure 10: Computed variation of void ratio for tests S1 and S5. Experimental results are provided for comparison. a) Load increase paths, b) suction decrease paths.

macrostructure. Figure 11b shows the parts of the interaction functions involved in the various stages of the test. Some of the positions of the LC yield curve during the performance of test S5 are shown in Figure 11c. It can be seen that during swelling (path B-D) the LC curve moves to the left in response to the irreversible swelling strains taking place in the macrostructure. Subsequent loading (path D-E) takes the LC again to the right to a final load value of 5.0 MPa. Indeed the yield point observed and computed

(Figure 10a) corresponds to the crossing of LC during this loading stage. Continuous information on the evolution of the LC yield curve can be obtained plotting the evolution of the hardening parameter,  $p_0^*$  (Figure 12). The reduction of  $p_0^*$  during swelling and its subsequent increase upon loading are readily apparent.

The behaviour of sample S1 is quite different (Figure 13). During the first stage of drying (path A-B) and

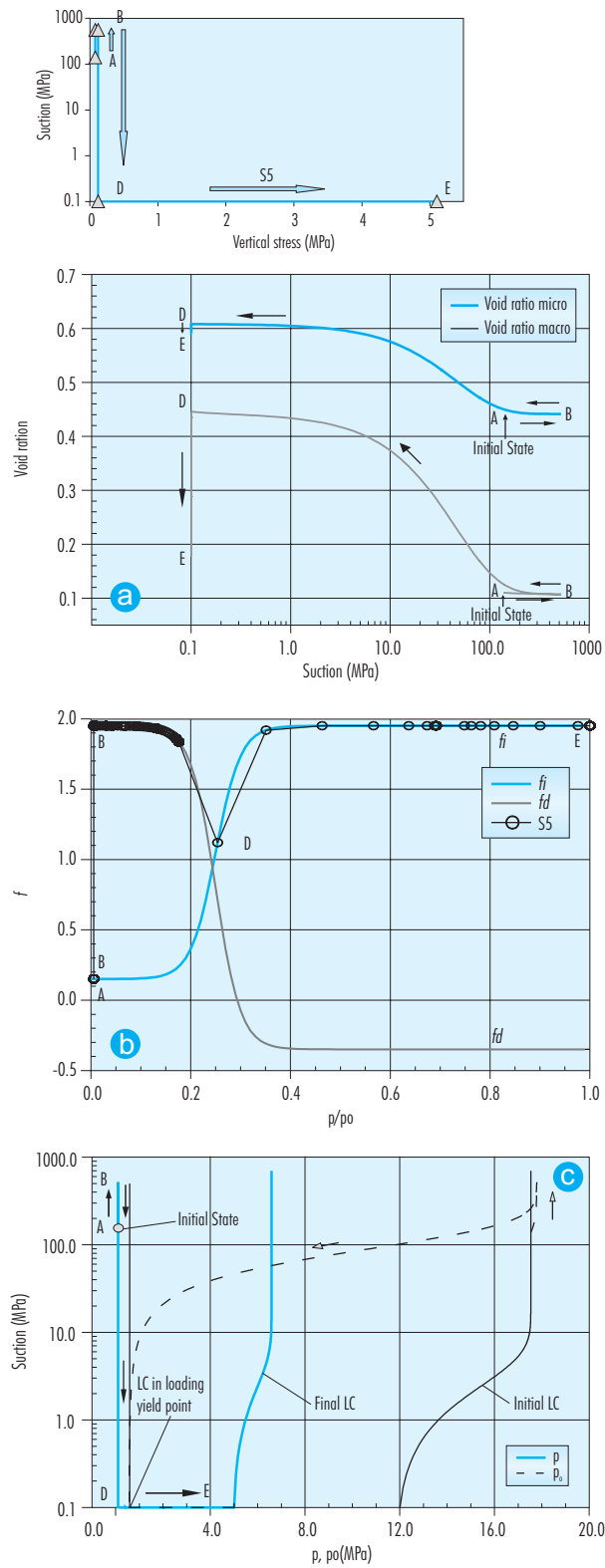


Figure 11: a) Evolution of the computed microstructural and macrostructural void ratio in test S5. b) Interaction functions involved in the various stages of test S5. c) Stress path and successive LC yield surfaces for test S5.

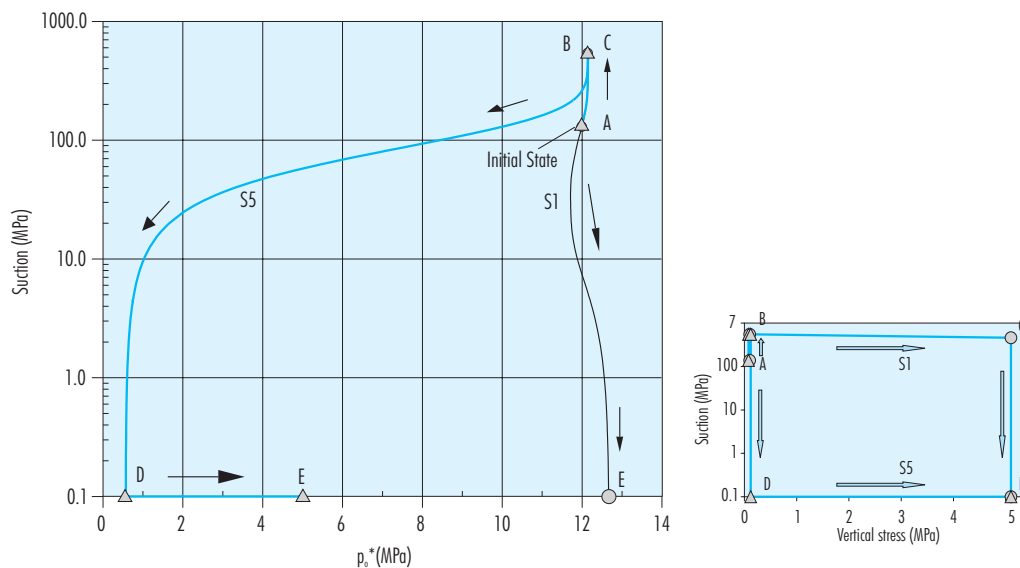


Figure 12: Evolution of the hardening parameter  $p_0^*$  for tests S1 and S5.

subsequent loading (path B-C), the microstructural volumetric strains are very small. The macrostructural strains are also small, even during loading, because of the high stiffness imparted to the sample by the large 500 MPa suction. During the swelling stage (path C-E) under a 5.1 MPa load, microstructural strains are significant, although smaller than for test S5 because of the higher load applied. The most significant difference is, however, that the macrostructural strains that are induced are quite small because now the stress state is much closer to the LC (Figure 13c), i.e. the sample is in a comparatively looser state and the potential for macrostructural disruption is much lower. The loading stage (path B-C) takes place inside the LC yield surface, so no yield is expected and none was observed. The evolution of the hardening parameter for test S1 has also been plotted in Figure 12. It can be observed that the changes are very slight (indicating a LC curve practically stationary) and that the final value of  $p_0^*$  is higher than in the case of test S5.

Now the basic reason for the stress path dependency of volumetric strains can be readily identified. The basic difference is that in test S5 the large swelling strains take place at low stress values and, consequently, the interaction with the macrostructure is

very strong and results in large plastic strains that are not fully recovered upon subsequent loading. In test S1, development of plastic strains in the macrostructure is quite reduced because, when the swelling of the microstructure takes place, the interaction between the two structural levels is small. The different states of the samples at the end of the test are reflected in the different final positions of the LC curves (and  $p_0^*$  values). Exactly the same analysis could be made regarding the results of tests S2, S3 and S4.

As a final test of the adequacy of the model to represent the behaviour of compacted swelling materials, it was applied to the modelling of the swelling pressure tests using the same set of parameters without any attempt of further calibration. Figure 14 shows the results of the model calculations, together with the experimental results. Although differences between computed and experimental results can be observed, the model is capable of producing swelling stress paths very similar to the observed ones, comprising the three phases of behaviour identified previously.

### 3.1.2 Retention curves at constant volume

The exact knowledge of the retention curve is a key question to predict the hydration process of the bar-

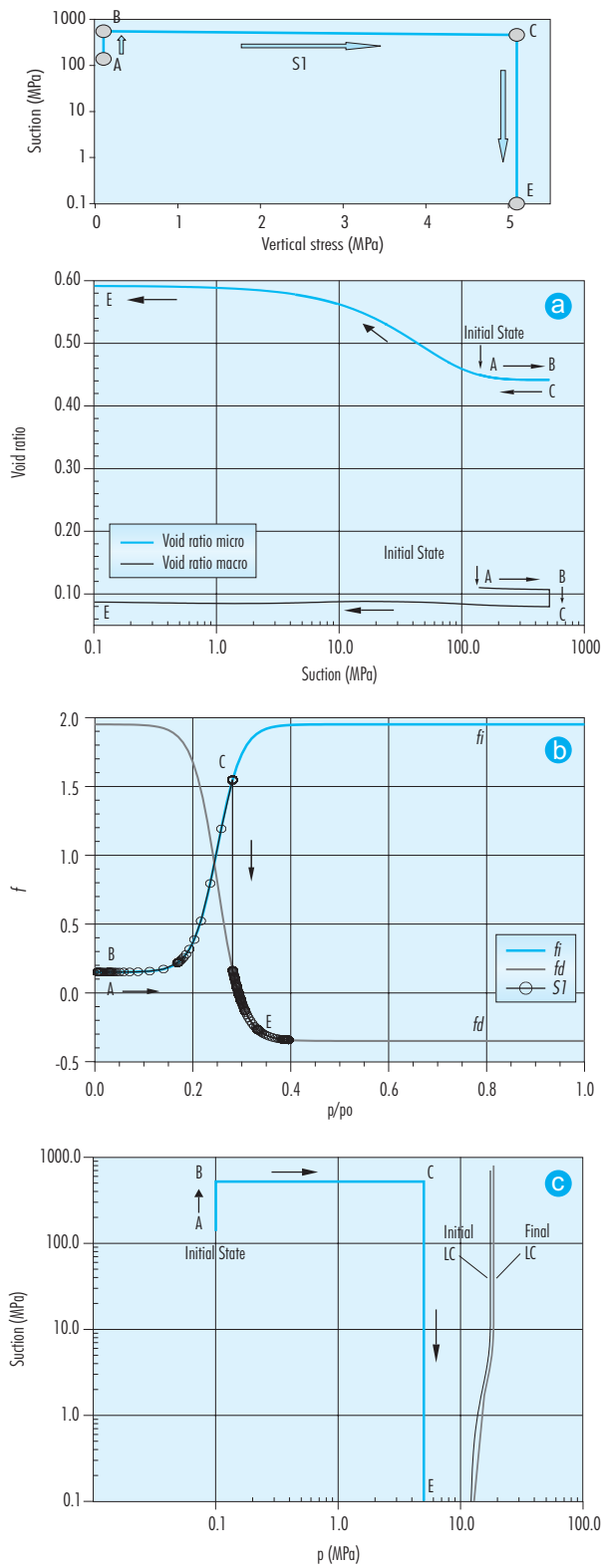


Figure 13: a) Evolution of the computed microstructural and macrostructural void ratio for test S1. b) Interaction function involved in the various stages of tests S1. c) Stress path and LC yield surfaces for test S1

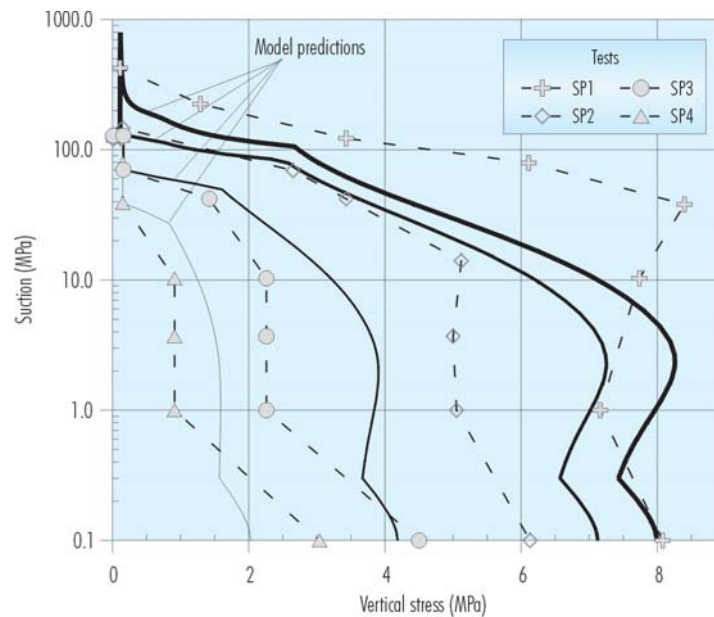


Figure 14: Computed stress paths for swelling pressure tests SP1 to SP4. Experimental results are provided for comparison.

rier. During FEBEX I it was shown that this curve, for the same initial conditions of the material, differs significantly depending on the volume restriction imposed to the sample during the determination. Water content for a given suction is much higher if the sample is free to swell than if its volume change is constrained. Only a few curves at constant volume were determined in FEBEX I, and these, were obtained using mainly suction controlled oedometers, in which the sample can be subjected to different suctions while its swelling is restricted by the application of the appropriate vertical loads. This methodology presents several technical limitations and is difficult to carry out without failures. For this reason, special cells were designed in the last phase of FEBEX I, what allows to determine the retention curves for different dry densities in a systematic and easy way (Figure 15 and Figure 16).

The cell shown in Figure 15 consists of a cylindrical body measuring 0.5 cm in thickness, with two perforated covers joined by bolts. The sample is compacted directly inside the cell, from the granulated clay at hygroscopic water content. The length of the specimen is 1.20 cm and its cross section 11.34 cm<sup>2</sup>. The cell is placed in a desiccator with a sulphuric acid solution and vacuum is created. The

suction control method is, therefore, through the control of relative humidity. The porous stone and the perforated covers allow for the exchange of water in the vapour phase between the clay and the atmosphere of the desiccator. This process is very slow –slower than when the retention curve under free volume conditions is determined in the desiccator– not only because not the entire surface of the sample acts as an exchange surface (but only the upper and lower parts) but also because the process is performed at constant volume. Once the water content of the clay is stable, the cell is weighed and the solution in the desiccator is changed by a lower concentration one in order to perform a wetting path.

In the device shown in Figure 16, the specimen's diameter is 50 mm and its height can vary between 10 and 20 mm. In order to reduce the time needed to reach the equilibrium after suction changes, a flow of humid air across the porous plates is induced by means of a peristaltic pump. Air humidity is controlled by means of saturated salt solutions. Changes in water content of the soil are measured by weighing of the entire cell. The use of strain-gauges on top cap (1/4 bridge configuration) allows measuring the swelling pressure of the material during the hydration path at constant volume. This

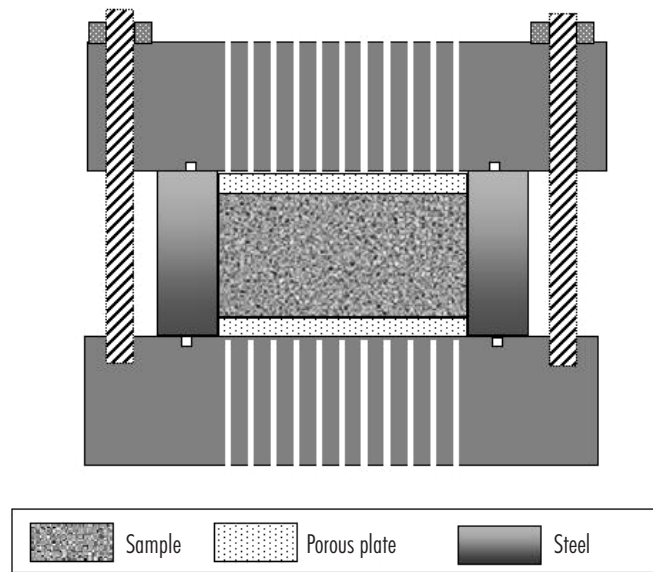


Figure 15: Non-deformable cell for the determination of the retention curve (CIEMAT).

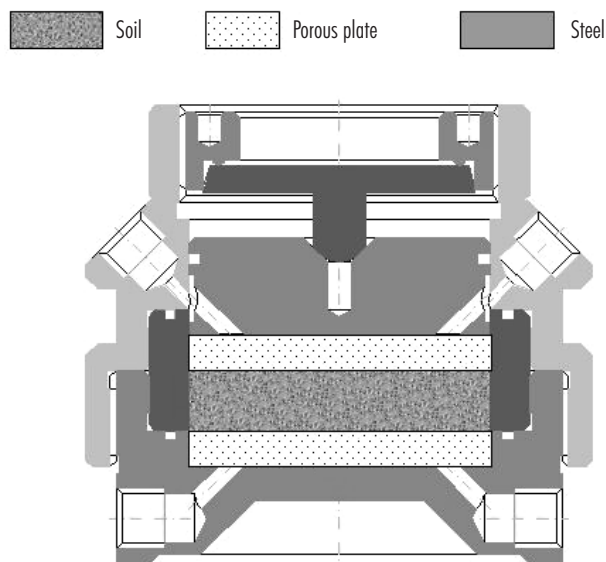


Figure 16: Schematic representation of the cell designed by CIMNE to determine the retention curves at constant volume.

loading system displays a maximum deformability of  $42.5 \mu\text{m}/\text{MPa}$  (middle point of the loading system).

CIEMAT carried out the determination of the retention curve at constant volume following a wetting path from 130 to 1 MPa, followed by a drying path of up to 130 MPa for dry densities of 1.60, 1.65 and  $1.70 \text{ g}/\text{cm}^3$ . The determination was performed at  $20^\circ\text{C}$ . Sulphuric acid solutions were used to control the suction in the desiccators where the cells are placed. The initial water content of the samples was the hygroscopic one (about 14 percent). The results obtained are shown in Table A.1 (Appendix A) and plotted in Figure 17. Although there are no major differences between the water content curves for the different dry densities –probably due to the fact that they are very close values– at the beginning of hydration the water content of the samples with a higher dry density is greater for the same values of suction. However, when lower values of suction are reached, the water content of the denser samples is lower. This occurs because the volume of small pores is higher in samples with a higher dry density, due to the fact that the volume of large pores is reduced during compaction, as a result of which the sample takes up more water at the beginning of hydration.

However, as suction decreases and the degree of saturation increases, the lower total porosity of the samples of greater density limits their possibility for water uptake (Villar 2000). Consequently, the repercussion of initial dry density on the value of water content reached is more obvious as suction decreases. On the other hand, the difference between wetting and drying paths is significant, although it must be taken into account that the density change cannot be controlled during the drying sequence, and it increases as indicated in the Table A.1 (Appendix A).

CIMNE has used the new cells (Figure 16) and is determining the water retention curves at  $22^\circ\text{C}$  on specimens compacted at dry densities of 1.55 and  $1.65 \text{ g}/\text{cm}^3$ . Suction was controlled by means of saturated salt solutions. Figure 18 and Table A.2 show the results obtained in terms of suction-water content relationship. Furthermore some measurements of swelling pressure evolution during suction changes were performed using instrumented cells; Figure 19 shows an example of the measurements carried out during a suction decrease step. One of the advantages of the system is the reduction in the time necessary to reach the equilibrium by means of the forced air flow; in the case presented in the fig-

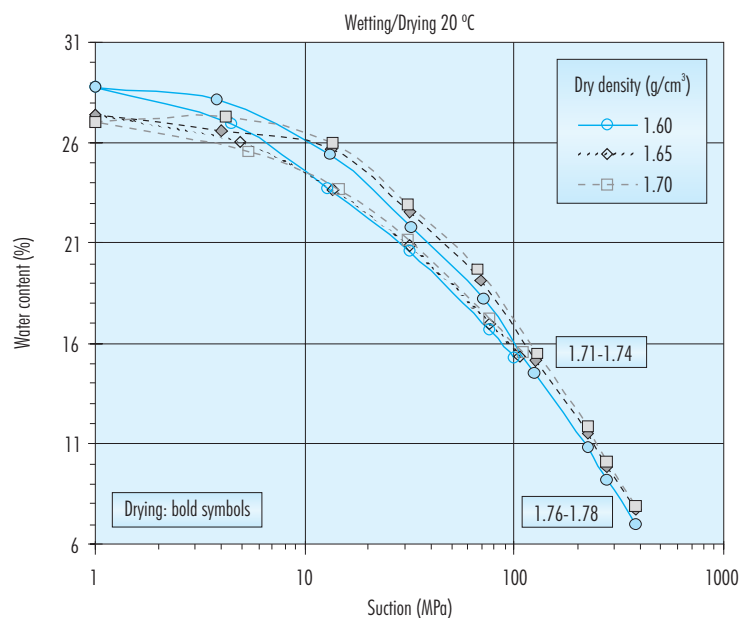


Figure 17: Retention curve at constant volume and at  $20^\circ\text{C}$  in a wetting/drying path (CIEMAT). The dry densities during the drying path are indicated in  $\text{g}/\text{cm}^3$ .

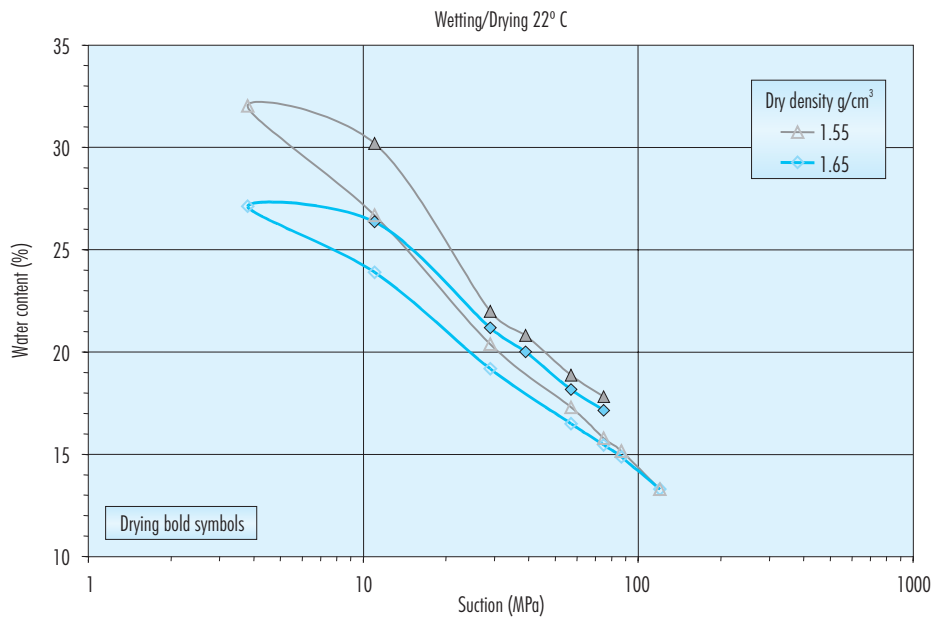


Figure 18: Retention curve at constant volume and at 22° C in a wetting/drying path (CIMNE).

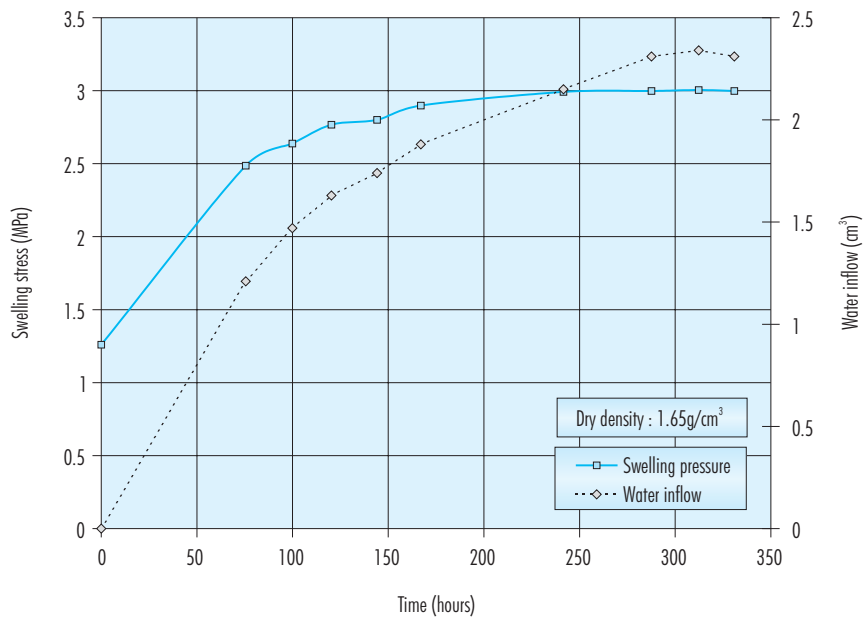


Figure 19: Evolution of swelling pressure and water inflow due to a change of suction from 57 MPa to 3.7 MPa at the ends of a bentonite specimen (initial dry density 1.65 g/cm³, height 1.05 cm).



ure, this equilibrium is reached in only 13 days. In Figure 20 the evolution of swelling pressure of two samples, due to all suction changes, is presented. These values (Table A.3 in Appendix A) are lower than the swelling pressure values measured in suction controlled oedometer tests during FEBEX I project (Figure 7, UPC 1999). This fact is due to some swelling pressure release caused by the loading system deformability. Figure 21 shows the stress–suction paths followed by the two samples tested, in comparison with the results of the swelling pressure tests carried out in suction controlled oedometers. Further improvements will be performed in the loading system in order to reduce its deformability.

### 3.1.3 Suction and temperature controlled oedometer tests

CIEMAT has performed suction and temperature controlled tests in suction-controlled oedometers, by means of sulphuric acid solutions that were already used during FEBEX I and whose schematic representation is shown in Figure 22.

The granulated clay is compacted with its hygroscopic water content inside the oedometer ring at a

dry density of  $1.70 \text{ g/cm}^3$  (except for test EDSC\_1, compacted at  $1.60 \text{ g/cm}^3$ ). The height of the specimens was 1.2 cm and its diameter 3.8 or 5.0 cm. Once in the oedometer cell, the samples are initially heated under a suction of 130 MPa (corresponding to the relative humidity of the laboratory) and a vertical pressure of 0.1 MPa. Afterwards, two different stress paths were followed (Figure 23):

- Test type E5: the sample is loaded using steps up to 5 or 8 MPa and finally, hydrated by reducing the suction to 4 or 1 MPa. In some cases, and in order to shorten the total duration of the tests, the duration of each loading step was fixed to 7 days and, in the case of suction reduction steps, to 20 days.
- Test type E6: Suction is decreased from the initial value to a minor value (3–6 MPa) maintaining a low vertical load (0.1 MPa). The sample is then vertically loaded under this value of suction up to the maximum value permitted by the equipment (9 MPa). In some tests the sample was finally unloaded.

A summary of the tests performed can be found in Table VI. Tests performed at  $20 \text{ }^\circ\text{C}$  following the same paths have also been included for compari-

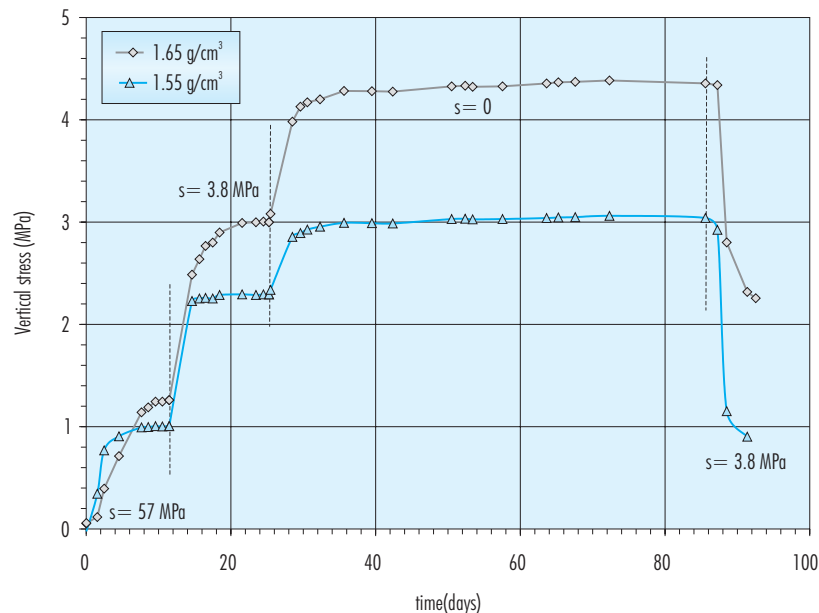


Figure 20: Evolution of swelling stress during a suction reduction/increment path in two samples of compacted bentonite.

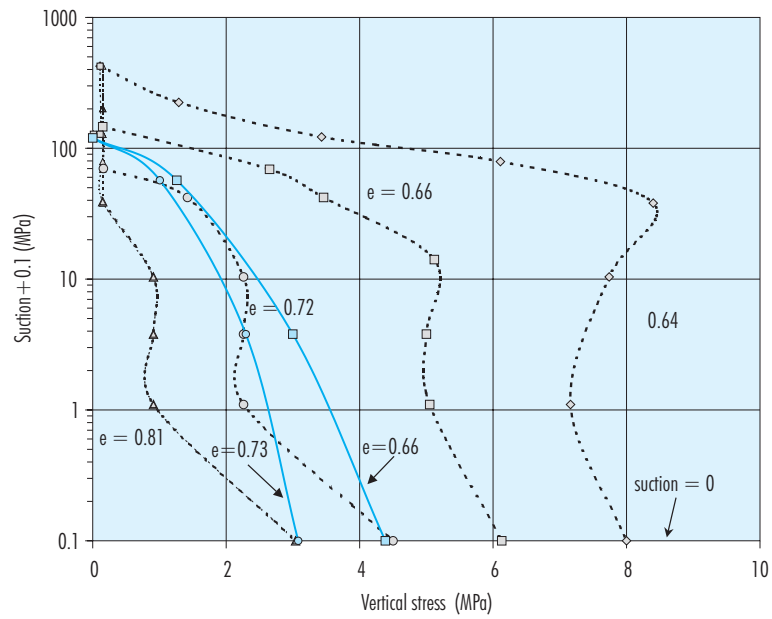


Figure 21: Vertical stresses measured during suction changes in retention curve determination in constant volume tests. Dashed lines correspond to swelling tests carried out in a suction controlled oedometer during FEBEX I project (Lloret et al. 2002).

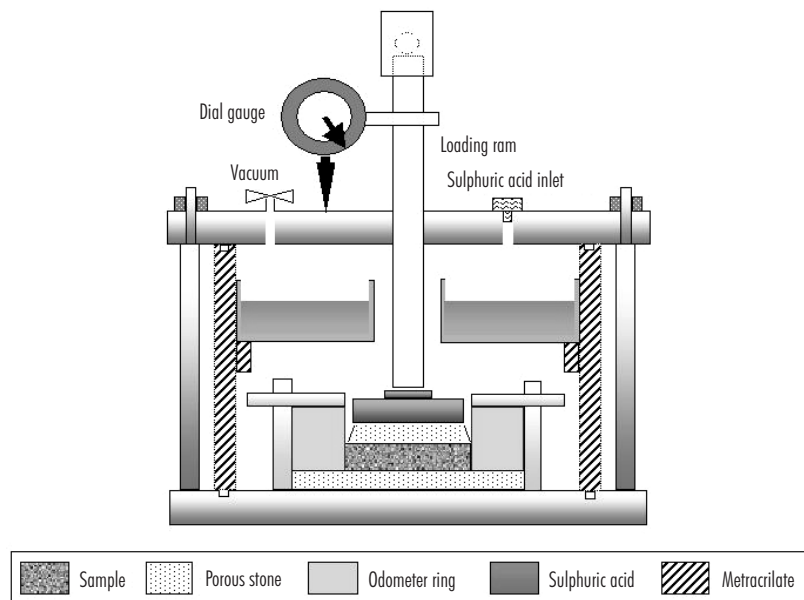


Figure 22: Schematic cross section of an oedometric cell with a deposit for solutions.

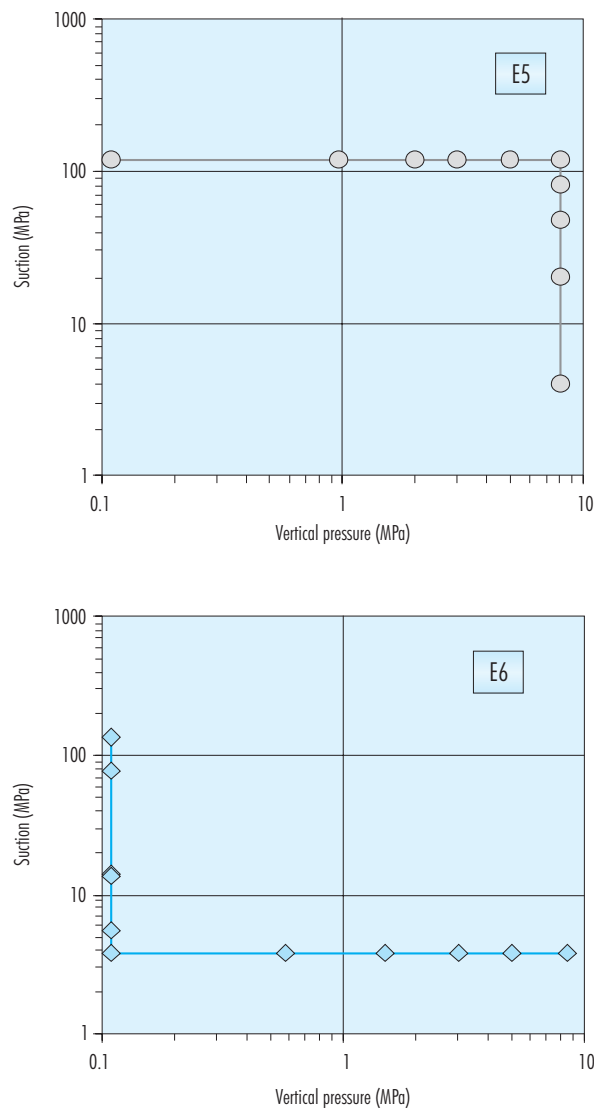


Figure 23: Stress paths for the suction and temperature controlled oedometric tests.

son. Two of them were already presented in Villar (2000, 2002). It has not been possible to carry out all the tests at high temperature foreseen, due to recurring breakdowns of the equipment. In fact, some of the results of the tests performed at high temperature must be considered preliminary. On the other hand, the possible effect of sulphuric vapour on the behaviour of the bentonite is unknown.

Path E5 starts by stabilising the sample at the suction corresponding to its equilibrium water content

(130 MPa) under a minor load (0.1 MPa). The void ratio of the tests performed at 50 °C increases during this first step, which does not happen in the tests performed at 20 °C, as seen in Figure 24. There is not a clear explanation for this observation, which could be due to the thermal expansion of the soil. However this expansion is higher than the one measured previously in FEBEX bentonite (linear thermal expansion of about 0.5% in unconfined samples heated from 20°C to 50°C (ENRESA 2000, Romero *et al.* in press)) and it could be an experimental arti-

Table VI  
Summary of the oedometer tests performed with suction and temperature control.

Reference	Type of path	Temperature (°C)	Initial $\rho_d$ (g/cm <sup>3</sup> )	Initial w (%)	Maximum vertical pressure (MPa)	Minimum suction (MPa)
EDS1_10*	E5	20	1.68	13.7	9	4 / 1
EDS1_13	E5	20	1.70	13.7	8	1
EDS5_8	E5	20	1.70	13.6	5	1
EDSC_6	E5	50	1.72	12.5	8	1
EDSC_8	E5	50	1.70	14.3	8	4
EDS2_9*	E6	20	1.71	12.9	8	4 / 1
EDS3_11	E6	20	1.72	13.2	9	3 / 1
EDSC_1	E6	40	1.60	11.0	9	6
EDSC_2	E6	40	1.72	12.3	0.1	51
EDSC_3	E6	60	1.70	13.5	9	4

\*Tests already presented in Villar (2000, 2002).

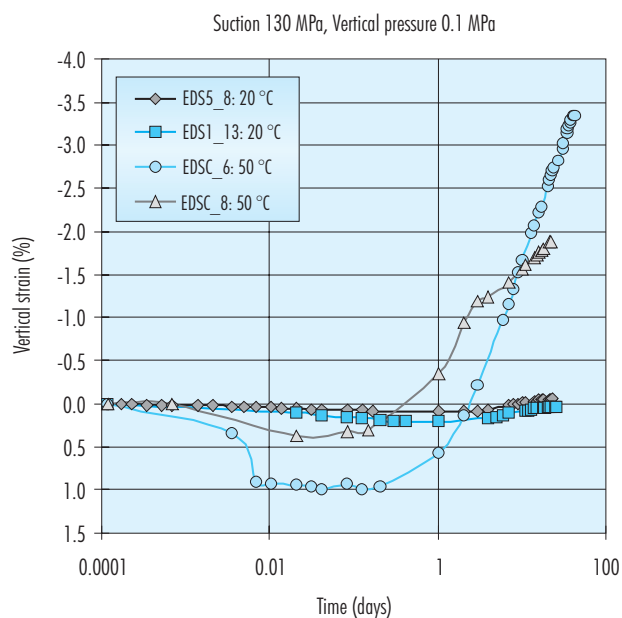


Figure 24: Evolution of vertical strain in the first step of oedometric tests following path E5 in Table VI (suction 130 MPa, vertical pressure 0.1 MPa).

fact. This initial difference determines the subsequent behaviour of the samples during the tests, which is shown in Figure 25. Although the stiffness of the soil, when loaded at hygroscopic conditions, becomes evident for all the temperatures, the compressibility during loading of samples tested at 50 °C is higher than for samples tested at 20 °C. This could be simply a consequence of the different void ratio at the beginning of compression. As it has been observed in saturated materials, temperature

increases the compressibility of bentonite. As in saturated soils, a reduction in the size of the elastic domain with the temperature can be observed (Hueckel & Borsetto 1990), in this case the apparent preconsolidation stress is only about 3 MPa when the temperature is 50°C and it is higher than 20 MPa when the temperature is 20°C.

The behaviours of the samples during wetting under a high vertical load were diverse and apparently not

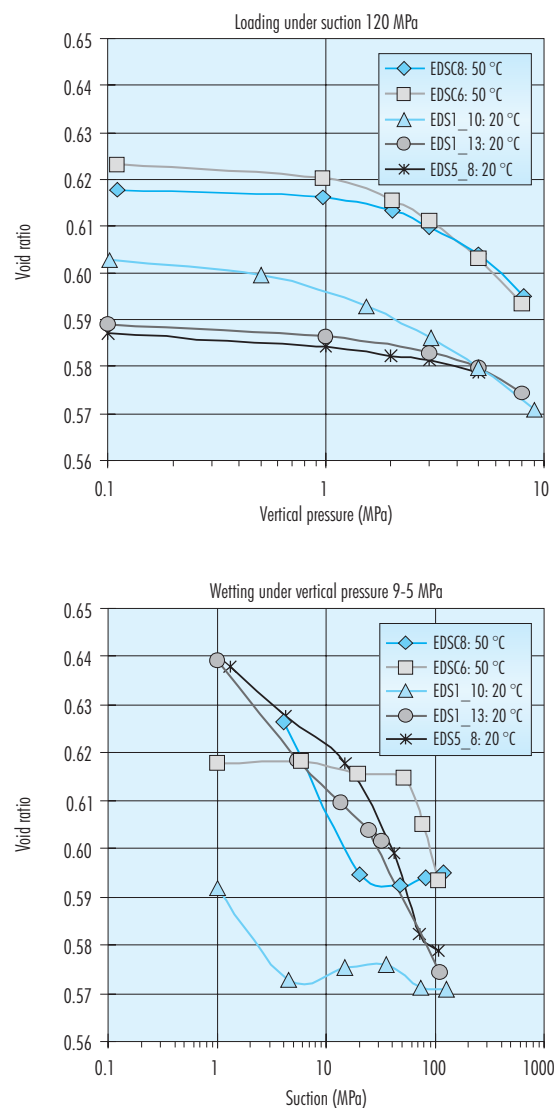


Figure 25: Evolution of void ratio in the different steps of the loading and wetting paths performed in suction controlled oedometers at different temperatures following path E5 in Table VI (initial nominal dry density 1.70 g/cm<sup>3</sup>).

determined by temperature. Overall the initial void ratios are recovered, although two tests suffered a small collapse at the beginning of wetting (EDS1\_10 and EDSC\_8).

The results of the tests performed following path E6 are plotted in Figure 26. The increase in void ratio during the initial wetting under a low vertical load is important in all tests. No different behaviour can be observed as a consequence of temperature. In the subsequent loading, the initial void ratio is not recov-

ered in any test, due to the irreversible macrostructural strains induced by microstructural deformations that occurred during the previous swelling to low suction values (Lloret *et al.* 2003). The comparison of the curves obtained during loading at different temperatures and constant suction (tests EDS3\_11 at 20 °C and EDSC\_3 at 60 °C) suggests that temperature increases the compressibility of bentonite and that some reduction in the size of the elastic domain with temperature takes place (Hueckel & Borsetto 1990).

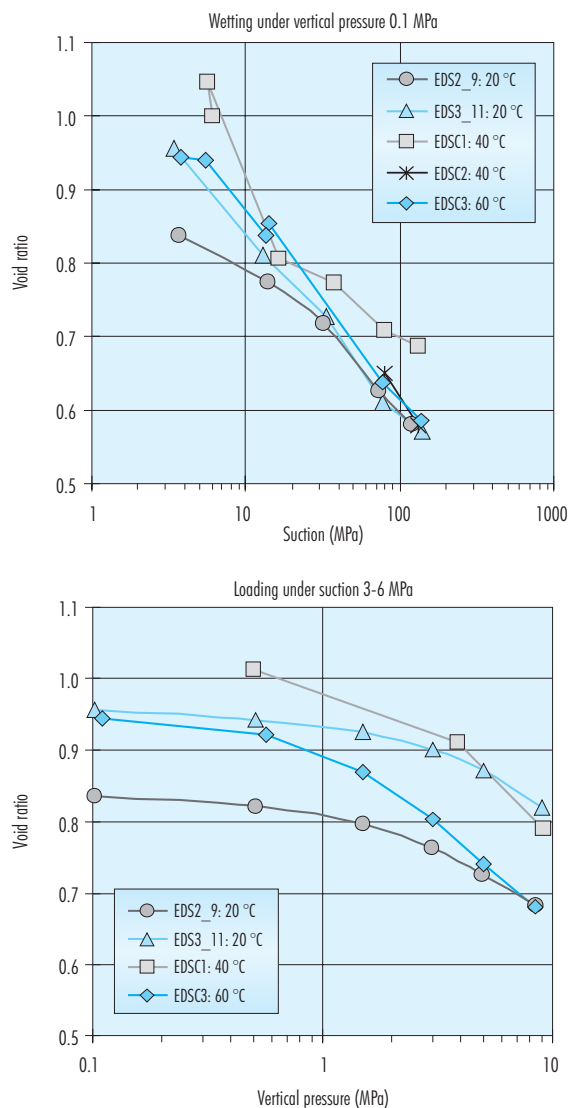


Figure 26: Evolution of void ratio in the different steps of the wetting and loading paths performed in suction controlled oedometers at different temperatures following path E6 (initial nominal dry density 1.70 g/cm<sup>3</sup>, except for EDSC1: 1.60 g/cm<sup>3</sup>).

The two paths tested have approximately the same initial and final states with respect to suction and vertical stresses. In particular, for test EDS1\_13 the path followed consisted in loading up to 8 MPa under a constant suction of 130 MPa and then wetting under this high vertical load. For test EDS3\_11 the path followed (E6) consisted in wetting under a constant vertical load of 0.1 MPa, and then loading to 9 MPa under a constant suction of 3 MPa. In Figure 27 the final void ratio of each step of the two tests is plotted against the correspondent suction or vertical load. As both variables have the same units, they are represented in the same axis (wetting paths are indicated with bold symbols). It becomes clear that when wetting takes place under a low vertical load (test EDS3\_11), the void ratio increases largely and the external load applied later is not able to counteract this swelling. However, if swelling during saturation is prevented by previous loading (test EDS1\_11), the final volume change is smaller.

These tests are an example of the irreversible macroscopic deformation induced by microstructural swelling, whose magnitude (of the plastic deformation) is stress-path dependent (Gens & Alonso 1992).

The same remarks could be made when comparing the results of tests EDSC\_8 (path E5) and EDSC\_3 (path E6) plotted in Figure 28. These tests were performed under temperatures of 50 and 60 °C, respectively. The behaviour of bentonite at high temperature is similar to that observed at 20 °C (Figure 27), which would suggest that the repercussion of the stress path on bentonite deformation is higher than that of temperature. The only significant difference between the tests performed at laboratory and those performed at high temperature, is the higher compressibility of quasi-saturated bentonite upon loading at high temperature (test EDSC\_3 with respect to test EDS3\_11), which has already been commented.

### 3.1.4 Infiltration tests in different conditions, interpreted by full modelling analysis

The back-analysis of infiltration tests allows the calibration of numerical models and the adjustment of parameters that are difficult to obtain by direct measurement. In the infiltration tests, compacted blocks of clay are introduced in a hermetic cell and satu-

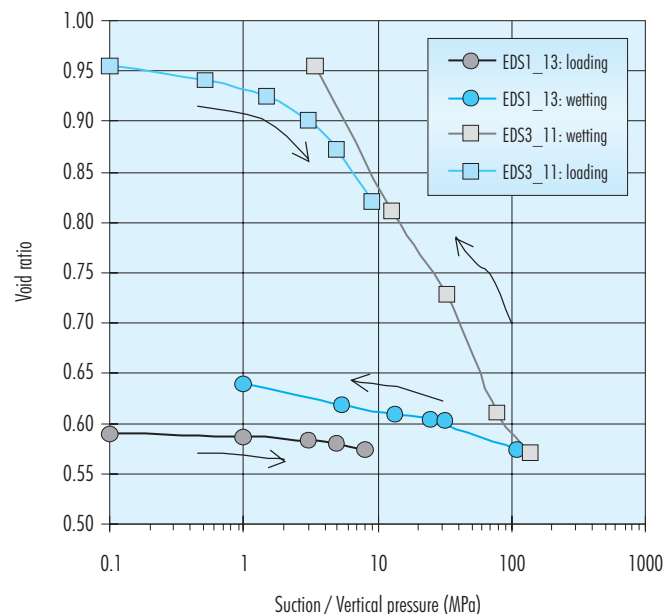


Figure 27: Comparison of void ratios at the end of each step on paths E5 (test EDS1\_13) and E6 (test EDS3\_11) performed in oedometers with control of suction at 20 °C (see Table VI for detailed stress paths).

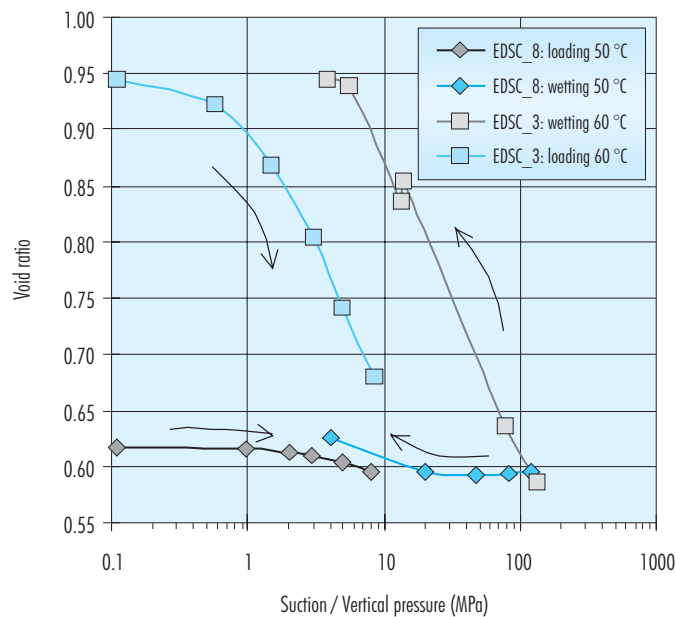


Figure 28: Comparison of void ratios at the end of each step on paths E5 (test EDSC\_8, 50 °C) and E6 (test EDSC\_3, 60 °C) performed in oedometers with control of suction at high temperature (see Table VI for detailed stress paths).

rated through the top, while thermal gradients may be applied. After a pre-fixed time, the cell is disassembled and the water content of clay is determined at different distances from the hydration front. If the infiltration test is performed with thermal gradients, the tortuosity factor that is involved in vapour flux modelling may also be obtained or validated.

The FEBEX bentonite response under the small-scale test conditions is very complex, due to the physical processes and interactions that take place during the simultaneous heating and hydration of clay under conditions of practically constant volume. Because of that, a coupled THM analysis becomes necessary, in order to simulate this problem. The THM formulation proposed by Olivella *et al.* (1994), was adopted as a general framework for the analyses, and the finite element code CODE\_BRIGHT (Olivella *et al.* 1996) was used to analyze small-scale tests as a boundary value problem. The simulations intend to reproduce the evolution of the main variables of the tests (water intake and temperature) and also the experimental data coming from the postmortem study. Regarding these studies, it is important to highlight that the most of the constitutive laws and parameters considered in the analyses are

the same as those adopted for the Operational Base Case (OBC) model of the “mock-up” test (ENRESA 2000). In that sense, the results obtained in this study are some kind of model predictions that allow the increment of confidence in the constitutive equations and parameters used.

The theoretical framework of numerical modelling is composed of three main parts: balance equations, constitutive equations and equilibrium restrictions. Regarding the mechanical problem, an extension of the constitutive model known as BBM (Barcelona Basic Model), which includes thermal effects, was adopted. A detailed derivation is given in Olivella *et al.* (1994), Gens (1995) and UPC (1997), and only a brief description of the most relevant constitutive equations and parameters is included in Appendix B.

### 3.1.4.1 Tests in 60-cm long cells

These tests were performed by CIEMAT during the phase I of FEBEX project (Villar 2001). Cylindrical cells with an inner length of 60 cm and a diameter of 7 cm were constructed (Figure 29). They are made of Teflon to prevent as much as possible lateral heat conduction and externally covered with steel semi-





Figure 29: Experimental set-up for the thermo-hydraulic tests (CIEMAT).

cylindrical pieces to avoid the deformation of the cell by bentonite swelling. Inside the cells, six compacted blocks of bentonite were piled-up, giving rise to a total length similar to the thickness of the bentonite barrier of the “mock-up” test of the FEBEX Project. To obtain the blocks, the clay with its hygroscopic water content (around 14 percent) was uniaxially compacted at a dry density of  $1.65 \text{ g/cm}^3$ .

The bottom part of the cell is a plane heater whose temperature is fixed to  $100 \text{ }^\circ\text{C}$ , which is the temperature expected on the surface of the waste container in the Spanish concept. Over the upper lid of the cell, there is a deposit in which water circulates at constant temperature ( $20\text{-}30 \text{ }^\circ\text{C}$ ). In this way, a constant gradient of  $1.1\text{-}1.3 \text{ }^\circ\text{C/cm}$  between top and bottom of the sample is imposed. Granitic water of a salinity of 0.02 percent is injected through the upper lid of the cell at a pressure of 1.2 MPa. This simulates the water that saturates the barrier in a repository excavated in granitic rock, and it is the same as that employed to saturate the “mock-up” test of the FEBEX Project (ENRESA 2000).

The duration of the tests was of 6 (test FQ1/2), 12 (test FQ1) and 24 (test FQ2) months. During the tests, the temperatures at different positions inside

the clay were measured by means of thermocouples and recorded, as well as the volume of water intake. The 5 thermocouples, T1 to T5, were placed at 50, 40, 30, 20 and 10 cm from the heater. At the end of the thermo-hydraulic treatment, the cell is dismantled and the clay blocks extracted. As the blocks are extracted, they are cut into cylindrical sections of 2.5 cm in thickness in which dry density and water content are determined.

The evolutions of temperature at different locations inside the clay and of the water intake during the 24-month test are shown in Figure 30. The repercussion of the laboratory temperature on the temperatures inside the clay was noticeable. The average temperatures recorded by each thermocouple for the period between 1000 hours after the beginning of the test and the end of the test are plotted in Figure 31 for three tests of different duration. There is a sharp temperature gradient in the vicinity of the heater, the temperature decreasing from  $100 \text{ }^\circ\text{C}$  in the heater surface to  $50 \text{ }^\circ\text{C}$  at 10 cm from it inside the clay. On the other hand, a decrease in temperature with saturation (longer tests) is observed, especially in the wetter zones, i.e. within the closest 20 cm to the hydration surface. This is due to the higher heat dissipation of wet clay.

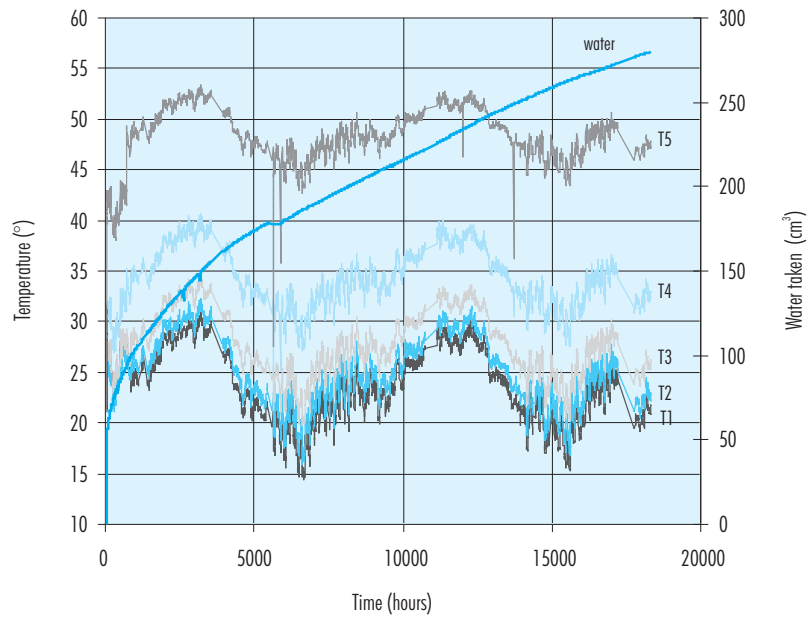


Figure 30: Evolution of temperatures at different locations inside the clay (T1 to T5, 50 to 10 cm from the heater) and of water intake in the 24-month test.

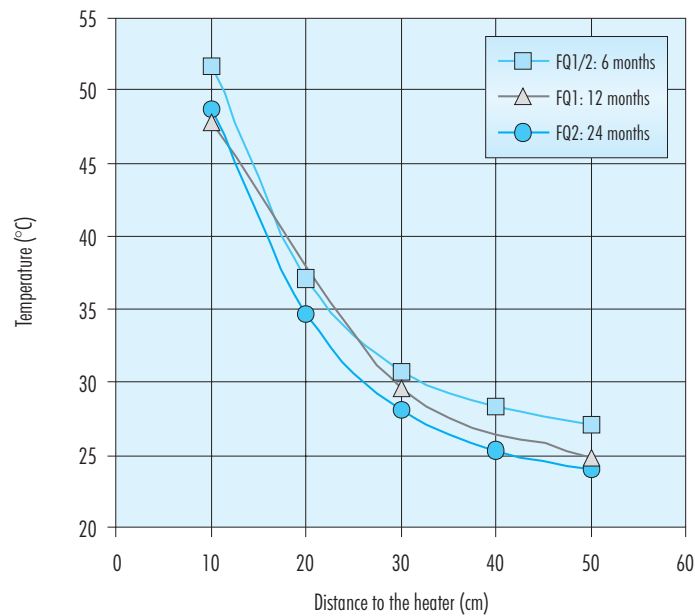


Figure 31: Average steady temperatures at different positions for three tests of different duration.

The final distribution of water content for three tests is shown in Figure 32. The water content reduction due to the temperature effect is similar for the three tests, which means that desiccation takes place rather quickly and only affects the 18 cm closest to the heater, where the water contents are lower than the initial ones, which were around 14 percent. In the 6-month test, there is a central zone, between 20 and 40 cm, in which the initial water content is barely modified. The effect of hydration, which is evident only in the closest 20 cm to the hydration surface in the 6-month test, is noticeable in the 40 upper centimetres at 12 months. In the next 12 months, the water content increases in these 40 upper centimetres, but does not change in the 18 cm closest to the heater, probably because in this zone the thermal effect is still predominant.

The final distribution of bentonite dry density is plotted in Figure 33. Dry density decreases from the heater towards the hydration surface with an approximately linear tendency. In the zones affected by hydration, dry density decreases below the initial value ( $1.65 \text{ g/cm}^3$ ), due to the expansion caused by saturation. On the contrary, near the heater, dry density increases, due to the shrinkage caused by desiccation. Despite the dispersion of data –caused

by the initial in-homogeneities and by the determination method–, it can be observed that the densities reached near the hydration surface are lower in the longer tests, due to the fact that their saturation and, consequently, their swelling deformation, is higher. Due to this density decrease, the degrees of saturation are lower than what could be expected by the high water content. In fact, a degree of saturation higher than 90 percent is only reached in the 3 cm closest to the hydration surface after 6 months of TH treatment, in 8 cm after 12 months and in 10 cm after 24 months.

On the other hand, near the heater (18 cm) the density remains the same from 6 to 24 months, and the degrees of saturation decrease from the initial 55-60 percent to values around 25 percent in the vicinity of the heater. An overall decrease of dry density was observed, since the average value measured was  $1.57 \text{ g/cm}^3$  for the 6 and 12-month tests and  $1.55$  for the 24-month tests, whereas the initial dry density of the blocks was  $1.65 \text{ g/cm}^3$ . This is due to the fact that the cells are made of Teflon, a material which slightly deforms because it is not able to withstand the high swelling pressure developed by clay as it saturates. This overall decrease of dry density is linked to the hydration of clay, and for

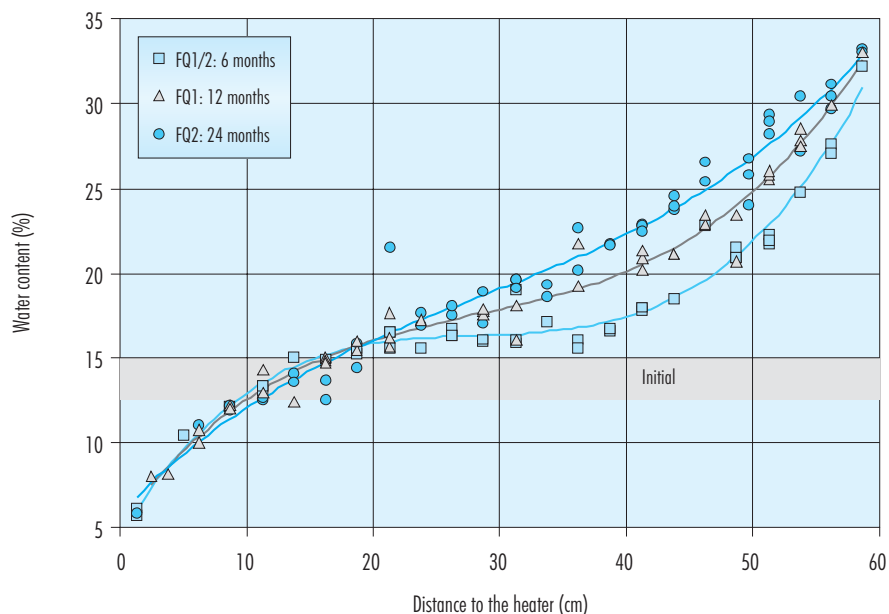


Figure 32: Final distribution of water content for tests of different duration.



Figure 33: Final distribution of dry density for tests of different duration.

this reason, is more important for the longer tests that have reached a higher degree of saturation.

The model parameters related to thermo-hydraulic behaviour that were used in the numerical analysis of the tests are shown in Table VII. The mechanical

model parameters, which are shown in Table VIII, were identified in the preoperational stage of the FEBEX project (UPC 1997). All parameters are basically the same as those adopted for the Operational Base Case (OBC) model of the “mock-up” test (ENRESA 2000).

**Table VII**  
Model parameters related to the thermo-hydraulic problem in the infiltration tests in 60-cm long Teflon cells. (See definition of parameters in Appendix B).

Intrinsic permeability	$k_0$ [m <sup>2</sup> ]	$b$	$\Phi_0$	
	$1.9 \cdot 10^{-21}$	30	0.40	
Relative permeability	$n$	$S_h$	$S_s$	
	3	0	1	
Retention curve	$P_o$ [MPa]	$\lambda_o$	$P_d$ [MPa]	$\lambda_d$
	28	0.18	1100	1.1
Vapour diffusion	$\tau$			
	0.8			
Thermal conductivity	$\lambda_{dry}$ [W/m°C]	$\lambda_{sat}$ [W/m°C]		
	0.47	1.15		

**Table VIII**  
**Model parameters (BBM model) related to the mechanical problem in the infiltration tests in Teflon cells.**  
**(See definition of parameters in Appendix B)**

$\kappa$	0.04	$\kappa_s$	0.25
$\nu$	0.4	$\alpha_{js}$	-0.003
$\alpha_{sp}$	-0.147	$\alpha_{ss}$	0.00
$\alpha_o$	$1.5 \times 10^{-4} (^{\circ}\text{C}^{-1})$	$\alpha_2$	0.00
$\lambda_0$	0.15	$p_c$	0.10 MPa
$p_0^*$	14 MPa	$\alpha$	0.395
$r$	0.75	$\beta$	0.05
$M$	1.5	$T_0$	20 °C
$k$	0.1	$\rho$	0.2

1-D axis-symmetrical models were used in these analyses. A mesh of 100 elements was adopted. A sensitivity analysis was also carried out to verify that the model results do not depend on the mesh. The initial and boundary conditions of the model were imposed in order to be the closest possible to the experiments. The initial water content of the bentonite block is close to 14 %, from the retention curve adopted an initial value of suction of 110 MPa was adopted. An initially uniform temperature of 22°C is assumed. Initial hydrostatic stresses of 0.15 MPa were adopted. Regarding the boundary conditions, a temperature of 100 °C was imposed in the contact between heater and bentonite (bottom of the cell), while a constant water pressure of 1.2 MPa was imposed in the other extreme of the cell (upper part). The thermal boundary condition along the sample was adopted in order to adjust the temperature field, in that sense, a temperature of 23°C was fixed with a radiation coefficient of 1. Regarding the mechanical problem, a small expansion of the cell was allowed, in order to consider the overall decrease of the dry density observed in the experiments. Finally, a constant gas pressure (0.1 MPa) was adopted in the analyses.

The 24-months test was modelled, and two sets of comparisons were presented: comparisons between evolutions of measured and computed variables, and comparisons corresponding to the analysis of the postmortem study. Figure 34 presents the evolution of temperature at different points of the cell. The cyclic variations of temperature, due to changes

in laboratory temperature, are not taken into account in the simulations. The model only intends to capture the whole thermal evolution of the test. In that sense, the temperature field is quite well reproduced.

The numerical results related to the hydraulic problem are also good, as it can be seen in Figure 35, in terms of the cumulative water intake and of the water intake rate, as well.

Concerning the comparisons related to postmortem analyses, Figure 36 presents the distribution of temperature along the sample at the end of the test. A strong reduction of the temperature in zones close to the heater (twice the imposed temperature at 10 cm) can be observed. A difference in the thermal problem between cell tests and “mock-up” experiment is that, in the first one, the dissipation of heat is greater, due to the relatively major amount of external surfaces.

The comparisons related to the distribution of water content along the cell (Figure 37) show that the results are not very good, especially in zones close to the heater. It is important to highlight that the simulation does not take into account the cooling phase, at which the samples were submitted during the dismantling of the test (before the determination of water content values). In any case, the simulations capture qualitatively well this variable. As in the ‘mock-up’ test, the effect of wetting can be observed in the lower part of the sample (approximately 10 cm), due to the condensation of water vapour coming from the bottom of the cell (where the heater is located).

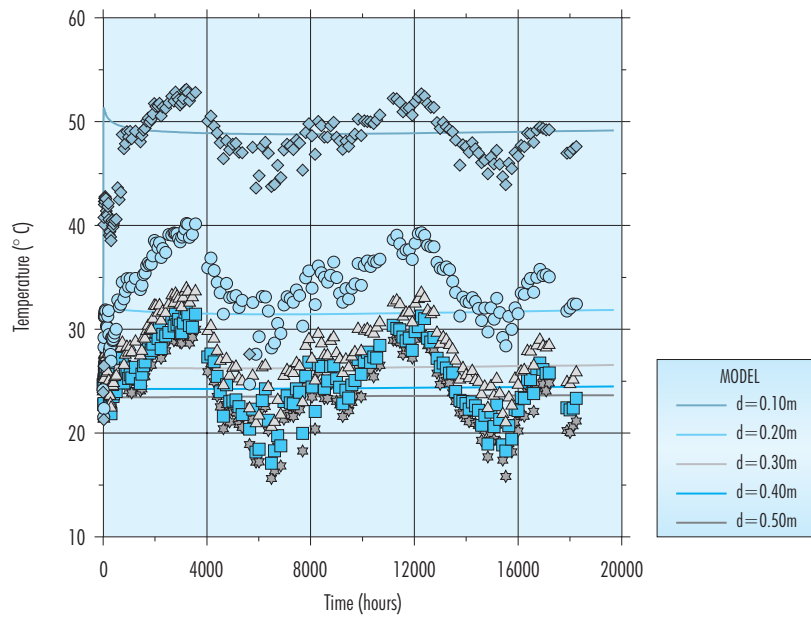


Figure 34: Evolution of temperature in the test, computed versus registered values.

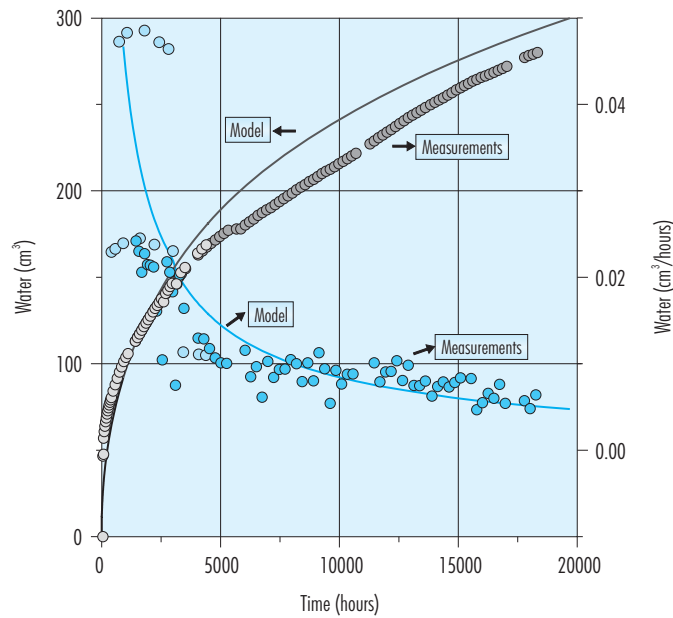


Figure 35: Computed values versus registered values of cumulative water intake and rate of water intake.

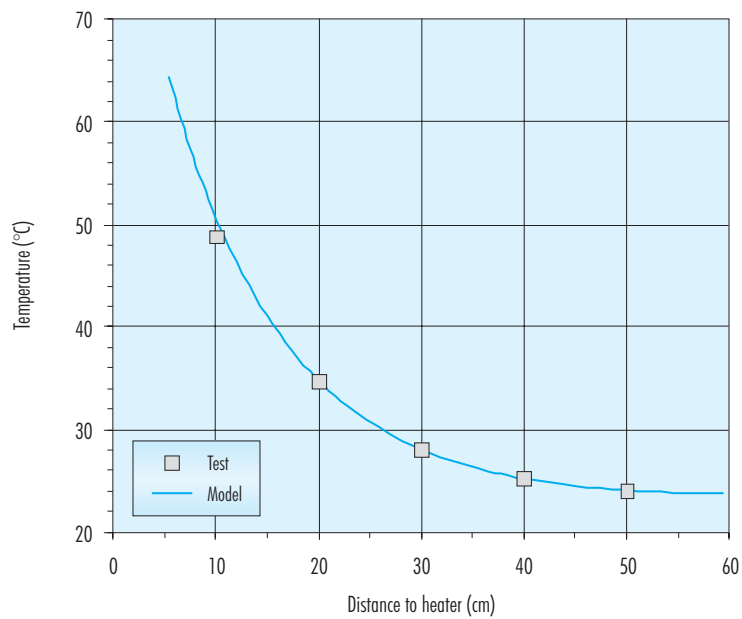


Figure 36: Distribution of temperature along the cell at the end of the 24-month test. Registered and computed values.

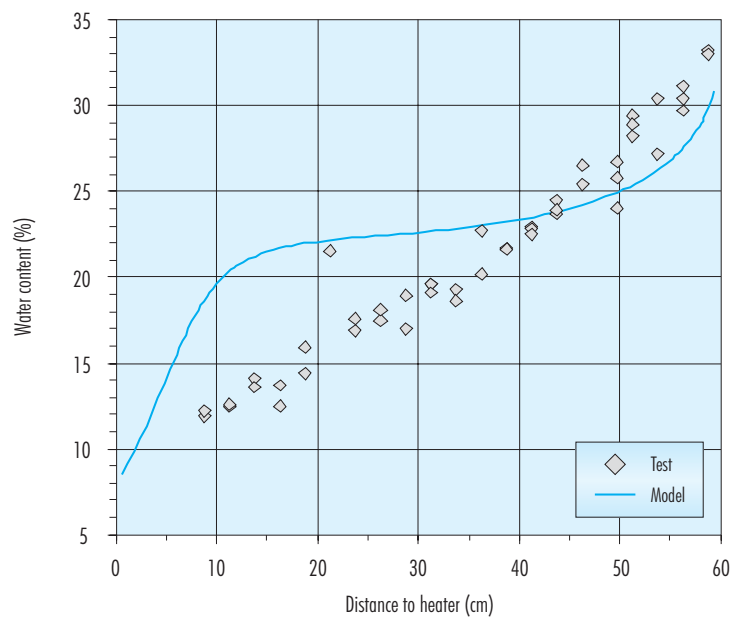


Figure 37: Distribution of water content along the cell at the end of the 24 month-tests. Registered and computed values.

Figure 38 shows the measured values of clay dry density, together with the model results. A clear density reduction can be observed in zones close to the hydration front (due to clay swelling) as well as higher densities as the distance to the heater diminishes. The model captures qualitatively the global trend of the test; but, as for water content, the agreements between model results and measurements are not good in zones close to the heater. The omission of the cooling and unload phases in the analyses could be the main reason for the discrepancies also in this case. On the other hand, it is important to have in mind that the *BBM* mechanical law is not the best one to model the behaviour of expansive clays, perhaps the adoption of a more proper mechanical model for FEBEX bentonite (*i.e.* the one described in section 3.1.1) could help to obtain better results.

Once the main variables of the problem are well captured, it is interesting to analyse its influence on other relevant variables, such as the permeability field. Generally, the main thermo-mechanical couplings considered in the permeability models are related to its dependence on dry density and on temperature (through the liquid viscosity and liquid density). Figure 39a shows the dependence of intrinsic

permeability on porosity, in this case, through the exponential model proposed (Eq. [B.8] in Appendix B). The highest intrinsic permeability is computed in zones close to the hydration front, due to the porosity increment in these areas (Figure 38). In the case of non-saturated flow, the relative permeability law implies also higher values of permeability as the clay saturation progresses (Eq. [B.9] in Appendix B). Finally, Figure 39b presents the final distribution of computed permeability, in which the effects of non-saturation and temperature are included.

### 3.1.4.2 New tests in ceramic cell

A new device was developed by CIMNE (Figure 40 and Figure 41) in order to run infiltration tests under a variety of different conditions, which were included in the initial Test Plan: isothermal conditions (22°C and 80°C), controlled temperature gradients (25°C – 80°C) and controlled heat flux (0.2 W/cm<sup>2</sup>). In order to avoid the volume changes due to deformability of Teflon cells and to reduce the lateral thermal losses of metallic cells, the sample was confined laterally by a cylinder of ceramic wall. Temperatures and swelling stresses (vertical and radial) developed during the infiltration process could be

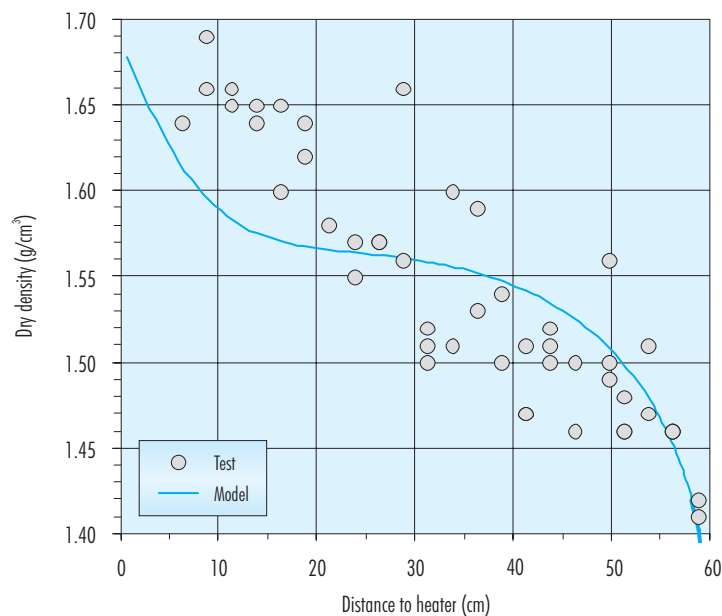


Figure 38: Distribution of dry density along the cell at the end of the 24-month test. Registered and computed values.



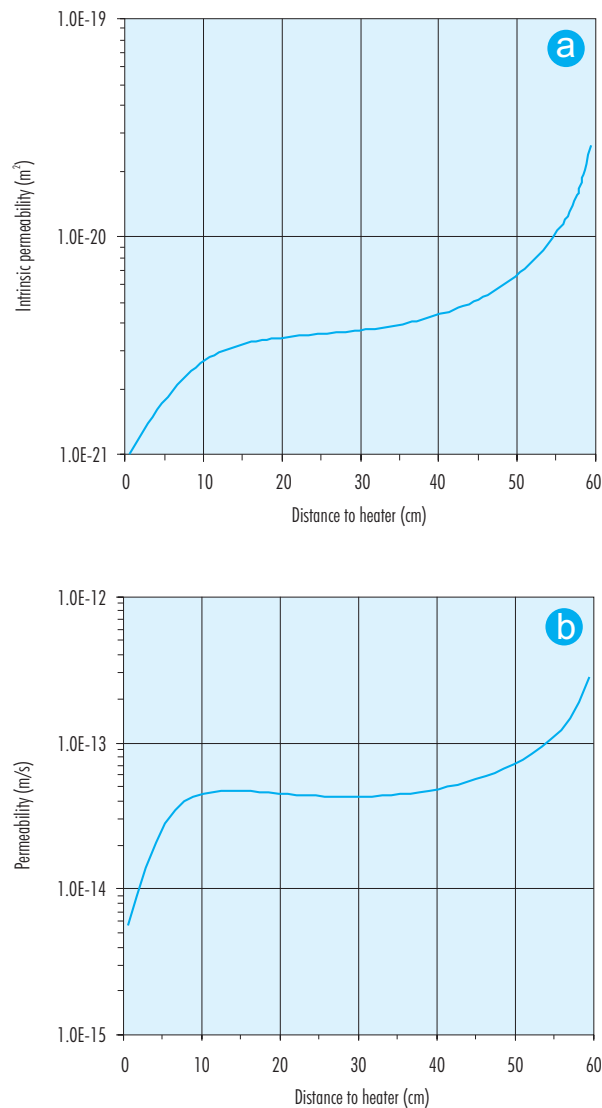


Figure 39: Computed intrinsic permeability (a) and water permeability (b) fields along the cell at the end of the 24-month test.

measured in several positions of the cell by means of thermocouples, a load cell and three total pressure sensors respectively.

In the preliminary test performed, distilled water was injected from the top of the cell under a hydraulic pressure of 0.1 MPa. The initial dry density of the specimen (70 mm in diameter and 140 mm in height) was 1.62 g/cm<sup>3</sup>, and the initial water content was 13.5%. The test was carried out in isothermal conditions at ambient temperature (22°C).

Figure 42 and Figure 43 show the results of the first preliminary test performed with this cell. The ceramic cylinder, where the soil sample was located during the test, was broken after approximately seven days from the beginning of the infiltration process, because the ceramic did not resist the swelling pressures of bentonite. Two diametrically opposed cracks were open along the cylinder walls starting, due to stress concentration, in the holes where the lateral stress gauges were located. The tendencies of water content observed in Figure 42 are similar

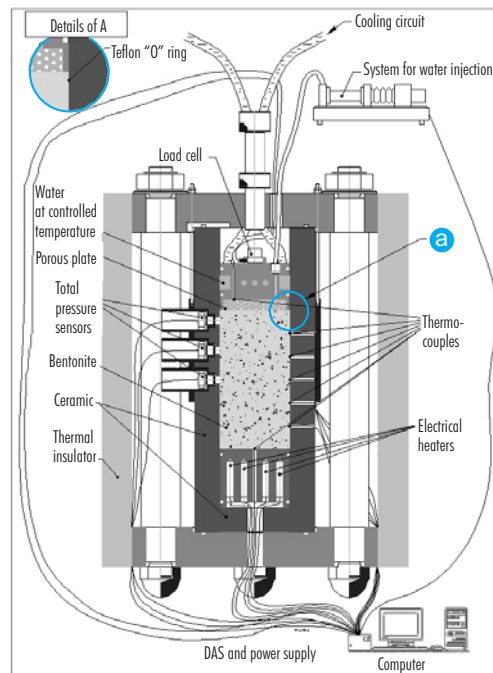


Figure 40: Schematic representation of the cell designed by CIMNE to perform infiltration tests at different temperatures.

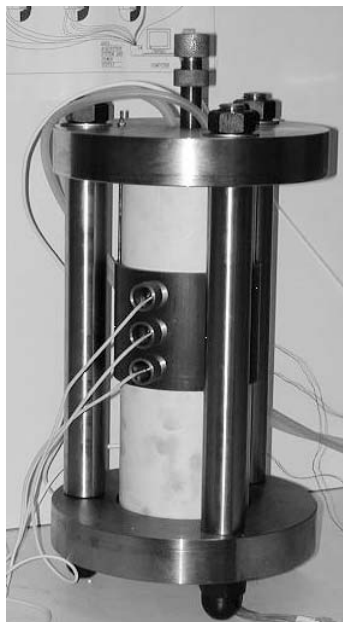


Figure 41: Cell designed by CIMNE to perform infiltration tests at different temperatures.

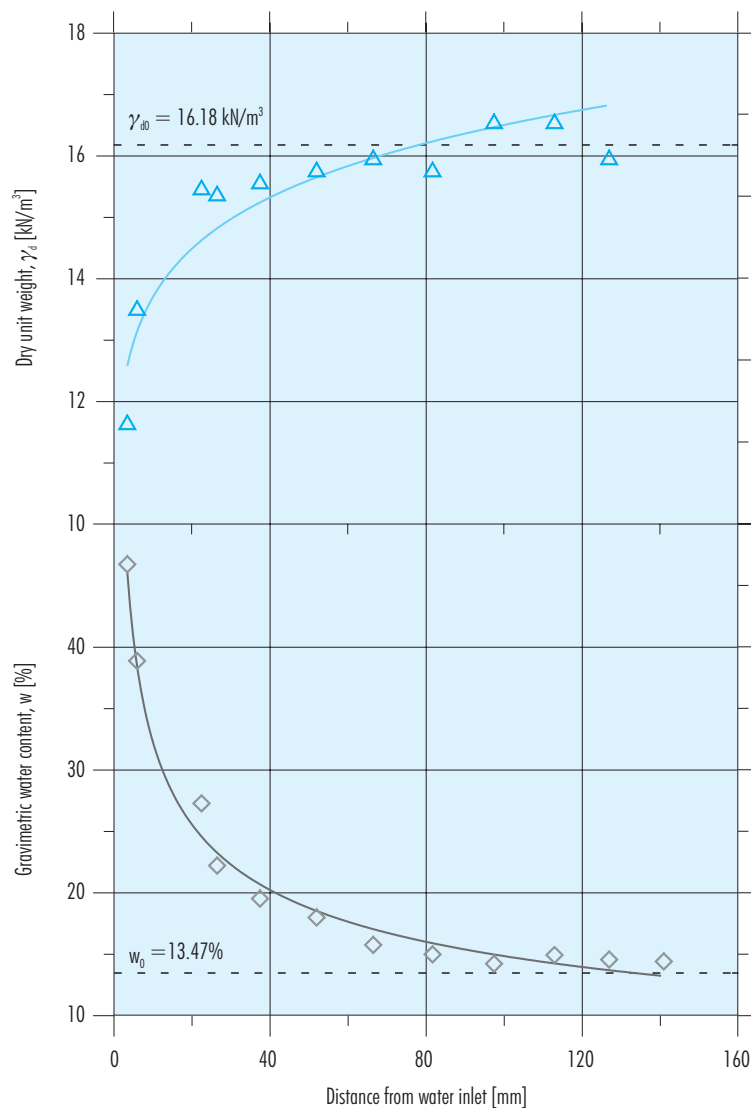


Figure 42: Preliminary results of the infiltration tests (CIMNE).

to those observed in the initial stage of the tests performed in large cells (Figure 37). On the other hand, due to the little time available, the increase in pore volume is concentrated very near of the water inlet.

In Figure 43a it is possible to see that the swelling vertical stress increased sharply; the stress increases more quickly than in other cases (“mock-up” and “in situ” experiments). This was due to the inexistence of gaps between bentonite blocks or between the bentonite and the cell walls since in the current tests, before beginning the experiment, the top cap

was adjusted on the sample and then was fixed to the load cell using a screw (Figure 40).

The test was modelled using the same numerical approach described in the previous section but in this case, isothermal conditions were considered. Vertical and lateral mechanical confinement was imposed until the failure of the ceramic wall, after that, the radial stresses were reduced in order to simulate the loss of lateral confinement. Table IX and Table X show the model parameters used in the analysis; in general, the parameters are the same as those pre-

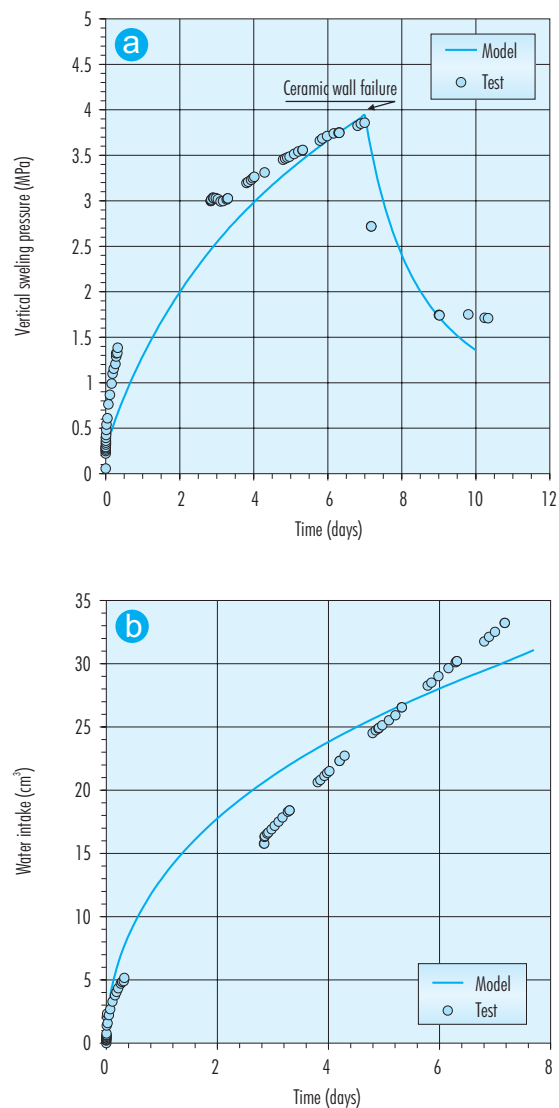


Figure 43: Evolution of swelling pressure and accumulated water intake in an infiltration test performed in the ceramic cell (CIMNE).

sented in the analysis of infiltration in the 60-cm long cells. Only small differences with the parameters shown in the Table VII and Table VIII were introduced in order to take into account the effect of the different dry density of the bentonite on the retention curve (parameter  $P_0$  in Table IX) and the inexistence of gaps between blocks on the swelling pressure development (parameters  $\kappa$ ,  $\kappa_s$  and  $\alpha_{is}$  in Table X).

The evolution of computed vertical swelling stress and water intake is shown in Figure 43, whereas

Figure 44 shows the profiles of water content and dry unit weight. A reasonable agreement is obtained between measured and computed values of the different variables. In particular, the decrease in vertical swelling strain after the failure of the confining cylinder was properly reproduced. Better results would have been obtained if a process of systematic curve fitting had been made; nevertheless, in this case the objective was to validate the model and the parameters used in the modelling of real scale experiments.

**Table IX**  
**Model parameters related to the thermo-hydraulic problem in the infiltration test in ceramic cell.**  
**(See definition of parameters in Appendix B).**

Intrinsic permeability	$k_0$ [m <sup>2</sup> ]	b	$\Phi_0$	
	1.9 10 <sup>-21</sup>	30	0.40	
Relative permeability	$N$	$S_{lr}$	$S_{ls}$	
	3	0	1	
Retention curve	$P_o$ [MPa]	$\lambda_o$	$P_d$ [MPa]	$\lambda_d$
	15	0.18	1100	1.1
Vapour diffusion	$\tau$			
	0.8			

**Table X**  
**Model parameters (BBM model) related to the mechanical problem in the infiltration tests in the ceramic cell.**  
**(See definition of parameters in Appendix B).**

$\kappa$	0.05	$\kappa_s$	0.38
$\nu$	0.4	$\alpha_{ls}$	-0.008
$\alpha_{sp}$	-0.147	$\alpha_{ss}$	0.00
$\alpha_o$	1.5x10 <sup>-4</sup> (°C <sup>-1</sup> )	$\alpha_2$	0.00
$\lambda_o$	0.15	$\rho_c$	0.10 MPa
$\dot{p}_o$	14 MPa	$\alpha$	0.395
$r$	0.75	$\beta$	0.05
$M$	1.5	$T_o$	20 °C
$k$	0.1	$\rho$	0.2

## 3.2 New T-H-M tests

Most of the THM tests carried out during FEBEX I were made under “standard conditions” (isothermal, at laboratory temperature...). However, it was observed that many parameters controlling the THM behaviour of the bentonite, which are very critical in terms of the sensitivity of the THM models to their variation, change significantly when the boundary conditions (temperature, swelling strains...) are different. The objective of the new THM tests is the determination of variations in critical parameters of the

buffer caused by changes in temperature, saturation, microstructure of bentonite, and chemical composition of porewater. As a result, improved knowledge of the variations introduced in the THM behaviour and bentonite parameters will be gained.

### 3.2.1 Temperature influence on the hydro-mechanical properties of the clay

The influence of dry density and water content on most of the properties of FEBEX bentonite was tested,

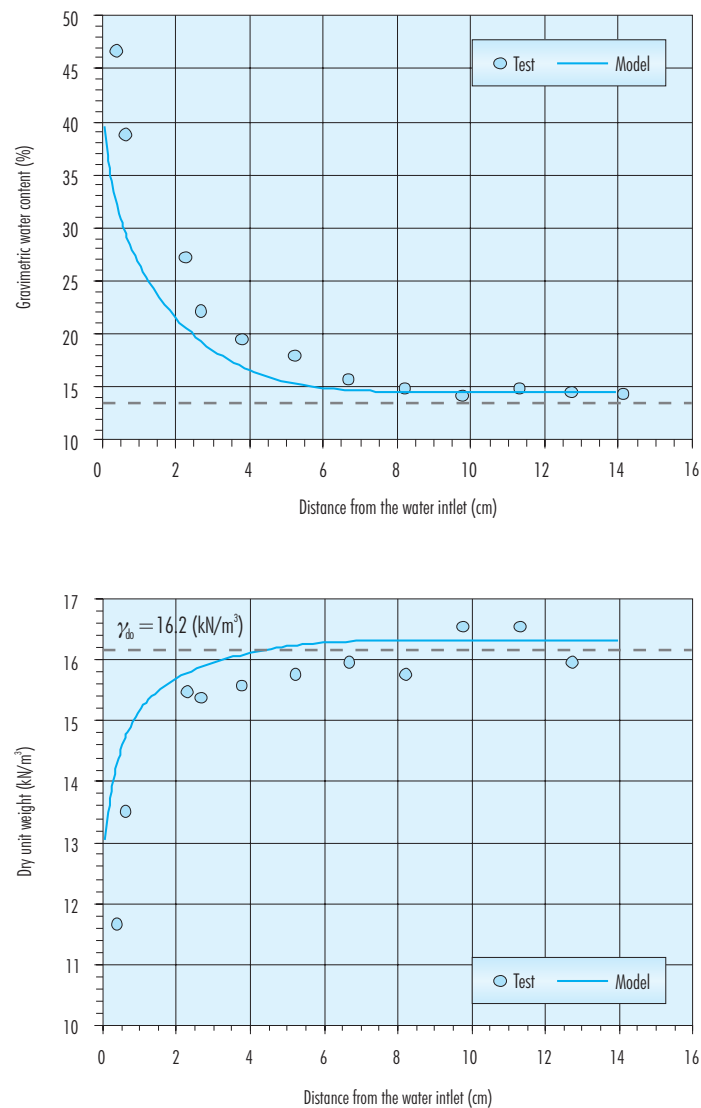


Figure 44: Water content and dry density profiles at the end of the infiltration test performed in the ceramic cell (CIMNE).

but most of the tests were performed at laboratory temperature. It is an objective of the project to make an effort to identify the influence of temperature on the modification of these properties.

### 3.2.1.1 Retention curves

The suction/water content relationship was determined both in confined and unconfined samples under different temperatures. Although the sealing material will be unconfined only in the outer part of the

barrier, where a void exists between compacted blocks and host rock, the determination of the suction/water content relationship in unconfined samples is justified because, being much easier to determine, it will still be useful in identifying the influence of temperature.

Besides, since the control of volume change in drying paths of the retention curve is difficult, the drying paths at different temperatures are being performed following the standard procedure (free volume).

The retention curve at constant volume, following a wetting/drying path, was determined by CIEMAT for two different dry densities (1.65 and 1.70 g/cm<sup>3</sup>) and a temperature of 40 °C, at 60 °C for dry density 1.65 g/cm<sup>3</sup>, and at 80 °C for dry densities 1.60 and 1.70 g/cm<sup>3</sup>. The curves follow a wetting path, from suction 130 MPa to 0.1 MPa, and afterwards, a drying path to 130 MPa. The initial water content of the samples was the hygroscopic one (about 14 percent). To hinder the swelling of clay during the determination, the samples were compacted in the cells shown in Figure 15. These cells were introduced in a vacuum desiccator with a sulphuric acid solution, which was, in turn, placed into an oven at controlled temperature (Figure 45).

The results obtained are shown in Table A.4 (Appendix A) for a temperature of 40 °C, in Table A.5 for a temperature of 60 °C and in Table A.6 for a temperature of 80 °C, and are plotted in Figure 46. The degrees of saturation obtained are higher than 100 percent because they were calculated considering the density of the water as 1.00 g/cm<sup>3</sup>, which was shown to be untrue for high plasticity materials (Villar 2000, Marcial 2003). The results shown the hysteretic behaviour of clay, being the water contents reached during drying higher than those ob-

tained during previous wetting. On the other hand, the retention capacity at higher temperature seems to be slightly lower. This is clearly seen in Figure 47, where only the wetting curves referring to a single dry density have been plotted.

The retention curve following a drying/wetting path was determined by CIEMAT in unconfined samples for temperatures of 80 and 60 °C. The results obtained are shown in Table A.7 and Table A.8, in Appendix A. In terms of water content, there are no differences regarding initial dry density; however there are differences in terms of the degree of saturation (Figure 48): for a given temperature and suction, the higher the initial dry density, the higher the degree of saturation. The curves obtained show hysteresis, being the water contents in the wetting paths lower than those reached for the same suction in previous drying. Figure 49 shows the results obtained for a dry density of 1.65 g/cm<sup>3</sup>, compared with those obtained at 20 °C during FEBEX I for a similar dry density. As in the tests performed in confined samples, the retention capacity is higher for the samples tested at laboratory temperature, although no difference can be appreciated in the drying path between the samples tested at 60 and 80



Figure 45: Experimental set-up for the determination of retention curves at constant volume and different temperatures (CIEMAT).

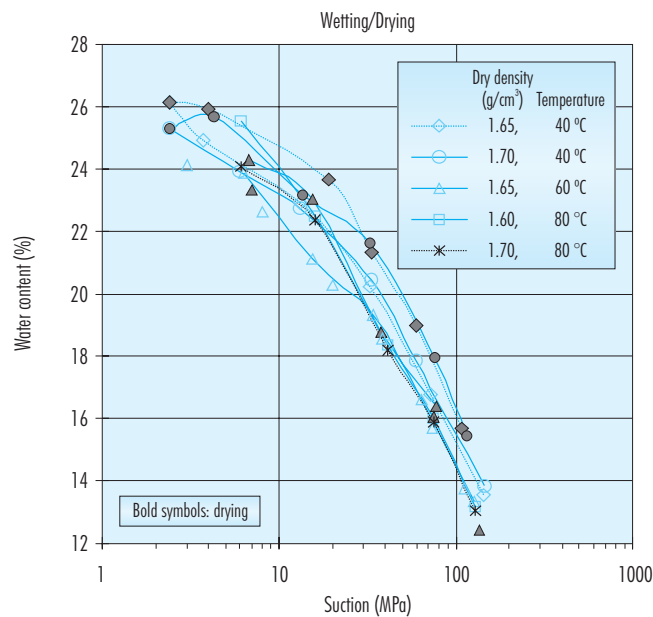


Figure 46: Retention curves at constant volume and at different temperatures in a wetting/drying path (CIEMAT).

°C. The lower retention capacity at higher temperature is clearer in the wetting after drying path.

Figure 50 shows the changes in dry density experienced by specimens with an initial dry density  $1.65 \text{ g/cm}^3$  during the determination of retention curves under unconfined conditions. For suctions higher than 100 MPa, volume changes are small and do not depend on temperature. However, for suctions lower than 100 MPa, the decrease in dry density in the wetting path becomes increasingly important and different for each temperature. Swelling is greater for specimens tested at room temperature, in accordance with the results presented in section 3.2.1.2.

Following the same paths CIMNE performed similar tests on samples compacted at dry densities of  $1.55$  and  $1.65 \text{ g/cm}^3$ , at a temperature of  $80^\circ\text{C}$ . Two small cells similar to the one shown in Figure 16 are introduced into an oven at controlled temperature with a system to circulate through them the vapour coming from salt or sulphuric acid solutions (Figure 51). Preliminary results of water retention curve determination at  $80^\circ\text{C}$  are shown in Figure 52 and Table A. 9 (Appendix A). Water content at 8.3 MPa should have been higher than the value indicated in the figure since hermetic conditions were not reached in the salt container during the application of this

suction. A new system of vapour circulation must be implemented in order to avoid vapour losses (closed system to vapour). Nevertheless, the lower retention capacity at high temperature becomes clear again.

### 3.2.1.2 Swelling capacity

The influence of temperature on the swelling capacity of clay is being checked by tests of swelling under vertical load. They were performed by CIEMAT in an oedometer whose cell is placed in a thermostatic bath with controlled temperature. Granulated bentonite, with its hygroscopic water content (about 14 percent), was compacted inside the cell ring, at room temperature, using static uniaxial compaction until it reached nominal dry densities of  $1.60 \text{ g/cm}^3$ . Vertical stresses between 22 and 30 MPa were applied to obtain specimens of 5.0 cm in diameter and 1.2 cm in height. The stabilisation of temperature is reached in less than 24 hours, and it gives place to a vertical strain of the sample around -0.6 percent. After having reached the stabilisation of the target temperature in the oedometer, vertical pressures of 0.1, 0.5, 1.5 and 3.0 MPa were applied to the samples. Immediately afterwards, they were soaked with deionised water at atmospheric pressure



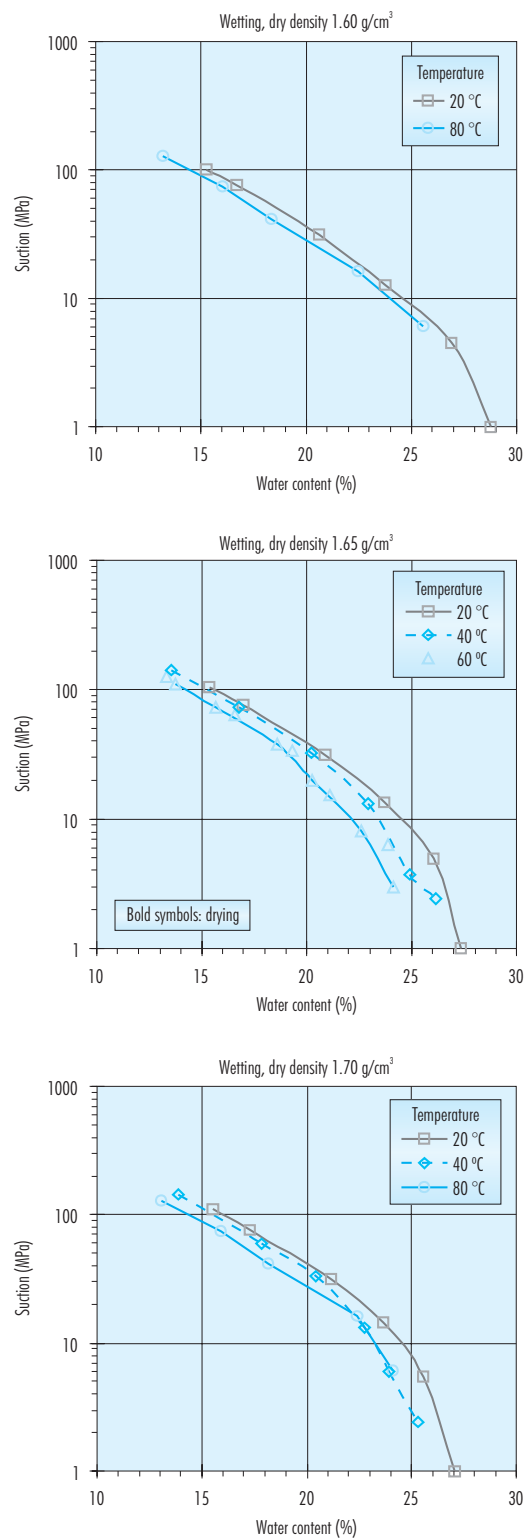


Figure 47: Retention curves at constant volume for different temperatures and dry densities.

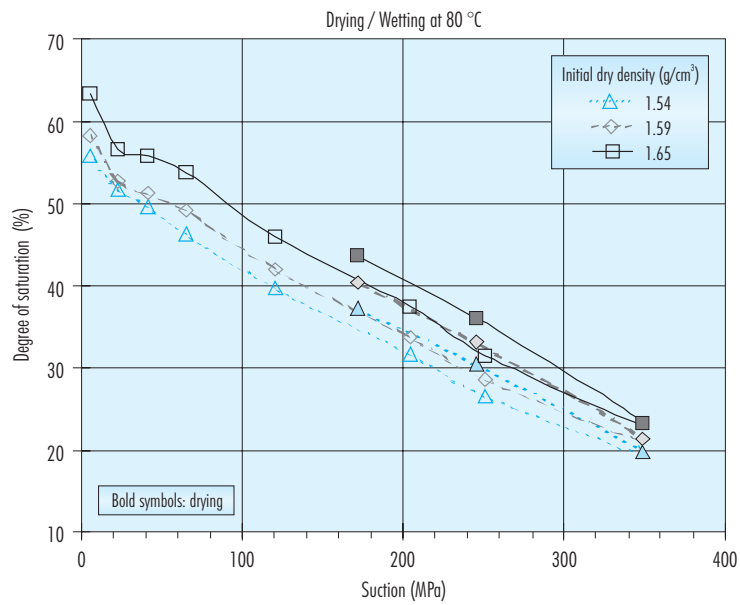


Figure 48: Retention curves following drying/wetting paths determined at 80 °C for unconfined samples of different initial dry density (CIEMAT).

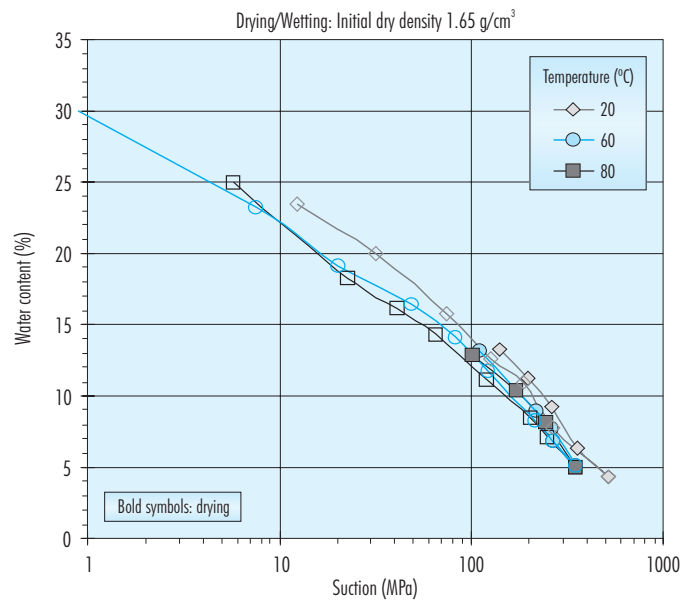


Figure 49: Retention curves following drying/wetting paths determined in unconfined samples of initial nominal dry density 1.65 g/cm<sup>3</sup> at different temperatures (CIEMAT).

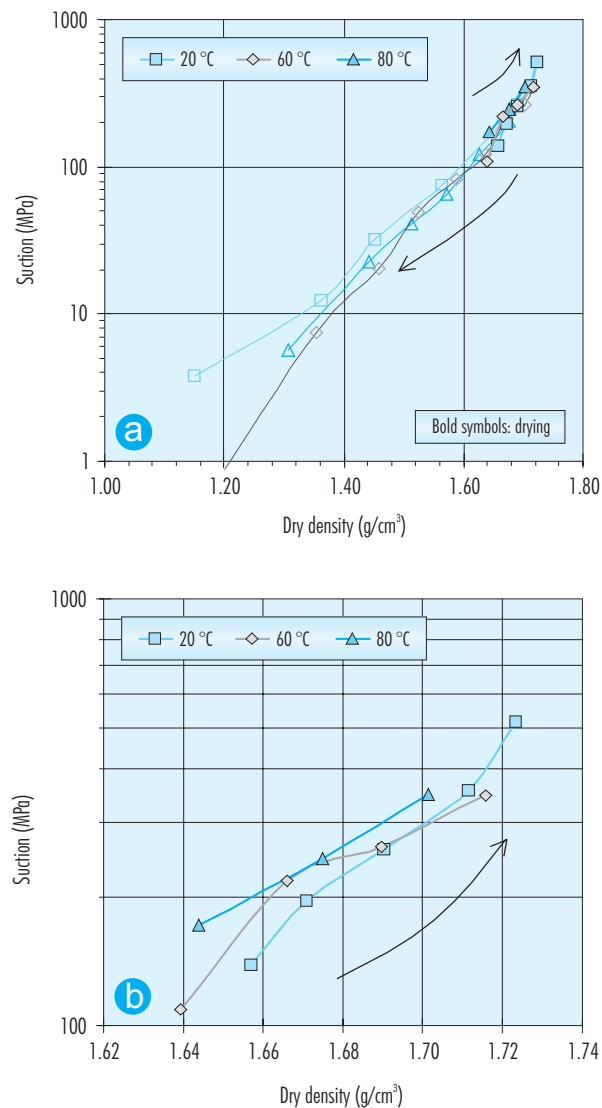


Figure 50: Evolution of dry density in the retention curves in unconfined specimens of bentonite compacted at an initial dry density of 1.65 g/cm<sup>3</sup>; A: drying/wetting paths, B: enlargement of drying paths.

from the bottom porous plate. The swelling strain experienced by the specimens upon saturation was recorded as a function of time until stabilisation. On completion of the tests the water content of the specimens was determined and full saturation was verified. The swelling strain experienced by the specimens upon saturation was determined for temperatures ranging from 30 to 80 °C.

The results are shown in Table A. 10 to Table A. 13, where the strain percentage is calculated as the in-

crease of height with respect to the initial height of the sample, the negative values indicating swelling strains.

The evolution of strain as a function of time in the tests performed under 0.5 and 1.5 MPa is shown in Figure 53. The final strains reached are plotted as a function of the temperature and overload of the test in Figure 54. As shown in the Figure, the swelling capacity decreases with temperature and linear fittings can be drawn between swelling strain and pres-



Figure 51: Isochoric cells and salt container to determine the retention curve at constant volume and different temperatures (CIMNE).

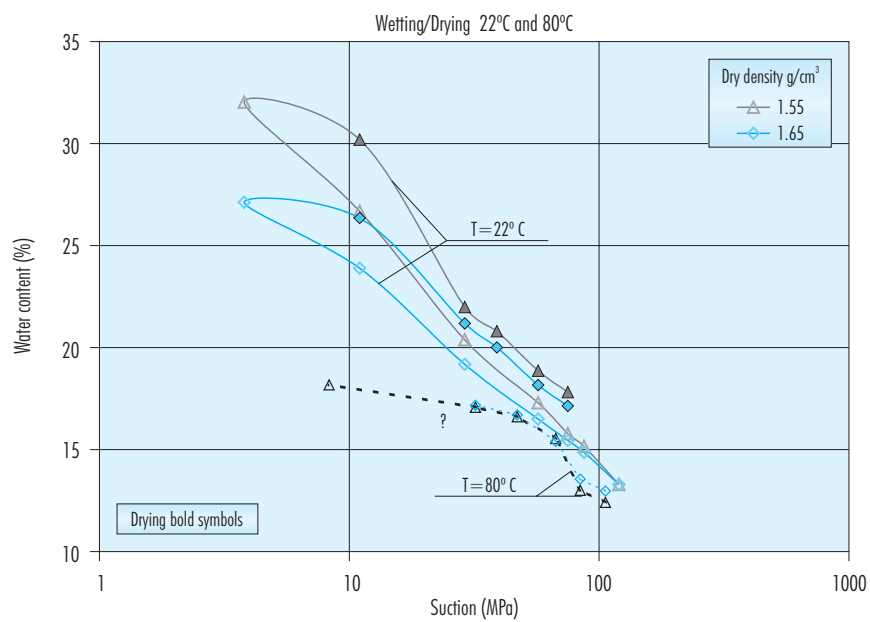


Figure 52: Preliminary results for two retention curves measured at 80°C (CIMNE).

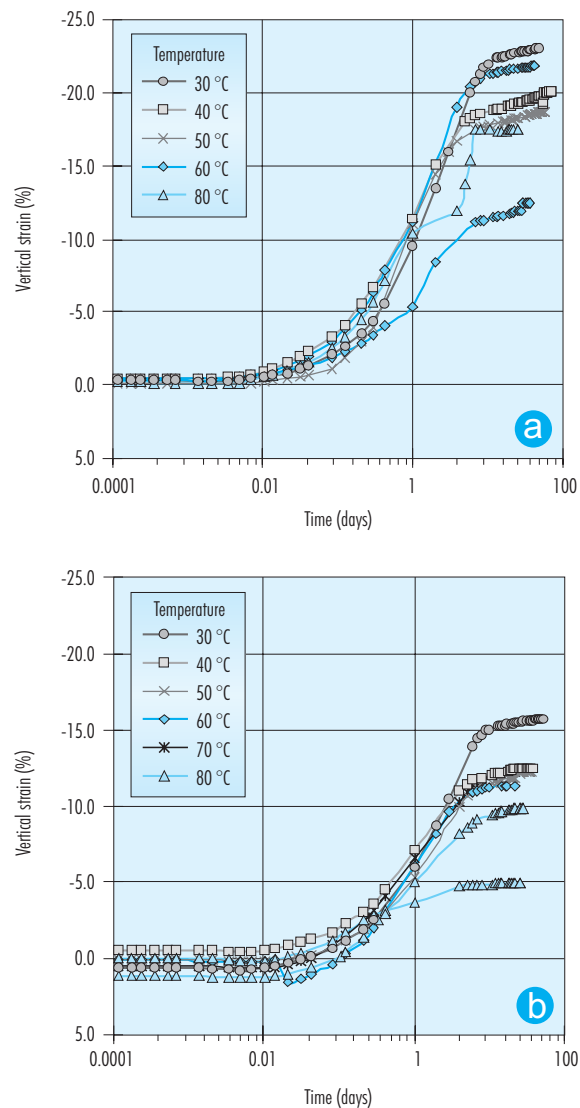


Figure 53: Evolution of strain of samples compacted to dry density  $1.60 \text{ g/cm}^3$  saturated with deionised water under a vertical pressure of  $0.5 \text{ MPa}$  (a) and  $1.5 \text{ MPa}$  (b) at different temperatures.

sure. Although the fittings come from tests performed at temperatures ranging from  $30$  to  $80 \text{ }^\circ\text{C}$ , the extrapolation of lines towards higher temperatures seems to indicate that the swelling capacity would stand for temperatures around  $100 \text{ }^\circ\text{C}$ .

### 3.2.1.3 Swelling pressure and permeability

The determination of the swelling pressure and permeability as a function of temperature is being per-

formed by CIEMAT in new high pressure oedometer equipments (Figure 55 and Figure 56). Granulated clay was compacted uniaxially and statically at room temperature in the oedometer ring, which had an inner diameter of  $5.0 \text{ cm}$ , the length of the resulting specimen being  $1.2 \text{ cm}$ . Nominal dry densities of  $1.60$  and  $1.50 \text{ g/cm}^3$  were reached by applying vertical stresses of  $15 \pm 1$  and  $11 \text{ MPa}$ , respectively.

The oedometer assemblage is placed inside a silicone oil thermostatic bath that keeps target temper-

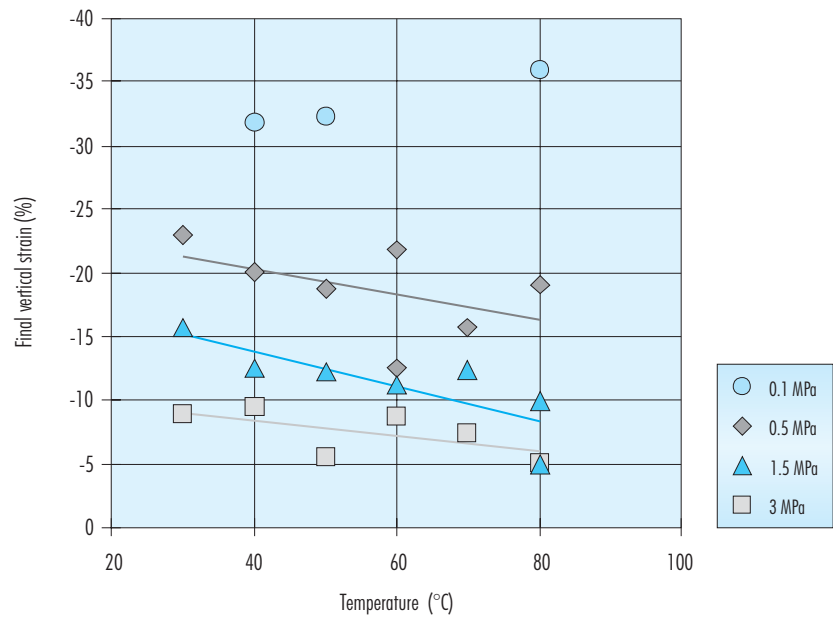


Figure 54: Final strain of samples compacted to dry density  $1.60 \text{ g/cm}^3$  saturated with deionised water under different vertical pressures and temperatures.

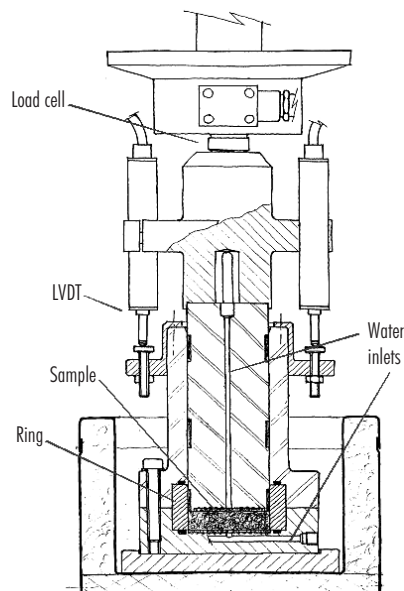


Figure 55: Schematic layout of the oedometric cell inside the thermostatic bath (CIEMAT).



Figure 56: Twin set of high pressure oedometers with one of them placed in the thermostatic bath (left).

ature. Once the temperature stabilises, the sample, confined between porous stainless steel sinters, is hydrated at constant volume through the bottom face with deionised water injected at a pressure of 0.6 MPa, while the upper outlet remains open to atmosphere. At the same time, a load cell installed in the loading frame measures the swelling pressure exerted by the clay. The small vertical deformation of the specimen, due mainly to load cell and frame deformability, is measured by two LVDTs. An automatic volume change apparatus measures the water exchange of the specimen. The values of load, strain and water exchange are automatically recorded.

Once the sample is completely saturated (which is assumed by the stabilisation of water intake and swelling pressure development), the injection of water is stopped, and the pressure registered is considered the swelling pressure value for the dry density attained. The actual density may differ slightly from the nominal one due to the small displacement allowed by the equipment (about  $10\ \mu\text{m}$  when a vertical stress of 2.2 MPa is applied).

Afterwards, hydraulic conductivity is determined in the same equipment and on the same samples, which were kept at constant volume. In order to per-

form this determination, the water pressure at the bottom of the samples is increased, while a back-pressure of 0.6 MPa is applied on top, resulting in hydraulic gradients between 11700 and 20000. The water outflow is measured and the hydraulic conductivity is calculated applying Darcy's law. Tests performed with different hydraulic gradients have confirmed that there is no effect of the gradient magnitude (in the interval tested) on the hydraulic conductivity value (Villar 2000, 2002).

The results are shown in Table A. 14 (Appendix A), in which the values of swelling pressure ( $P_s$ ) and hydraulic conductivity ( $k_w$ ) are indicated. The swelling pressure results are plotted in Figure 57, where the dispersion of data can be mostly attributed to the variations in dry density (whose average value was in fact  $1.58\ \text{g/cm}^3$ ). This is caused by the small displacement allowed by the equipment, as the swelling pressure value is very sensitive to little density changes (see Equation [3]). The error bars shown in the figure were obtained from values measured in tests performed at laboratory temperature to obtain Equation [3]. A decrease of swelling pressure, as a function of temperature, is observed. However, the extrapolation of the logarithmic correlation towards higher temperatures would indicate that swelling

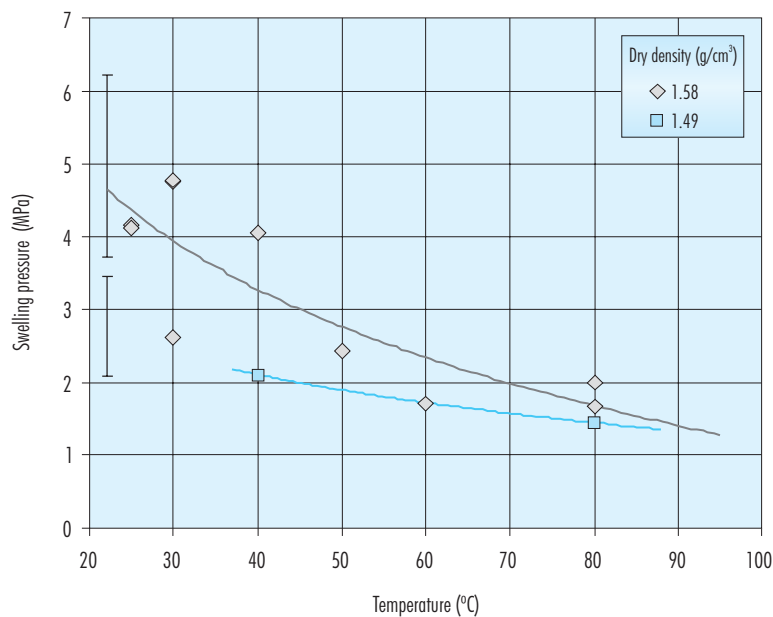


Figure 57: Swelling pressure as a function of temperature for saturated FEBEX clay compacted to different nominal dry densities (the error bars correspond to samples of dry density  $1.58 \text{ g/cm}^3$  and  $1.49 \text{ g/cm}^3$  tested at laboratory temperature, Equation [3]).

pressures higher than 1 MPa would be developed even for temperatures of 100 °C. This would be in accordance with the results obtained in soaking under load tests, which predict a decrease in swelling capacity with temperature. Lingnau *et al.* (1996) also observed a reduction in swelling pressure with temperature for a sand/bentonite mixture, although it did not show any loss in the self-healing capability of the material, even for temperatures of up to 100 °C.

The hydraulic conductivity results are plotted in Figure 58. The error bars shown were obtained from values measured in tests performed at laboratory temperature to obtain Equation [2]. The effect of temperature on permeability is less evident than on swelling pressure, although it slightly increases in a logarithmic way with temperature, as expected from the decrease in water kinematic viscosity. The extremely high values of permeability measured for nominal dry density  $1.49 \text{ g/cm}^3$  have to be confirmed.

### 3.2.1.4 Oedometric tests

The two oedometers described in the previous section, in which vertical pressures of up to 20 MPa

can be applied, are being used by CIEMAT to perform oedometric tests at different temperatures. The initial dry density of the samples was of  $1.70 \text{ g/cm}^3$ , and clay was compacted uniaxially with its hygroscopic water content inside the oedometer ring (diameter of 5.0 cm, length of the specimen of 1.2 cm). A vertical pressure between 22 and 26 MPa was applied to manufacture the specimens.

Two kind of tests were designed. In both of them the stress path is similar, but in one of them the sample is previously saturated (type 1) while in the other one it is not (type 2).

- Type 1: the sample is heated up to the desired temperature under a low vertical load and then loaded to 1 MPa. Afterwards, the sample is saturated under this load until it reaches stabilisation and later, loaded progressively up to 2, 4, 6, 12 and 20 MPa.
- Type 2: the sample is heated up to the desired temperature under a low vertical load (0.4 MPa). Afterwards, the sample is loaded progressively up to 1, 2, 4, 6, 12 and 20 MPa. During all the process the sample keeps its initial water content, *i.e.* it remains unsaturated.



After some preliminary tests, tests at 25, 60 and 80 °C were performed satisfactorily. Their characteristics are shown in Table XI. Saturation of type 1 tests took place by injecting deionised water through the bottom inlet of the cell at the pressure given by a 1-m column.

During saturation and loading, the upper outlet of the cell was open to atmosphere. In the type 2 tests the two inlets of the cell were closed, to avoid any

water exchange with the environment. The duration of each loading step was fixed to 7 days.

Figure 59 shows the evolution of swelling during saturation under a vertical load of 1 MPa, at two different temperatures, for samples of initial dry density 1.70 g/cm<sup>3</sup> (type 1 tests EAP2\_10 and EAP2\_11). The increase of water permeability and the decrease of the swelling capacity of bentonite with temperature can be observed.

Table XI  
Summary of oedometric tests performed.

Reference	Temperature (°C)	Initial $\rho_d$ (g/cm <sup>3</sup> )	Initial $w$ (%)	Initial $S_r^*$ (%)	Final $\rho_d$ (g/cm <sup>3</sup> )	Final $w$ (%)	Final $S_r^*$ (%)
EAP1_10	25	1.70	14.5	67	1.76	13.9	71
EAP1_11	80	1.72	13.0	62	1.81	11.6	63
EAP1_12	60	1.70	14.0	64	1.78	13.4	71
EAP2_10	25	1.71	13.7	64	1.71	26.6	123
EAP2_11	80	1.69	14.4	65	1.58	28.7	109

\*calculated considering the density of water 1.00 g/cm<sup>3</sup>.

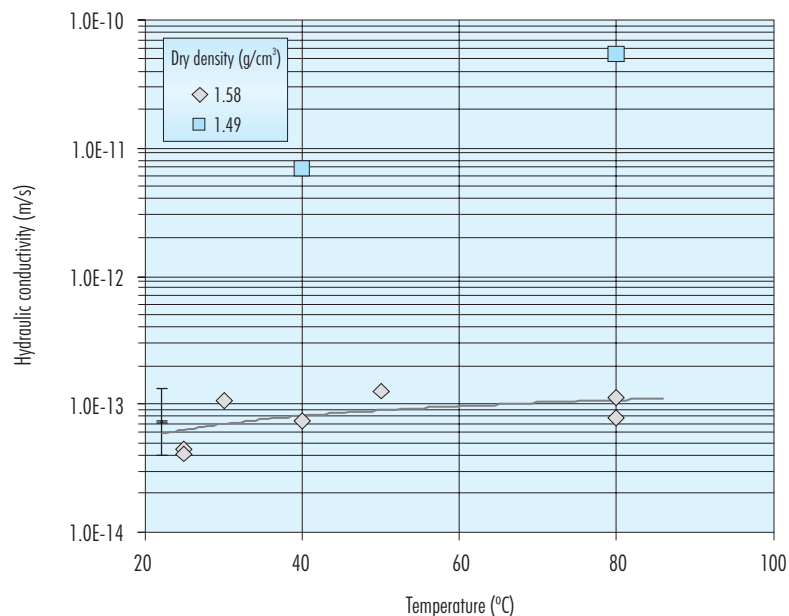


Figure 58: Hydraulic conductivity as a function of temperature for saturated FEBEX clay compacted to different nominal dry densities (the error bars correspond to samples of dry density 1.58 g/cm<sup>3</sup> and 1.49 g/cm<sup>3</sup> tested at laboratory temperature, Equation [2]).

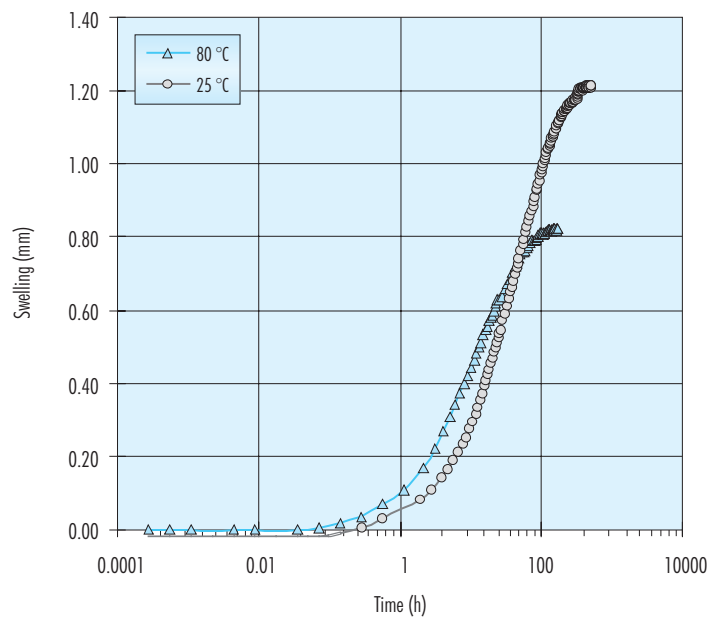


Figure 59: Swelling during saturation of bentonite under a vertical stress of 1 MPa.

The volume changes measured during loading are plotted in Figure 60 in the form of oedometric curves. Logically, the void ratios at the beginning of loading are higher in the tests in which the sample was previously saturated (type 1). Hydration induces a significant increase of pore volume in both samples, but this swelling is greater in the sample tested at 25 °C (Figure 59), following the same trend of soaking under load tests. This increase of volume is associated to irreversible changes in the macrostructure of the material and reduces the apparent preconsolidation stress of bentonite (Gens & Alonso 1992, Alonso *et al.* 1999). These structural changes prevail over the increase of compressibility of bentonite with temperature, and the cold sample presents the smallest preconsolidation pressure and the biggest volume change under load application. On the other hand, the comparison of the curves obtained during loading at different temperatures and constant water content (type 2 tests) suggests that the temperature increases the compressibility of bentonite, as it was observed in saturated materials. As in the suction controlled test (Figure 25), a certain reduction in the size of the elastic domain with temperature can be observed (Hueckel & Borsetto 1990), despite the fact that the vertical stresses applied are smaller than the compaction load.

### 3.2.2 Study of the microstructure

The hydration of bentonite generates microstructural changes that modify both its hydraulic and mechanical properties. As a consequence, the evolution of porosity and microstructure influence greatly the hydration transient state. From a fundamental point of view, measurements and observations at this microstructural level, involving clay units and their aggregations, are very important, since they should help in further understanding of higher structural levels and their consequences on material properties and behaviour, under various hydro-mechanical stress state conditions. As the microstructural studies are a complex matter, several techniques would be applied. Some of them are, in fact, indirect methods of determining the evolution of microstructure with hydration.

#### 3.2.2.1 Mercury intrusion porosimetry

The quantitative examination of the microstructural level has been usually focused on the distribution of the sizes of soil voids. Pore size distribution is an essential fabric element, which is related to some soil properties and behavioural characteristics, such as water, air and heat conductivity properties, absorp-

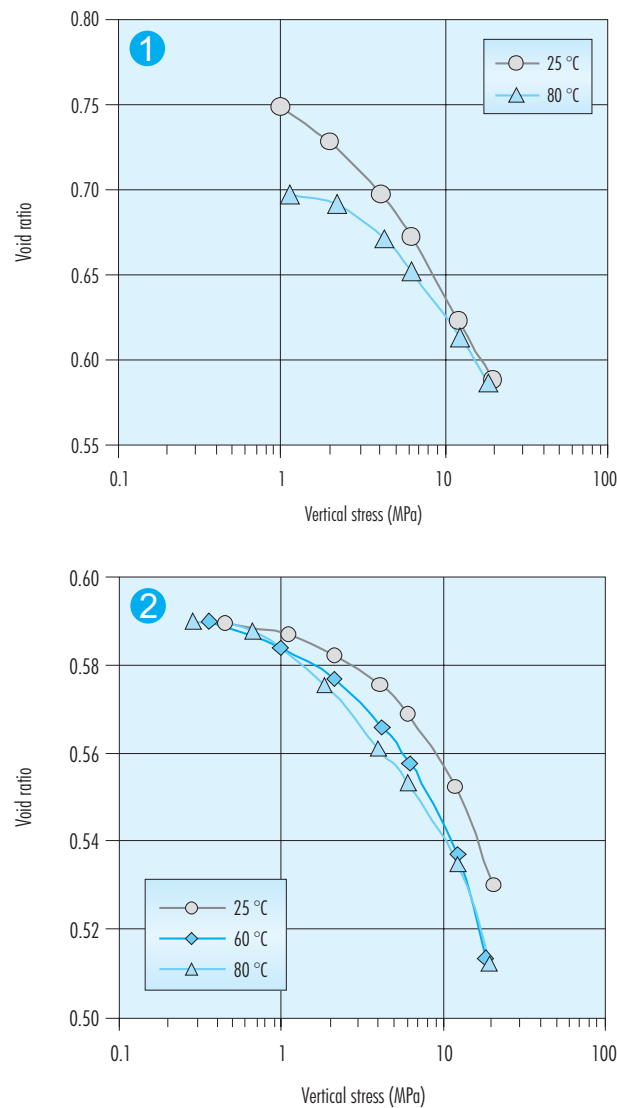


Figure 60: Oedometric curves of the type 1 and type 2 tests performed at different temperatures (initial void ratio 0.59).

tion and desorption properties, and skeleton deformability (rearrangement of fabric units). A very useful technique for the quantitative study at this microscale is mercury intrusion porosimetry (MIP), which was used in this research to describe the microstructure of bentonite and to provide information about factors influencing its microstructural changes. The wide range of pore diameters that can be examined (around 6 nm to 400  $\mu\text{m}$ ) allows MIP to be very suitable for the study of the microstructure of clays. MIP tests were performed on a "Micromeritics-

Autopore IV" equipment, attaining maximum intrusion pressures of 220 MPa. To avoid excessive shrinkage, a freeze drying process was used to prepare the dehydrated samples required by MIP tests. Details of the procedure can be found in Delage *et al.* (1982) and Delage *et al.* (1996).

The influence of various mechanical (loading) and hydraulic (wetting / drying) stress paths on the pore size distribution of compacted bentonite was analysed. The mechanical paths involved loading paths

at hygroscopic water content (about 13%, total suction of around 120 MPa). Maximum vertical compaction stresses varied between 8 and 38 MPa to achieve target dry densities of 1.40 to 1.80 g/cm<sup>3</sup>. Figure 61 and Table XII show the stress paths followed on loading (L-U), which also includes an unloading stage prior to the performance of the MIP test. It is assumed that irreversible loading mechanisms predominate over the reversible mechanisms of the unloading stage. The stress path does not include the freeze-drying stage, in which it is assumed that suction is increased without appreciable change of soil volume.

A series of hydraulic stress paths included wetting under isochoric (constant volume) or constant vertical stress conditions. The wetting paths performed under isochoric conditions, started from the as-compacted state reaching in a single-stage procedure a final state with a prefixed suction or saturated conditions (path WIC-U in Figure 61 and Table XII). The wetting paths were performed under constant stress states: under unconfined conditions (path W-L-U) and under a constant vertical net stress (L-W-U). Under unconfined conditions, the sample was saturated in a single stage tending to slurry, which was then loaded to a maximum vertical net stress of

1.5 MPa. A series of hydraulic stress paths on the naturally-aggregated material also included drying paths under unconfined conditions (D-W) starting from the as-compacted state at a dry density of 1.65 g/cm<sup>3</sup>. The maximum total suction applied was 310 MPa, before going back to 100 MPa. All the hydraulic paths include an unloading stage prior to the performance of the MIP test.

In compacted clays, three different types of pore spaces within the microstructure of clays are usually considered. The pore size ranging between 0.2 and 2 nm can be identified as the intra-particle (inter-platelet) pore space. On the other hand, the inter-particle (intra-aggregate) pore space and the inter-aggregate pore domain can be distinguished.

The conditioning of FEBEX bentonite in the quarry, and later in the factory, was strictly mechanical and included the crumbling of clods. Finally, the clay was sieved by a 5-mm square mesh to obtain the bentonite grains to be compacted in the laboratory. Due to this physical treatment, the pore size distribution of FEBEX bentonite, resulting after the compaction, presents a new type of pore between the grains that can be denominated inter-granular pore domain.

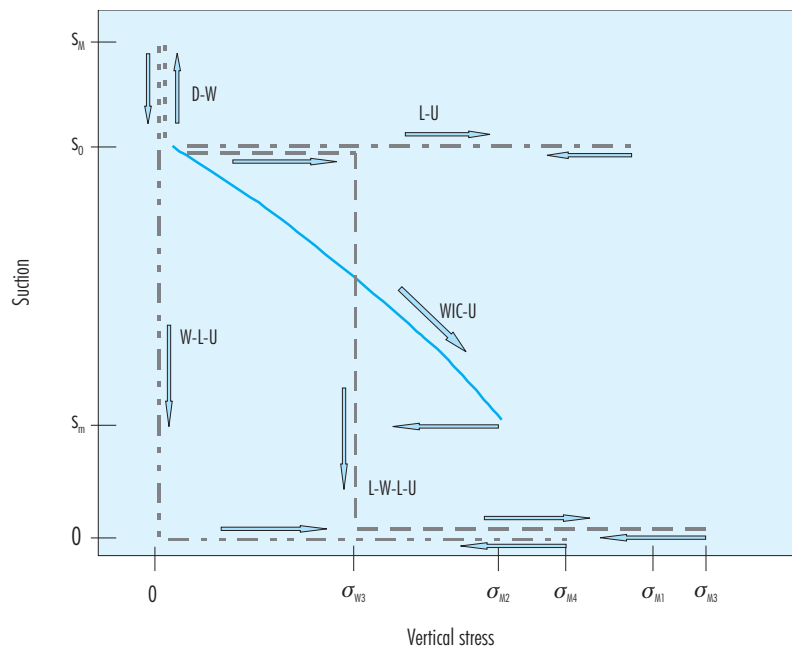


Figure 61: Stress paths followed before MIP tests.

Table XII  
Initial conditions, stress paths and final conditions followed before MIP tests

Test	Initial conditions		Path	Final conditions	
	$\rho_d$ (g/cm <sup>3</sup> )	w (%)		$\rho_d$ (g/cm <sup>3</sup> )	w(%)
1	0.62	125.0	WLU; $\sigma_{M4} = 1.5$ MPa	1.15	49.9
2			LU; $\sigma_{M4} = 8$ MPa	1.40	13.0
3	1.40	13.0	WICU; $s_m = 0$	1.29	37.5
4			LWLU; $\sigma_{W3} = \sigma_{M3} = 0.2$ MPa	1.15	49.9
5			LU; $\sigma_{M4} = 22$ MPa	1.65	12.6
6			DW; $s_m = 310$ MPa	1.73	8.7
7			WICU; $s_m = 39$ MPa	1.55	20.3
8	1.65	12.6	WICU; $s_m = 4$ MPa	1.46	23.3
9			WICU; $s_m = 0$ MPa	1.43	29.6
10			LWLU; $\sigma_{W3} = 0.5$ MPa; $\sigma_{M3} = 2$ MPa	1.37	36.0
11			LU; $\sigma_{M4} = 24$ MPa	1.68	13.0
12	1.68	13.0	LWLU; $\sigma_{W3} = \sigma_{M3} = 0.2$ MPa	1.41	33.9
13	1.50	$\approx 3$	LU; $\sigma_{M4} \approx 10$ MPa	1.50	$\approx 3$
14	1.80	$\approx 3$	LU; $\sigma_{M4} = 36$ MPa	1.80	$\approx 3$
15	1.95	$\approx 4$	LU; $\sigma_{M4} \approx 200$ MPa	1.95	$\approx 4$

Usually, the pore size distribution is represented in terms of incremental intruded pore volume vs. entrance pore diameter. This differential plot takes the incremental increase in intrusion between the pore diameters, associated to the different pressures used in the test, and consequently, the appearance of the pore size histogram depends largely on the number and size of the pressure intervals. An alternative possibility to show the pore size distribution is to use the derivative of the accumulative pore volume, in terms of void ratio, with respect to the decimal logarithm of the pore diameter. This derivative is computed using a finite differences approach, and the resulting pore size distribution plot is less dependent on the pressure intervals used in the test. Figure 62 shows the pore size distribution of samples of bentonite compacted at a dry density of 1.68 g/cm<sup>3</sup>, using the two approaches indicated. The influence

of the number of pressure steps in the mercury intrusion process is notorious when the incremental representation is used; consequently the derivative of intruded volume was adopted to illustrate the pore size distribution of bentonite.

On the other hand, it must be pointed out that the mercury intrusion process is divided into two parts that correspond to two pressure intervals (between 2.4 kPa and 150 kPa (low pressure range) and between 150 kPa and 220 MPa (high pressure range)). In order to change the pressure range in the test, it is necessary to stop the intrusion process and disassemble the equipment. These operations usually produce a distortion and a false peak in the pore size distribution curve, which corresponds to a diameter of about 6000 nm (shaded area indicated in Figure 62). This distortion was manually filtered in the results that will be presented in this section.

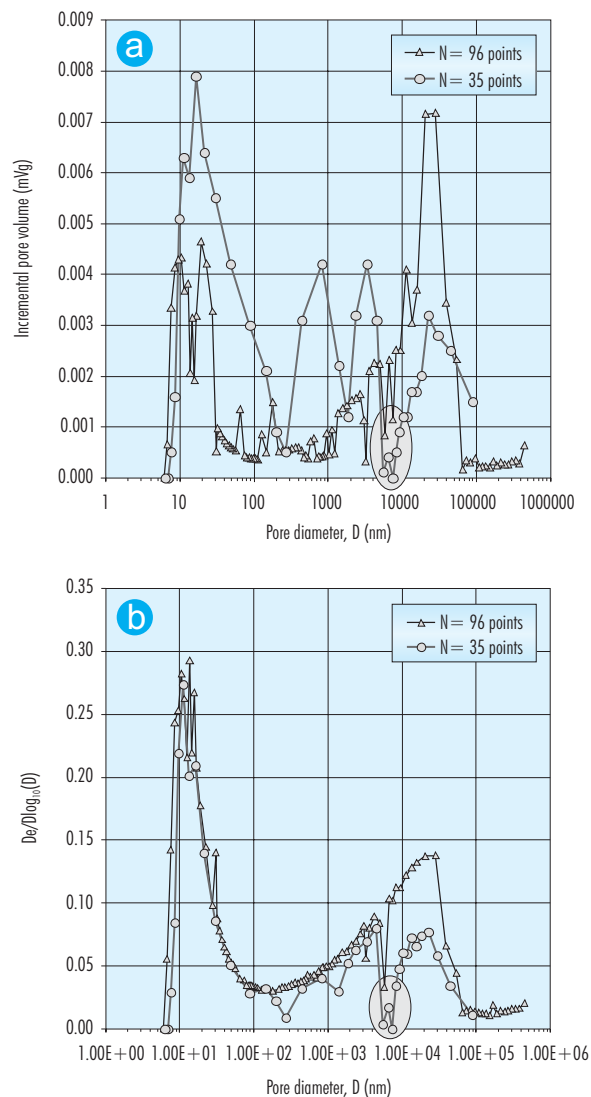


Figure 62: Pore size distribution of samples compacted at a dry density of 1.68 g/cm³. In terms of incremental pore volume (a); and slope of void ratio - pore diameter logarithm relationship (b). The shaded zone corresponds to the change of mercury intrusion system.

Figure 63 shows the pore size distribution (PSD) obtained in samples compacted to very different values of dry density (from 1.4 g/cm³ to 1.68 g/cm³) and hygroscopic water content (paths L-U in Figure 61), in terms of logarithmical increment of void ratio ( $\Delta e / \Delta \log_{10}(\text{pore diameter})$ ). It can be observed that the pore size distribution is clearly bi-modal, which is very characteristic of this type of materials (Alonso *et al.* 1987). The dominant values are 10 nm, which would correspond to the pores inside clay aggregates, and a larger pore size, which depends on

the compaction dry density and ranges from 20  $\mu\text{m}$  (for  $\rho_d = 1.68 \text{ g/cm}^3$ ) to 30  $\mu\text{m}$  (for  $\rho_d = 1.4 \text{ g/cm}^3$ ). These larger voids would correspond to the inter-granular pores. The boundary between the two pore size families can be situated around 150-200 nm, as pores smaller than this size do not appear to be affected by the magnitude of the compaction load. Clearly the samples differ only in the proportion of macropores having a diameter bigger than 2  $\mu\text{m}$ . As Figure 63 clearly shows, compaction affects mainly the pore structure of the inter-granular pores.

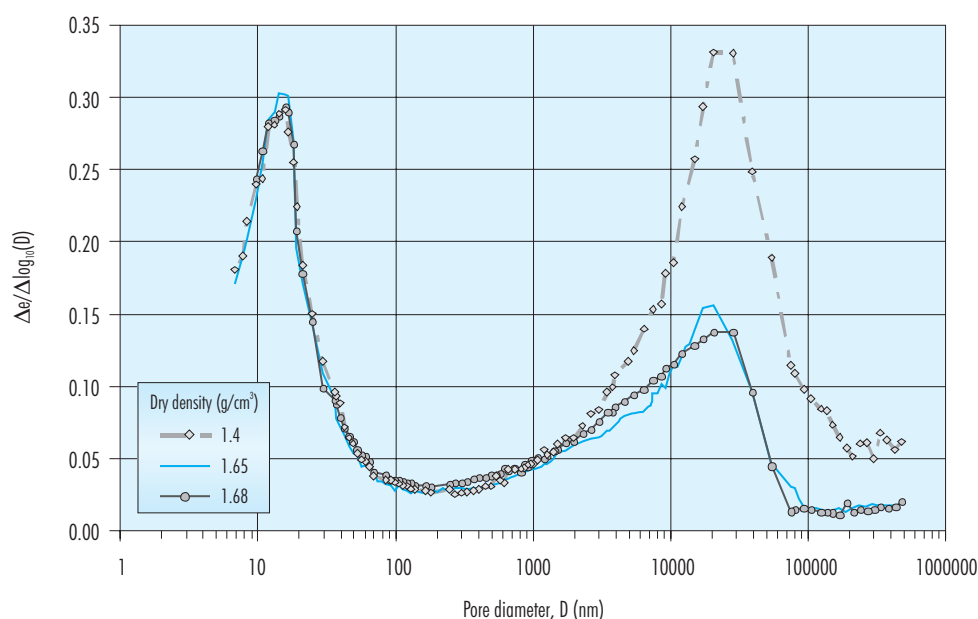


Figure 63: Porosimetry of samples compacted to different dry densities with a water content of about 13%.

As it is shown in Figure 64, similar conclusions concerning macroporosity can be achieved considering the samples compacted at low water content (tests 13, 14 and 15 in Table XII).

As observed, the PSD curves of the as-compacted states at dry densities, varying between 1.4 and 1.95 g/cm<sup>3</sup>, only display two modes. It appears that the dominant inter-granular pore mode overlaps the intra-particle pore volume that cannot be distinguished. Following this hypothesis, it is admitted that the as-compacted states present three pore modes; even so only two are distinguished.

Figure 65 shows the relationship of pore diameter with intruded pore volume for two samples compacted at dry densities, 1.40 g/cm<sup>3</sup> and 1.68 g/cm<sup>3</sup>. It can be noted that there exists a significant pore volume into which the mercury could not penetrate or that has a diameter larger than the resolution of the equipment. In the case of the sample with a dry density of 1.68 g/cm<sup>3</sup>, this pore volume practically only corresponds to pores smaller than 6 nm, ( $e = 0.26$ ), but in the case of the sample with a dry density of 1.40 g/cm<sup>3</sup>, part of this volume corresponds also to pores bigger than 480  $\mu\text{m}$ . Assuming that the magnitude of the pore volume associated to

pores of diameter smaller than 6 nm (not intruded by mercury) is the same for the two specimens, the volume, with diameter bigger than 480  $\mu\text{m}$  in the less dense specimen, which is not considered is about 0.16. Indeed the intra-aggregate and intra-particle pore volumes are very similar for the two samples with void ratio values around 0.41. The remaining of the pore space corresponds, therefore, to inter-aggregate and inter-granular pores, accounting for about 56% of the voids ( $e = 0.52$ ), in the sample with a dry density of 1.4 g/cm<sup>3</sup>, and about 33% ( $e = 0.20$ ), in the sample with a dry density of 1.68 g/cm<sup>3</sup>.

Additional information on the soil fabric can be inferred from the examination of retention curves obtained under free swelling and constant volume conditions (Figure 17). It can be observed that the water retained at suctions higher than about 15 MPa is independent from the total void ratio (or dry density). It seems plausible that the water retained at those high suctions belongs to the intra-aggregate pores, where total porosity plays no relevant role (Romero *et al.* 1999). The fact that the water content corresponding to intra-aggregate pores appears to be somewhat higher than their pore volume (as measured in MIP tests) may be due to the

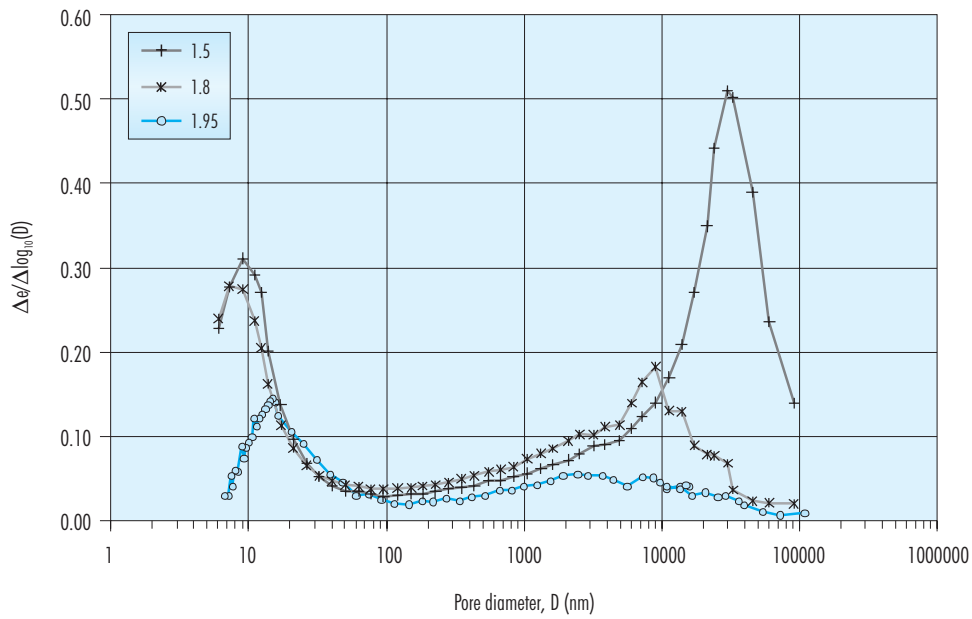


Figure 64. Porosimetry of samples compacted to different dry densities with a water content of about 3-4(%)

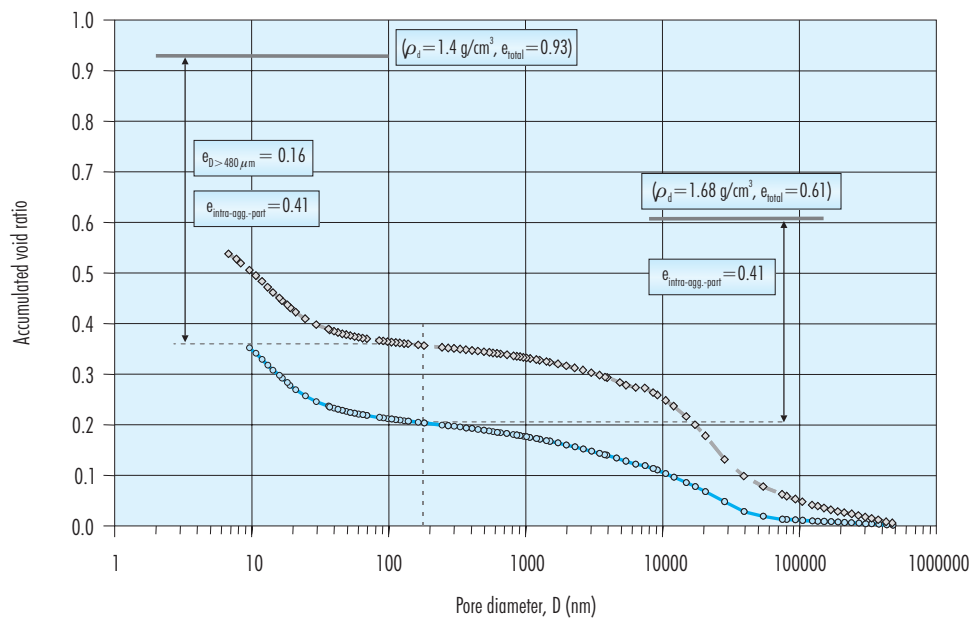


Figure 65: Relationship between pore diameter and intruded pore volume for two samples compacted at different dry densities.



fact that the density of the water tightly bound to clay particles is higher than that of free water (Martin 1962, Villar 2000). It is also likely that part of the water is retained on the surface of the aggregates. Summarising, all observational data concerning the fabric of compacted bentonite at hygroscopic water content indicates a clear presence of two structural levels in the material: a microstructure inside the aggregates and a macrostructure, constituted by the ensemble of aggregates and inter-aggregate pores. Microstructure features appear to be largely independent from compaction effort. Figure 66 presents a summary of the inter-granular pore sizes as a function of the dry density in the as-compacted state.

Figure 67 shows the porosimetry of a bentonite specimen, which was obtained remoulding the clay in saturated condition, in order to obtain a slurry, which was subsequently loaded to 1.5 MPa (path W-L-U in Figure 61). The state after the loading path presented a dry density of around 1.15 g/cm<sup>3</sup>. The PSD function displays a clear dominant pore size mode at 430 nm, which corresponds to the inter-aggregate pore space. It can be observed that inter-granular pores disappear due to the slurry condition of the sample. Important differences are observed

between the PSD functions of the as-compacted states presented in Figure 63 and this saturated material.

Figure 68 presents the results of the drying path carried out (path D-W). As observed, the as-compacted microstructure is still preserved after the drying path, in which a dominant inter-granular pore size mode is identified. The inter-aggregate porosity remains hidden.

The evolution of the PSD function on wetting specimens initially compacted to 1.65 and 1.4 g/cm<sup>3</sup> are presented in Figure 69 and Figure 70 respectively. The different dry densities of the materials, before the performance of the freeze-drying process, are indicated in these figures. It can be seen that the hindered and latent inter-aggregate pore size mode emerges. Simultaneously, and as a consequence of the constant volume condition during wetting (Test 9), inter-granular porosity is reduced, tending to its occlusion. Due to limitations of the method, the evolution of the intra-aggregate pore size mode cannot be registered, which is expected to increase on wetting. The emerging inter-aggregate pore mode displays values between 350 and 1100 nm. It appears that wetting induces the progressive splitting of the original structure of the pseudomorphs, which are

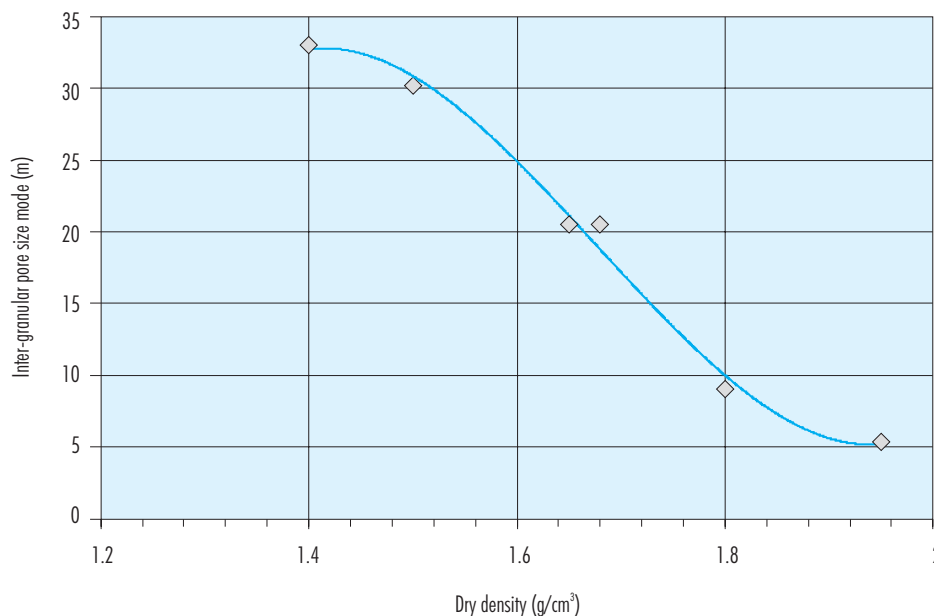


Figure 66: Pore size mode for the inter-granular voids as a function of dry density.

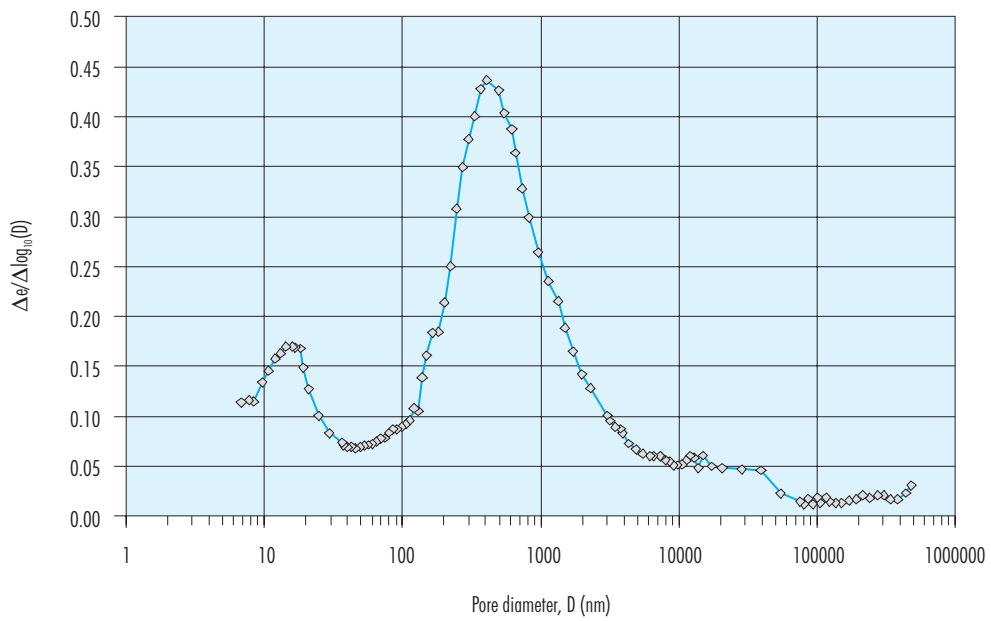


Figure 67: Porosimetry of consolidated slurry; path (W-L-U).

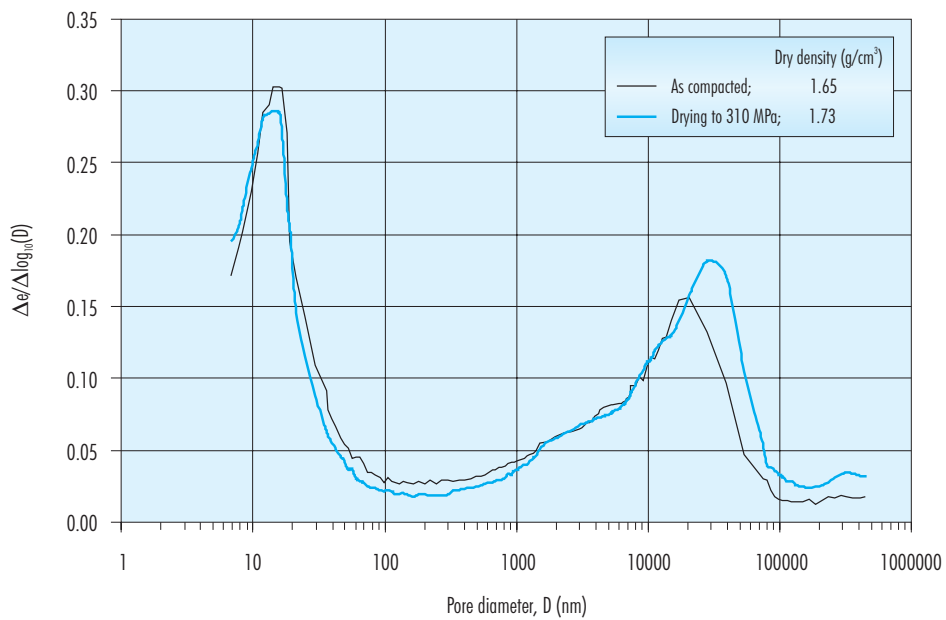


Figure 68: Evolution of PSD functions on drying, under null confining stress (D-W).

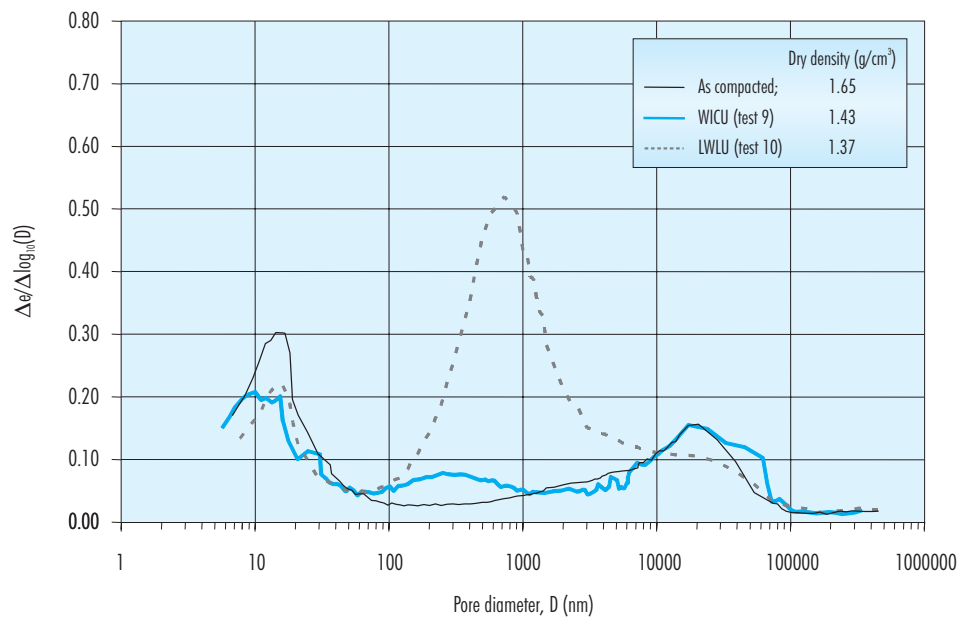


Figure 69: Evolution of PSD functions on wetting at constant vertical net stress (L-W-L-U, test 10) and on wetting at constant volume (WIC-U, test 9). Initial dry density: 1.65 g/cm<sup>3</sup>.

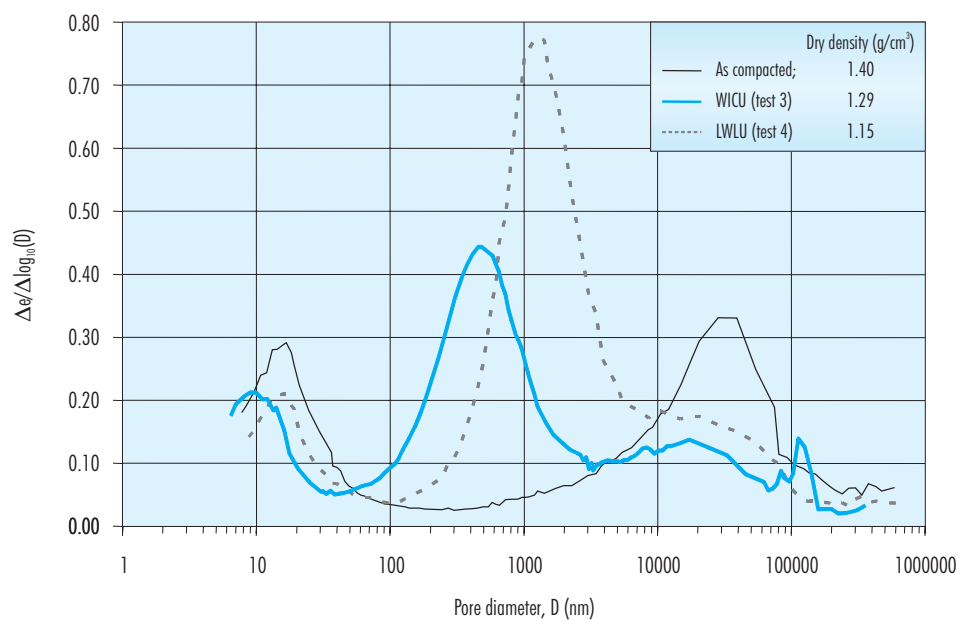


Figure 70: Evolution of PSD functions on wetting at constant vertical net stress (L-W-L-U, test 4) and on wetting at constant volume (WIC-U, test 3). Initial dry density: 1.40 g/cm<sup>3</sup>.

purely smectitic piles (Villar 2000). The progressive subdivision originates the increase in the number of reactive surfaces and the emerging inter-aggregate porosity.

Figure 71 compares the PSD functions of bentonite under saturated conditions, after the wetting paths under constant vertical load (path LWU in Figure 61), and under isochoric conditions (path WICU in Figure 61). It can be observed that the inter-aggregate mode that emerges due to saturation reaches systematic higher peaks on wetting under constant load paths, in which the swelling strains are higher than the small strains imposed in isochoric conditions. The changes due to wetting are more evident in samples with lower density.

Finally, Figure 72 shows the PSD curves of bentonite equilibrated at different suctions under isochoric conditions. Suctions were applied using the vapour transfer technique. The initial conditions of the samples were the same dry density ( $1.65 \text{ g/cm}^3$ ) and hygroscopic water content (about 13%). The dry densities indicated in the figure correspond to conditions before the freeze-drying process and the different densities are due to the different swelling strains experienced

during unloading after the isochoric hydration. The initial as-compacted microstructure with dominant inter-granular and intra-aggregate pore size modes is nearly preserved and the inter-aggregate mode is still latent. It appears that the predominant changes occur due to the transfer of liquid water.

The effect of a heating cycle in the pore size distribution was studied observing the PSD curves of two samples. Both specimens were initially compacted at  $22^\circ\text{C}$  to a dry density of  $1.65 \text{ g/cm}^3$  at hygroscopic water content. The first sample (path LUT, test 16) was heated to  $150^\circ\text{C}$  under unconfined conditions, then was cooled at ambient temperature (water content of 0.54%; dry density of  $1.6 \text{ g/cm}^3$ ) and subjected to the freeze-drying process. The second sample (path WICTU test 17) was saturated under isochoric conditions at a temperature of  $80^\circ\text{C}$  and later heated to  $150^\circ\text{C}$ . After cooling and unload at ambient conditions the resulting water content and dry density were 0.49 % and  $1.58 \text{ g/cm}^3$  respectively. Finally it was subjected to the usual freeze drying process. Figure 73 indicates a certain decrease in the size of intra-aggregate pores and small changes in the inter-aggregate and inter-platelet pore domains, as a consequence of these thermal treatments.

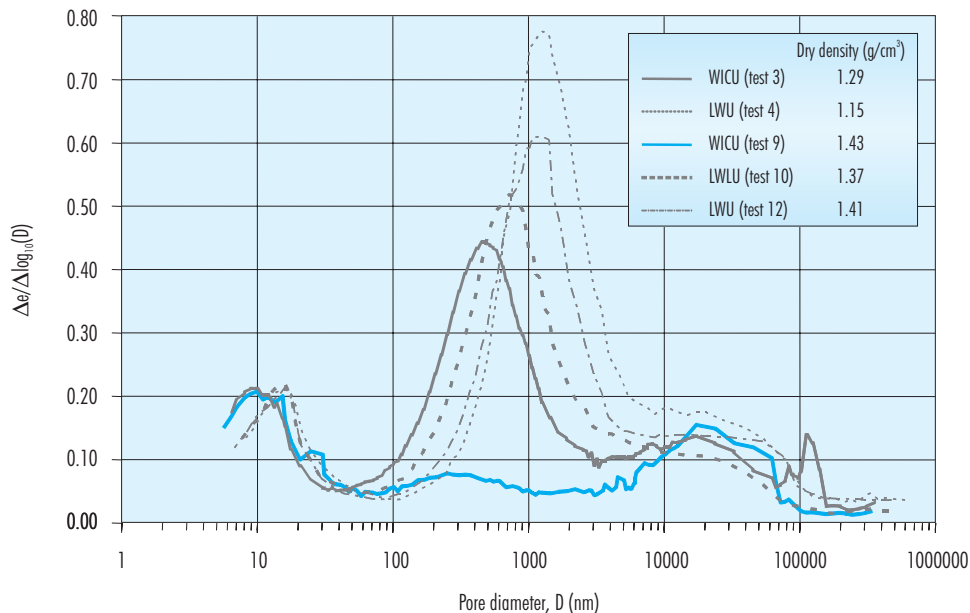


Figure 71: Evolution of PSD functions on wetting at constant vertical net stress (L-W-L-U, tests 4, 10 and 12) and on wetting at constant volume (WIC-U, tests 3 and 9) for initial dry densities of  $1.40 \text{ g/cm}^3$  (tests 3 and 4),  $1.65 \text{ g/cm}^3$  (tests 9 and 10) and  $1.68 \text{ g/cm}^3$  (test 12).

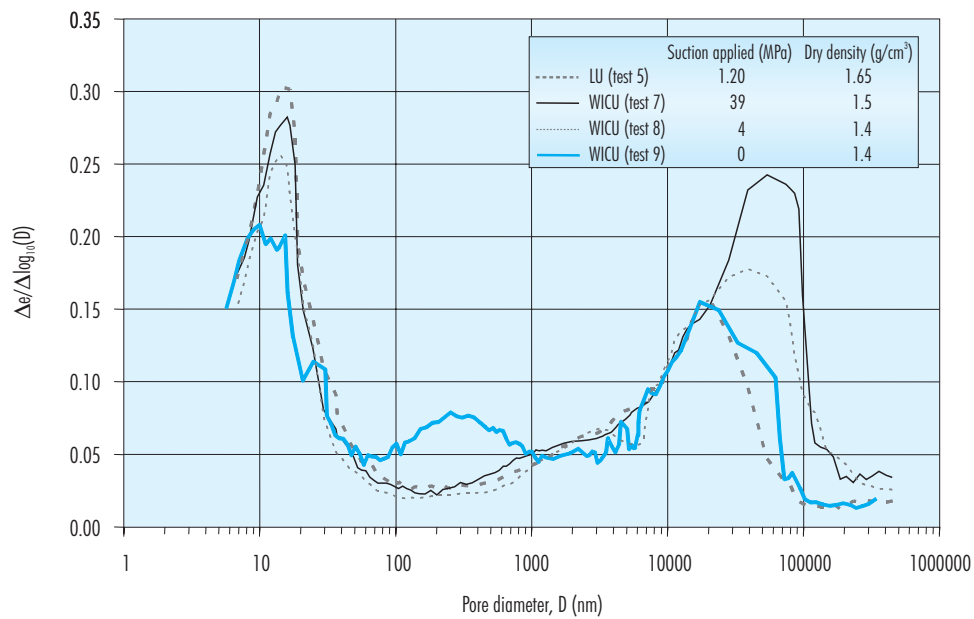


Figure 72: Evolution of PSD functions on wetting at constant volume (WIC-U, tests 7, 8 and 9) for an initial dry density of 1.65 g/cm³.

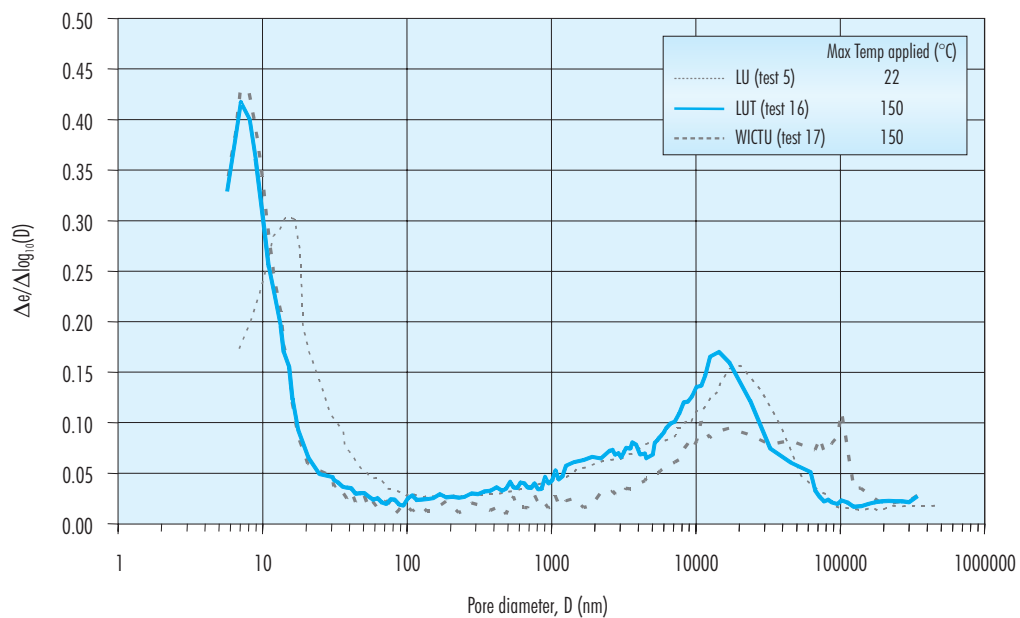


Figure 73: Effect of a heating cycle in the PSD of compacted bentonite (initial dry density 1.65 g/cm³).

### 3.2.2.2 Observations in the environmental scanning electron microscope (ESEM)

A systematic observation of some specimens that were used in the mercury intrusion porosimetry (Table XII) were performed by means of an environmental scanning electron microscope (ESEM). In the microscope used, (Electroscan 2020 ESEM of the Department of Materials Science and Metallurgy of Technical University of Catalonia), a specific environment can be maintained for the purpose of experimentation. An important capability of the equipment is the observation of samples during controlled wetting and drying by regulating separately the temperature and vapour pressure around them. On the other hand, in order to visualize thermal effects, the temperature of the sample can be easily increased over one hundred degrees. Although the observations mainly provide qualitative information, the use of this technique is of interest to enhance the knowledge of the structure changes due to wetting and drying paths. In addition, some samples were observed using the classical scanning electron microscope (SEM) after a process of freeze-drying.

Using the capabilities of the equipment, the microphotographs were made under different environ-

mental conditions of temperature and relative humidity. The used magnification varies generally between 300 and 6000, although in some samples values of 150 or 12000 were used. Table XIII summarises the observations performed, indicating the initial conditions, the path followed by the sample (according to Figure 61) and the environmental conditions in the microscope chamber during the observations. All the microphotographs obtained on the observed samples are shown in Appendix C.

The effect of the type of sample origin can be observed in Figure 74, where the differences between consolidated slurry (test 1 in Table XII) and a compacted sample (test 2 in Table XII) are presented with the same magnification. The consolidated slurry possesses a more uniform and homogeneous structure (matrix structure), in which peds are not clearly distinguished, according to the mercury porosimetry, and the pore size distribution presents a clear mode in a diameter of  $0.4 \mu\text{m}$ . The compacted sample, displaying an aggregated structure, shows denser peds separated by pores of greater dimensions (inter-granular pores).

The effect of compaction intensity can be observed in Figure 75, where the microphotographs of sam-

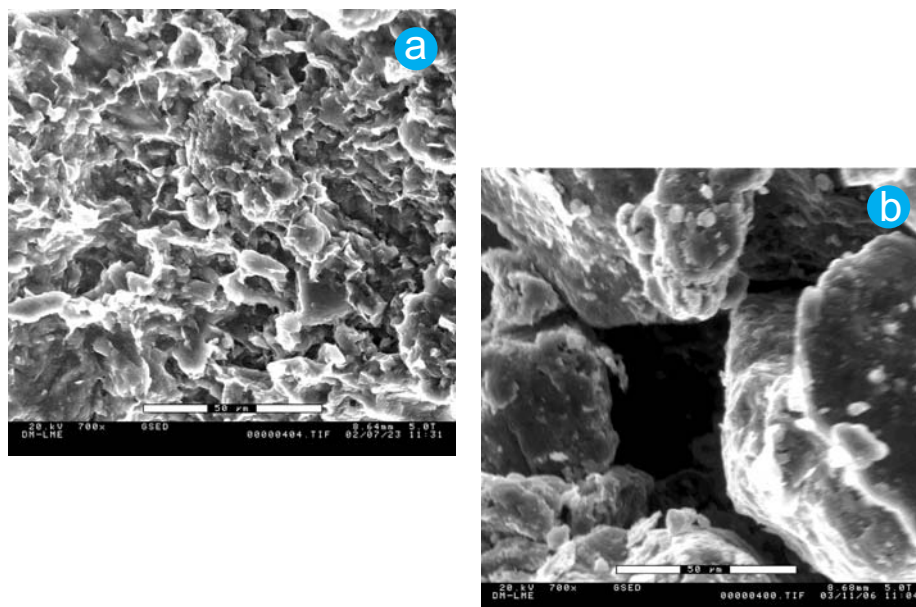


Figure 74: Fabric of bentonite samples ( $\times 700$ ). a) Consolidated slurry ( $\rho_d=1.15 \text{ g/cm}^3$ ). b) Compacted bentonite with hygroscopic water content ( $\rho_d=1.40 \text{ g/cm}^3$ ).

Table XIII

Initial conditions, stress paths (Figure 61) and final conditions before microscope observations, environmental conditions during observations and numbering of microphotographs in Appendix C.

Test	Initial conditions		Path (Figure 61)	Conditions before observations		Environmental conditions in ESEM		Microphotographs in Appendix C			
	$\rho_d$ (g/cm <sup>3</sup> )	w (%)		$\rho_d$ (g/cm <sup>3</sup> )	w (%)	T (°C)	RH (%)				
1	0.62	125	WLU; $\sigma_{M4} = 1.5$ MPa	1.15	49.9	5	75	C.1			
2a	1.40	13	LU; $\sigma_{M4} = 8$ MPa	1.40	13.0	15	41	C.2, C.3			
2b						15	75	C.2			
2c						SEM		C.2, C.10			
3a			WICU; $s_m = 0$	1.29	37.5	16	100	C.3			
3b						17.5	27	C.3			
5a			LU; $\sigma_{M4} = 22$ MPa	1.65	12.6	16	41	C.4, C.5, C.6, C.11			
5b						16	75	C.4			
5c						16	100	C.4			
6						DW; $s_m = 310$ MPa	1.73	8.7	22	15	C.5
7a									23	67	C.5, C.7
7b,c,d	WICU; $s_m = 39$ MPa	1.55	20.3	53 108 151	—	C.7					
8a	WICU; $s_m = 10$ MPa	1.46	23.3	15	75	C.6, C.8					
8b				150	—	C.8					
8c				SEM		C.8, C.10					
9a	WICU; $s_m = 0$ MPa	1.43	29.6	15	75	C.6, C.9					
9b				150	—	C.9					
9c				SEM		C.9, C.10					
16a				LUT; $\sigma_{M4} = 22$ MPa; T: 22→150→22 °C	1.60	0.5	16	41	C.11		
16b	150	—	C.11								

ples compacted to 1.40 and 1.65 g/cm<sup>3</sup> with hygroscopic water content are presented. The size of inter-granular pores is clearly bigger in the sample with smaller dry density. At larger magnification, the differences between the two samples are less evident.

The structure changes, originated by the progressive wetting of compacted bentonite with an initial dry

density of 1.65 g/cm<sup>3</sup>, can be observed in Figure 76. Suction changes in isochoric conditions were applied to samples before the observation in the ESEM (tests 5a, 8a and 9a in Table XIII). The differences in final dry density are due to the rebound experienced by the bentonite after unloading. The progressive occlusion of inter-granular pores due to particle swelling is qualitatively appreciable. The same

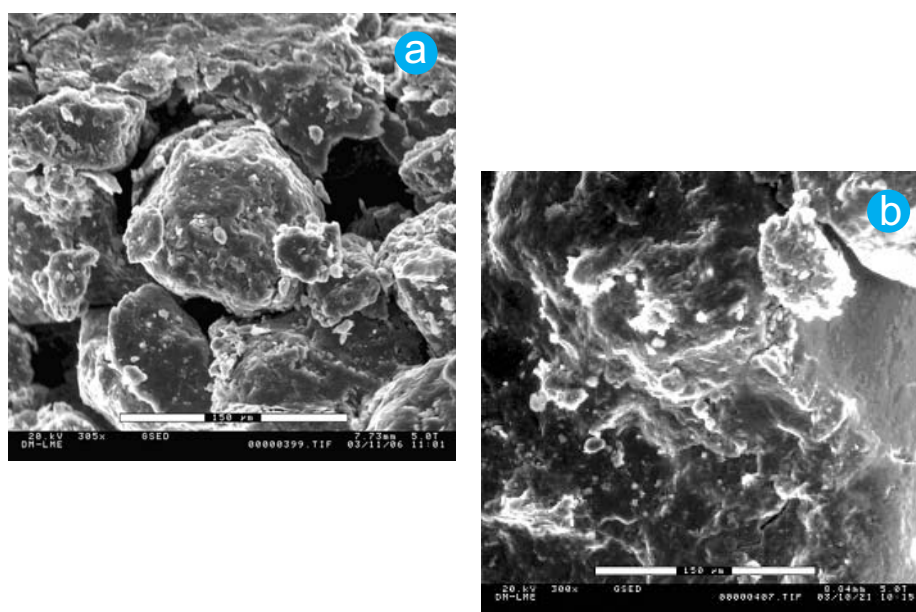


Figure 75: Micrographs of bentonite compacted with hygroscopic water content ( $\times 300$ ). a)  $\rho_d = 1.40 \text{ g/cm}^3$ ; b)  $\rho_d = 1.65 \text{ g/cm}^3$ .

effect can be observed at larger magnification in Figure 77, using the SEM equipment on samples corresponding to tests 2c, 8c and 9c, in Table XIII.

The changes in the structure of compacted bentonite, due to a heating/cooling cycle from  $22^\circ\text{C}$  to  $150^\circ\text{C}$  before the ESEM observation (test 16a), are difficult to appreciate in the microphotographs, due to original differences between the samples (see figures in Table C.11 of the Appendix C). On the other hand, the effect of temperature was also studied varying the temperature of the microscope chamber during some ESEM observations. Figure 78 shows the effects of heating to  $150^\circ\text{C}$  in the microscope chamber on a sample of bentonite that was saturated under isochoric conditions (test 9b in Table XIII;  $\rho_{d \text{ final}} = 1.43 \text{ g/cm}^3$ ). It is difficult to separate, in the small changes observed, the effect of direct thermal effects on mineral particles from the effect of shrinkage due to the loss of water, which seems that would have to be predominant.

In the context of the study of swelling clay behaviour the most relevant feature of the ESEM devices is the possibility of changing the relative humidity of the microscope chamber in order to change the total suction of clay. This possibility allows visualizing the

structural changes in bentonite associated to the changes of water content. Nevertheless, it is necessary to take into account that during the observation, the samples are not confined, which makes difficult to observe the occlusion of inter-granular pores due to the expansion of clay aggregates.

Shrinkage due to drying to ambient conditions from a relative humidity of 100% to 27 % for a sample that was previously saturated under isochoric conditions (tests 3a and 3b in Table XIII) can be observed in Figure 79. On the other hand, swelling experienced by a sample compacted at hygroscopic water content in the microscope chamber, when the relative humidity was increased from 41% to 75 %, is presented in Figure 80 (tests 2a, and 2b in Table XIII).

These relative humidity changes in the microscope chamber were previously performed in the same device by CIEMAT. Figure 81 shows the aspect of clay aggregates in a sample compacted at a dry density of  $1.70 \text{ g/cm}^3$  and observed under a relative humidity of 50 percent. This sample was progressively hydrated during 5 hours in the microscope chamber, by increasing the relative humidity, while keeping the temperature constant. Figure 81 also shows the final aspect of the same sample under a relative



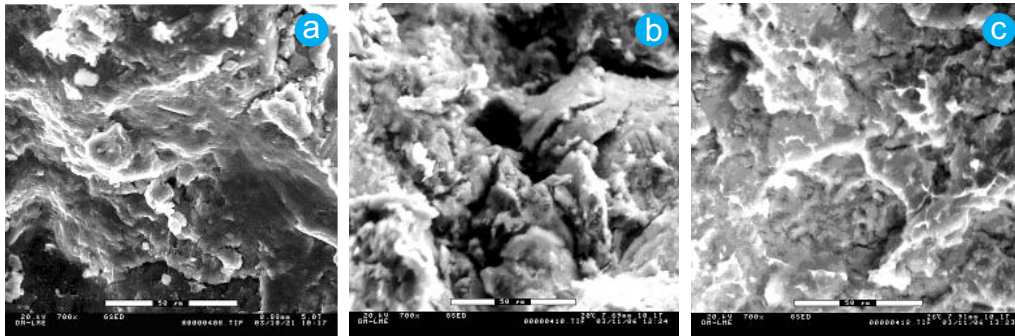


Figure 76: Micrographs ( $\times 700$ ) of bentonite initially compacted with hygroscopic water content, to  $\rho_d = 1.65 \text{ g/cm}^3$ : a) as compacted; b) after application of a suction of 10 MPa under isochoric conditions ( $\rho_{d \text{ final}} = 1.46 \text{ g/cm}^3$ ); and c) after saturation under isochoric conditions ( $\rho_{d \text{ final}} = 1.43 \text{ g/cm}^3$ ).

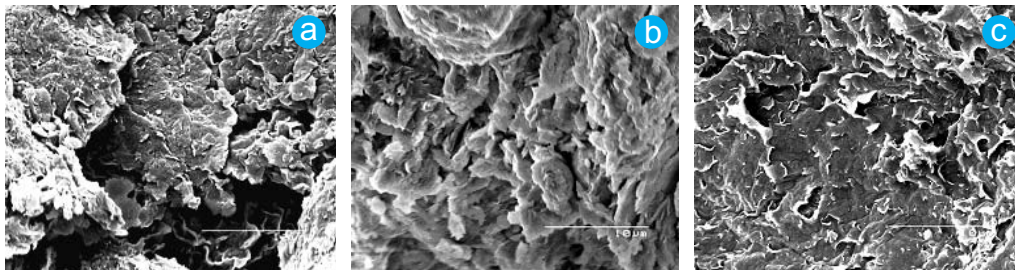


Figure 77: Micrographs (SEM,  $\times 6000$ ): a) compacted with hygroscopic water content to  $\rho_d = 1.40 \text{ g/cm}^3$ ; b) after application of a suction of 10 MPa under isochoric conditions ( $\rho_{d \text{ final}} = 1.46 \text{ g/cm}^3$ ) on bentonite initially compacted under hygroscopic conditions to  $\rho_d = 1.65 \text{ g/cm}^3$ ; and c) after saturation under isochoric conditions ( $\rho_{d \text{ final}} = 1.43 \text{ g/cm}^3$ ) on bentonite initially compacted with hygroscopic water content to  $\rho_d = 1.65 \text{ g/cm}^3$ .

humidity of 100 percent. A decrease of the size of some voids can be observed.

Additional photomicrographs of high-density fabrics were carried out in order to complement the information of aggregate swelling/shrinkage in a wetting/drying path (Figure 82). Measurements of volume changes in ESEM photomicrographs were calculated using digital imaging techniques, as indi-

cated in Figure 83. Swelling/shrinkage results were complemented with wetting and drying paths, performed at macro-scale using vapour equilibrium technique. Reversible and irreversible features of both micro and macroscales are clearly observed in Figure 83 for the same high-density fabric. At micro-scale strains are almost reversible, due to the reversibility of the physical and chemical phenomena that take place at particle level.

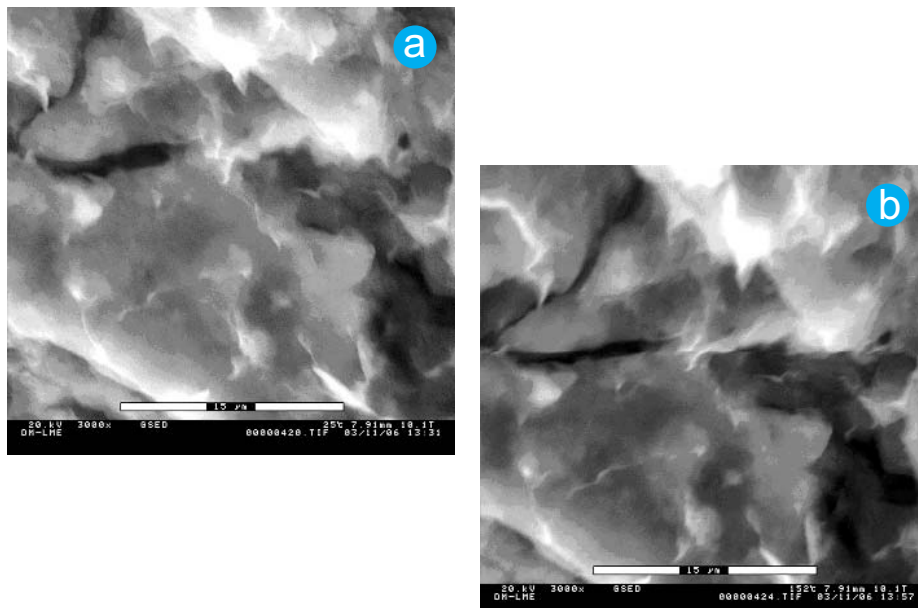


Figure 78: Micrographs of bentonite compacted with hygroscopic water content and subjected to saturation under isochoric conditions (x3000). a) Temperature in the ESEM chamber: 15°C; b) temperature in the ESEM chamber: 150°C.

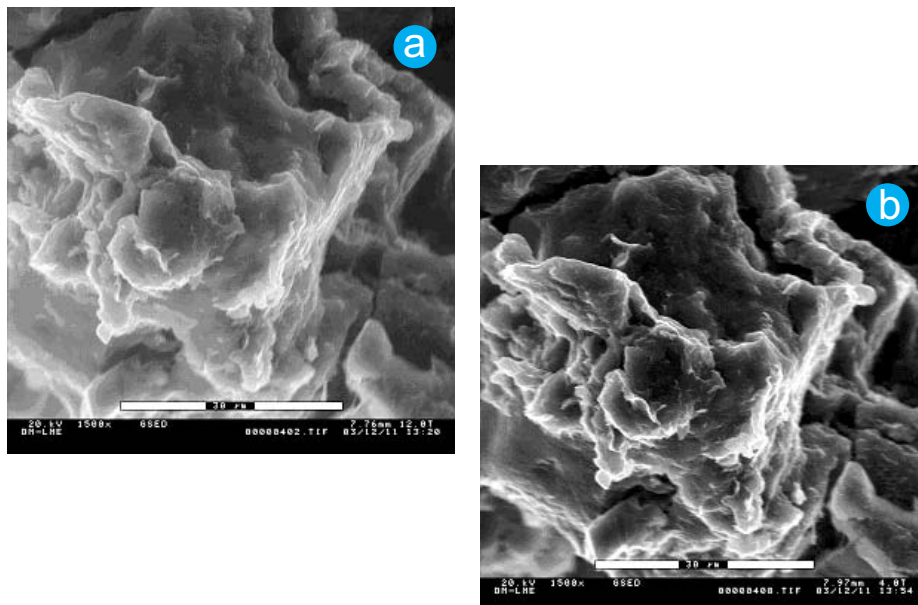


Figure 79: Micrographs of bentonite compacted with hygroscopic water content and subjected to saturation under isochoric conditions (x1500). a) Relative humidity in the ESEM chamber: 100%; b) Relative humidity in the ESEM chamber: 27%.

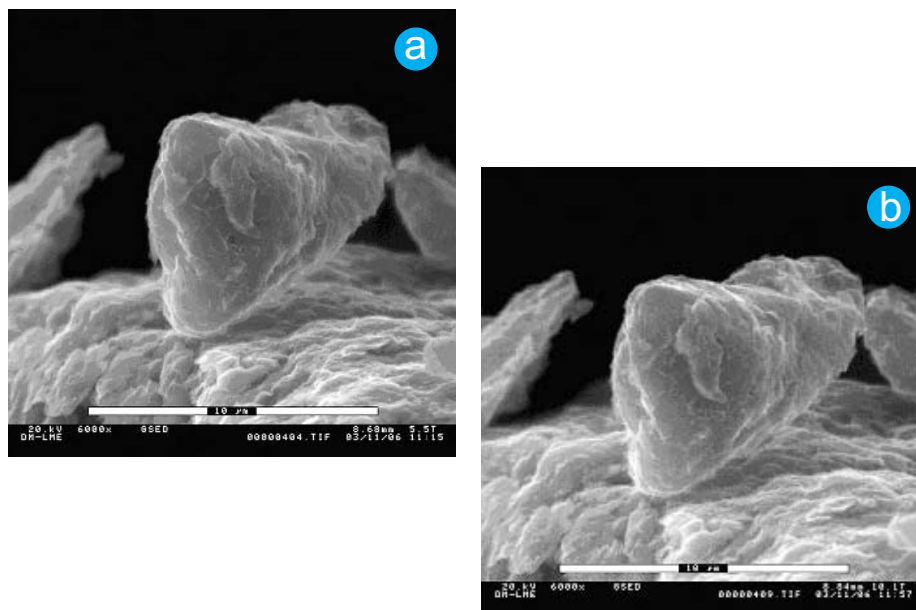


Figure 80: Micrographs of bentonite compacted with hygroscopic water content ( $\times 6000$ ). a) Relative humidity in the ESEM chamber: 41%; b) Relative humidity in the ESEM chamber: 75%.

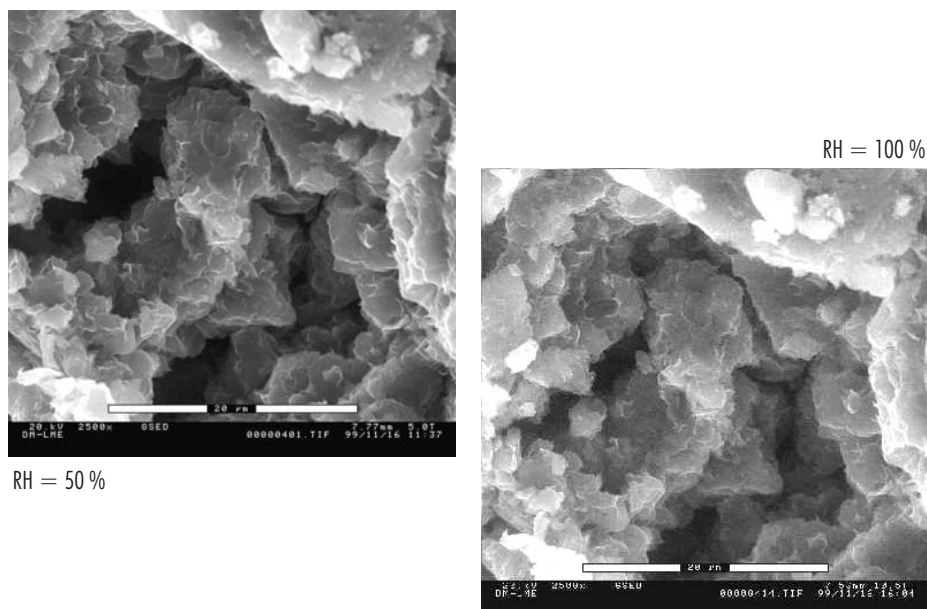


Figure 81: Image analysis evolution of volume change behaviour referring to a compacted bentonite sample at  $\rho_d = 1.7 \text{ g/cm}^3$  (CIEMAT).

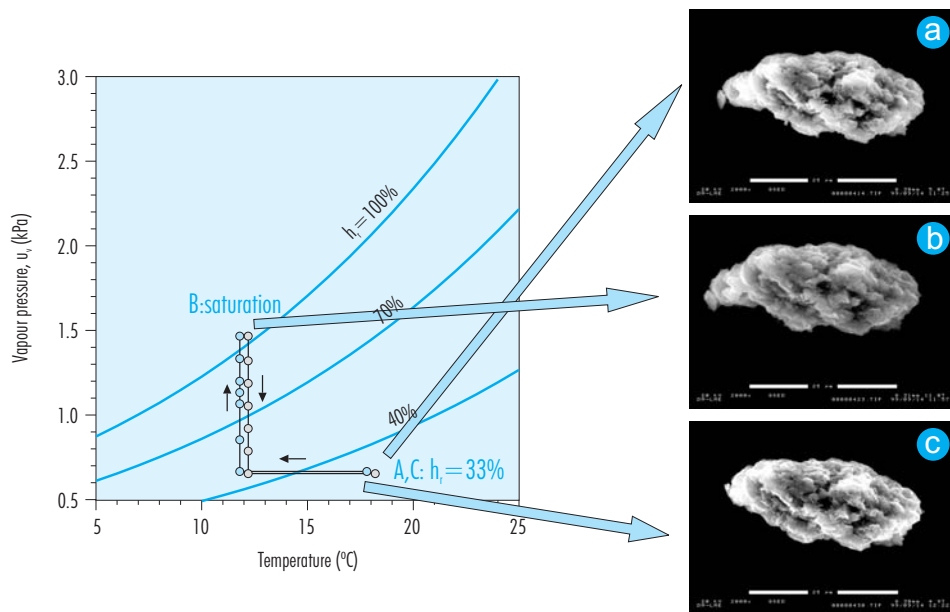


Figure 82: Relative humidity paths followed in the ESEM. Photomicrographs of high-density fabrics at different relative humidity values (CIMNE).

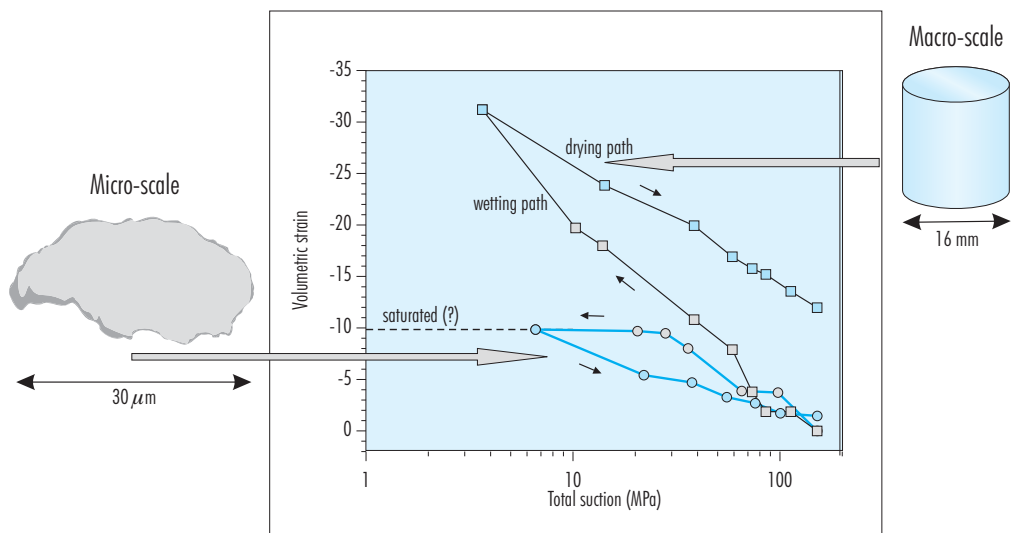


Figure 83: Swelling/shrinkage response at micro and macroscale for high-density fabrics (CIMNE).

### 3.2.3 Influence of solutes in the THM behaviour of the clay

In order to evaluate the influence of solutes in the mechanical behaviour of bentonite, some simple mechanical and hydraulic tests were performed. The work can be divided into two parts. In the first part, performed by CIMNE, the influence of solutes was studied using mainly solutions including variable concentrations of NaCl and CaCl<sub>2</sub>. In the second part, performed by CIEMAT, the solutions that were used are a granitic water and a saline water, similar respectively to the water existing in a Spanish granite and to FEBEX bentonite interstitial water.

#### 3.2.3.1 Preliminary oedometric tests with high salinity solutions

CIMNE performed preliminary tests in which the bentonite, initially compacted at a dry density of 1.63 g/cm<sup>3</sup> with its hygroscopic water content, was hydrated under a vertical pressure of 0.05 MPa using different solutions. Distilled water and saturated solutions of K<sub>2</sub>SO<sub>4</sub>, CaCl<sub>2</sub> and MgCl<sub>2</sub> were used. The results obtained are shown in Figure 84.

In addition, the mechanical effect of solutes in compacted bentonite (dry density 1.68 g/cm<sup>3</sup> and hygroscopic water content) was studied by CIMNE under oedometric conditions. Figure 85 shows the evolution of volumetric strains induced by the following stages:

- saturation by a saline solution (NaCl 5.5M),
- replacement of saline water by distilled water, and
- replacement of distilled water by a saline solution (NaCl 5.5M).

An unloading-reloading stage was performed, before the imbibition stage with distilled water, in order to clean the bottom coarse porous stone. Another unloading-reloading cycle was performed during the transient phase of the distilled water imbibition stage in order to replace the distilled water. An important irreversibility was detected in these loading cycles. A clear shrinkage is induced in the last stage, when the distilled water is replaced by the saline solution. Further improvements in the experimental procedure will be carried out to minimise the mechanical disturbances due to unloading processes.

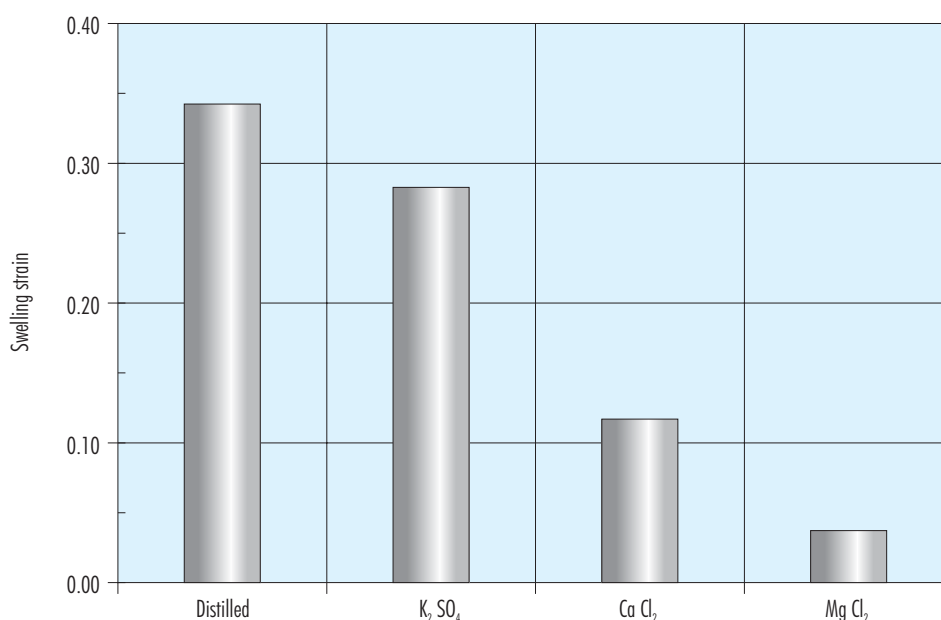


Figure 84: Preliminary results by CIMNE on the influence of the saturating solution on swelling capacity (bentonite compacted at a dry density of 1.63 g/cm<sup>3</sup> and saturated under a vertical pressure of 0.05 MPa).

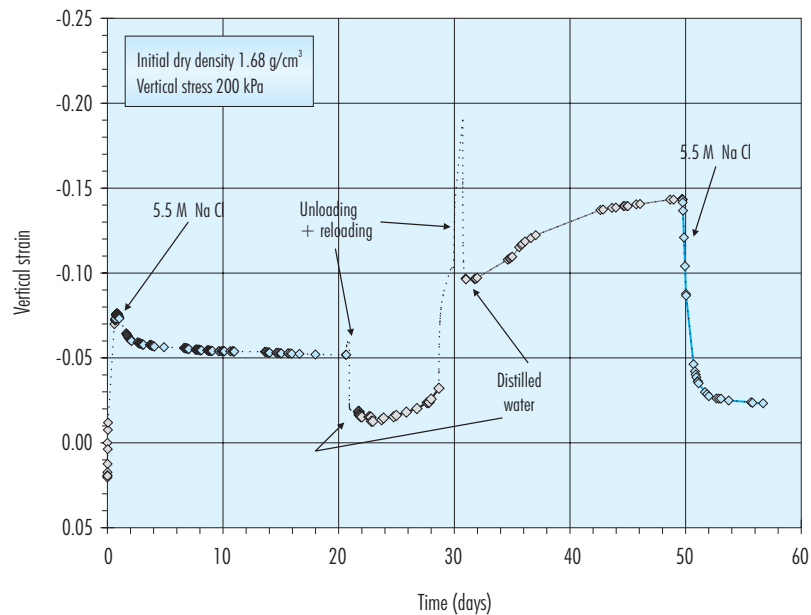


Figure 85: Effect of the substitution of the water composition in saturated compacted bentonite under oedometric conditions (CIMNE).

### 3.2.3.2 Tests using NaCl and CaCl<sub>2</sub> solutions

The experimental programme includes the determination of the effect of salt concentration on Atterberg liquid limit, retention curve, swelling pressure, swelling under load, stiffness, permeability and fabric.

The liquid limit was obtained mixing the FEBEX bentonite powder with distilled water, as well as with solutions of NaCl and CaCl<sub>2</sub>, whose concentration varied in a range of 0.1 up to 5.5 M. Figure 86 shows that the liquid limit diminishes considerably when the concentration of the saturation solution is increased. It can be appreciated that for the same molar concentration the values of liquid limit obtained from samples saturated with solutions of CaCl<sub>2</sub> are smaller than those obtained with samples saturated with solutions of NaCl.

The retention curves of compacted bentonite samples were obtained following wetting paths. The water content of the samples was increased progressively adding three types of fluid: distilled water and NaCl solutions with concentrations of 2.5 and 5.5 M. In each step the total suction was measured using a SMI transistor psychrometer (approximate measurement range between 100 MPa and 0.5 MPa). The

samples (14.6 mm in diameter and 10 mm high) were initially compacted with hygroscopic water content to a dry density of 1.65 g/cm<sup>3</sup>. During the wetting process, the samples were confined only laterally in the psychrometric chamber and the volume changes were not measured. Two types of paths were performed; in the first one (Figure 87), the samples were wetted starting from the hygroscopic water content and in the second one (Figure 88), the samples were dried after compaction, in order to start the wetting process from almost null water content. In the samples wetted with saline solutions, at saturation, the measured total suction tends to the osmotic pressure induced by each solution (33 MPa in the case of 5.5 M NaCl and 12.2 MPa in the case of 2.5 M NaCl). Assuming that the osmotic suction, due to the salinity of natural bentonite water (see Table XV), is small, it is possible to estimate the matrix suction in the tests. The retention curve computed using this matrix suction tends to the retention curve obtained in the sample wetted with distilled water. In the Figures the empirical expression obtained in FEBEX I (eq. [4]) to describe the retention curves in unconfined conditions is also included. It must be noted that at low suctions, the water content is affected by the important volume increment of the

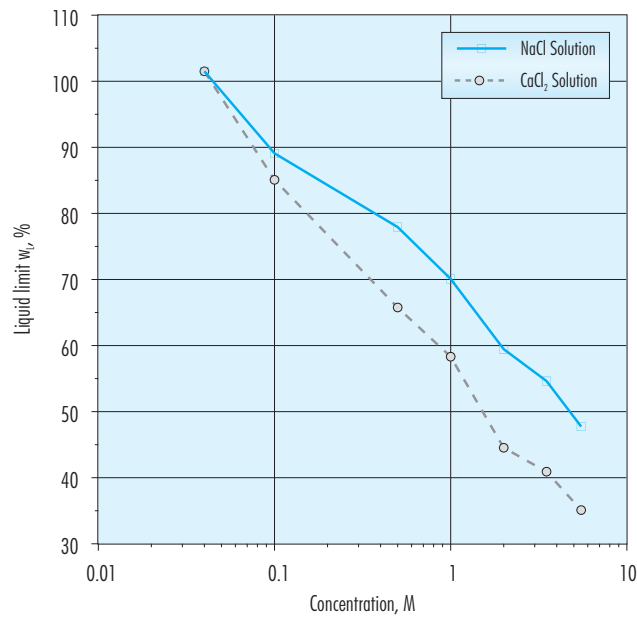


Figure 86: Influence of solutes in liquid limit.

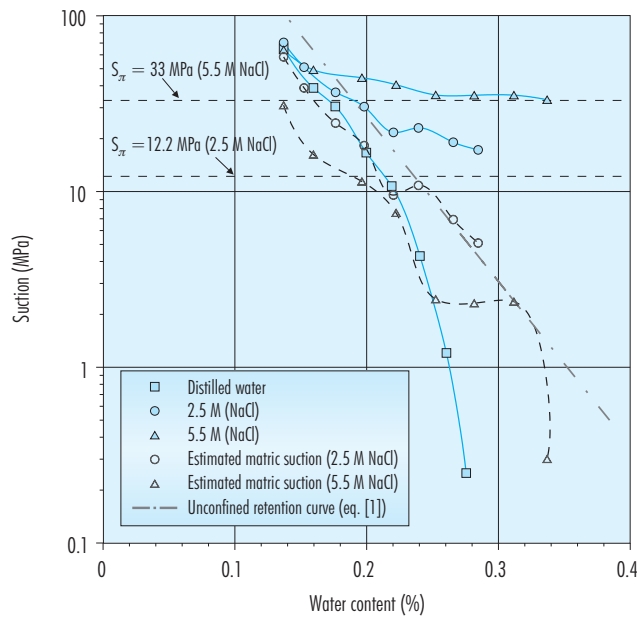


Figure 87: Retention curves of bentonite in wetting paths using water with different salinity (starting from hygroscopic state).

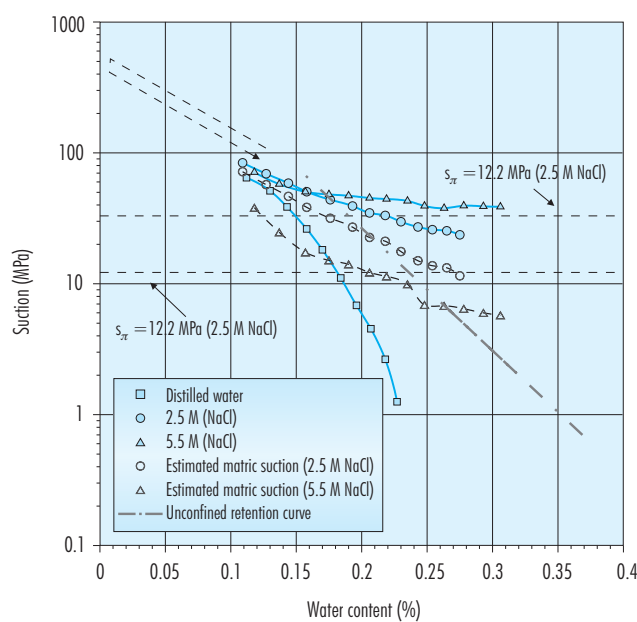


Figure 88: Retention curves of bentonite in wetting paths using water with different salinity (starting from dried state).

Table XIV  
Summary of swelling pressure tests using NaCl and CaCl<sub>2</sub> solutions for bentonite compacted at  $\rho_d = 1.65 \text{ g/cm}^3$ .

Test	Cell	Solution	Liquid injection pressure (MPa)	Time to reach swelling pressure (days)	Swelling pressure (MPa)
1	Conventional oedometer	Distilled water	0.0	15	4.49
2	Isochoric cell	Distilled water	0.2	7	4.43
3	Isochoric cell	Distilled water	0.2	8	4.42
4	Conventional oedometer	0.1 M NaCl	0.0	13	3.99
5	Conventional oedometer	2.5 M NaCl	0.0	3.8	2.88
6	Conventional oedometer	5.5 M NaCl	0.0	2.3	2.64
7	Isochoric cell	6.3 M NaCl	0.2	2.4	2.42
8	Isochoric cell	4.2 M CaCl <sub>2</sub>	0.2	4.8	2.75



samples that were not measured in the tests; these volume changes and the measurement errors of the equipment in the low range of suctions may explain the discrepancies observed between the retention curve obtained using the estimated matrix suction and the retention curve measured with distilled water.

The effect of water salinity in swelling pressure was investigated measuring the swelling pressure of bentonite that was saturated under isochoric conditions using solutions of NaCl and CaCl<sub>2</sub> at different concentrations. Initially, the bentonite was compacted at a dry density of 1.65 g/cm<sup>3</sup> at hygroscopic conditions. Some tests were performed in a conventional oedometer, in which the lever arm was fixed to prevent the swelling of the soil. Other tests were performed in the small isochoric cells shown in Figure 16, in this last case an overpressure of 0.2 MPa was applied on the water input to reduce the duration of the tests. In all tests, the thickness of the specimens was 10.5 mm and the diameter was 50 mm. Table XIV shows a summary of the tests performed and results obtained.

The values of swelling pressure obtained with distilled water are significantly lower than those obtained previously using other devices (eq. [3]). This fact may be

explained taking into account the small swelling strains experienced by the soil in both types of cells. However, the values obtained in this series of tests are comparable and repeatable (see results of tests 1, 2 and 3) and therefore they may be used to study qualitatively the role of salinity in the swelling pressure of bentonite. Figure 89 and Figure 90 show the evolution in time of swelling pressure, when the bentonite is saturated using solutions with different salinity. It can be observed that an increase of salt concentration reduces the swelling pressure (see Figure 91). This reduction could be related to an increase of osmotic suction, however, it must be noted that the osmotic suction associated to the solution 6.3 M of NaCl and to the solution 4.2 M of CaCl<sub>2</sub> is equal to 40 MPa in both cases, but the reduction of swelling pressure is bigger when the NaCl is used as a solute (see Figure 91). On the other hand, the reduction of the time necessary to reach the final swelling pressure that was observed in the tests (see Table XIV), when concentration of NaCl is increased, may be attributed to an increase of the permeability with salinity.

In order to evaluate the effect of salinity on swelling strains, tests were performed in conventional oedometers (sample thickness 10.5 mm and diameter 50

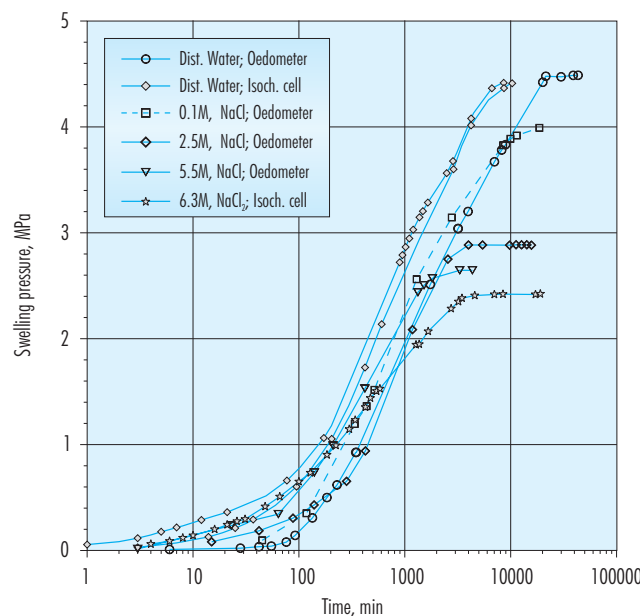


Figure 89: Evolution of swelling pressures measured using water at different concentrations of NaCl, ( $\rho_d = 1.65 \text{ g/cm}^3$ ).

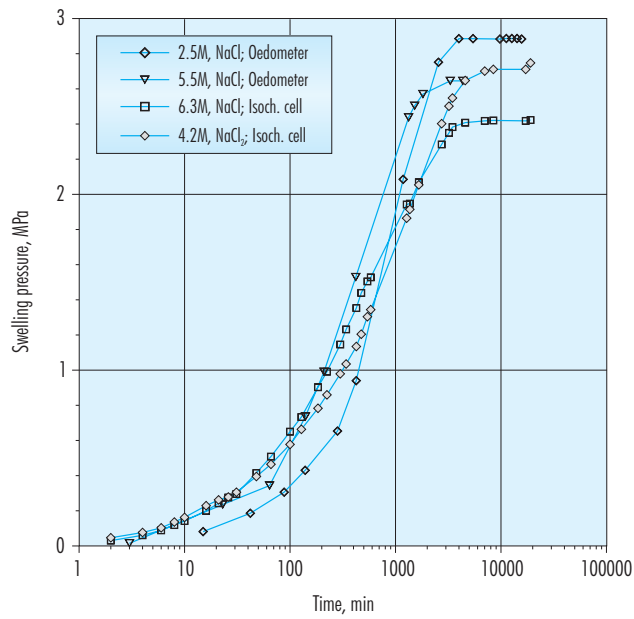


Figure 90: Evolution of swelling pressures measured using water at different concentrations of NaCl and CaCl<sub>2</sub>, ( $\rho_d = 1.65 \text{ g/cm}^3$ ).

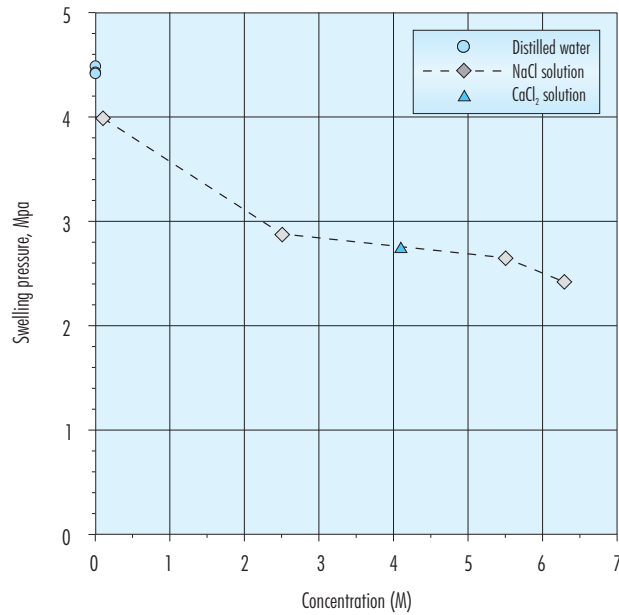


Figure 91: Swelling pressure values for different concentrations and solutions, ( $\rho_d = 1.65 \text{ g/cm}^3$ ).

mm). In these tests bentonite compacted to a dry density of  $1.65 \text{ g/cm}^3$  was soaked under a load of  $0.5 \text{ MPa}$  using different solutions. After soaking, the bentonite was loaded under oedometric conditions up to  $2 \text{ MPa}$ , in order to evaluate the bentonite stiffness and permeability. The first loading up to  $0.5 \text{ MPa}$  was performed in two days using small steps ( $0.02, 0.05, 0.1$  and  $0.5 \text{ MPa}$ ) and maintaining the hygroscopic water content. During this loading stage the volume changes were very small, since the applied load was lower than the compaction stress

(about  $23 \text{ MPa}$ ). In the wetting stages the time necessary to reach the stabilisation of vertical displacements was about 5 days, but this stage was extended to two weeks. After the saturation stage, the vertical load was increased following the ordinary oedometric procedure up to  $1$  and  $2 \text{ MPa}$ . The unloading stage was performed in two steps.

Figure 92 shows the results of soaking under load tests in terms of changes in void ratio. The evolution of volumetric strains during wetting is presented in

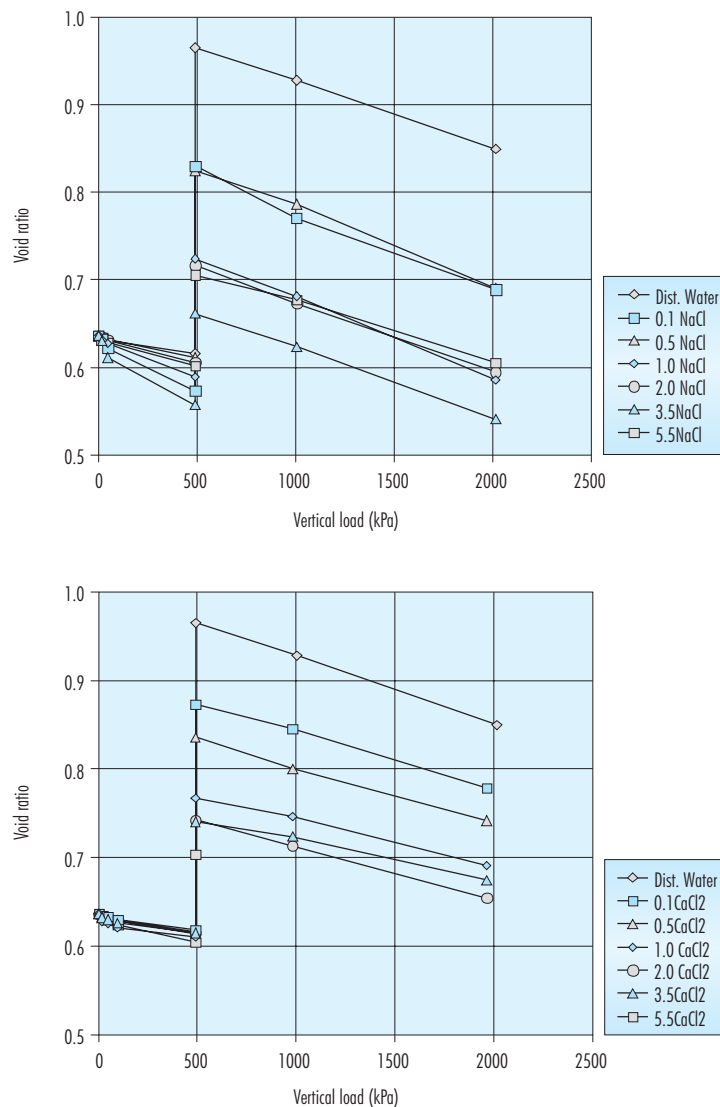


Figure 92: Changes in void ratio during soaking under load tests using different solutions (initial  $\rho_d = 1.65 \text{ g/cm}^3$ ).

Figure 93, and Figure 94 shows the values of the final swelling strains. It can be observed that the swelling capacity decreases significantly with salinity. On the other hand, samples wetted with  $\text{CaCl}_2$  solutions swell slightly more than those wetted with  $\text{NaCl}$ . If the osmotic pressure of the solution is considered, the effect of changes in salt concentration can be compared with the changes measured in suction controlled oedometers. Figure 95 shows that the volume changes, measured in a suction controlled oedometer test (Figure 4) during suction reduction

stages, are comparable with the volume changes measured in soaking tests using salt solutions.

The evolution in time of vertical settlements measured after the application of a vertical load on saturated samples is shown in Figure 96, for the case of samples saturated with  $\text{NaCl}$  solutions, and in Figure 97, for the case of  $\text{CaCl}_2$  solutions. In these Figures, despite the dispersion of the results, it is possible to observe that the samples saturated with solutions containing high concentrations are less de-

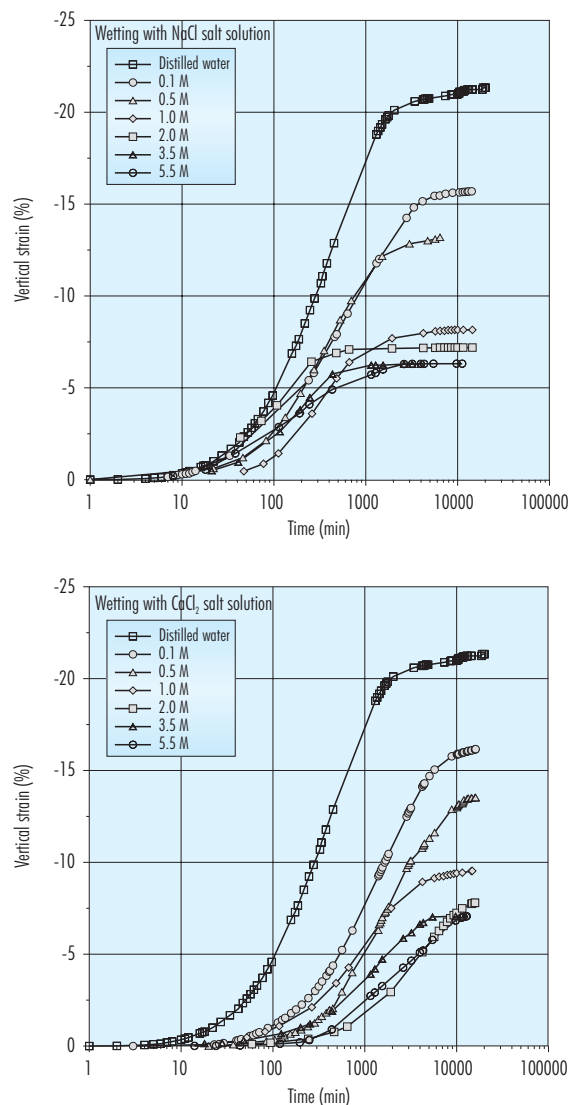


Figure 93: Evolution of swelling strains during wetting under a vertical load of 0.5 MPa with different solutions (initial  $\rho_d = 1.65 \text{ g/cm}^3$ ).

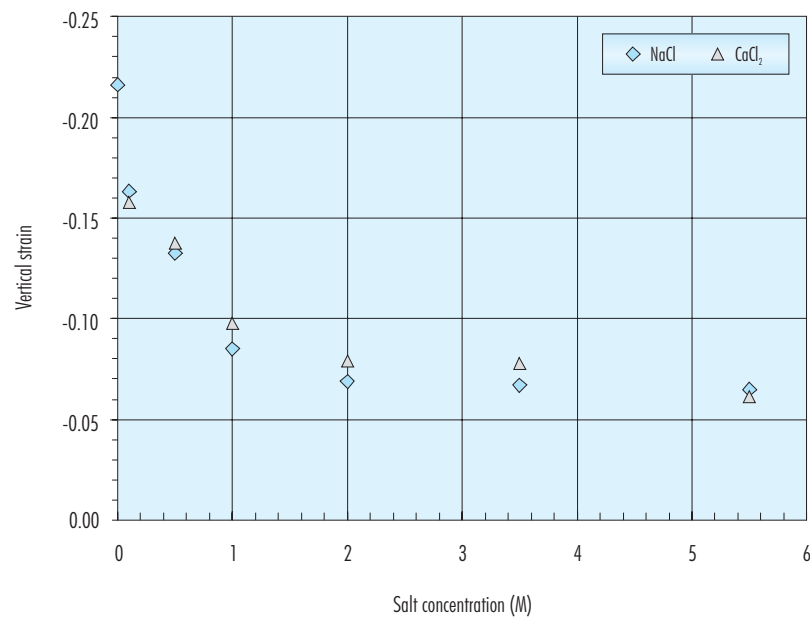


Figure 94: Variation of swelling strains due to wetting with different solutions under a vertical stress of 0.5 MPa, (initial dry density 1.65 g/cm<sup>3</sup>).

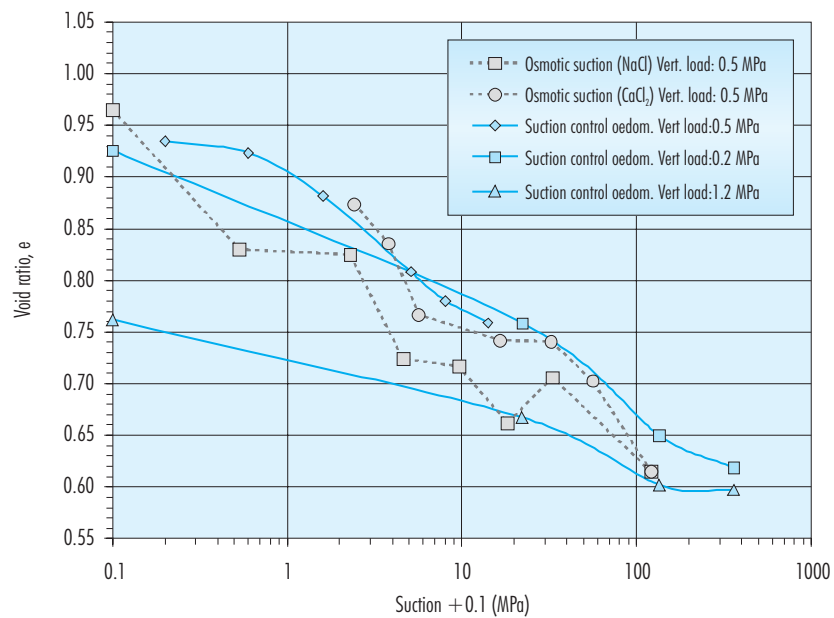


Figure 95: Comparison between swelling strains due to suction reduction and strains due to soaking with different NaCl and CaCl<sub>2</sub> concentrations.

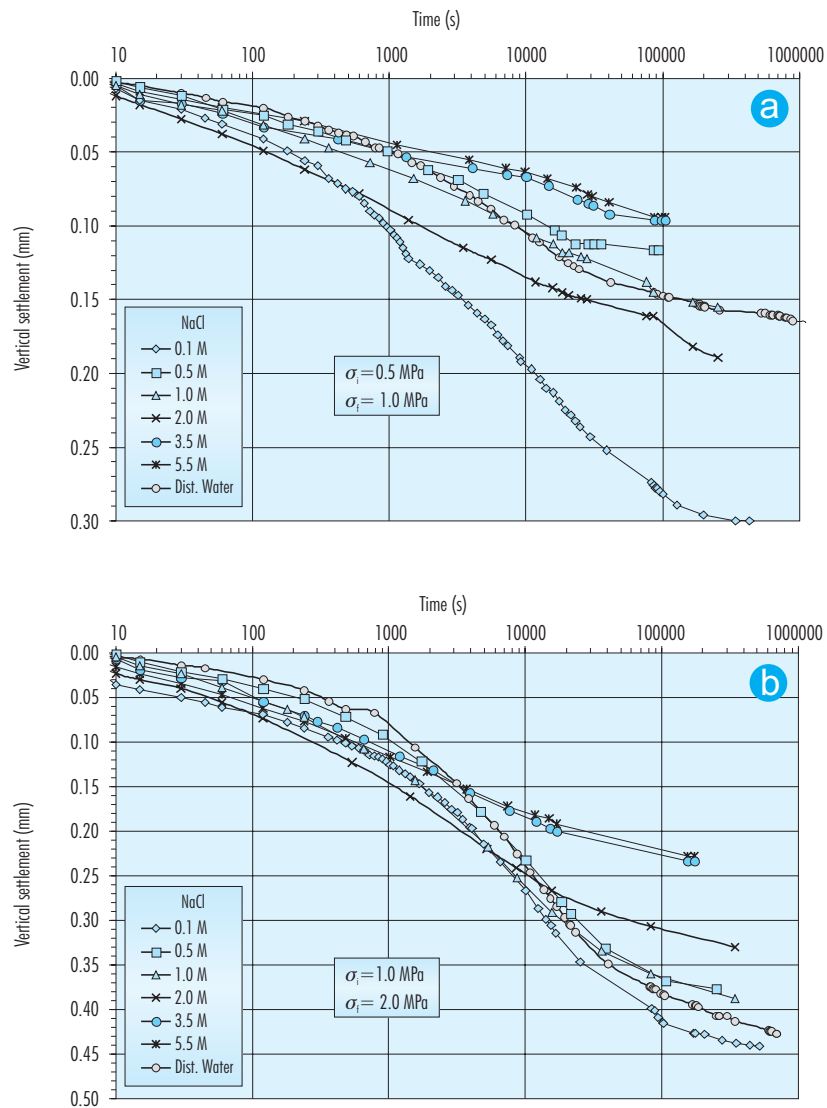


Figure 96: Evolution of vertical settlements due to loading under oedometric conditions of samples saturated with solutions of NaCl at different concentrations. a) loading from 0.5 to 1.0 MPa; b) loading from 1.0 to 2.0 MPa.

formable and consolidate more rapidly than the samples saturated with low salinity solutions. Using the Terzaghi's 1D consolidation theory it is possible to obtain the consolidation coefficient ( $c_v$ ), the consolidated elastic modulus ( $E_m$ ) and the water permeability ( $k$ ); in addition, from the same curves, the secondary consolidation coefficient ( $C_{\alpha}$ ) can be measured. The values obtained for these parameters are summarised in Table A.15 and Figure 98. The increase with salinity of the consolidation coefficient, water perme-

ability and stiffness ( $E_m$  and  $C_{\alpha}$ ) can not be attributed only to solute effects; in fact, the different structure (void ratio) of the samples after saturation plays a significant role in the value of these parameters.

In order to eliminate the effect of dry density in the comparison of the values of water permeability using different solutions, the permeability obtained from these oedometric tests can be compared with the values of deionised water permeability at the

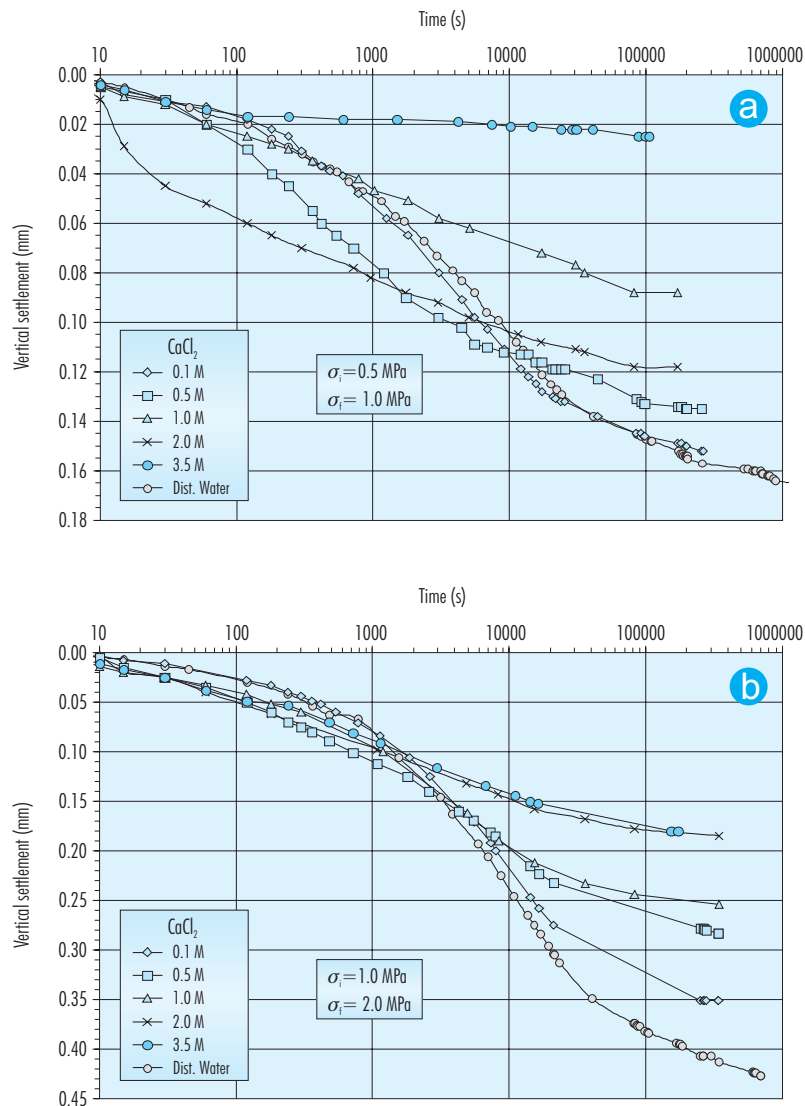


Figure 97: Evolution of vertical settlements due to loading under oedometric conditions of samples saturated with solutions of  $\text{CaCl}_2$  at different concentrations a) loading from 0.5 to 1.0 MPa; b) loading from 1.0 to 2.0 MPa.

same void ratio that can be obtained using the regression of equation [2]. Figure 99 shows that the influence of salinity on saturated permeability is significant. On the other hand, from the tests performed it is not possible to clearly obtain conclusions about the effect of the solute type on the variation of permeability due to salinity.

Finally, in order to evaluate the effect of salinity on pore size distribution, a mercury intrusion porosimetry

(MIP) test was performed on a sample after a swelling under load test. The sample compacted initially to a dry density of  $1.65 \text{ g/cm}^3$  was wetted with a solution  $\text{NaCl}$  0.5 M under a vertical load of 0.5 MPa, later the sample was loaded up to 2 MPa and finally unloaded and subjected to the conventional freeze drying process. Figure 100 shows the comparison of the pore size distribution curve of this sample with the sample soaked with distilled water and with the as compacted state. The structure of

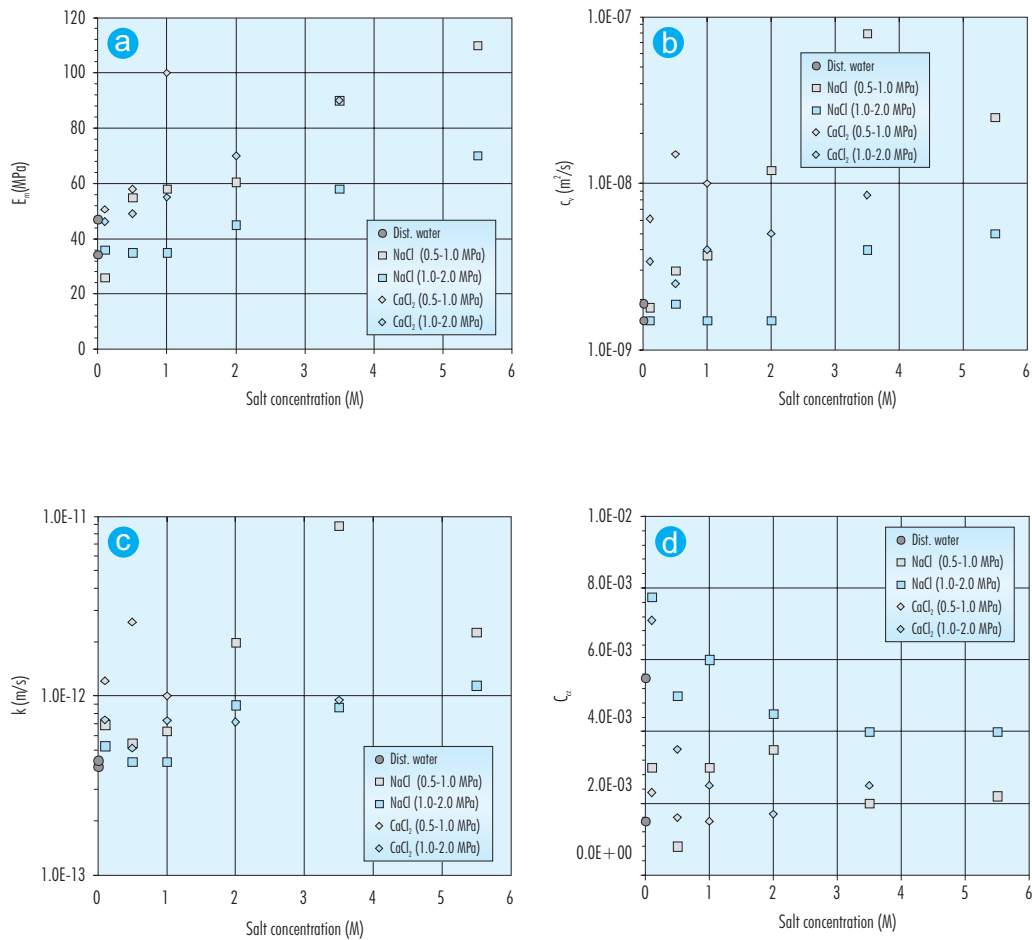


Figure 98: Variation with salinity of parameters obtained from oedometric tests on samples saturated with different solutions.

the sample soaked with the NaCl solution is similar to that of the sample saturated with distilled water. In the saline sample, the smaller volume associated to the inter-aggregate pores may be attributed to the value of the swelling strains experienced during the saturation process that were smaller than those measured when the sample was soaked with distilled water.

### 3.2.3.3 Tests with low concentration solutions

The swelling capacity of bentonite was determined by CIEMAT on samples compacted at a dry density of  $1.60 \text{ g/cm}^3$  with its hygroscopic water content

(around 14 percent), saturated in oedometers under different vertical loads. Deionised, saline and granitic waters were used as saturation liquid. Granitic water simulates the conditions of the outer part of the barrier, and saline water simulates the situation in the internal part of the barrier, where water is loaded with ionic species dissolved during its inward movement (Table XV). The latter has a chemical composition similar to that bentonite interstitial water (Fernández & Cuevas 1998), but simplified to include only the major elements.

The results obtained are gathered in Table A. 16, for deionised water, Table A. 17, for saline water and Table A. 18, for granitic water, where the strain per-



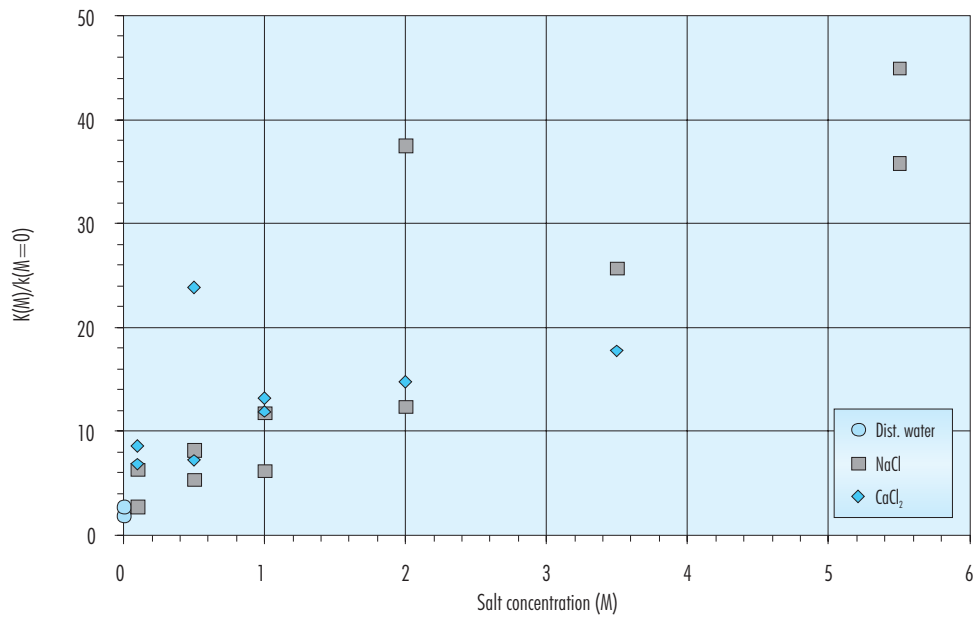


Figure 99: Relationship between the values of permeability, estimated from oedometric tests on samples saturated with different solutions, and the values of the permeability at the same void ratio, measured directly using distilled water (equation [2]).

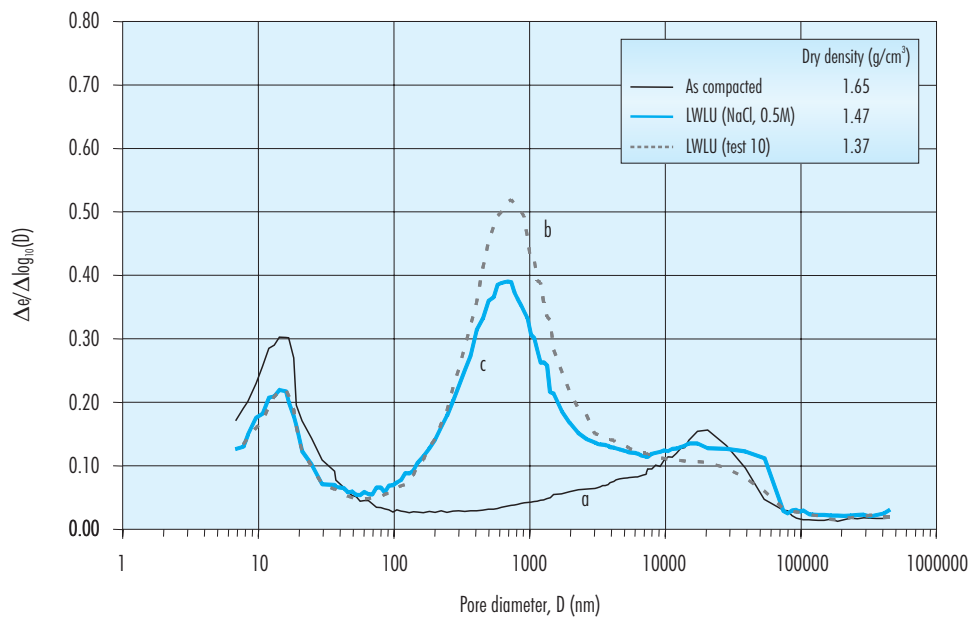


Figure 100: Pore size distribution curves of bentonite compacted to 1.65 g/cm³, soaked under a vertical stress of 0.5 MPa and loaded up to 2 MPa. a) As compacted state, b) soaked with distilled water (Test 10 of Table XII) and c) soaked with a solution of 0.5 M of NaCl.

Table XV  
Chemical composition of the water used in the tests by CIEMAT.

Element (mmol/l)	Granitic	Saline
Cl <sup>-</sup>	0.37	100
SO <sub>4</sub> <sup>2-</sup>	0.15	15
HCO <sub>3</sub> <sup>-</sup>	2.36	
Mg <sup>2+</sup>	0.39	15
Ca <sup>2+</sup>	1.12	10
Na <sup>+</sup>	0.48	80
K <sup>+</sup>	0.026	
pH	8.3	7

centage is calculated as the increase of height with respect to the initial height of the sample, and the negative values indicate swelling strains.

Final strains as a function of vertical pressure are represented in Figure 101, for the nominal dry density of 1.50 g/cm<sup>3</sup>, in Figure 102, for the nominal dry density of 1.60 g/cm<sup>3</sup> and in Figure 103, for the nominal dry density of 1.70 g/cm<sup>3</sup>. The fittings obtained for the different types of water are also shown in these figures. Taking into account all the results, the following fittings between final swelling strain ( $\varepsilon$ , %) and vertical pressure ( $\sigma$ , MPa), as a function of the initial dry density ( $\rho_d$ , g/cm<sup>3</sup>), were found:

For deionised water:

$$\varepsilon = (5.40 \rho_d - 1.32) \ln \sigma + (-48.25 \rho_d + 63.69) \quad [12]$$

For saline water:

$$\varepsilon = 6.47 \ln \sigma + (-48.71 \rho_d + 66.13) \quad [13]$$

For granitic water:

$$\varepsilon = (-6.49 \rho_d + 16.53) \ln \sigma + (-43.59 \rho_d + 58.14) [14]$$

A higher swelling capacity was observed in samples saturated with deionised water, although this difference becomes less apparent for higher vertical pressures.

### 3.3 New test performed up to the dismantling

In order to understand the unexpected behaviour observed in the “mock-up” test, *i.e.* the reduction in

the water uptake rate (FEBEX Meeting 28-29 March 2002), several specific tests were proposed, whose aim is to ascertain if the causes proposed to explain this behaviour were confirmed. Among the aspects considered as possible explanations to the phenomena observed were:

- ❑ Misfunction of the geotextile, by filling-up of its pores, which would reduce its permeability and the amount of water entering the system.
- ❑ Long term variations of the permeability of clay, by changes in its microstructure.
- ❑ Unexpected variation of the hydro-mechanical properties of clay as a consequence of the high temperature.
- ❑ Overestimated permeability of the clay: the values of permeability were obtained under high hydraulic gradients –not representative of the actual conditions in the “mock-up”–, which, besides, has hindered the observation of the existence of a critical gradient.

Taking into account these hypotheses, discussed in the meeting of the Spanish participants held in ENRESA (meeting minutes 70-ST-C-0-57, June 15<sup>th</sup> 2001) the following laboratory tests were proposed to be performed by CIEMAT: permeability tests and infiltration tests with and without thermal gradient. Besides, a study of the repercussion of the high hydraulic gradients applied for the determination of hydraulic conductivity on the values obtained was proposed.

On the other hand, in the same context and in order to gain insight into the knowledge of the effect of the temperature on the hydromechanical behav-

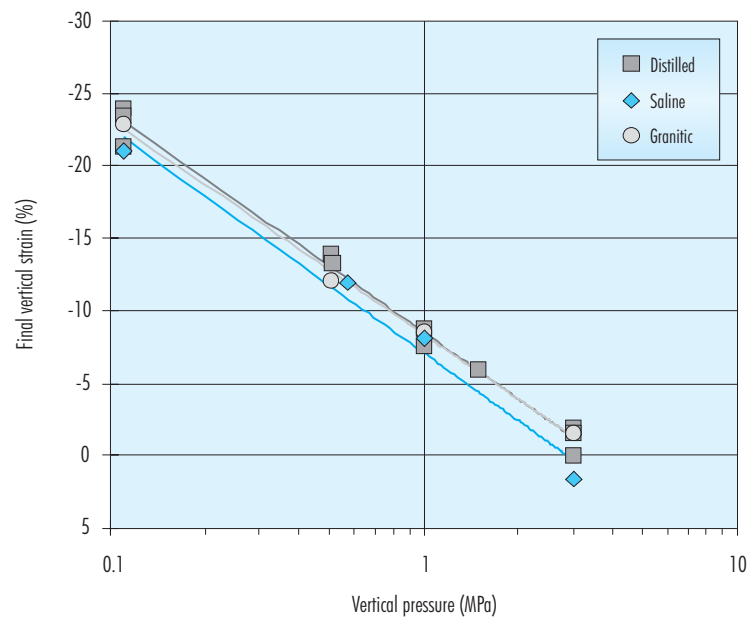


Figure 101: Final strain of samples of dry density  $1.50 \text{ g/cm}^3$  saturated under different vertical pressures with different waters (CIEMAT).

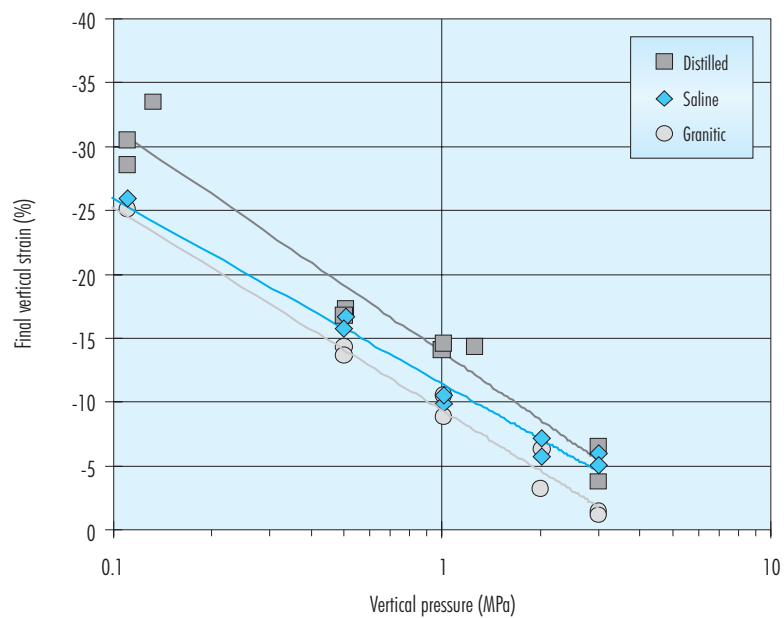


Figure 102: Final strain of samples of dry density  $1.60 \text{ g/cm}^3$  saturated under different vertical pressures with different waters (CIEMAT).

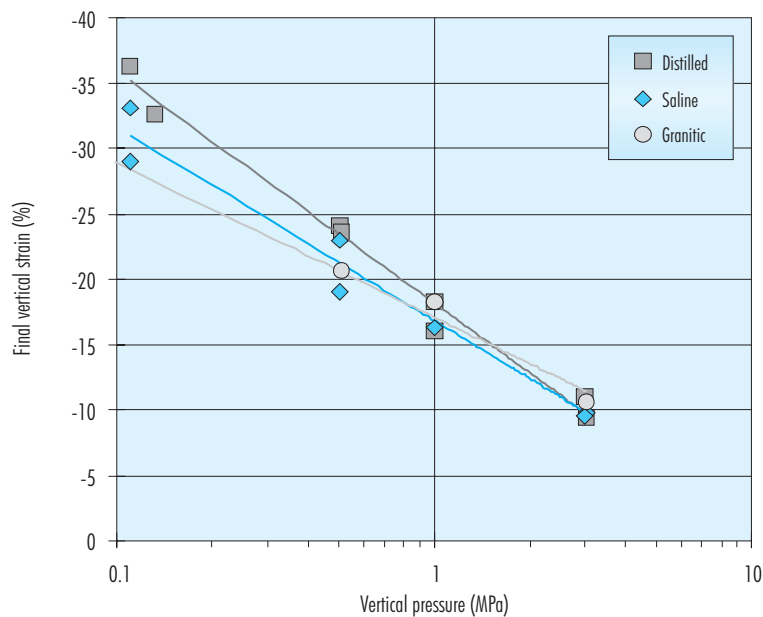


Figure 103: Final strain of samples of dry density  $1.70 \text{ g/cm}^3$  saturated under different vertical pressures with different waters (CIEMAT).

our of the bentonite, CIMNE performed suction controlled oedometer tests in non isothermal conditions, which complement the results presented in section 3.1.3.

In designing the tests, two main objectives were borne in mind: the adequacy of the tests to the aspects that need to be explored, and the short timing allocated for its performance. The results obtained are given below.

### 3.3.1 Permeability tests

In order to check the variation of permeability with time, two long term tests were performed by CIEMAT. In both of them the FEBEX clay was compacted at a dry density of  $1.70 \text{ g/cm}^3$  inside a stainless steel cell and saturated with granitic water by both ends under a pressure of  $0.6 \text{ MPa}$ . Once saturated, the hydraulic conductivity was determined every two months by increasing the injection pressure at the bottom to  $1.8 \text{ MPa}$ , while measuring water outflow at the top of the sample. The experimental set-up, which was already used during FEBEX I, is shown in Figure 104.

A porous stone was placed on top of the sample, and at the bottom of the sample a stainless steel

sinter and 4 layers of geotextile, in contact with the clay, were placed instead of the porous stone, in order to check if the geotextile clogs with time. The geotextile was of the same kind than the one used in the “mock-up” test (TERRAM 4000). Formaldehyde was added to the saturation water, in order to avoid the multiplication of microorganisms.

The characteristics of the tests performed are summarised in Table XVI, in which the average value of hydraulic conductivity measured ( $k_w$ ) is included. Test F2 was dismantled by mistake and a new sample was compacted in the same cell (F3), keeping the same discs of geotextile as a porous interface. Due to the fact that the geotextile is compressible and allows some expansion of the bentonite, its dry density decreased to  $1.45 \text{ g/cm}^3$ . The hydraulic conductivity values obtained are plotted in Figure 105, as a function of the time elapsed since the beginning of saturation. The expected permeability for a sample of dry density  $1.45 \text{ g/cm}^3$ , as calculated from Equation [1], is plotted in the figure as an error bar. The temperature of the laboratory during the determinations is also indicated, as it may have an influence on the value of permeability, due to its repercussion on the viscosity of water.

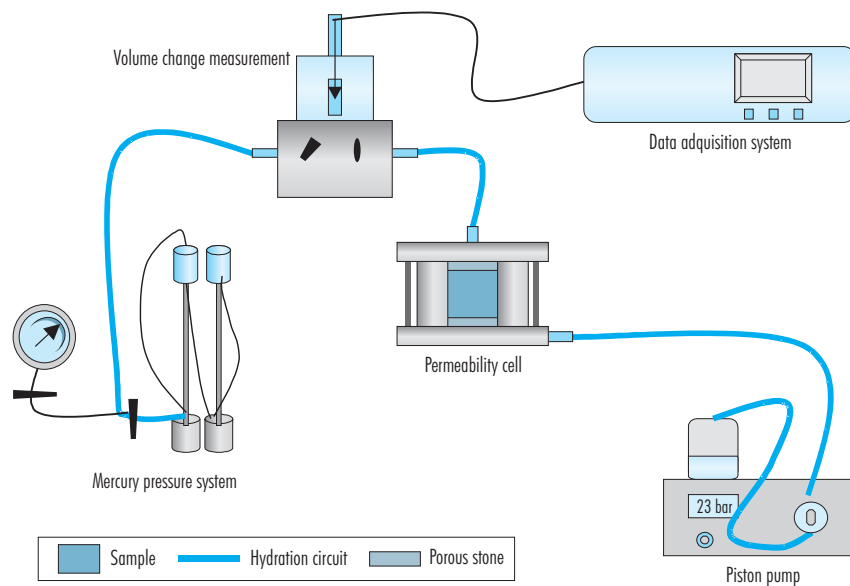


Figure 104: Schematic representation of permeability measuring assembly for expansive soils.

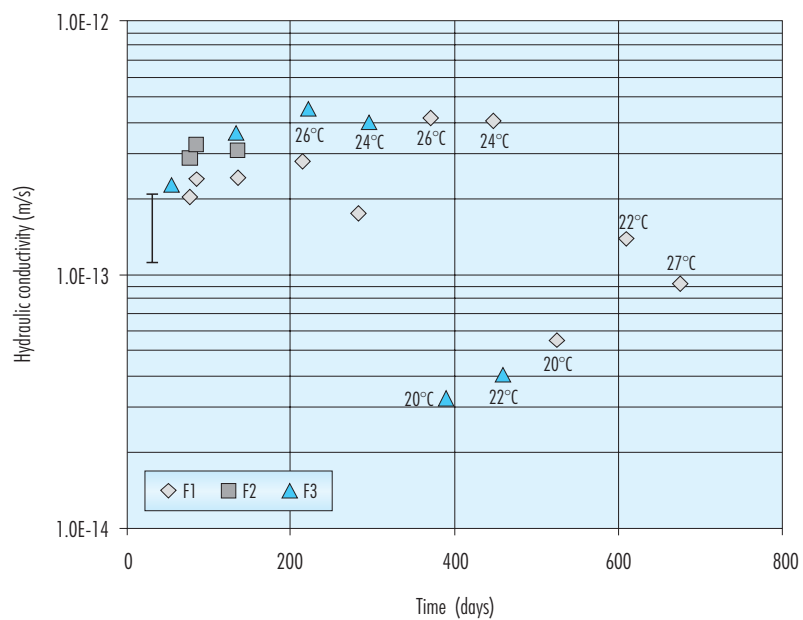


Figure 105: Evolution of hydraulic conductivity with time in samples of dry density  $1.45 \text{ g/cm}^3$  infiltrated through geotextile (the error bar was obtained by means of Equation [1] for a sample of the same dry density).

Table XVI  
Characteristics of the long term permeability tests.

Reference	$\rho_d$ (g/cm <sup>3</sup> )	Initial $w$ (%)	Average $k_w$ (m/s)	Final $w$ (%)	Final $S_r$ (%)	Duration (days)
F1	1.45	13.9	$2.1 \cdot 10^{-13}$	32.4	101	627
F2	1.44	15.4	$3.1 \cdot 10^{-13}$	33.4	103	136
F3	1.45	14.1	$2.2 \cdot 10^{-13}$	32.3	101	527

At the end of the tests, the geotextile was analysed by scanning electron microscopy (Figure 106). It was observed that smectite fills the voids between fibres and also some circular voids, originally present in the fibres.

The geotextile was also dyed and observed with an optical microscope, with the aim of checking the existence of bacteria. Only a few were found and no biofilm or microbial mat was detected. On the other hand, the clay samples in contact with the geotextile, the geotextile and a stainless steel sinter, which presented black stains, were subjected to cultivation in media appropriate for the growth of sulphate-re-

ducing bacteria (Posgate-B and Posgate-E media). The number of bacteria was estimated by the Most Probable Number method, the following values being obtained:

- ❑ Sample F1: 2300 bacteria/g
- ❑ Sample F3: 2000 bacteria/g
- ❑ Geotextile in contact with the sinter: >12000 bacteria/cm<sup>2</sup>
- ❑ Geotextile in contact with the clay: 5000 bacteria/cm<sup>2</sup>

The quantity of sulphate-reducing bacteria in untreated FEBEX bentonite, estimated by the same me-

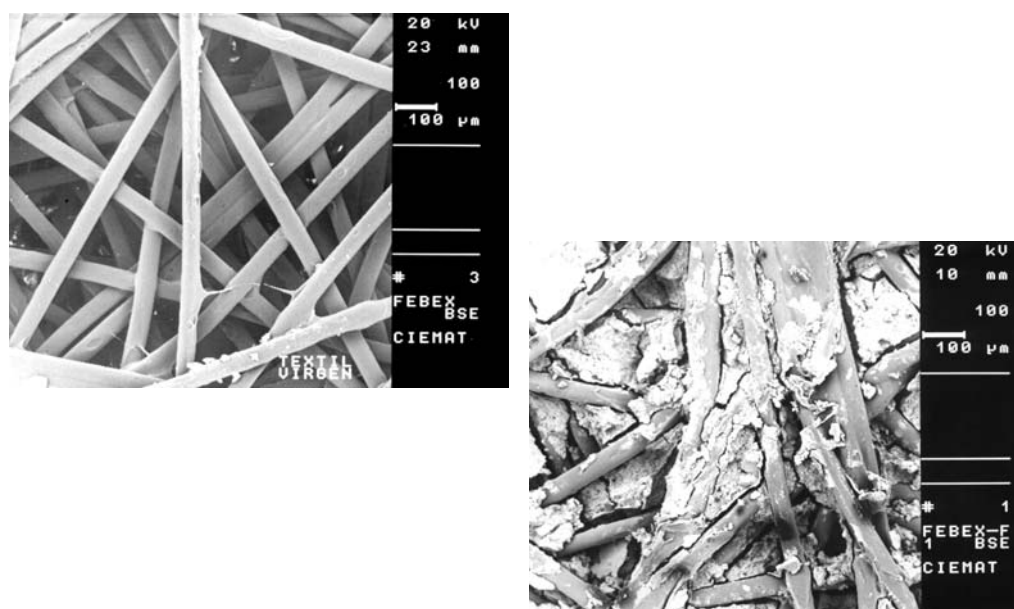


Figure 106: Scanning electron microscope image of the untreated geotextile (left) and of the geotextile used in test F1 (right).

thod, is 48 bacteria/g (Mingarro *et al.* 2000). Despite the increase in the amount of bacteria found in saturated clay after the tests, the number of bacteria is still low and is not considered responsible for the decrease of permeability.

In addition to these tests, the results of a long term test performed with a different purpose were evaluated (A.M. Fernández, *unpub. data* 2002). The test was performed with FEBEX bentonite compacted at a nominal dry density of  $1.70 \text{ g/cm}^3$ , in the same permeability cell described above, but using porous stones at the top and bottom surfaces. Granitic water was injected through the bottom porous stone at a pressure of 4 MPa for more than 1000 days. The water outflow was periodically measured, which allowed the computation of the permeability corresponding to different time intervals. The results obtained are shown in Figure 107. Hydraulic conductivity remains rather constant and it becomes clear that it has not decreased after more than 4 years.

### 3.3.2 Infiltration tests

These tests are being performed by CIEMAT in the cylindrical teflon cells, already used during FEBEX I

(Villar 2001; see section 3.1.4.1), whose internal diameter is 7 cm (Figure 108). The cells were modified in order to give them a final internal length of 40 cm. Five blocks of FEBEX clay compacted with its hygroscopic water content at an initial nominal dry density of  $1.65 \text{ g/cm}^3$  were piled up inside each cell. Three of the blocks have a length of 10 cm, while the two placed at the ends of the cells have a length of 5 cm. An average compaction pressure of 30 MPa was applied to manufacture the blocks. Hydration with granitic water takes place through the upper surface under an injection pressure of 1.2 MPa. In one of the tests the clay is being heated through the bottom surface at a temperature of  $100 \text{ }^\circ\text{C}$ , while the other test is being carried out at isothermal conditions (laboratory temperature). The cells are instrumented with relative humidity sensors (VAISALA HMP3) at three different levels. The water intake and the relative humidity and temperature evolution at different levels inside the clay are being measured as a function of time. The two cells in operation are shown in Figure 109.

In the case of the test performed under thermal gradient (GT40), infiltration begun after the stabilisation of the temperature registered by the sensors. The phase of temperature stabilisation in this test took

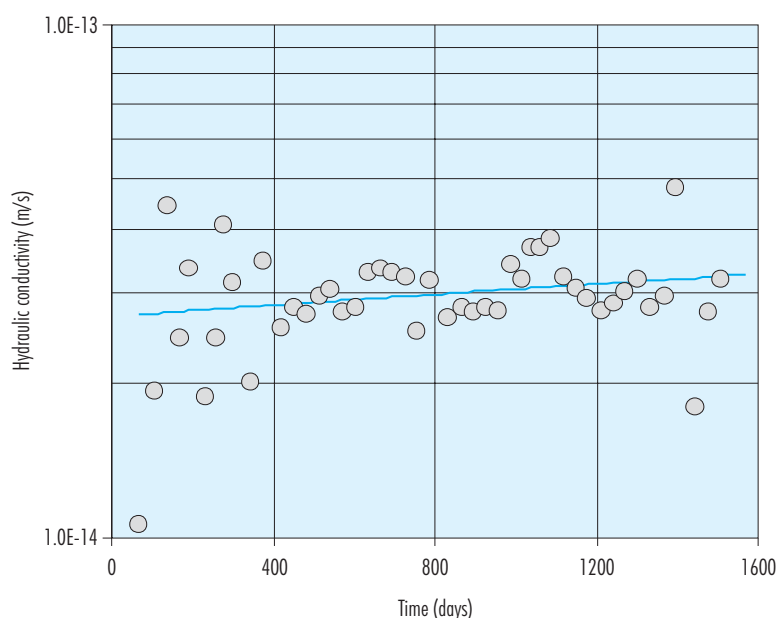


Figure 107: Evolution of saturated permeability under high injection pressure.

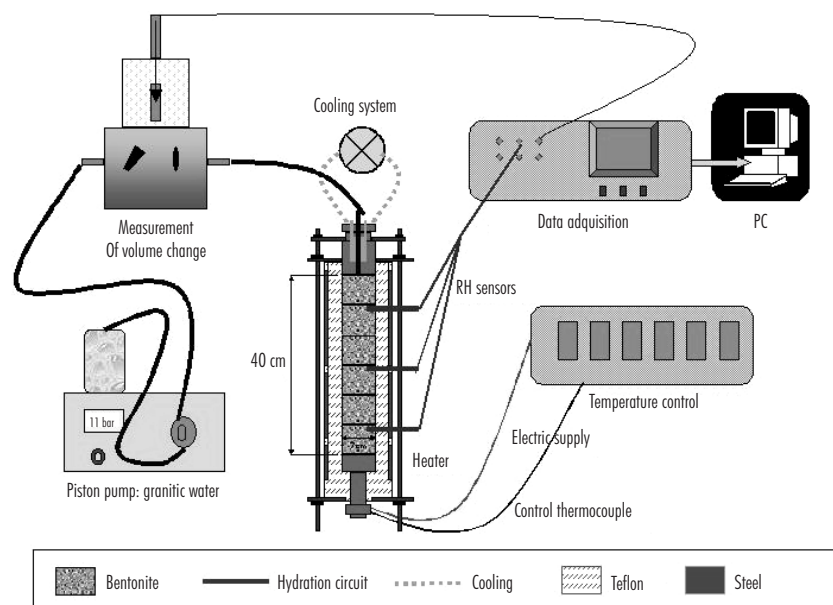


Figure 108: Experimental set-up for the infiltration tests.

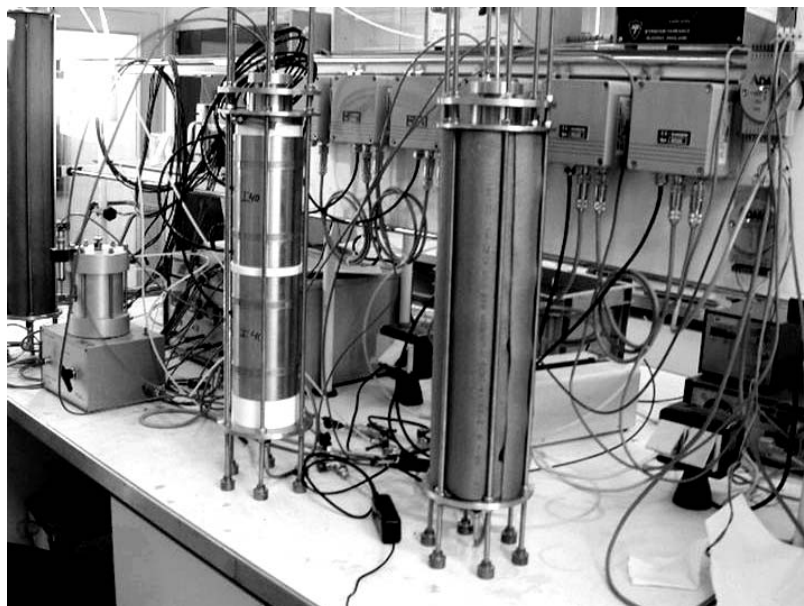


Figure 109: Infiltration cells in operation: isothermal (left) and with thermal gradient (right).



three days (Figure 110). During this time, an increase in relative humidity was registered by the sensor placed 10 cm from the bottom (RH3) and, to a lesser extent, by sensors placed 20 (RH2) and 30 cm (RH1), which reveals the quick migration of water in the vapour phase, from the bentonite in contact with the heater towards cooler zones.

The evolution of temperature and relative humidity in the test performed under thermal gradient (GT40) is shown in Figure 111. The values shown are those measured during infiltration, which begun after stabilisation of the temperature registered by the sensors, as explained above. For this reason, an initial difference in the relative humidity measured at different levels is observed in Figure 111. This tendency is reversed when hydration starts, a clear increase of relative humidity being registered by the two upper sensors (RH1 and RH2), while desiccation starts to affect the zone in which sensor RH3 is placed: at least the 10 cm closest to the heater reduce its relative humidity after 300 hours of heating. This decrease of relative humidity goes down to values around 35 percent, which keep approximately constant during more than 10000 hours of hydration. Afterwards, a slight increase of relative humidity in this zone was observed.

The evolution of relative humidity in the test performed under isothermal conditions (I40) is shown in Figure 112. The sensor placed 10 cm from the hydration surface (RH1) shows a steady increase of relative humidity, which was noticeable after 250 hours of hydration. The sensor placed 20 cm from the hydration surface (RH2) started to register an increase of relative humidity after 1200 hours of hydration, and the sensor placed towards the bottom (RH3), after 2500 hours of hydration. After 5000 hours of hydration, sensor RH3 records the sharpest increase, while relative humidity in the upper parts of the bentonite column (sensors RH1 and RH2) increases in a softer way.

The comparison of Figure 111 and Figure 112 seems to reveal a quicker initial hydration in the test performed under thermal gradient, as the increase in humidity registered by the first sensor (RH1) is higher in test GT40 and the sensor placed further (RH2) starts to perceive the humidity increase much earlier in the case of infiltration under thermal gradient than in the case of infiltration at laboratory temperature. In the latter case the humidity recorded by sensor RH2 could come in the form of water vapour from the lower part of the column. Otherwise, the increase of hydraulic conductivity with temperature would account for this initial quicker hydration of

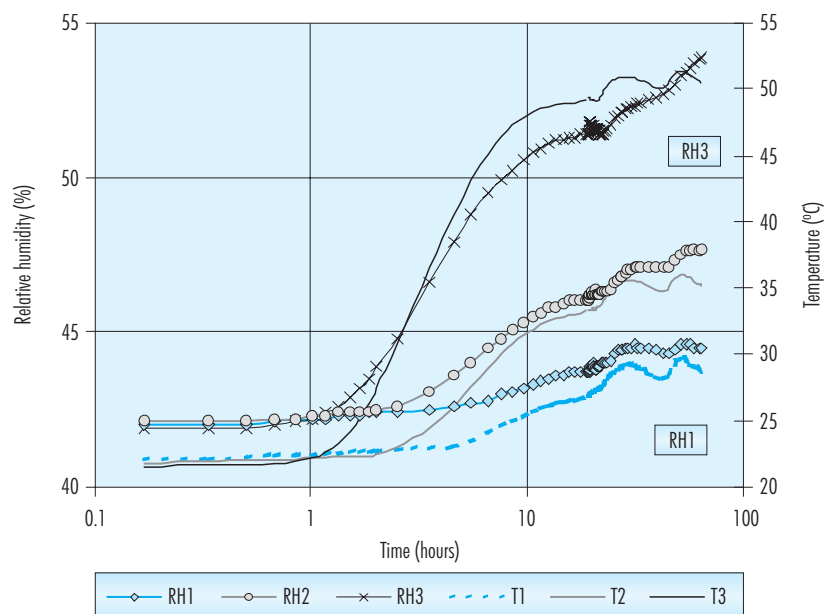


Figure 110: Initial stabilisation of temperature in test GT40 (sensor 1 placed 30 cm from the bottom, sensor 2 at 20 cm and sensor 3 at 10 cm).

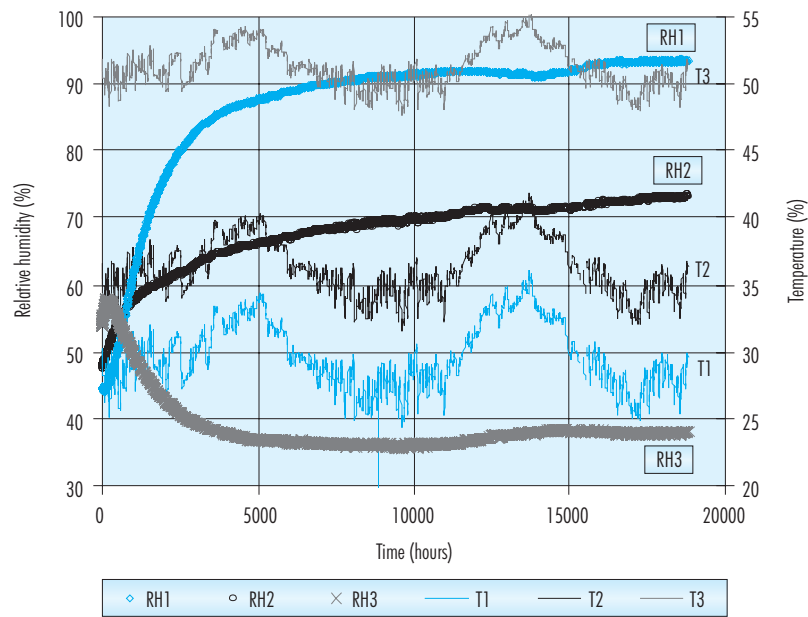


Figure 111: Evolution of temperature and relative humidity in the test performed under thermal gradient (GT40) during infiltration (sensor 1 placed 30 cm from the bottom, sensor 2 at 20 cm and sensor 3 at 10 cm).

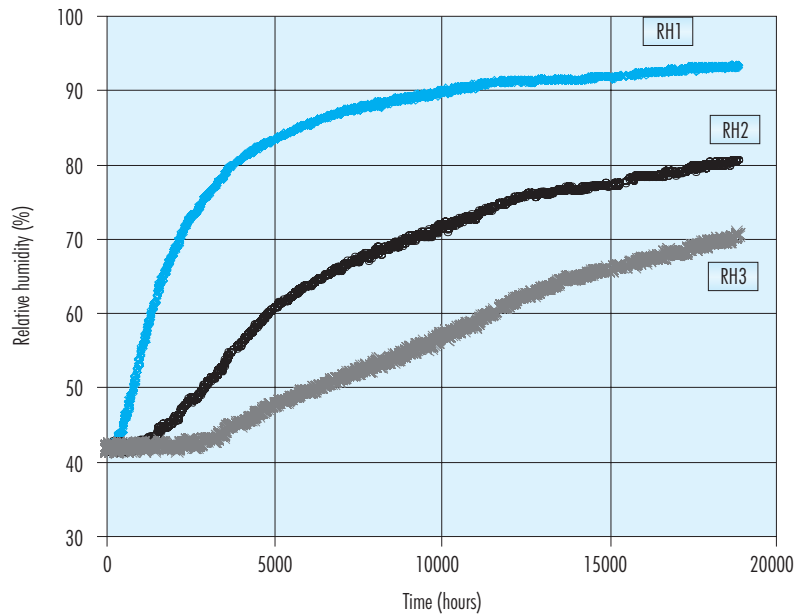


Figure 112: Evolution of relative humidity in the test performed under isothermal conditions (I40) during infiltration (sensor 1 placed 30 cm from the bottom, sensor 2 at 20 cm and sensor 3 at 10 cm).

the test under thermal gradient. However this behaviour is reversed as saturation proceeds and at the present moment, after 19000 hours (more than 2 years) of hydration, the average relative humidity recorded by the three sensors in test GT40 is 68 percent, and in test I40 is 82 percent. This is confirmed by the water intake measured by the volume change apparatus, which is higher for the isothermal test (Figure 113).

### 3.3.3 Study of the repercussion of the hydraulic gradient

The application of Darcy's law for the calculation of the coefficient of permeability requires that the velocity of the flow be proportional to the hydraulic gradient, that is to say, that the value of the coefficient obtained be independent of the hydraulic gradient applied during determination. This means that the relationship between flow and hydraulic gradient is linear, and that this linear relationship crosses the origin. For different reasons, this condition may not be fulfilled, thus invalidating the use of Darcy's expression. By the other hand, the values of bentonite permeability used in the modelling of FEBEX experi-

ments were obtained by CIEMAT under high hydraulic gradients, necessary to induce a measurable flow in such low permeability materials.

Specifically, the values of applied hydraulic head in the tests ranged between 7000 cm, for dry densities of 1.30 g/cm<sup>3</sup>, and 66000 cm, for dry densities of 1.84 g/cm<sup>3</sup>. Taking into account that the length of the specimen is 2.5 cm, the average hydraulic gradient was 15200 m/m. All the samples were tested with at least two different hydraulic gradients suitable for their dry density, in other words, sufficiently high so as to provide a measurable flow. The values of hydraulic conductivity obtained during FEBEX I for the two hydraulic gradients applied in each test are represented in Figure 114 (Villar 2000). The points joined by lines correspond to the same test; *i.e.* to the measurements performed on a specific sample of a given dry density. It may be observed that, although there may be some difference between the value of conductivity obtained with the different gradients for the same sample, such variations are probably the result of the experimental method, since there is no trend for one variable with respect to the other. This would confirm the independence of the flow observed from the hydraulic gradient applied, and therefore the validity of Darcy's law for

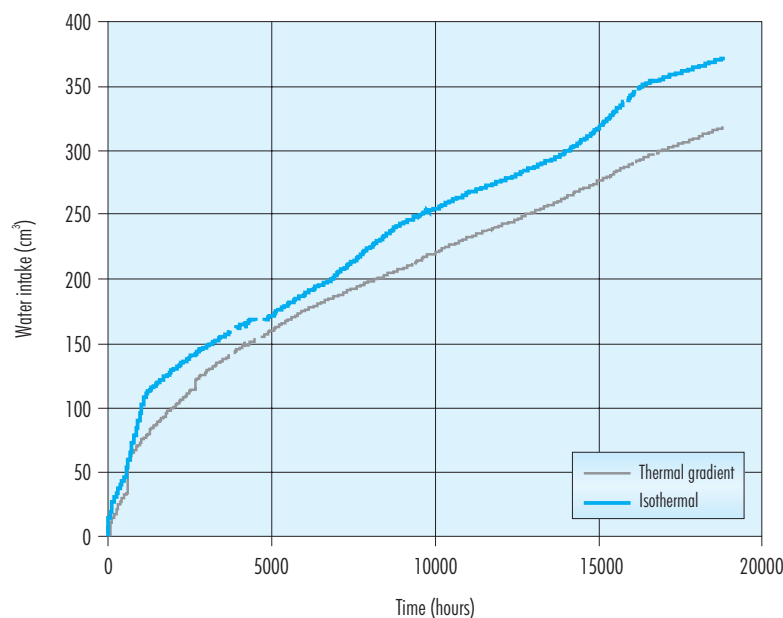


Figure 113: Water intake in the two infiltration tests (preliminary curves, to be adjusted at the end of the tests).

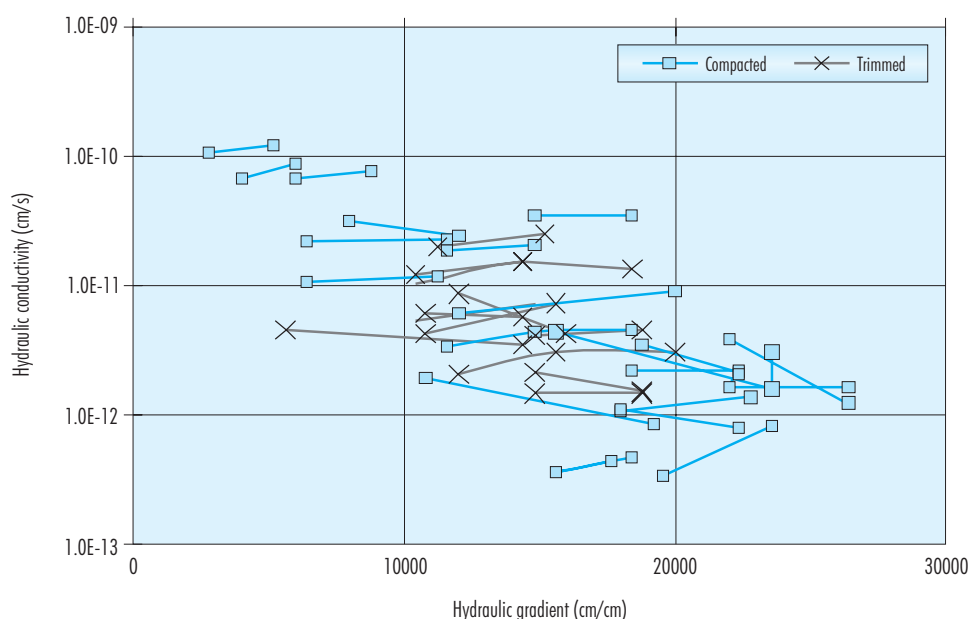


Figure 114: Variation in hydraulic conductivity obtained for different samples versus the hydraulic gradient as a function of the kind of sample preparation (points joined by lines correspond to the same sample).

the calculation of the coefficient of permeability, at least in the range of gradients that was considered.

It may also be appreciated in Figure 114 that, as the permeability of the sample decreases, in other words, as its dry density increases, the value of the hydraulic gradients applied for performance of the measurement increases, this being necessary in order to be able to measure very low flows. However, it was not possible to determine whether no flow occurs in the case of lower hydraulic gradients, or whether it is simply not possible to measure it with the available technique. Consequently, it has not been established whether or not the threshold hydraulic gradient pointed to by several authors exists, below which the relation between flow and gradient in clays deviates from linearity. If a threshold gradient exists, it would be lower for samples of lower dry density. This would appear to be confirmed by the fact that lower hydraulic gradients need to be applied in samples with lower dry densities, although as explained above, this might be due simply to the fact that for these densities flows are larger and easier to measure.

In order to deepen in the investigation on the existence of a threshold gradient, the values of flow rate

for the two hydraulic gradients applied in each of the tests mentioned above were plotted in Figure 115 and Figure 116, the latter being an enlargement of the former. Again, the points joined by lines correspond to the same test; *i.e.* to the measurements performed on a specific sample of a given dry density. If we assume that the relationship between gradient and flow is linear, and we extrapolate these lines towards flow 0, despite the variation found among the different tests, we would observe a tendency to find gradients higher than 0 to have a measurable flow, around 5000 cm/cm, and even higher in the case of the highest densities (Figure 116). However, this aspect should be confirmed with more refined and specific tests.

To clarify the effect of hydraulic gradient on the value of hydraulic conductivity, it was tried to measure the hydraulic conductivity of a FEBEX clay sample under low hydraulic gradients and injection pressures. For that, the same cell and methodology described above (Figure 104) was used. The granulated clay with its hygroscopic water content was compacted inside the cell to a nominal dry density of 1.50 g/cm<sup>3</sup>, the dimensions of the specimen being 5.0 cm in diameter and 2.5 cm in height. The sample

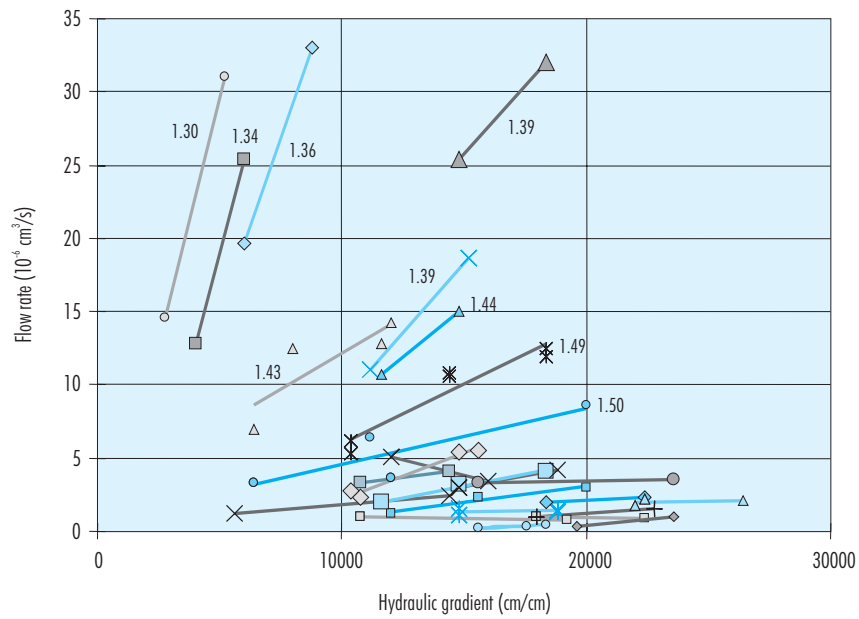


Figure 115: Variation in flow rate obtained for different samples versus hydraulic gradient (points joined by lines correspond to the same sample).

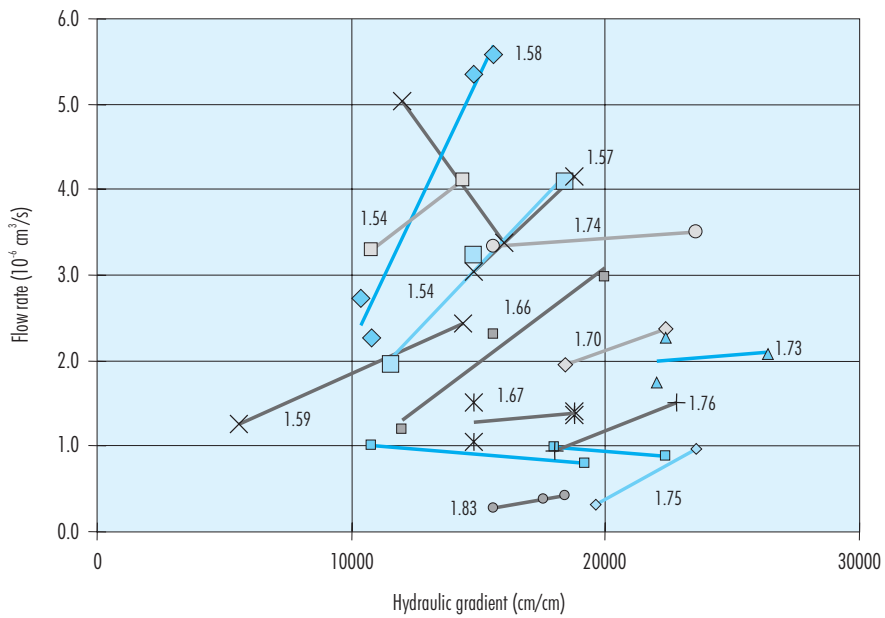


Figure 116: Variation in flow rate obtained for different samples of high density versus hydraulic gradient (points joined by lines correspond to the same sample).

was saturated with deionised water injected at a pressure of 0.6 MPa by the upper and lower surfaces through porous stones. The water intake was measured and, after approximately 100 hours, it was ceased. An automatic pressure/volume controller by GDS was used to saturate the sample. Afterwards, the bottom inlet was connected to an injection pump, while the upper outlet remained connected to the GDS apparatus. A combination of different pressures was applied in order to obtain different hydraulic gradients, the pressure at the bottom of the sample being always higher than at the top. In all the cases the water outflow was measured in the upper outlet by the GDS automatic pressure/volume controller. For the lowest injection pressures, a GDS controller was also used at the bottom inlet, to allow for a higher accuracy in the pressure applied. The results obtained are plotted in Figure 117. The hydraulic gradients applied ranged from 200 to 2400 and the injection pressures, between 0.45 and 1.20 MPa. These hydraulic gradients are much lower than the ones used to determine Equation [2], which, for dry densities around 1.50 g/cm<sup>3</sup>, were in the order of 14000. The expected hydraulic conductivity value for the same dry density, obtained with Equation [2], is also indicated in the figure. It can be

seen that overall the values obtained are higher (up to an order of magnitude) than those obtained with higher hydraulic gradients. There is not a tendency of the values as a function of the hydraulic gradients applied in the measurement. The test went on for more than 400 days, but no steady evolution of permeability with time was either found (Figure 118).

The results are thus not conclusive and must be considered as preliminary. A new series of similar tests has started.

### 3.3.4 Suction and temperature oedometric tests

Two bentonite samples at hygroscopic water content (laboratory air relative humidity about 52% and estimated initial suction about 90 MPa) were statically compacted at a dry density of 1.7 g/cm<sup>3</sup> and at a temperature of 22°C. The tests were performed in controlled-suction oedometer cells specifically designed for accurate temperature control (Figure 119). Figure 120 shows the layout of the oedometer cell, the system for control of temperature and suction, and a number of auxiliary devices necessary to perform the tests. The oedometer ring was placed inside

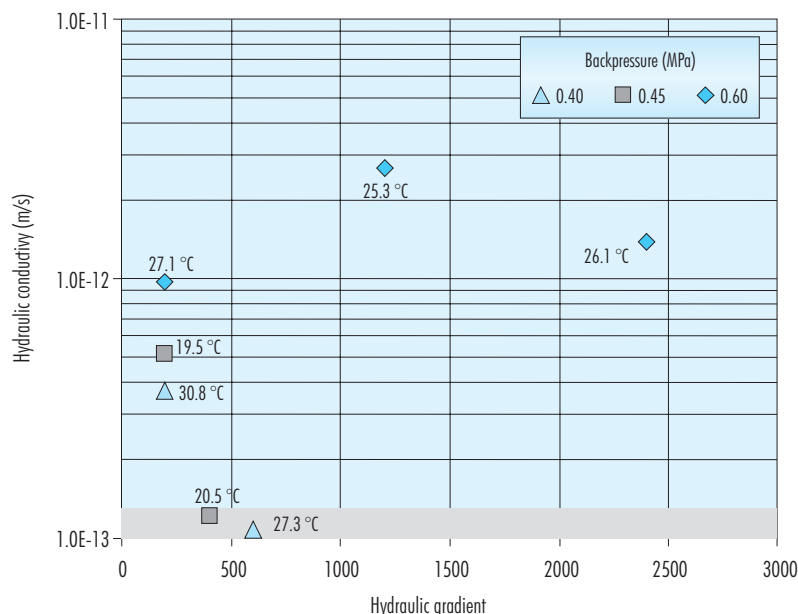


Figure 117: Hydraulic conductivity of a FEDEX sample compacted at dry density 1.49 g/cm<sup>3</sup> obtained under low hydraulic gradients (the shadowed bar corresponds to the range of expected values obtained for the same dry density with Equation [2]).

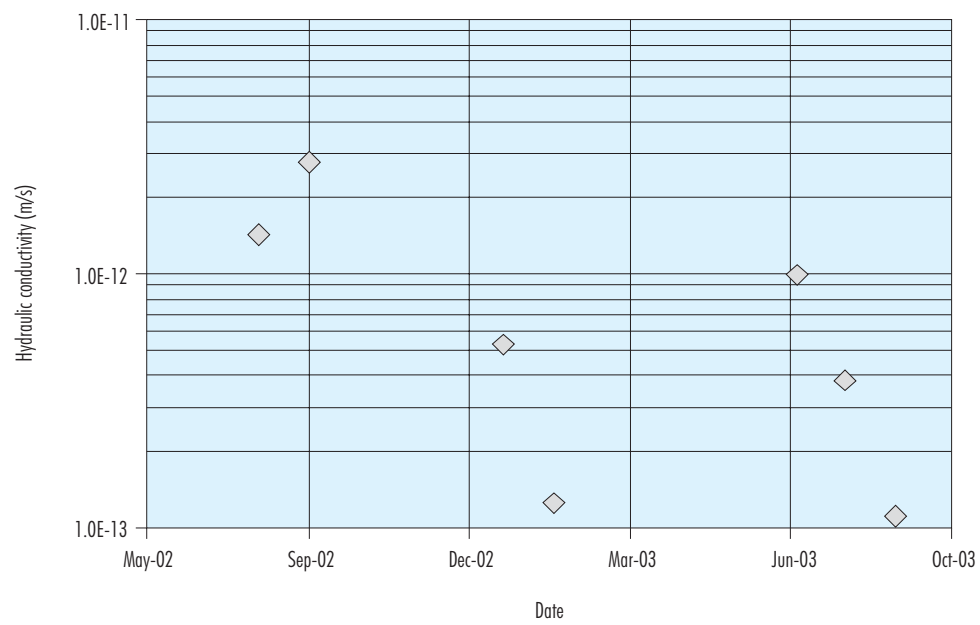


Figure 118: Evolution in time of the hydraulic conductivity measured under different low hydraulic gradients of a specimen of FEBEX clay compacted at dry density  $1.49 \text{ g/cm}^3$ .

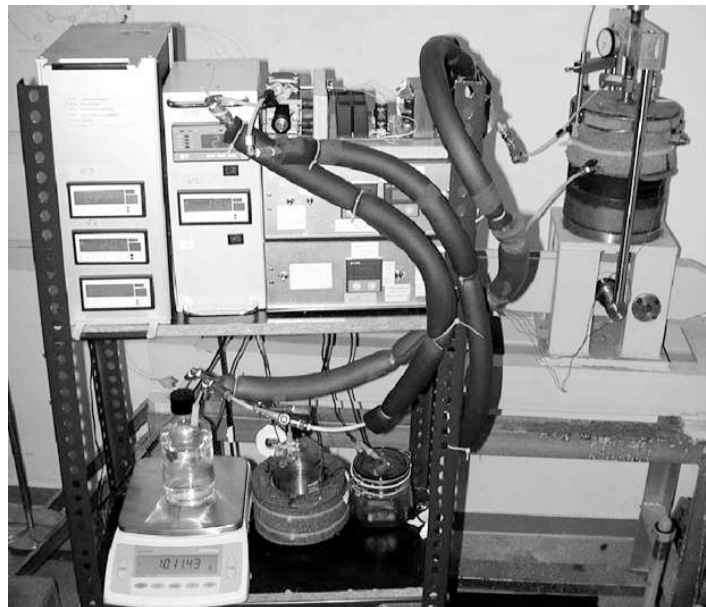


Figure 119: Equipment to perform the suction and temperature oedometric tests.

1) Silicone oil bath and heater; 2) Soil sample; 3) and 4) Coarse porous disc

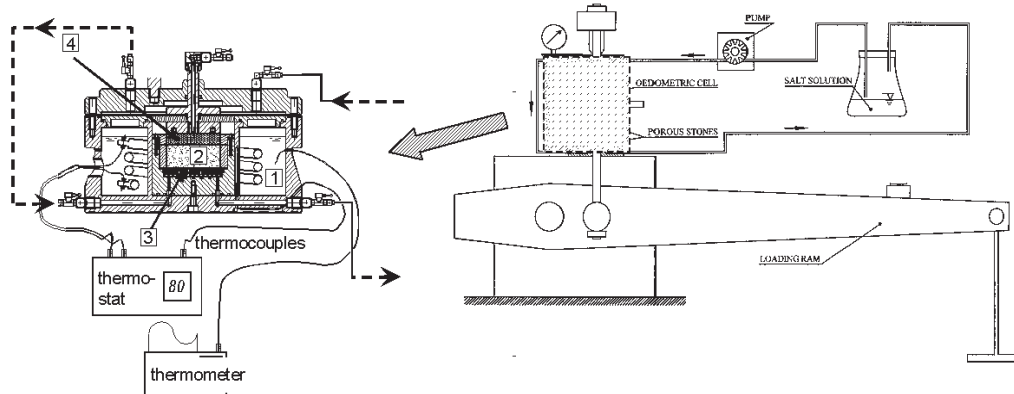


Figure 120: Schematic layout of the experimental system with simultaneous control of suction and temperature.

a silicon oil bath containing the heater, in order to maintain thermal stability (heater and silicone oil bath are indicated by number 1 in Figure 120). The soil sample (50 mm diameter and 20 mm thickness, number 2 in Figure 120) is located between two coarse porous stones (numbers 3 and 4 in Figure 120). Soil temperatures were measured with a thermocouple located close to the sample, which was used as a feedback signal acting on a programmable thermostat that controlled the heater. Another thermocouple recorded the temperature in the silicon oil bath.

Soil suction was applied by prescribing a value of the relative humidity of the atmosphere in contact with the sample (Villar 2000). Suction and relative humidity are related by the psychrometric (Kelvin's) law. In turn, relative humidity is controlled by the use of solutions of sulphuric acid at various concentrations or of saturated solutions of various salts. Temperature must be strictly controlled, as the activity of the solution is very sensitive to thermal fluctuations. The efficiency of the system is increased using a pump to force the flow of humid air between the reservoir and the cell. A balance that controls continuously the weight of solution in the reservoir allows the measurement of water changes in the sample, however, due to humid air losses in the circuit these measurements have not been used.

Figure 121 shows the generalised stress paths followed in the experimental programme in a three-

dimensional stress-suction-temperature space. Initially, in the two tests performed, the soil is loaded at 22 °C up to 0.1 MPa, maintaining constant its water content (closed system), (path AB in Figure 121). In the first test, the soil was heated with a rate of 40°C/h up to reach a temperature of 70 °C with the same conditions (constant water content); during this stage (path BB'' in Figure 121) probably the suction of the soil decreased due to a change in temperature (Figure 47). The second sample was maintained at 22°C. Both samples were equalised at a suction of 110 MPa using the vapour control technique with a saturated solution of  $K_2CO_3 \cdot 2H_2O$ . Once suction equilibrium was reached, a loading path was followed at constant suction and temperature (path B'C in Figure 121) using the following vertical stress steps: 0.1, 1.2, 2.2, 3.3, 5.5 and 8.6 MPa. In the loading process, equalisation stages lasted 1 minute for the loads up to 3.3 MPa at 22°C, 1 hour for loads up to 1.2 MPa at 70°C and 24 h in the rest of loading stages. Once the target net stress was reached, the samples were wetted at constant stress following these suction steps: 110, 4 and 0 MPa (path CDE in Figure 121). The suction of 4 MPa was applied with an unsaturated solution of NaCl. The null suction was applied by soaking the soil sample. Equalisation stages lasted about 21 days.

Finally, the sample that was loaded and saturated at 22°C was heated up to 78°C (path EF in Figure 121).



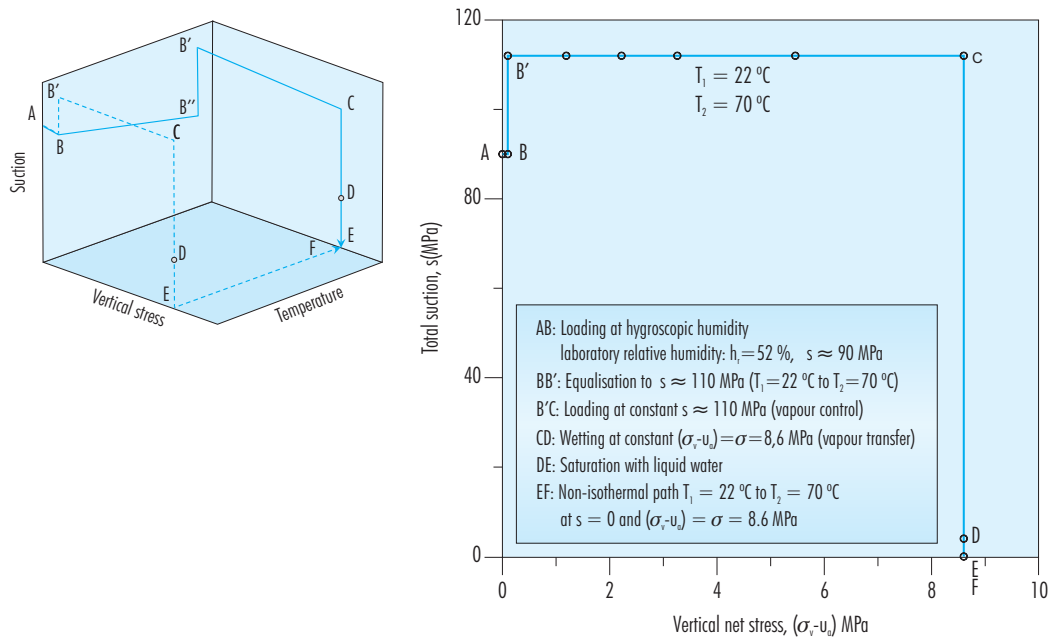


Figure 121: Generalised stress paths used in the testing programme.

Figure 122 shows the evolution of vertical strains and temperature during the heating stage at constant water content. From this stage and if the volume changes due to suction variation are not taken into account, a value of the linear coefficient of thermal expansion  $\alpha = 4 \cdot 10^{-4}$  is obtained. This value is similar to those obtained in the unconfined tests performed during the first phase of the FEBEX project (ENRESA, 2000). During the equalisation of suction at 110 MPa negligible vertical strains were measured in the sample tested at  $22^\circ\text{C}$ . However in the sample tested at  $70^\circ\text{C}$ , an important shrinkage was observed (vertical strain of 3.5%). This shrinkage compensates the initial thermal swelling and the resulting dry density is higher than the dry density of the sample tested at  $22^\circ\text{C}$ .

The vertical strains measured in the isothermal loading paths (B'C in Figure 121) are shown in Figure 123. It can be observed that the compressibility of the bentonite is similar at both temperatures. However it must be pointed out that the sample loaded at  $70^\circ\text{C}$  has an initial dry density of  $1.724 \text{ g/cm}^3$ , whereas the sample tested at  $22^\circ\text{C}$  has a dry density of  $1.70 \text{ g/cm}^3$ .

Therefore, the increase of compressibility due to temperature that was observed in other tests (see

sections 3.1.3 and 3.2.1.4) is compensated by the reduction due to the increase in dry density.

Swelling strains due to suction reduction were higher in the sample wetted at low temperature. Figure 124 shows the vertical strains measured during suction reduction stages from 110 MPa to 4 MPa and from 4 MPa to null suction. During the suction equalisation to 4 MPa after an initial swelling, the sample began to undergo shrinkage due to losses of water vapour under humid air conductions; when this shrinkage was observed the sample was soaked in order to reach null suction. The observed influence of temperature on the swelling strains experienced during hydration agrees with the results obtained in the tests presented in section 3.2.1.2.

In Figure 125 the evolution with temperature of the vertical strains observed during the heating up to  $78^\circ\text{C}$ , of the sample that was loaded and saturated at  $22^\circ\text{C}$ , is included. In this case, due to the higher vertical stress applied (8.6 MPa), the thermal expansion is smaller than that observed under a vertical stress of 0.1 MPa. In the present case, the linear thermal expansion coefficient is only about  $0.4 \cdot 10^{-4}$ .

Finally, the volume changes experienced by the two samples during the different stages of the tests are summarised in Figure 126.

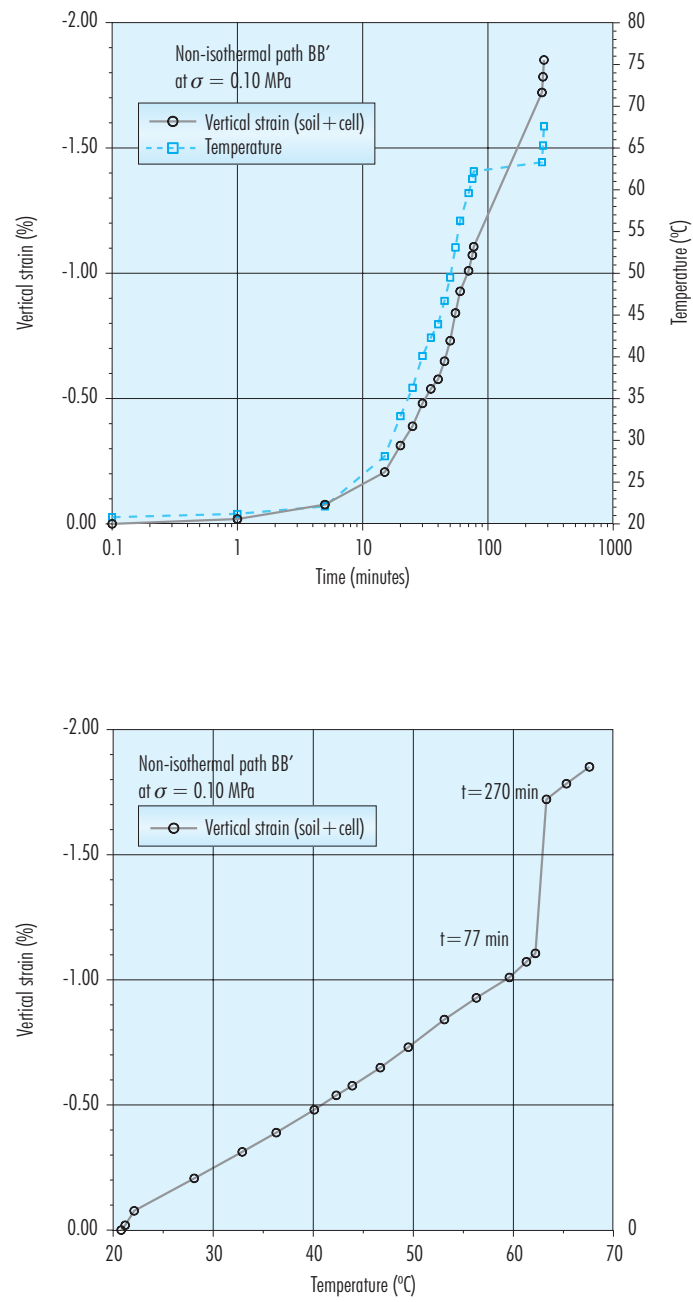


Figure 122: Evolution of vertical strains during the heating from 22 to 70 °C (vertical stress 0.1 MPa).

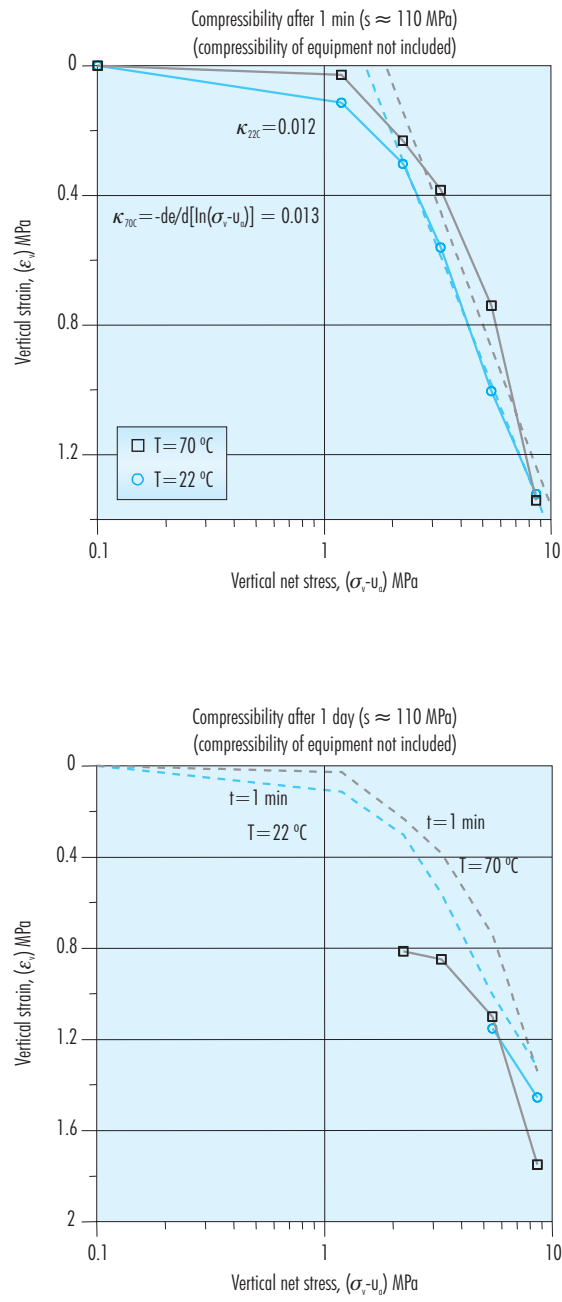


Figure 123: Volumetric strains after 1 min and 24 hours after the application of the load steps at constant suction and temperature.

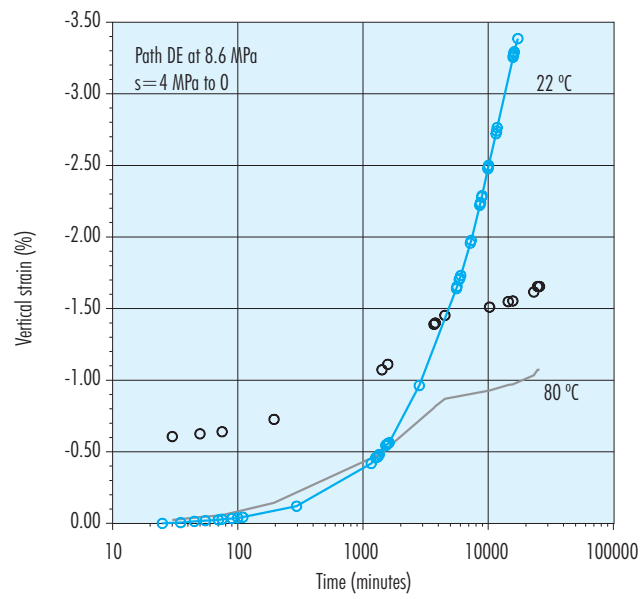
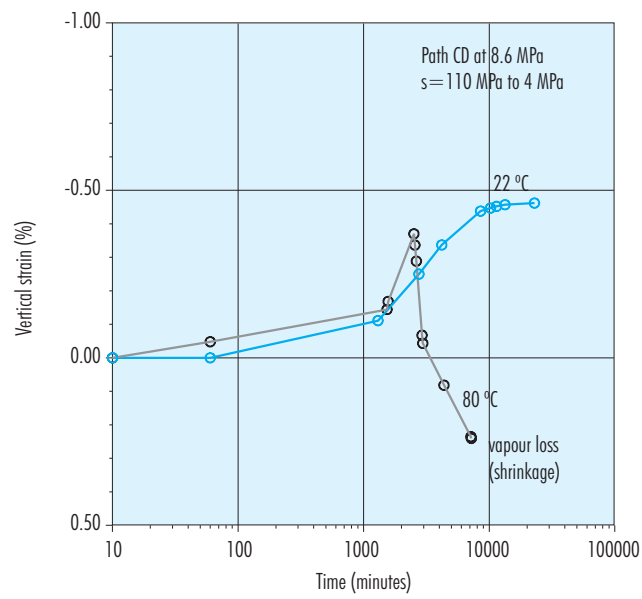


Figure 124: Swelling strains due to suction reduction at constant vertical stress and temperature.

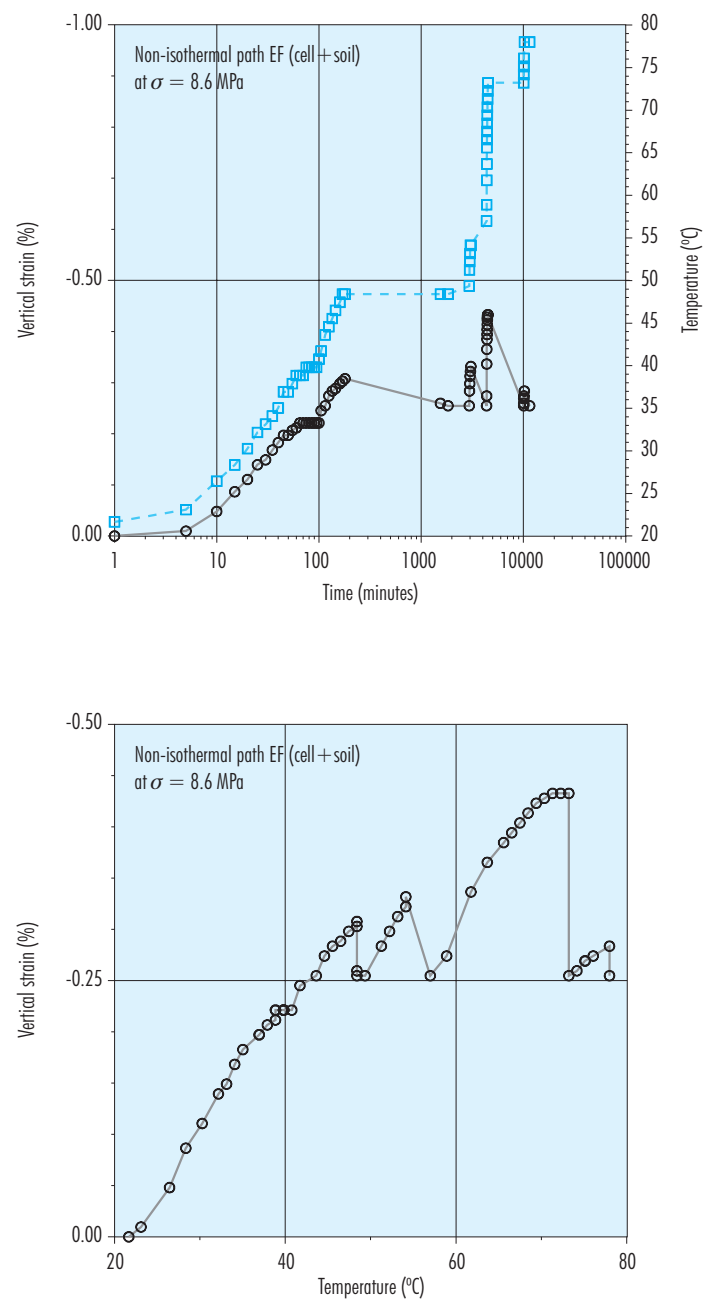


Figure 125: Evolution of vertical strains during the heating from 22 to 78  $^{\circ}$ C (vertical stress 8.6 MPa).

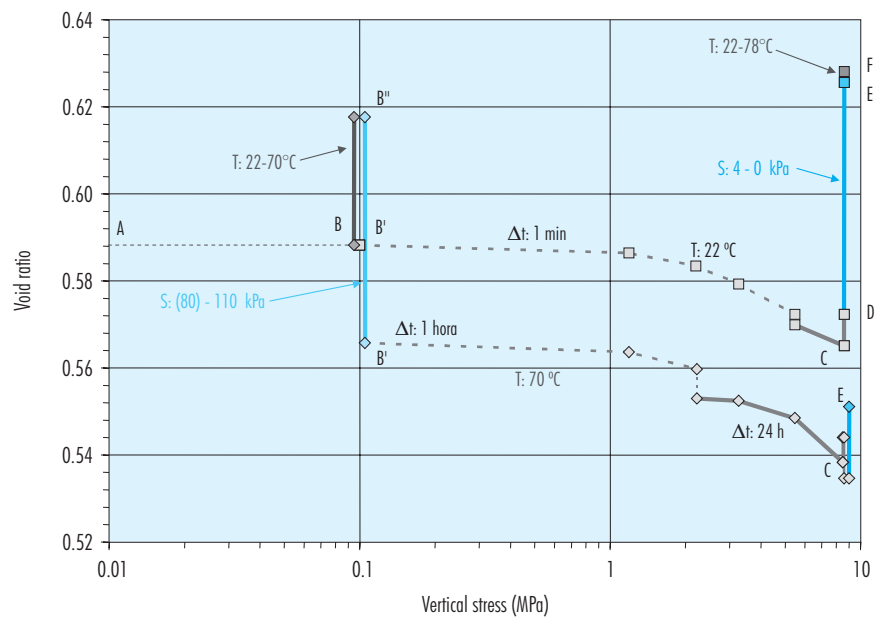


Figure 126: Summary of volume change experienced by two samples tested in suction and temperature controlled oedometer.

## 4. Conclusions

## 4. Conclusions



The FEBEX II project included a wide laboratory tests programme that focused on those aspects not sufficiently covered during FEBEX I and on the new processes and scenarios considered in the second phase of the project. Hence, the laboratory test programme of FEBEX II continued in part with the works carried out during FEBEX I in those areas where more data about material properties were required. These activities relate mainly to tests aimed to the calibration of the models, the acquisition of parameters by back-analysis and the improvement of the knowledge on the behaviour of expansive clays. But the programme also included tests on new areas. Specifically, the new tests centred on investigations about the influence of the microstructure changes in bentonite, of temperature and of the solute concentration on the behaviour of clay. Besides, several tests were proposed in order to understand the unexpected behaviour observed in the "mock-up" test, towards the end of year 2. The information obtained and described below will help in the interpretation of the results obtained in the "mock-up" and the "in situ" tests.

The mechanical behaviour of compacted bentonite was investigated during FEBEX I by the performance of a testing programme, carried out in suction-controlled oedometers, capable of applying high suctions and large vertical loads. The analysis of the results revealed significant features of behaviour, such as yield phenomena, dependency of swelling strains on applied stresses, stress path dependency of strains, and compound stress paths in swelling pressure tests. In spite of the complexity of the behaviour, a good understanding of the behaviour is possible by considering explicitly the fabric of the soil that was independently studied revealing a dual arrangement with microstructural and macrostructural components. A deeper insight of the behaviour of compacted bentonite, and of the basic mechanisms controlling it, was achieved during FEBEX II using an elastoplastic framework that incorporates the interplay between microstructural and macrostructural fabric levels in a simplified manner. Most of the main features of behaviour are correctly reproduced by the model, allowing a more detailed examination of the role that the different variables play on the explanation of the overall behaviour of the soil.

In order to study the thermo-hydro-mechanical processes during water infiltration, the results of infiltration tests performed by CIEMAT during FEBEX I and by CIMNE during FEBEX II were backanalysed as a boundary value problem using the code

CODEBRIGHT. The numerical model can reproduce the global tendencies observed in the small-scale tests; both, the results related to the evolution of the main variables of the test and those related to the postmortem study. One important point is that the constitutive model and most of the parameters assumed in the analysis are the same as those adopted for the Operation Base Case of the mock-up test model (OBC, ENRESA 2000). Tests like those presented in this work, in which the expansive clay and the THMC conditions are very similar to the ones expected in a large-scale test, are very useful to study the response of bentonite. But, due to relevant processes taking place at a high saturation level (Sánchez & Gens 2002), it is necessary to extend the duration of the tests for a very long period of time. It can be concluded that the combinations of this kind of tests and coupled THMC numerical analysis can help to a better understanding of the FEBEX bentonite behaviour under repository conditions.

Temperature effects on water retention curves in confined and unconfined conditions were determined and swelling pressure, hydraulic conductivity and swelling and consolidation strains as a function of temperature were successfully measured. Different experimental techniques and equipments were developed to study thermal induced changes under partially saturated states, covering a wide range of suctions.

In the retention curves at constant volume it was observed that, at the beginning of hydration, the water content of the samples with a higher dry density is slightly greater for the same values of suction, but when lower values of suction are reached, the water content of the densest samples is lower. The repercussion of initial dry density on the value of water content reached is more obvious as suction decreases. It became also patent the hysteretic behaviour of the clay, being the water contents reached during drying higher than those obtained during the previous wetting (in confined samples), and the water contents in the wetting paths lower than those reached for the same suction in the previous drying (in unconfined samples). The degrees of saturation obtained in the wetting paths at constant volume, for suctions lower than around 10 MPa, are higher than 100 percent because they were calculated considering the density of the water as 1.00 g/cm<sup>3</sup>, which was shown to be untrue for high plasticity materials. On the other hand, both in confined and unconfined conditions, the retention capacity at higher

temperature seems to be slightly lower: at a constant degree of saturation, the higher the temperature of the sample the lower its suction.

Bentonite swelling strains are a function of temperature. In particular, at high temperatures the swelling capacity of clay decreases. In the same way, a clear decrease of swelling pressure as a function of temperature (down to 2.5 MPa at 80 °C) was observed. Oedometric tests have shown that saturation seems to induce a decrease in the apparent preconsolidation pressure regardless the temperature of the tests. Samples with hygroscopic water content (suctions around 100 MPa) are very stiffen for vertical pressures of up to 8 MPa. This phenomenon does not seem to depend on temperature, which indicates that the effect of temperature on the elastic behaviour of bentonite is small. On the other hand, temperature increases the compressibility of bentonite, both saturated and unsaturated, which would imply that a certain reduction in the size of the elastic domain takes place with temperature. Nevertheless, it seems that the deformation of bentonite is more dependent on the stress and suction path than on temperature. In tests with suction reduction, structure changes due to hydration are more relevant in the subsequent mechanical behaviour of bentonite, than the effects of temperature. It was measured how the temperature increases the water saturated permeability of FEBEX bentonite, although this measured increase is slightly lower than what would be expected on the basis of the thermal changes in water kinematic viscosity. Thermo-chemical effects altering clay fabric (flocculation or dispersion), porosity redistribution (creating preferential pathways or blocking macropores) and pore fluid chemistry (affecting viscosity) could be relevant issues regarding the effect of temperature on permeability.

FEBEX bentonite remains suitable as a sealing material in HLW repositories (from the hydro-mechanical point of view) for temperatures of up to 80 °C, as it keeps its high water retention capacity, low permeability and self-healing ability. No data are still available for higher temperatures, although the extrapolation of results points out to the preservation of properties for at least up to 100 °C.

Mercury intrusion porosimetry and environmental scanning electron microscopy provided promising results in order to characterise the bentonite microstructure. A series of mercury intrusion porosimetry tests were performed to characterise the microstructural changes observed on compacted bentonite subjected to different hydro-mechanical paths. Hy-

dro-mechanical paths included loading at constant water content, wetting under constant volume or constant vertical stress, unloading and, finally, freeze-drying at zero confining stress. Loading paths reduce larger pores (*i.e.* inter-granular pores). In the as-compacted state, the dominant inter-granular pore mode hides the inter-aggregate porosity, which cannot be distinguished. Suction reduction influenced the inter-aggregate pore size mode. On progressive wetting, the hidden and latent inter-aggregate pore size mode systematically emerged, probably due to the progressive splitting of the original structure of the pseudomorphs. The emerging inter-aggregate porosity was only detected when liquid water was transferred. Due to limitations of the equipment, the evolution of the active intra-aggregate pore size mode during wetting could not be followed. Further studies may be necessary to complement and provide more information about the mechanisms influencing pore size distribution changes on high active clays.

The environmental scanning electron microscopy allows observing the volumetric strains of a clay sample induced by humidity and temperature changes, however it is difficult to extract general and quantitative conclusions from these observations. In general, the changes induced by hydration under isochoric conditions tend to favour the existence of structures similar to that observed in compacted slurry samples, which present a structure more uniform than the one observed in unsaturated samples. The use of digital imaging techniques allowed verifying that at micro-scale level, where chemical phenomena prevail, strains are almost reversible as it is considered in the two-level elasto-plastic models.

The swelling capacity of clay, saturated with highly saline water, reduces drastically, osmotic consolidation being even observed. The swelling strains of clay upon saturation with different kinds of water (deionised, granitic and saline with different salts and concentrations) were measured as a function of initial dry density and overload. The effects of salinity on bentonite stiffness and permeability were also investigated. Fittings between final swelling strain and vertical pressure as a function of initial dry density were found for each kind of water. A higher swelling capacity was observed in samples saturated with deionised water, although this difference becomes less patent for higher vertical loads. The swelling strains measured when the samples were soaked with different saline concentrations are similar to the strains measured in suction controlled oedometer

tests, in which it is applied a final suction equal to the osmotic suction of the saline solutions. The hydraulic conductivity of bentonite increases depending on saline concentration, when saline water is used instead of deionised water as the permeating agent, especially in the case of low densities.

New tests were proposed in order to understand the unexpected reduction in water uptake rate observed in the “mock-up” test. Specifically, permeability tests, infiltration tests with and without thermal gradient, a study of the repercussion of the high hydraulic gradients applied for the determination of hydraulic conductivity, on the values obtained, and two new suction and temperature controlled oedometer tests were undertaken. The main conclusions from these new activities reached up to now are:

- The correct performance of the geotextile used as hydration interface in the “mock-up” test was checked at laboratory temperature during about 700 days. No important development of microbes was observed either in it or in the adjacent clay.
- The permeability of compacted bentonite seemed to remain constant for 700 days.
- The infiltration tests have shown that the permeability to water vapour of dry bentonite is very high. On the other hand, the initial saturation of compacted bentonite takes place quicker under thermal gradient than at laboratory temperature. The increase of hydraulic conductivity with temperature would account for this. Afterwards, the water intake is higher for the sample tested under room temperature, since the hot zones of the sample tested under thermal gradient remain desiccated for a long time.
- An analysis of the bentonite permeability tests performed during FEBEX I allowed proving the independence between the hydraulic gradient

applied and the hydraulic conductivity obtained. However, there seems to be a tendency to find gradients higher than 0 to have a measurable flow, around 5000 cm/cm, and even higher, in the case of the highest densities, which would point out the existence of a threshold gradient. This aspect should be confirmed with more refined and specific tests.

- The measurement of hydraulic conductivity under low hydraulic gradients was undertaken. The preliminary results indicate that there is not a dependence of the hydraulic gradient on the value of hydraulic conductivity.
- The results of the new non isothermal oedometric tests confirm the tendencies obtained in the previous tests performed, in order to characterise the effect of temperature on the mechanical behaviour of bentonite.

In summary, most of the thermo-hydro-mechanical features of compacted bentonite were experimentally studied during the two phases of the project. In general, the behaviour of the clay may be explained taking into account its double structure. The interactions between the two structural levels are responsible of the main features of the mechanical aspects of this behaviour. On the other hand, temperature induced transfers between intra-aggregate adsorbed water –of density higher than that of free water– and inter-aggregate free water could explain most of the features related with the temperature observed.

However, more research effort must be dedicated to study certain punctual aspects such as the water flow under low hydraulic gradients, the effect of osmotic and temperature gradients on this flow and the effects of deviatoric stresses on the mechanical behaviour, and, more generally, to relate the actual knowledge about the physico-chemical aspects of clay microstructure to the macroscopic behaviour of compacted bentonite.



## 5. References

## 5. References

- Alonso, E.E., Gens, A. and Hight, D.W. (1987). Special problem soils. General report. *Proc. 9<sup>th</sup> Eur. Conf. SMFE*, 3, 1987-1146.
- Alonso, E.E., Gens, A. and Josa, A. (1990). A constitutive model for partially saturated soils. *Géotechnique* 40 (3), 405-430.
- Alonso, E.E., Vaunat, J. & Gens, A. (1999). Modelling the mechanical behaviour of expansive clays. *Eng. Geol.* 54: pp. 173-183.
- Brackley, I.J., (1973). Swell pressure and free swell in compacted clay. *Proc. III Int. Conference on Expansive Soils*, Academic Press, Haifa, 1, 169-176.
- CIEMAT (1999). Ensayos THM para el proyecto FEBEX. *Internal report CIEMAT/DIAE/54111/9/99. FEBEX report 70-IMA-M-L-66*. 115 pp. Madrid.
- Delage, P., Tessier, D. & Audiguier, M.M. (1982). Use of the cryoscan apparatus for observation of freeze- fractured planes of a sensitive Quebec clay in scanning electron microscopy. *Can. Geotech. J.*, 19: 111-114.
- Delage, P., Audiguier, M., Cui, Y.-J. & Howat, D. (1996). Microstructure of a compacted silt. *Can. Geotech. J.*, 33: 150-158.
- ENRESA (1995). Almacenamiento geológico profundo de residuos radiactivos de alta actividad (AGP). Diseños conceptuales genéricos. *Publicación Técnica ENRESA 11/95*. 105 pp. Madrid.
- ENRESA (1998). FEBEX. Bentonite: origin, properties and fabrication of blocks. *Publicación Técnica ENRESA 4/98*. 146 pp. Madrid.
- ENRESA (2000). FEBEX Project. Full-scale engineered barriers experiment for a deep geological repository for high level radioactive waste in crystalline host rock. Final Report. *Publicación Técnica ENRESA 1/2000*. 354 pp. Madrid.
- Fernández A.M. (2003): Caracterización y modelización del agua intersticial en materiales arcillosos. Estudio de la bentonita de Cortijo de Archidona. *Ph. D. Thesis*. Universidad Autónoma de Madrid, 505 pp. (In Spanish).
- Fernández, A.M. & Cuevas, J. (1998). Estudios del agua intersticial de la arcilla FEBEX. *Internal report CIEMAT. FEBEX report 70-IMA-L-9-44*. Madrid.
- Gens, A. (1995): Constitutive laws. In: A. Gens, P. Jouanna, & B.A. Schrefler (Eds.), *Modern issues in non-saturated soils*. Springer Verlag, Viena, 129-158.
- Gens, A. & Alonso, E.E. (1992). A framework for the behaviour of unsaturated expansive clays. *Can. Geotech. J.* 29: pp. 1013-1032.
- Hueckel, T. & Borsetto, M. (1990). Thermoplasticity of saturated soils and shales: constitutive equation s. *J. Geotech. Eng. ASCE* 116(12): 1765-1777.
- Justo, J.L. Delgado, A., Ruiz, J. (1984). The influence of stress-path in the collapse-swelling of soils at the laboratory. *Proc. V Int. Conference on Expansive Soils*, Inst. of Civil Eng of Australia, Adelaide, 67-71.
- Lingnau, B.E., Graham, J., Yarechewski, D., Tanaka, N. & Gray, M.N., (1996). Effects of temperature on strength and compressibility of sand-bentonite buffer. *Eng. Geol.* 41 (1-4), 103-115.
- Lloret, A.; Villar, M.V. & Pintado, X. (2002): Ensayos THM: Informe de síntesis. Internal report CIEMAT/DIAE/54111/9/99. *FEBEX report 70-UPC-M-0-04*. 97 pp. Barcelona.
- Lloret, A.; Villar, M.V.; Sánchez, M.; Gens, A.; Pintado, X. & Alonso, E.E. (2003). Mechanical behaviour of heavily compacted bentonite under high suction changes. *Géotechnique* 53(1): 27-40.
- Marcial, D.(2003): Comportement hydromécanique et microstructural des matériaux de barrière ouvragée. *Ph. D. Thesis*. École Nationale des Ponts et Chaussées, Paris. 316 pp. (In French).
- Martin, R.T. (1962). Adsorbed water on clay: a review. *9<sup>th</sup> Nat. Conf. On Clays and Clay Minerals*. Pergamon, Oxford, 28-70.
- Mingarro, M., Rodríguez, V. & García, J. (2000). Estudios microbiológicos de la arcilla FEBEX. *Internal report CIEMAT/IMA/54223/4/00. FEBEX report 70-IMA-L-0-68*. Madrid. 66 pp.
- Olivella, S., Carrera, J., Gens, A. & Alonso, E.E. (1994). Nonisothermal Multiphase Flow of Brine and Gas Through Saline Media. *Transport in Porous Media* 15: 271-293.
- Olivella, S., Gens, A., Carrera, J. & Alonso E.E. (1996). Numerical formulation for a simulator (CODE-BRIGHT) for the coupled analysis of saline media. *Engineering Computations* 13: 87-112.
- Pintado, X. (2002). Caracterización del comportamiento termo-hidro-mecánico de arcillas expansivas. *Ph.D. Thesis*. Universitat Politècnica de Catalunya. Barcelona. (In Spanish).
- Romero, E., Villar, M.V. & Lloret, A. (in press). Thermo-hydro-mechanical behaviour of two heavily overconsolidated clays. *Engineering Geology*.
- Romero, E., Gens, A. & Lloret, A. (1999). Water permeability, water retention and microstructure of unsaturated Boom clay. *Engineering Geology*, 54: 117-127.
- Sánchez, M. (2004). Thermo-hydro-mechanical coupled analysis in low permeability media. *Ph. D. Thesis*. Universidad Politècnica de Cataluña. Barcelona.
- Sánchez, M. & Gens, A. (2002). Second report on THM modelling results. FEBEX II. UPC Geomechanical Group. *Internal report UPC-FEBEX report 70-UPC-L-5-011*. Barcelona
- Sánchez, M., Gens, A. Gimaraes, L.N. & Olivella, S. (2001). Generalized plasticity model for THM simulations involving expansive clays. *6<sup>th</sup> Int. Workshop on Key Issues on Waste Isolation Research*, Paris, 397-415.
- UPC (1997). Preoperational Thermo-Hydro-Mechanical (THM) Modelling of the 'MOCK-UPC test. *Internal*

- report UPC-FEBEX report 70-UPC-M-3-002. Barcelona.
- UPC (1999). Ensayos THM para el proyecto FEBEX realizados por la UPC-DIT. *Internal report UPC-FEBEX report 70-UPC-M-0-03*. 157 pp. Barcelona.
- Villar, M.V.(2000). Caracterización termo-hidro-mecánica de una bentonita de Cabo de Gata. *Ph. D. Thesis*. Universidad Complutense de Madrid. 387 pp. Madrid. (In Spanish).
- Villar, M.V.(2001). Ensayos termohidráulicos en celdas grandes: propiedades hidro-mecánicas. *Internal report CIEMAT/DIAE/54520/1/00. FEBEX report 70-IMA-L-0-76*. 65 pp. Madrid.
- Villar, M.V. (2002): Thermo-hydro-mechanical characterisation of a bentonite from Cabo de Gata. A study applied to the use of bentonite as sealing material in high level radioactive waste repositories. *Publicación Técnica ENRESA 01/2002*. 258 pp. Madrid.
- Villar, M.V.; Martín, P.L.; Lloret, A. & Romero, E. (2002): 2nd Report on Thermo-hydro-mechanical laboratory tests. Deliverable D-17/2. September 00-March 02. May 2002. CIEMAT/DIAE/54520/6/02. *FEBEX report 70-IMA-L-0-97*. 53 pp. Madrid.





Appendix A  
Tables with the results  
of tests



Appendix A. Tables with the results of tests

**Table A.1**  
Results of the retention curve at constant volume for different dry densities at 20 °C (CIEMAT).

1.60 g/cm <sup>3</sup>			1.65 g/cm <sup>3</sup>			1.70 g/cm <sup>3</sup>		
Suction (MPa)	w (%)	$\rho_d$ (g/cm <sup>3</sup> )	Suction (MPa)	w (%)	$\rho_d$ (g/cm <sup>3</sup> )	Suction (MPa)	w (%)	$\rho_d$ (g/cm <sup>3</sup> )
100	15.3	1.60	105	15.4	1.65	110	15.5	1.70
76	16.7	1.60	76	17.0	1.65	76	17.3	1.70
32	20.6	1.60	31	20.9	1.65	31	21.2	1.70
13	23.7	1.60	14	23.7	1.65	14	23.6	1.70
5	26.9	1.60	5	26.0	1.65	5	27.1	1.70
1	28.8	1.60	1	27.3	1.65	1	27.3	1.70
4	28.1	1.60	4	26.6	1.65	4	26.0	1.70
13	25.4	1.60	13	25.7	1.65	14	22.9	1.70
32	21.8	1.60	32	22.5	1.65	31	19.7	1.70
71	18.2	1.60	69	19.1	1.65	67	27.1	1.70
124	14.5	1.71	126	15.2	1.74	128	15.5	1.73
223	10.8	1.74	223	11.5	1.76	223	11.9	1.75
276	9.2	1.73	276	9.9	1.77	276	10.1	1.77
377	6.9	1.76	377	7.8	1.78	377	7.9	1.77

**Table A.2**  
Results of the retention curve at constant volume for different dry densities at 22 °C (CIMNE).

$\rho_d = 1.55 \text{ g/cm}^3$		$\rho_d = 1.65 \text{ g/cm}^3$	
Suction (MPa)	w (%)	Suction (MPa)	w (%)
120	13.3	120	13.3
87	15.2	87	14.9
75	15.8	75	15.4
57	17.3	57	16.5
29	20.4	29	19.2
11	26.7	11	23.9
3.8	32.0	3.8	27.1
11	30.2	11	26.4
29	22.0	29	21.2
39	20.8	39	20.0
57	18.9	57	18.2
75	17.8	75	17.1
87	16.7	87	16.1
100	16.3	100	15.9

Table A.3

Results of the retention curve at constant volume with measurement of swelling pressure, for different dry densities at 22 °C (CIMNE).

$\rho_d = 1.55 \text{ g/cm}^3$			$\rho_d = 1.65 \text{ g/cm}^3$		
Suction (MPa)	w (%)	$P_s$ (MPa)	Suction (MPa)	w (%)	$P_s$ (MPa)
120	13.3	0	120	13.3	0
57	17.2	1.00	57	17.5	1.26
3.8	25.6	2.24	3.8	24.3	3.00
0	30.1	3.08	0	27.9	4.38
3.8	26.9	0.90	3.8	25.3	2.25

Table A.4

Results of the retention curve at constant volume and at 40 °C for different dry densities (CIEMAT).

1.65 g/cm <sup>3</sup>			1.70 g/cm <sup>3</sup>		
Suction (MPa)	Water content (%)	$S_r$ (%)	Suction (MPa)	Water content (%)	$S_r$ (%)
149.4	13.6	58	151.3	13.9	64
71.0	16.8	71	58.1	17.8	82
31.6	20.2	86	32.2	20.4	94
12.0	22.9	97	12.3	22.7	104
3.2	24.9	106	5.2	23.9	110
2.3	26.1	110	2.3	25.3	116
3.6	25.9	110	3.8	25.7	118
18.1	23.7	101	12.7	23.2	106
33.1	21.3	90	32.8	21.6	99
59.5	19.0	81	76.4	17.9	82
107.1	15.7	67	115.3	15.4	71

Table A.5

Results of the retention curve at constant volume and at 60 °C for dry density 1.65 g/cm<sup>3</sup> in two series of tests (CIEMAT).

Suction (MPa)	Water content (%)	$S_r$ (%)	Suction (MPa)	Water content (%)	$S_r$ (%)
126	13.3	57	111	13.8	58
64	16.6	70	73	15.7	66
34	19.3	82	38	18.6	79
15	21.1	90	20	20.3	86
6	23.8	101	8	22.6	96
7	24.3	103	3	24.1	102
15	23.0	98	7	23.3	99
38	18.8	80	74	16.0	68
77	16.4	70	136	12.4	53

Table A.6  
Results of the retention curve at constant volume and at 80 °C for different dry densities (CIEMAT).

1.60 g/cm <sup>3</sup>			1.70 g/cm <sup>3</sup>		
Suction (MPa)	Water content (%)	S <sub>r</sub> (%)	Suction (MPa)	Water content (%)	S <sub>r</sub> (%)
128.3	13.2	52	128.3	13.0	60
74.7	16.0	63	74.7	15.9	73
41.2	18.3	72	41.2	18.2	83
16.1	22.5	88	16.1	22.4	103
6.1	25.6	100	6.1	24.1	111

Table A.7  
Results of the retention curves in unconfined samples for different initial dry densities at 80 °C (CIEMAT).

Suction (MPa)	1.54 g/cm <sup>3</sup>			1.59 g/cm <sup>3</sup>			1.65 g/cm <sup>3</sup>		
	$\rho_d$ (g/cm <sup>3</sup> )	w (%)	S <sub>r</sub> (%)	$\rho_d$ (g/cm <sup>3</sup> )	w (%)	S <sub>r</sub> (%)	$\rho_d$ (g/cm <sup>3</sup> )	w (%)	S <sub>r</sub> (%)
101	1.50	13.5	46	1.57	12.9	48	1.62	12.9	52
172	1.54	10.4	37	1.59	10.4	40	1.64	10.4	44
246	1.56	8.2	30	1.61	8.2	33	1.67	8.1	36
349	1.59	5.1	20	1.64	5.1	21	1.70	5.0	23
251	1.57	7.1	27	1.62	7.1	29	1.68	7.1	31
204	1.56	8.5	32	1.61	8.5	34	1.68	8.4	37
121	1.53	11.2	40	1.57	11.2	42	1.63	11.2	46
65	1.47	14.3	46	1.51	14.3	49	1.57	14.3	54
41	1.44	16.2	50	1.46	16.2	51	1.51	16.2	56
23	1.37	18.7	52	1.39	18.3	53	1.44	18.3	57
6	1.25	24.0	56	1.28	24.1	58	1.31	25.0	63
0.05		50.2	0.98	43.5	61	1.00	55.5	88	

**Table A.8**  
Results of the retention curves in unconfined samples for different initial dry densities at 60 °C (CIEMAT).

Suction (MPa)	1.56 g/cm <sup>3</sup>			1.61 g/cm <sup>3</sup>			1.66 g/cm <sup>3</sup>		
	$\rho_d$ (g/cm <sup>3</sup> )	w (%)	$S_r$ (%)	$\rho_d$ (g/cm <sup>3</sup> )	w (%)	$S_r$ (%)	$\rho_d$ (g/cm <sup>3</sup> )	w (%)	$S_r$ (%)
110	1.55	13.1	48	1.60	13.1	51	1.64	13.2	55
218	1.58	9.0	34	1.64	9.0	38	1.67	8.9	39
262	1.58	7.7	29	1.64	7.7	32	1.69	7.7	35
347	1.62	5.2	21	1.67	5.2	23	1.72	5.1	24
266	1.60	7.0	28	1.66	6.9	29	1.70	6.9	32
212	1.58	8.4	32	1.63	8.4	35	1.67	8.5	37
121	1.55	11.8	43	1.59	11.8	46	1.64	11.8	49
82	1.50	14.2	48	1.54	14.0	50	1.59	14.3	55
49	1.45	16.2	50	1.49	16.3	54	1.52	16.6	58
20	1.40	18.9	55	1.42	19.1	57	1.46	19.3	61
8	1.31	22.2	57	1.33	22.7	60	1.35	23.3	63
0.3	1.09	30.5	56	1.08	34.8	62	1.16	31.9	65

**Table A.9**  
Results of the retention curves in confined samples for different initial dry densities at 80 °C (CIMNE).

$\rho_d = 1.55 \text{ g/cm}^3$		$\rho_d = 1.65 \text{ g/cm}^3$	
w (%)	Suction (MPa)	w (%)	Suction (MPa)
12.4	106	13.0	106
13.0	84	13.6	84
15.5	67	15.4	67
16.6	47	16.7	47
17.1	32	17.2	32
18.2	8.3		

**Table A.10**  
Results of the swelling under vertical pressure (0.1 MPa) tests for different temperatures (CIEMAT).

Temperature (°C)	Initial $\rho_d$ (g/cm <sup>3</sup> )	Initial w (%)	Final strain (%)	Duration (days)	Final w (%)	Final $\rho_d$ (g/cm <sup>3</sup> )
40	1.62	12.2	-31.8	110	45.6	1.23
50	1.64	11.3	-32.2	71	43.0	1.24
80	1.62	13.4	-35.9	77	46.3	1.19

Table A.11

Results of the swelling under vertical pressure (0.5 MPa) tests for different temperatures (CIEMAT).

Temperature (°C)	Initial $\rho_d$ (g/cm <sup>3</sup> )	Initial w (%)	Final strain (%)	Duration (days)	Final w (%)	Final $\rho_d$ (g/cm <sup>3</sup> )
30	1.61	13.0	-23.0	49	39.7	1.31
40	1.59	15.5	-20.1	55	44.8	1.32
50	1.63	11.5	-18.7	57	39.5	1.37
60	1.61	12.8	-12.5	37	37.9	1.43
60	1.61	13.1	-21.8	43	37.3	1.32
70	1.60	12.8	-9.8	35	36.5	1.39
80	1.62	12.1	-6.3	40	40.3	1.36
80	1.64	10.4	-17.4	26	35.2	1.40

Table A.12

Results of the swelling under vertical pressure (1.5 MPa) tests for different temperatures (CIEMAT).

Temperature (°C)	Initial $\rho_d$ (g/cm <sup>3</sup> )	Initial w (%)	Final strain (%)	Duration (days)	Final w (%)	Final $\rho_d$ (g/cm <sup>3</sup> )
30	1.62	13.1	-15.7	51	35.3	1.40
40	1.60	12.8	-12.5	39	35.7	1.43
50	1.58	14.6	-12.2	36	34.0	1.41
60	1.62	12.8	-11.3	23	32.7	1.46
70	1.61	12.5	-12.3	29	30.8	1.44
80	1.60	13.1	-5.0	26	34.0	1.52
80	1.62	12.4	-9.8	28	31.2	1.48

Table A.13

Results of the swelling under vertical pressure (3.0 MPa) tests for different temperatures (CIEMAT).

Temperature (°C)	Initial $\rho_d$ (g/cm <sup>3</sup> )	Initial w (%)	Final strain (%)	Duration (days)	Final w (%)	Final $\rho_d$ (g/cm <sup>3</sup> )
30	1.61	13.0	-8.9	44	31.0	1.48
40	1.60	14.1	-9.4	44	31.7	1.46
50	1.61	12.9	-5.5	30	31.0	1.53
60	1.61	13.0	-8.7	37	29.3	1.48
70	1.62	12.9	-7.4	35	28.9	1.51
80	1.61	13.2	-5.1	30	28.8	1.53

Table A.14  
Results of the swelling pressure and hydraulic conductivity test at different temperatures for nominal dry densities 1.60 and 1.50 g/cm<sup>3</sup> (CIEMAT).

Temperature (°C)	$\rho_d$ (g/cm <sup>3</sup> )	$P_s$ (MPa)	Final w (%)	$k_w$ (m/s)
25	1.50	3.9	33.5	$4.4 \cdot 10^{-14}$
25	1.55	3.9		$4.1 \cdot 10^{-14}$
30	1.58	2.6		$1.1 \cdot 10^{-13}$
30	1.59	4.5	31.5	
30	1.59	4.8	31.4	
40	1.55	3.8	35.1	
40	1.55	2.7		
50	1.57	2.4		$1.2 \cdot 10^{-13}$
60	1.58	1.5	25.5	
80	1.57	1.7	29.0	$1.1 \cdot 10^{-13}$
80	1.60	2.0	34.8	$7.9 \cdot 10^{-14}$
40	1.49	2.1	35.9	$6.8 \cdot 10^{-12}$
80	1.49	1.4	36.4	$5.3 \cdot 10^{-11}$



Table A.15  
Parameters obtained from oedometric tests on samples saturated with different solutions (CIMNE)

Solute	Vertical Load Increment (MPa)	Concentration (M)	Void Ratio	Oedometric modulus $E_m$ (MPa)	Consolidation coefficient $c_v$ ( $m^2/s$ )	Saturated permeability $k$ (m/s)	Secondary consolidation coefficient $C_\alpha$		
Distilled Water	0.5-1.0	0	0.946	47	$1.9 \cdot 10^{-09}$	$4.0 \cdot 10^{-13}$	$1.5 \cdot 10^{-03}$		
	1.0-2.0		0.889	34.3	$1.5 \cdot 10^{-09}$	$4.4 \cdot 10^{-13}$	$5.5 \cdot 10^{-03}$		
NaCl	0.5-1.0	0.1	0.821	26	$1.8 \cdot 10^{-09}$	$6.9 \cdot 10^{-13}$	$3.0 \cdot 10^{-03}$		
			0.808	55	$3.0 \cdot 10^{-09}$	$5.5 \cdot 10^{-13}$	$8.0 \cdot 10^{-04}$		
			0.702	58	$3.7 \cdot 10^{-09}$	$6.4 \cdot 10^{-13}$	$3.0 \cdot 10^{-03}$		
			0.698	60.5	$1.2 \cdot 10^{-08}$	$2.0 \cdot 10^{-12}$	$3.5 \cdot 10^{-03}$		
			0.642	90	$8.0 \cdot 10^{-08}$	$8.9 \cdot 10^{-12}$	$2.0 \cdot 10^{-03}$		
			0.691	110	$2.5 \cdot 10^{-08}$	$2.3 \cdot 10^{-12}$	$2.2 \cdot 10^{-03}$		
	1.0-2.0	0.1	0.889	35.9	$1.5 \cdot 10^{-09}$	$5.3 \cdot 10^{-13}$	$7.8 \cdot 10^{-03}$		
			0.729	35	$1.9 \cdot 10^{-09}$	$4.3 \cdot 10^{-13}$	$5.0 \cdot 10^{-03}$		
			0.740	35	$1.5 \cdot 10^{-09}$	$4.3 \cdot 10^{-13}$	$6.0 \cdot 10^{-03}$		
			0.634	45	$1.5 \cdot 10^{-09}$	$8.9 \cdot 10^{-13}$	$4.5 \cdot 10^{-03}$		
			0.634	58	$4.0 \cdot 10^{-09}$	$8.6 \cdot 10^{-13}$	$4.0 \cdot 10^{-03}$		
			0.583	70	$5.0 \cdot 10^{-09}$	$1.1 \cdot 10^{-12}$	$4.0 \cdot 10^{-03}$		
			0.5-1.0	0.1	0.868	50.6	$6.1 \cdot 10^{-09}$	$1.2 \cdot 10^{-12}$	$2.3 \cdot 10^{-03}$
					0.819	58	$1.5 \cdot 10^{-08}$	$2.6 \cdot 10^{-12}$	$1.6 \cdot 10^{-03}$
0.756	100	$1.0 \cdot 10^{-08}$			$1.0 \cdot 10^{-12}$	$1.5 \cdot 10^{-03}$			
1.0-2.0	0.1	0.817			46.2	$3.4 \cdot 10^{-09}$	$7.4 \cdot 10^{-13}$	$7.1 \cdot 10^{-03}$	
		0.745			49	$2.5 \cdot 10^{-09}$	$5.1 \cdot 10^{-13}$	$3.5 \cdot 10^{-03}$	
		0.721			55	$4.0 \cdot 10^{-09}$	$7.3 \cdot 10^{-13}$	$2.5 \cdot 10^{-03}$	
		0.684	70	$5.0 \cdot 10^{-09}$	$7.1 \cdot 10^{-13}$	$1.7 \cdot 10^{-03}$			
		0.699	90	$8.5 \cdot 10^{-09}$	$9.4 \cdot 10^{-13}$	$2.5 \cdot 10^{-03}$			

Table A.16  
Results of the swelling under load tests performed with deionised water (CIEMAT).

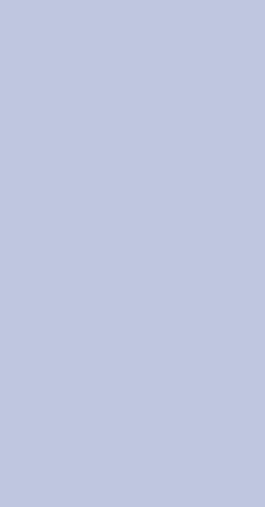
Initial $\rho_d$ (g/cm <sup>3</sup> )	Initial w (%)	Vertical pressure (MPa)	Final strain (%)	Duration (days)	Final w (%)	Final $\rho_d$ (g/cm <sup>3</sup> )
1.37	14.3	1.0	-3.1	13	36.6	1.33
1.50	13.0	0.1	-23.9	23	49.0	1.21
1.51	13.5	0.1	-21.3	15	44.7	1.24
1.50	14.5	0.1	-23.5	19	47.2	1.21
1.49	14.2	0.5	-13.9	16	41.7	1.30
1.49	14.2	0.5	-13.3	17	37.5	1.32
1.50	13.9	1.0	-8.8	16	40.7	1.38
1.50	14.4	1.0	-7.6	15	36.5	1.39
1.48	15.1	1.5	-5.9	14	33.3	1.39
1.49	14.1	3.0	0.0	14	31.2	1.49
1.51	14.0	3.0	-1.9	28	30.4	1.48
1.46	14.6	3.0	-1.5	13	31.5	1.44
1.71	13.3	0.1	-33.4	17	45.9	1.28
1.61	13.5	0.1	-28.5	14	46.9	1.25
1.60	14.3	0.1	-30.5	14	46.7	1.23
1.60	13.7	0.5	-17.3	18	35.7	1.36
1.60	14.2	0.5	-16.8	16	37.1	1.37
1.60	13.9	1.0	-14.1	18	33.5	1.40
1.60	14.3	1.0	-14.6	12	38.4	1.39
1.61	14.2	1.3	-14.3	32	37.1	1.41
1.60	13.5	3.0	-3.7	20	28.5	1.54
1.60	14.5	3.0	-6.5	15	32.6	1.50
1.69	14.0	0.1	-32.6	15	44.0	1.27
1.71	14.0	0.1	-36.3	32	44.9	1.25
1.68	14.5	0.5	-24.1	15	38.5	1.36
1.70	14.4	0.5	-23.5	28	35.5	1.38
1.68	14.3	1.0	-18.3	15	34.0	1.42
1.70	13.8	1.0	-16.1	18	32.8	1.47
1.69	13.8	3.0	-9.4	14	27.3	1.55
1.69	14.4	3.0	-10.9	14	30.4	1.52

Table A.17  
Results of the swelling under load tests performed with saline water (CIEMAT).

Initial $\rho_d$ (g/cm <sup>3</sup> )	Initial w (%)	Vertical pressure (MPa)	Final strain (%)	Duration (days)	Final w (%)	Final $\rho_d$ (g/cm <sup>3</sup> )
1.71	13.0	0.1	-29.0	9	43.8	1.33
1.70	13.4	0.1	-33.1	14	43.7	1.28
1.72	12.7	0.5	-19.0	11	35.2	1.45
1.69	14.2	0.5	-23.0	14	39.3	1.38
1.70	14.1	1.0	-18.2	10	36.6	1.44
1.71	13.0	1.0	-16.3	17	31.9	1.47
1.68	15.0	3.0	-9.7	10	31.9	1.53
1.71	13.0	3.0	-9.5	17	28.5	1.56
1.60	13.6	0.1	-25.9	15	43.2	1.27
1.58	15.4	0.1	-25.8	11	36.8	1.25
1.61	12.9	0.5	-16.7	15	33.6	1.39
1.63	11.6	0.5	-15.7	8	40.4	1.41
1.60	13.4	1.0	-9.9	8	35.1	1.46
1.61	13.3	1.0	-10.6	9	37.1	1.45
1.59	14.5	2.0	-7.2	10	29.5	1.48
1.60	14.1	2.0	-5.7	7	34	1.51
1.59	14.6	3.0	-6.1	8	29.2	1.50
1.59	14.1	3.0	-5.1	8	29.3	1.52
1.50	13.3	0.1	-21.1	14	45.3	1.24
1.50	13.3	0.6	-11.9	13	39.4	1.34
1.51	13.1	1.0	-8.2	13	33.4	1.39
1.50	13.9	3.0	1.6	11	32.4	1.52


Table A.18  
Results of the swelling under load tests performed with granitic water (CIEMAT).

Initial $\rho_d$ (g/cm <sup>3</sup> )	Initial w (%)	Vertical pressure (MPa)	Final strain (%)	Duration (days)	Final w (%)	Final $\rho_d$ (g/cm <sup>3</sup> )
1.72	14.0	0.1	-28.6	7	35.1	1.34
1.72	13.9	0.5	-20.6	7	32.5	1.43
1.72	13.1	1.0	-18.3	21	32.1	1.46
1.72	13.0	3.0	-10.6	13	28.8	1.55
1.62	13.1	0.1	-25.1	7	41.0	1.29
1.61	13.1	0.1	-24.5	15	38.7	1.29
1.62	13.4	0.5	-14.4	7	38.3	1.41
1.54	18.4	0.5	-13.7	9	39.5	1.35
1.61	13.6	1.0	-10.6	7	36.6	1.46
1.61	13.0	1.0	-8.8	16	34.0	1.48
1.60	13.7	2.0	-3.3	9	32.2	1.54
1.62	12.5	2.0	-6.4	11	29.5	1.52
1.60	13.3	3.0	-1.5	8	30.5	1.57
1.60	13.3	3.0	-1.2	7	30.0	1.58
1.52	12.7	0.1	-22.9	10	46.3	1.23
1.51	13.5	0.5	-12.1	10	40.4	1.34
1.50	14.2	1.0	-8.5	13	34.2	1.38
1.49	15.0	3.0	-1.5	13	32.0	1.46
1.62	13.2	0.5	-17.8	15	39.3	1.37
1.60	14.6	0.5	-17.2	21	40.1	1.37
1.61	13.3	0.5	-12.1	14	38.4	1.44
1.62	13.0	0.5	-17.8	14	38.3	1.37
1.62	12.8	0.5	-17.2	15	39.1	1.39
1.59	14.2	0.9	-15.8	20	36.7	1.39
1.61	13.7	0.9	-14.7	19	36.6	1.40
1.59	15.0	0.9	-13.4	20	37.2	1.40



Appendix B

**Thermo-hydro-mechanical  
model used  
for the analysis  
of the infiltration tests**



Appendix B. Thermo-hydro-mechanical model  
used for the analysis of the infiltration tests

## B.1 Balance equations

Equations for mass balance were established following the compositional approach, which consists of balancing the species rather than the phases. The mass balance of solid present in the medium is written as:

$$\frac{\partial}{\partial t}(\rho_s(1-n)) + \nabla \cdot (\mathbf{j}_s) = 0 \quad [\text{B.1}]$$

where  $\rho_s$  is the mass of solid per unit volume of solid,  $\mathbf{j}_s$  is the flux of solid,  $t$  is time and  $\nabla$  is the divergence operator.

Water is present in liquid and gas phases. The total mass balance of water is expressed as:

$$\frac{\partial}{\partial t}(\theta_l^w S_l n + \theta_g^w S_g n) + \nabla \cdot (\mathbf{j}_l^w + \mathbf{j}_g^w) = f^w \quad [\text{B.2}]$$

where  $\theta_l^w$  and  $\theta_g^w$  are the masses of water per unit volume of liquid and gas respectively.  $S_l$  is the volumetric fraction of pore volume, occupied by the alpha phase ( $\alpha = l, g$ ).  $\mathbf{j}_l^w$  and  $\mathbf{j}_g^w$  denote the total mass fluxes of water in the liquid and gas phases (water vapour), with respect to a fixed reference system.  $f^w$  is an external supply of water.

Dry air is present in liquid and gas phases. The total mass balance of dry air is expressed as:

$$\frac{\partial}{\partial t}(\theta_l^a S_l n + \theta_g^a S_g n) + \nabla \cdot (\mathbf{j}_l^a + \mathbf{j}_g^a) = f^a \quad [\text{B.3}]$$

where  $\theta_l^a$  and  $\theta_g^a$  are the masses of dry air per unit volume of liquid and gas respectively.  $S_\alpha$  is the volumetric fraction of pore volume, occupied by the alpha phase ( $\alpha = l, g$ ).  $\mathbf{j}_l^a$  and  $\mathbf{j}_g^a$  denote the total mass fluxes of dry air in the liquid and gas phases, with respect to a fixed reference system.  $f^a$  is an external supply of dry air.

Regarding the thermal problem, equilibrium between the phases is assumed. Therefore, the temperature is the same for all the phases. Consequently, only one equation is needed for the energy balance. If either the complexity of the problem or the experimental evidence justifies the necessity of a more detailed treatment of this equation, different temperatures can easily be considered. The total internal energy, per unit volume of porous media, is obtained adding the internal energy of each phase corresponding to each medium. Applying the balance equation to this quantity, the following equation is obtained:

$$\begin{aligned} & \frac{\partial}{\partial t}(E_s \rho_s(1-\phi) + E_l \rho_l S_l \phi + E_g \rho_g S_g \phi) + \\ & + \nabla \cdot (\mathbf{i}_c + \mathbf{i}_{E_s} + \mathbf{i}_{E_l} + \mathbf{i}_{E_g}) = f^E \end{aligned} \quad [\text{B.4}]$$

where  $E_s$  is the solid specific internal energy;  $E_l$  and  $E_g$  are specific internal energies corresponding to liquid and gas phase, respectively,  $\rho_s$  is the solid density;  $\rho_l$  and  $\rho_g$  are the liquid and gas phase densities;  $\mathbf{i}_c$  is the conductive heat flux;  $\mathbf{i}_{E_s}$  is the advective energy flux of solid phase respect to a fixed reference system;  $\mathbf{i}_{E_l}$  and  $\mathbf{i}_{E_g}$  are the advective energy flux of liquid and gas phases, respectively, with respect to a fixed reference system;  $f^E$  are the energies supply per unit volume of medium.

Finally, the balance of momentum for the porous medium reduces to the equilibrium equation in total stresses:

$$\nabla \cdot \boldsymbol{\sigma} + \mathbf{b} = 0 \quad [\text{B.5}]$$

where  $\boldsymbol{\sigma}$  is the stress tensor and  $\mathbf{b}$  is the vector of body forces.

## B.2 Constitutive equations: Thermo-hydraulic model

Concerning the hydraulic problem it is assumed that the liquid and gas flows follow Darcy's law:

$$\mathbf{q}_\alpha = -\mathbf{K}_\alpha (\nabla P_\alpha - \rho_\alpha \mathbf{g}); \quad \alpha = l, g \quad [\text{B.6}]$$

where  $P_l$  and  $P_g$  are liquid and gas pressures respectively,  $\rho_l$  is the liquid density,  $\rho_g$  is the gas density,  $\mathbf{g}$  is the gravity vector and  $\mathbf{K}_\alpha$  is the permeability tensor of the alpha phase ( $\alpha = l, g$ ), which is given by:

$$\mathbf{K}_\alpha = \mathbf{k} \frac{k_{r\alpha}}{\mu_\alpha}; \quad \alpha = l, g \quad [\text{B.7}]$$

The intrinsic permeability tensor ( $\mathbf{k}$ ) depends on the pore structure of the porous medium.  $k_{r\alpha}$  is the value of relative permeability that controls the variation of permeability in the unsaturated regime and  $\mu_\alpha$  denotes the dynamic viscosity.  $\alpha$  may stand for either  $l$  or  $g$  depending on whether liquid or gas flow is considered. The variation of intrinsic permeability with porosity is given by:

$$\mathbf{k} = \mathbf{k}_o e^{(b(\phi - \phi_o))} \quad [\text{B.8}]$$

where  $\mathbf{k}_o$  is the intrinsic permeability corresponding to  $\phi_o$  (a reference porosity), and  $b$  is a material pa-

parameter. The relative permeability of liquid ( $k_{rl}$ ) phases is made dependent on  $S_e$  (effective degree of saturation) according to:

$$k_{rl} = S_e^n; \quad S_e = \frac{S_l - S_{lr}}{S_{ls} - S_{lr}} \quad [B.9]$$

where  $S_l$  is degree of saturation,  $S_{lr}$  and  $S_{ls}$  are residual and maximum degree of saturation, respectively, and  $n$  is a material parameter.

Another relevant law related to the hydraulic problem is the retention curve. A modified van Genuchten law was adopted to model the dependence of the degree of saturation on suction:

$$S_l = \left[ 1 + \left( \frac{s}{P_0} \right)^{\frac{1}{1-\lambda_o}} \right]^{-\lambda_o} f_d; \quad f_d = \left( 1 - \frac{s}{P_d} \right)^{\lambda_d} \quad [B.10]$$

where  $s$  ( $s = P_g - P_l$ ), is the suction,  $P_0$  is a parameter related to the capillary pressure (the air entry value) and  $\lambda_o$  is a parameter that controls the shape of the curve. The function  $f_d$  is included to obtain more suitable values at high suctions,  $P_d$  is related with the suction at 0 degree of saturation and  $\lambda_d$  is a model parameter (when is null the original model is recovered).

The molecular diffusion of vapour water in gas phase is governed by Fick's law, through:

$$\mathbf{i}_g^w = -\mathbf{D}_g^w \nabla \omega_g^w = -(\phi \rho_g S_g \tau D_m^w \mathbf{I} + \rho_g \mathbf{D}_g') \nabla \omega_g^w \quad [B.11]$$

where  $\mathbf{i}_g^w$  is the non advective mass flux of water in gas,  $\mathbf{D}_g^w$  is the dispersion tensor,  $\omega_g^w$  is the mass fraction of water in gas,  $\tau$  is the tortuosity factor and  $\mathbf{D}_g'$  the mechanical dispersion tensor.  $D_m^w$  is the molecular diffusion coefficient of vapour in gas.

Regarding the thermal problem the Fourier's law was adopted for the conductive flux of heat:

$$i_c = -\lambda \nabla T \quad [B.12]$$

Thermal conductivity depends on the hydration state of the clay and is expressed by a variant of the geometric mean:

$$\lambda = \lambda_{sat}^{s_i} \lambda_{dry}^{(1-s_i)} \quad [B.13]$$

where  $\lambda$  is the global thermal conductivity; and  $\lambda_{dry}$  and  $\lambda_{sat}$  are the thermal conductivity of bentonite in dry and saturated conditions respectively.

## B.3 Constitutive equations: Mechanical model

The mechanical law adopted is the Barcelona Basic Model (BBM). This model extends the concept of critical state for saturated soils to the unsaturated conditions, including the dependence of yield surface on suction. Two stress variables are considered: the net stresses ( $\sigma - P_g \mathbf{m}$ ) and capillary suction. Net stress is the excess of total stress over gas pressure. If full saturation is achieved, net mean stress becomes effective stress. For simplicity net stress will also be denoted by  $\sigma$ .

A thermoplastic constitutive law (Alonso *et al.*, 1990; Gens 1995) was selected based on a generalised yield surface that depends not only on stresses but on temperature and suction as well:

$$f = f(\sigma, \varepsilon_v^p, s, \Delta T) \quad [B.14]$$

$\Delta T (= T - T_0)$  is the temperature difference with respect to an arbitrary reference temperature,  $T_0$ . In terms of invariants:

$$f = f(\rho, J, \theta, \varepsilon_v^p, s, \Delta T) \quad [B.15]$$

where:

$$\rho = \left( \frac{1}{3} \right) (\sigma_x + \sigma_y + \sigma_z) \quad [B.16]$$

$$J^2 = \frac{1}{2} \text{trace}(\mathbf{s}^2) \quad [B.17]$$

$$\theta = -\frac{1}{3} \sin^{-1}(1.5\sqrt{3} \det \mathbf{s} / J^3) \quad [B.18]$$

$$\mathbf{s} = \sigma - \rho \mathbf{I} \quad [B.19]$$

$\mathbf{I}$  is the identity tensor. For simplicity, a form of the classical Modified Cam-clay model is taken as the reference isothermal saturated constitutive law:

$$F = \frac{3J^2}{g_y^2} - L_y^2 (\rho + P_s)(P_0 - \rho) = 0 \quad [B.20]$$

Volumetric strain is defined as:

$$\varepsilon_v = \varepsilon_x + \varepsilon_y + \varepsilon_z \quad [B.21]$$

and  $\varepsilon_v^p$  is the plastic volumetric strain.

The basic assumption is that the pre-consolidation pressure,  $P_{or}$ , is made dependent on both suction and temperature:



$$P_o = P^c \left( \frac{P_c}{P^c} \right)^{\frac{\lambda(o) - k_{io}}{\lambda(s) - k_{io}}} \quad [B.22]$$

$$P_c = P_o^* + 2(\alpha_1 \Delta T + \alpha_2 \Delta T(T)) \quad [B.23]$$

$$L_y = \frac{M}{g_y(\theta = -\pi/6)} \quad [B.24]$$

$$\lambda(s) = \lambda(o)[(1-r)\exp(-\beta s) + r] \quad [B.25]$$

In addition:

$$P_s = k \exp(-\rho \Delta T) s \quad [B.26]$$

In common with other critical state models, it is assumed that hardening depends on plastic volumetric strain only according to:

$$\dot{P}_o^* = \frac{1+e}{\lambda(0) - k_{io}} P_o^* \dot{\mathcal{E}}_v^p \quad [B.27]$$

and the plastic potential:

$$G = \frac{3J^2}{g_p^2} - \alpha L_p^2 (p + P_s)(P_o - p) \quad [B.28]$$

$$L_p = \frac{M}{g_p(\theta = -\pi/6)} \quad [B.29]$$

If  $\alpha = 1$ , an associated plastic model results.

The variation of stress-stiffness with suction and, especially, the variation of swelling potential with stress and suction have been carefully considered. The resulting elastic model is as follows:

$$\dot{\mathcal{E}}_v^e = \frac{k_i}{1+e} \frac{\dot{P}}{P} + \frac{k_s}{1+e} \frac{\dot{s}}{s+0.1} + (\alpha_o + 2\alpha_2 \Delta T) \dot{T} \quad [B.30]$$

$$k_i = k_{io}(1 + \alpha_{is}s) \quad [B.31]$$

$$k_s = k_{so}(1 + \alpha_{sp} \ln p/P_r) \exp(\alpha_{ss}s) \quad [B.32]$$

$$\dot{\mathcal{E}} = \dot{J}/G; \quad G = E/2(1+\nu) \quad [B.33]$$





Appendix C

**Observations  
in Environmental  
Scanning Electron  
Microscope**



## Appendix C. Observations in environmental scanning electron microscope

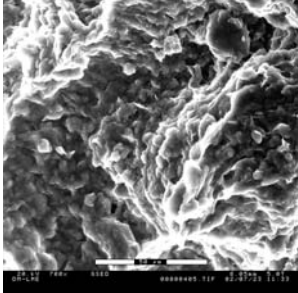
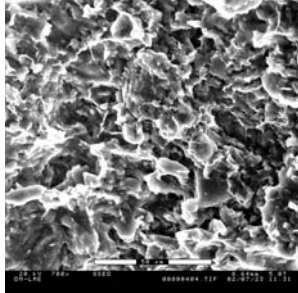
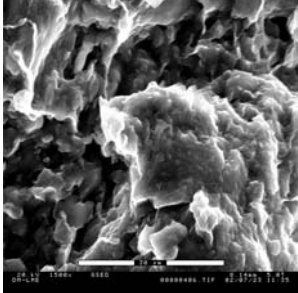
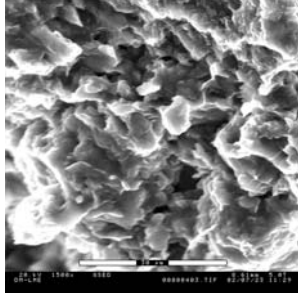
$\rho_s = 1.65 \text{ g/cm}^3$ $s = 0 \text{ MPa}$	$P_g = 5 \text{ Torr } T = 5^\circ\text{C RH} = 75 \%$	$P_g = 5 \text{ Torr } T = 5^\circ\text{C RH} = 75 \%$
$\times 700$		
$\times 1500$		

Table C.1: Compacted slurry.

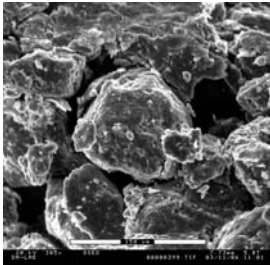
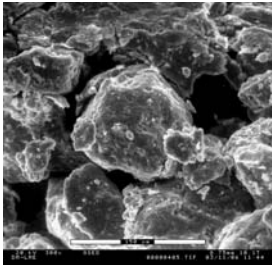
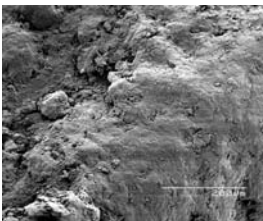
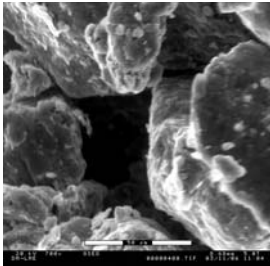
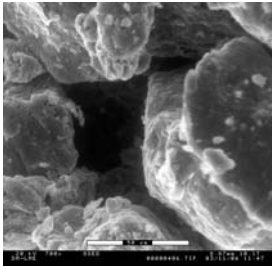

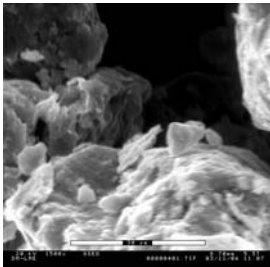
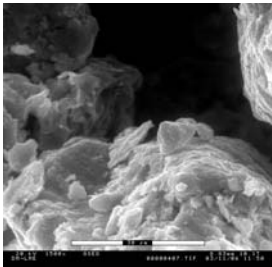
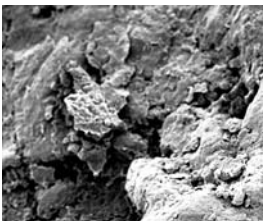
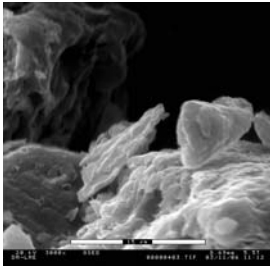
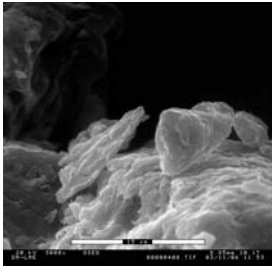
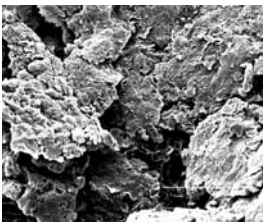
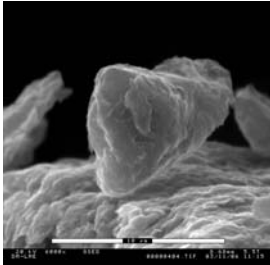
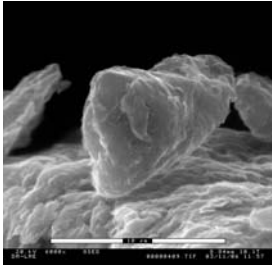
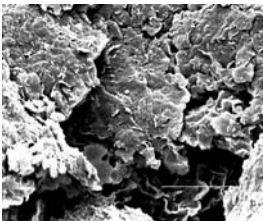
$\rho_d = 1.40 \text{ g/cm}^3$ $s = 120 \text{ MPa}$	$P_0 = 5.5 \text{ Tor}$ T=15°C RH= 41 %	$P_0 = 10.1 \text{ Tor}$ T=15°C RH= 75 %	$P_0 = 0 \text{ Tor}$ SEM
× 300			
× 700			
× 1500			
× 3000			
× 6000			

Table C.2: Sample compacted at  $1.40 \text{ g/cm}^3$  and hygroscopic water content observed in SEM and ESEM at different relative humidity.

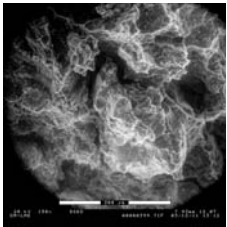
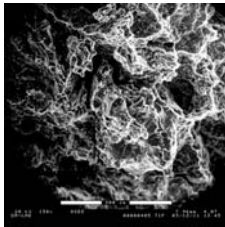
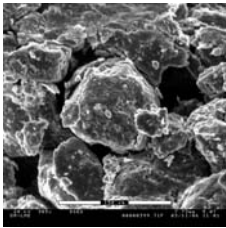
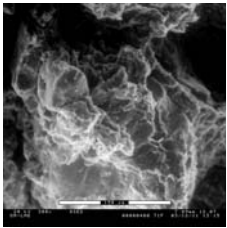
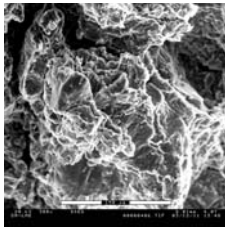
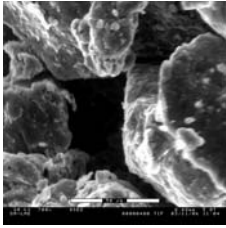
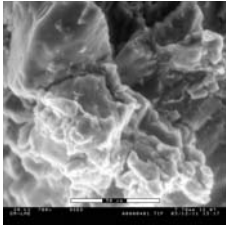
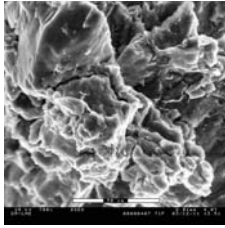
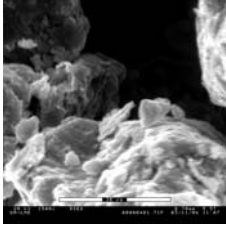
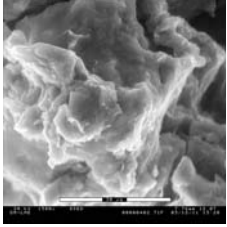
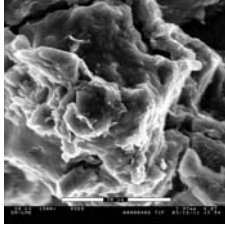
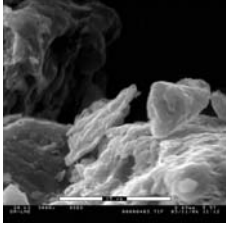
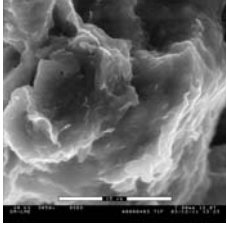
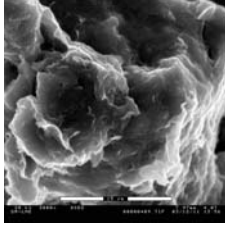
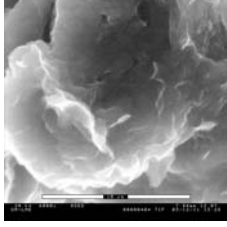
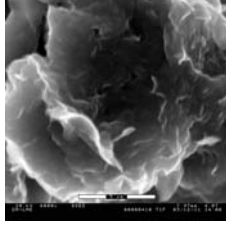
	$\rho_d = 1.40 \text{ g/cm}^3$ $s = 120 \text{ MPa}$ $P_g = 5.5 \text{ Tor}$ $T = 15^\circ\text{C}$ $\text{RH} = 41 \%$	$\rho_d = 1.29 \text{ g/cm}^3$ $s = 0 \text{ MPa}$ $P_g = 12 \text{ Tor}$ $T = 16^\circ\text{C}$ $\text{RH} = 100 \%$	$\rho_d = 1.29 \text{ g/cm}^3$ $s = 0 \text{ MPa}$ $P_g = 4 \text{ Tor}$ $T = 17.5^\circ\text{C}$ $\text{RH} = 27 \%$
$\times 150$			
$\times 300$			
$\times 700$			
$\times 1500$			
$\times 3000$			
$\times 6000$			

Table C.3: Samples initially compacted at  $1.40 \text{ g/cm}^3$  and hygroscopic conditions ( $s=120 \text{ MPa}$ ) and saturated under isochoric conditions (final  $\rho_d = 1.29 \text{ g/cm}^3$ ).

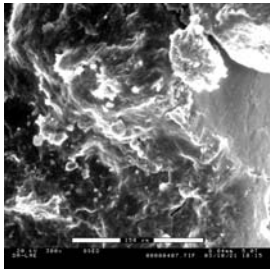
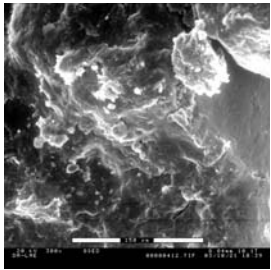
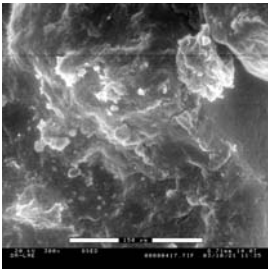
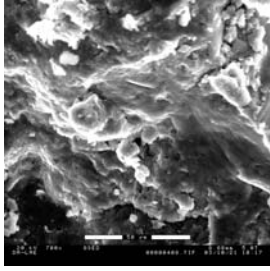
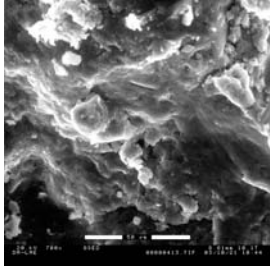
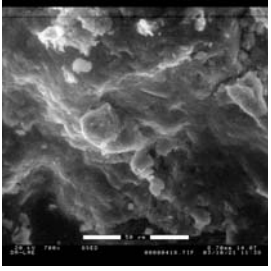
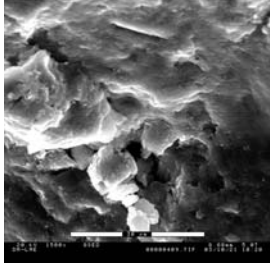
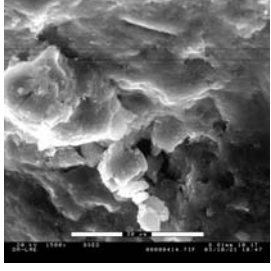
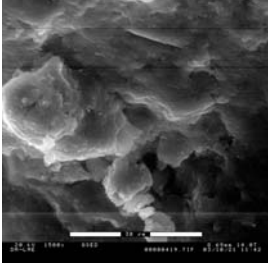
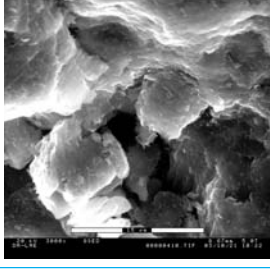
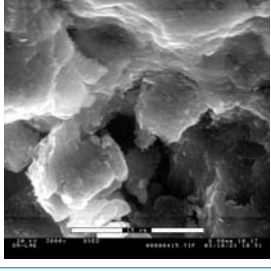
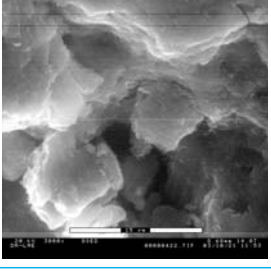
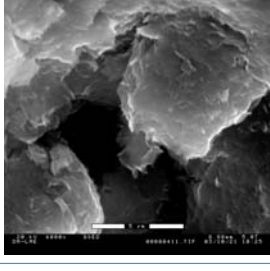
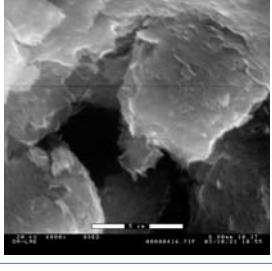
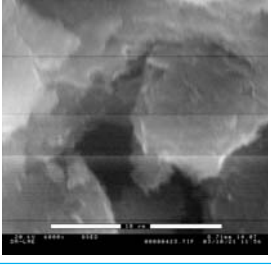
$\rho_d = 1.65 \text{ g/cm}^3$ $s = 120 \text{ MPa}$	$P_g = 5.5 \text{ Tor } T = 16^\circ\text{C } RH = 41 \%$	$P_g = 10.1 \text{ Tor } T = 16^\circ\text{C } RH = 75 \%$	$P_g = 14 \text{ Tor } T = 16^\circ\text{C } RH = 100 \%$
$\times 300$			
$\times 700$			
$\times 1500$			
$\times 3000$			
$\times 6000$			

Table C.4: Sample compacted at  $1.65 \text{ g/cm}^3$  and hygroscopic water content observed in ESEM at different relative humidity.



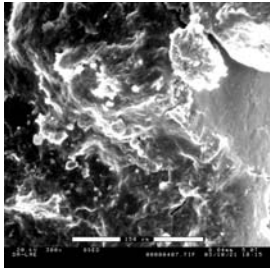
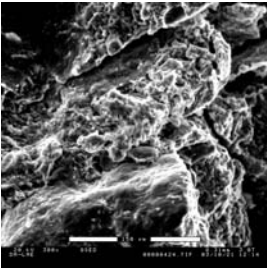
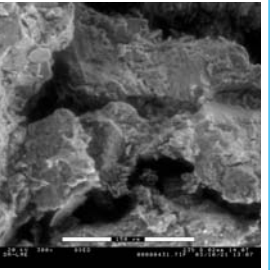
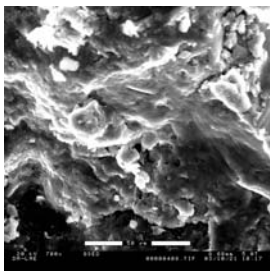
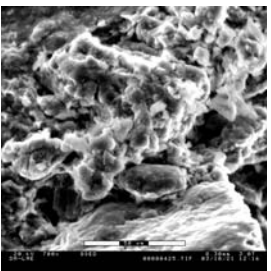
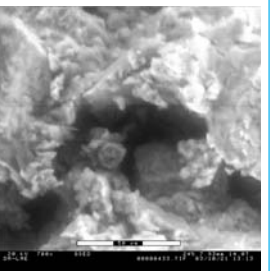
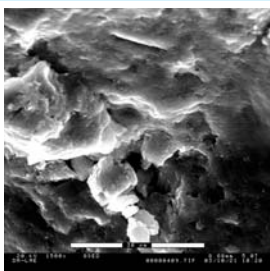
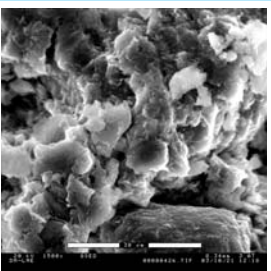
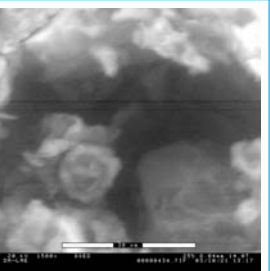
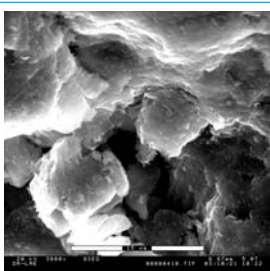
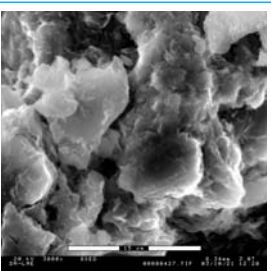
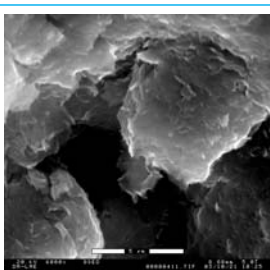
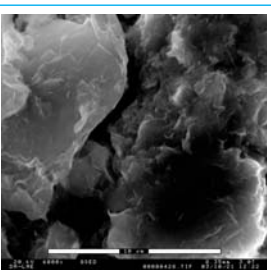
	$\rho_d = 1.65 \text{ g/cm}^3 \text{ s} = 120 \text{ MPa}$ $P_0 = 5.5 \text{ Tor T} = 16^\circ\text{C RH} = 41 \%$	$\rho_d = 1.73 \text{ g/cm}^3 \text{ s} = 310 \text{ MPa}$ $P_0 = 3.0 \text{ Tor T} = 22^\circ\text{C RH} = 15 \%$	$\rho_d = 1.55 \text{ g/cm}^3 \text{ s} = 39 \text{ MPa}$ $P_0 = 14.0 \text{ Tor T} = 23^\circ\text{C RH} = 67\%$
$\times 300$			
$\times 700$			
$\times 1500$			
$\times 3000$			
$\times 6000$			

Table C.5: Samples compacted at  $1.65 \text{ g/cm}^3$  and hygroscopic water content ( $s=120 \text{ MPa}$ ) subjected to suction increase (to  $s=310 \text{ MPa}$ ) and decrease (to  $s= 39 \text{ MPa}$ ) in isochoric conditions.

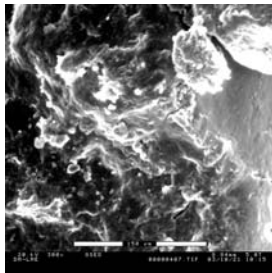
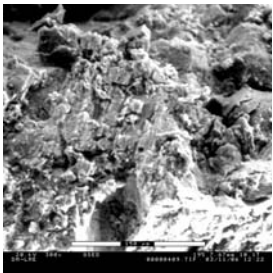
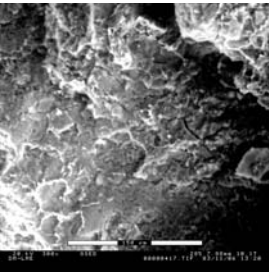
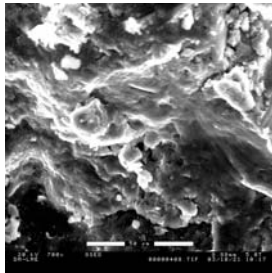
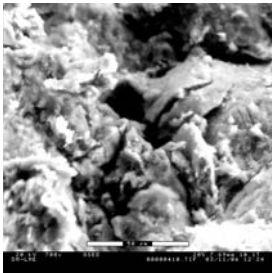
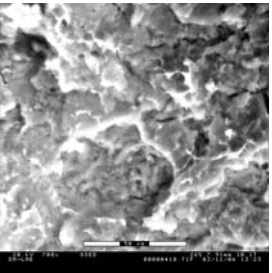
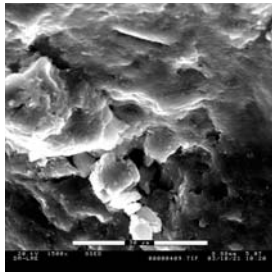
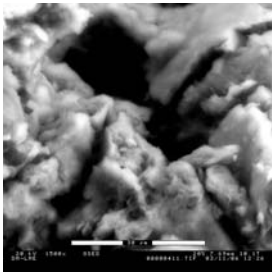
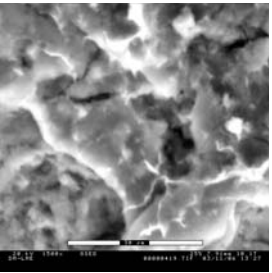
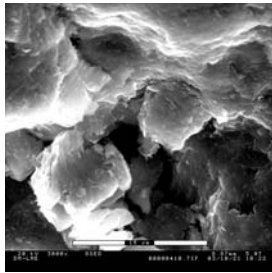
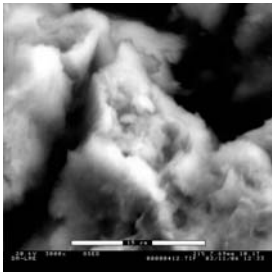
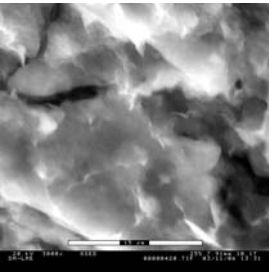
	$\rho_d = 1.65 \text{ g/cm}^3 \text{ } s = 120 \text{ MPa}$ $P_g = 5.5 \text{ Tor } T = 16^\circ\text{C } RH = 41 \%$	$\rho_d = 1.46 \text{ g/cm}^3 \text{ } s = 10 \text{ MPa}$ $P_g = 10.1 \text{ Tor } T = 15^\circ\text{C } RH = 75 \%$	$\rho_d = 1.43 \text{ g/cm}^3 \text{ } s = 0 \text{ MPa}$ $P_g = 10.1 \text{ Tor } T = 15^\circ\text{C } RH = 75 \%$
$\times 300$			
$\times 700$			
$\times 1500$			
$\times 3000$			

Table C.6: Samples compacted at  $1.65 \text{ g/cm}^3$  and hygroscopic water content ( $s=120 \text{ MPa}$ ) subjected to suction decrease (to  $s=10 \text{ MPa}$  and  $s=0$ ) in isochoric conditions.

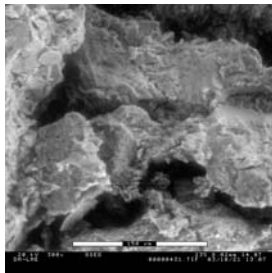
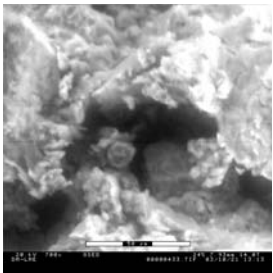
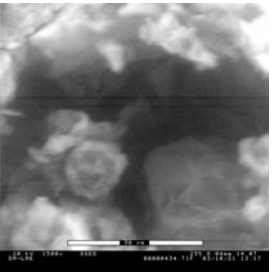
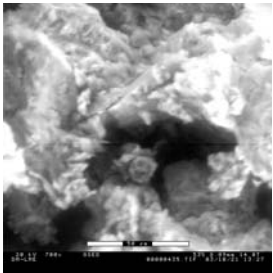
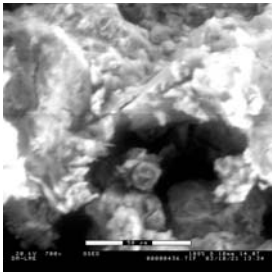
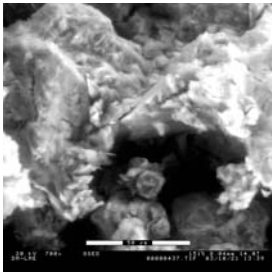
$\rho_d = 1.55 \text{ g/cm}^3$ $s = 39 \text{ MPa}$	$\times 300$	$\times 700$	$\times 1500$
$P_g = 14.0 \text{ Tor}$ $T = 23^\circ\text{C}$ $\text{RH} = 67\%$			
$P_g = 14.0 \text{ Tor}$ $T = 53^\circ\text{C}$			
$P_g = 14.0 \text{ Tor}$ $T = 108^\circ\text{C}$			
$P_g = 14.0 \text{ Tor}$ $T = 151^\circ\text{C}$			

Table C.7: Sample compacted at  $1.65 \text{ g/cm}^3$  and hygroscopic water content ( $s=120 \text{ MPa}$ ) subjected to suction decrease (to  $s=39 \text{ MPa}$ ) in isochoric conditions observed in ESEM at different temperature conditions.

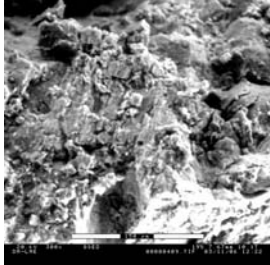
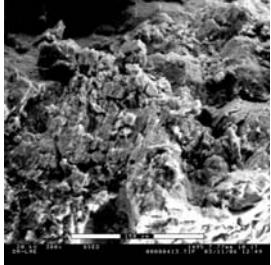
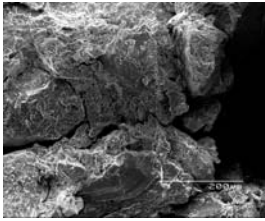
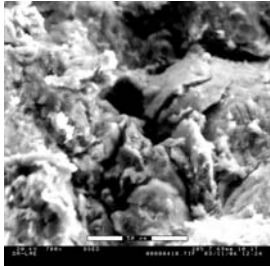
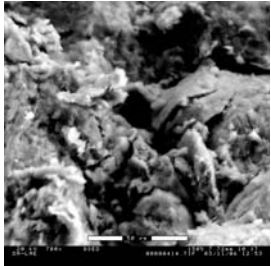
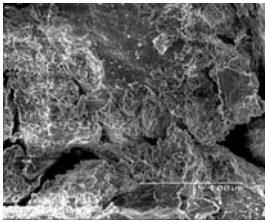
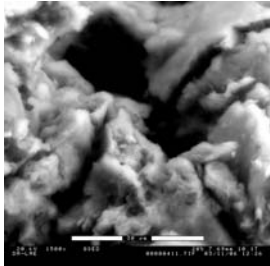
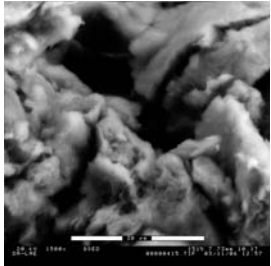
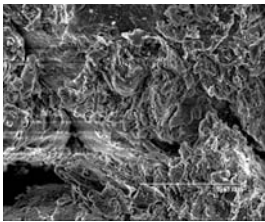
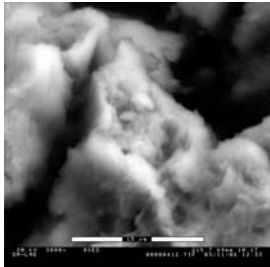
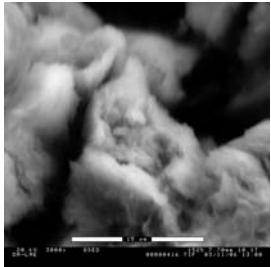
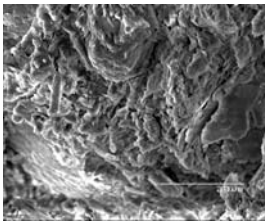


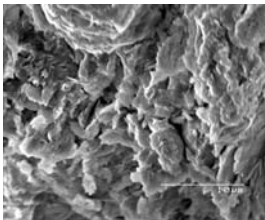
$\rho_d = 1.46 \text{ g/cm}^3$ $s = 10 \text{ MPa}$	$P_0 = 10.1 \text{ Tor } T = 15^\circ\text{C } RH = 75\%$	$P_0 = 10.1 \text{ Tor } T = 150^\circ\text{C}$	$P_0 = 0 \text{ Tor } T = 22^\circ\text{C SEM}$
$\times 300$			
$\times 700$			
$\times 1500$			
$\times 3000$			
$\times 6000$			

Table C.8: Sample compacted at  $1.65 \text{ g/cm}^3$  and hygroscopic water content subjected to suction decrease (to  $s = 10 \text{ MPa}$ ) in isochoric conditions observed in SEM and ESEM at different temperature conditions.

$\rho_d = 1.43 \text{ g/cm}^3$ $s = 0 \text{ MPa}$	$P_g = 10.1 \text{ Tor}$ $T = 15^\circ\text{C}$ HR = 75%	$P_g = 10.1 \text{ Tor}$ $T = 150^\circ\text{C}$	$P_g = 0$ $T = 22^\circ\text{C SEM}$
$\times 300$			
$\times 700$			
$\times 1500$			
$\times 3000$			
$\times 6000$			

Table C.9: Sample compacted at  $1.65 \text{ g/cm}^3$  and hygroscopic water content subjected to saturation ( $s = 0 \text{ MPa}$ ) in isochoric conditions observed in SEM and ESEM at different temperature conditions.

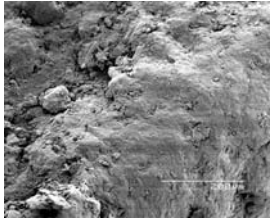
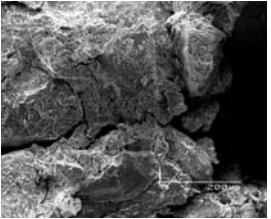
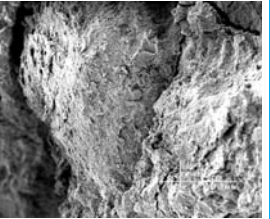
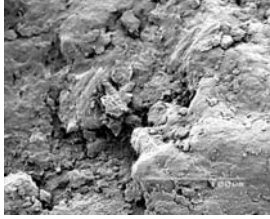
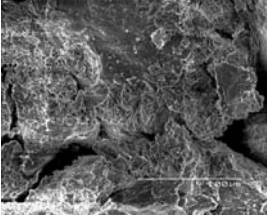
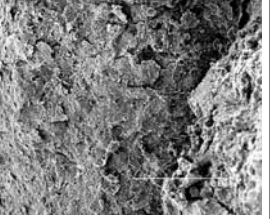

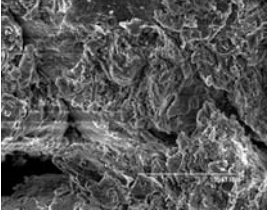
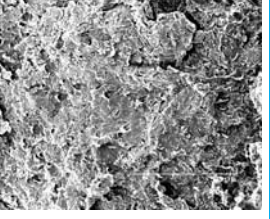
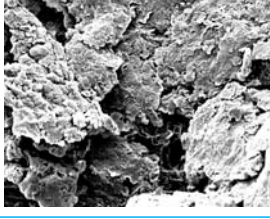
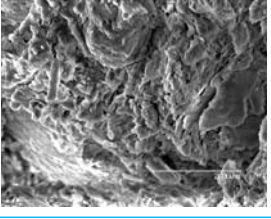
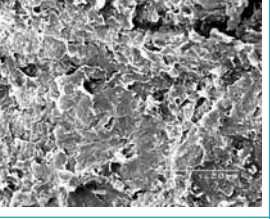
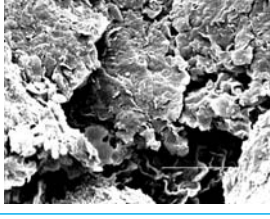
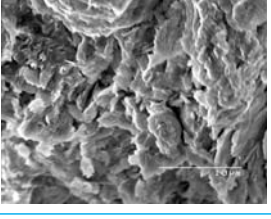
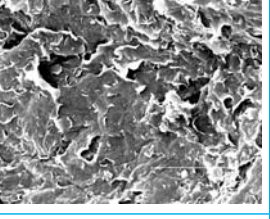
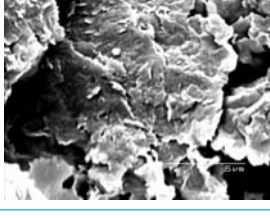
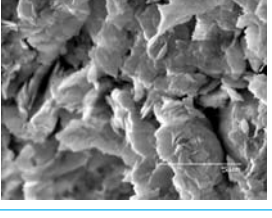
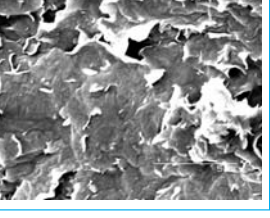
	$\rho_d = 1.40 \text{ g/cm}^3$ $s = 120 \text{ MPa}$ SEM	$\rho_d = 1.46 \text{ g/cm}^3$ $s = 10 \text{ MPa}$ SEM	$\rho_d = 1.43 \text{ g/cm}^3$ $s = 0 \text{ MPa}$ SEM
$\times 300$			
$\times 700$			
$\times 1500$			
$\times 3000$			
$\times 6000$			
$\times 12000$			

Table C.10: Sample compacted at  $1.4 \text{ g/cm}^3$  and hygroscopic water content and samples compacted to  $1.65 \text{ g/cm}^3$  subjected to suction decrease ( $s = 10$  and  $s = 0 \text{ MPa}$ ) in isochoric conditions observed in SEM.

	$\rho_d = 1.65 \text{ g/cm}^3$ $s = 120 \text{ MPa}$ T = 22°C P <sub>g</sub> = 5.5 Tor T = 16°C RH = 41 %	$\rho_d = 1.60 \text{ g/cm}^3$ w = 0.51% T = 22 → 150 → 22°C P <sub>g</sub> = 5 Tor T = 17°C RH = 41 %	$\rho_d = 1.60 \text{ g/cm}^3$ w = 0.51% T = 22 → 150 → 22°C P <sub>g</sub> = 5 Tor T = 148°C
× 150			
× 300			
× 700			
× 1500			

Table C.11: Sample compacted at 1.65 g/cm<sup>3</sup> and hygroscopic water content at 22°C, subjected to a temperature increase up to 150°C and observed in ESEM at different temperatures.

This page blank



## PUBLICACIONES TÉCNICAS

1991

- 01 REVISIÓN SOBRE LOS MODELOS NUMÉRICOS RELACIONADOS CON EL ALMACENAMIENTO DE RESIDUOS RADIACTIVOS.
- 02 REVISIÓN SOBRE LOS MODELOS NUMÉRICOS RELACIONADO CON EL ALMACENAMIENTO DE RESIDUOS RADIACTIVOS. ANEXO 1. Guía de códigos aplicables.
- 03 PRELIMINARY SOLUBILITY STUDIES OF URANIUM DIOXIDE UNDER THE CONDITIONS EXPECTED IN A SALINE REPOSITORY.
- 04 GEOESTADÍSTICA PARA EL ANÁLISIS DE RIESGOS. Una introducción a la Geoestadística no paramétrica.
- 05 SITUACIONES SINÓPTICAS Y CAMPOS DE VIENTOS ASOCIADOS EN "EL CABRIL".
- 06 PARAMETERS, METHODOLOGIES AND PRIORITIES OF SITE SELECTION FOR RADIOACTIVE WASTE DISPOSAL IN ROCK SALT FORMATIONS.

1992

- 01 STATE OF THE ART REPORT: DISPOSAL OF RADIOACTIVE WASTE IN DEEP ARGILLACEOUS FORMATIONS.
- 02 ESTUDIO DE LA INFILTRACIÓN A TRAVÉS DE LA COBERTERA DE LA FUA.
- 03 SPANISH PARTICIPATION IN THE INTERNATIONAL INTRAVEL PROJECT.
- 04 CARACTERIZACIÓN DE ESMECTITAS MAGNÉSICAS DE LA CUENCA DE MADRID COMO MATERIALES DE SELLADO. Ensayos de alteración hidrotermal.
- 05 SOLUBILITY STUDIES OF URANIUM DIOXIDE UNDER THE CONDITIONS EXPECTED IN A SALINE REPOSITORY. Phase II
- 06 REVISIÓN DE MÉTODOS GEOFÍSICOS APLICABLES AL ESTUDIO Y CARACTERIZACIÓN DE EMPLAZAMIENTOS PARA ALMACENAMIENTO DE RESIDUOS RADIACTIVOS DE ALTA ACTIVIDAD EN GRANITOS, SALES Y ARCILLAS.
- 07 COEFICIENTES DE DISTRIBUCIÓN ENTRE RADIONUCLEIDOS.
- 08 CONTRIBUTION BY CIN-JPM TO THE PSACON LEVEL-5 EXERCISE.
- 09 DESARROLLO DE UN MODELO DE RESUSPENSIÓN DE SUELOS CONTAMINADOS. APLICACIÓN AL ÁREA DE PALOMARES.
- 10 ESTUDIO DEL CÓDIGO FFSM PARA CAMPO LEJANO. IMPLANTACIÓN EN VAX.
- 11 LA EVALUACIÓN DE LA SEGURIDAD DE LOS SISTEMAS DE ALMACENAMIENTO DE RESIDUOS RADIACTIVOS. UTILIZACIÓN DE MÉTODOS PROBABILISTAS.
- 12 METODOLOGÍA CANADIENSE DE EVALUACIÓN DE LA SEGURIDAD DE LOS ALMACENAMIENTOS DE RESIDUOS RADIACTIVOS.
- 13 DESCRIPCIÓN DE LA BASE DE DATOS WALKER.

### Publicaciones no periódicas

PONENCIAS E INFORMES, 1988-1991.  
SEGUNDO PLAN DE I+D, 1991-1995. TOMOS I, II Y III.  
SECOND RESEARCH AND DEVELOPMENT PLAN, 1991-1995, VOLUME I.

1993

- 01 INVESTIGACIÓN DE BENTONITAS COMO MATERIALES DE SELLADO PARA ALMACENAMIENTO DE RESIDUOS RADIACTIVOS DE ALTA ACTIVIDAD. ZONA DE CABO DE GATA, ALMERÍA.
- 02 TEMPERATURA DISTRIBUTION IN A HYPOTHETICAL SPENT NUCLEAR FUEL REPOSITORY IN A SALT DOME.
- 03 ANÁLISIS DEL CONTENIDO EN AGUA EN FORMACIONES SALINAS. Su aplicación al almacenamiento de residuos radiactivos
- 04 SPANISH PARTICIPATION IN THE HAW PROJECT. Laboratory Investigations on Gamma Irradiation Effects in Rock Salt.
- 05 CARACTERIZACIÓN Y VALIDACIÓN INDUSTRIAL DE MATERIALES ARCILLOSOS COMO BARRERA DE INGENIERÍA.
- 06 CHEMISTRY OF URANIUM IN BRINES RELATED TO THE SPENT FUEL DISPOSAL IN A SALT REPOSITORY (I).
- 07 SIMULACIÓN TÉRMICA DEL ALMACENAMIENTO EN GALERÍA-TSS.
- 08 PROGRAMAS COMPLEMENTARIOS PARA EL ANÁLISIS ESTOCÁSTICO DEL TRANSPORTE DE RADIONUCLEIDOS.
- 09 PROGRAMAS PARA EL CÁLCULO DE PERMEABILIDADES DE BLOQUE.
- 10 METHODS AND RESULTS OF THE INVESTIGATION OF THE THERMOMECHANICAL BEHAVIOUR OF ROCK SALT WITH REGARD TO THE FINAL DISPOSAL OF HIGH-LEVEL RADIOACTIVE WASTES.

### Publicaciones no periódicas

SEGUNDO PLAN DE I+D. INFORME ANUAL 1992.  
PRIMERAS JORNADAS DE I+D EN LA GESTIÓN DE RESIDUOS RADIACTIVOS. TOMOS I Y II.

1994

- 01 MODELO CONCEPTUAL DE FUNCIONAMIENTO DE LOS ECOSISTEMAS EN EL ENTORNO DE LA FÁBRICA DE URANIO DE ANDÚJAR.
- 02 CORROSION OF CANDIDATE MATERIALS FOR CANISTER APPLICATIONS IN ROCK SALT FORMATIONS.
- 03 STOCHASTIC MODELING OF GROUNDWATER TRAVEL TIMES
- 04 THE DISPOSAL OF HIGH LEVEL RADIOACTIVE WASTE IN ARGILLACEOUS HOST ROCKS. Identification of parameters, constraints and geological assessment priorities.
- 05 EL OESTE DE EUROPA Y LA PENÍNSULA IBÉRICA DESDE HACE 120.000 AÑOS HASTA EL PRESENTE. Isostasia glacial, paleogeografía paleotemperaturas.
- 06 ECOLOGÍA EN LOS SISTEMAS ACUÁTICOS EN EL ENTORNO DE EL CABRIL.
- 07 ALMACENAMIENTO GEOLÓGICO PROFUNDO DE RESIDUOS RADIACTIVOS DE ALTA ACTIVIDAD (AGP). Conceptos preliminares de referencia.
- 08 UNIDADES MÓVILES PARA CARACTERIZACIÓN HIDROGEOQUÍMICA
- 09 EXPERIENCIAS PRELIMINARES DE MIGRACIÓN DE RADIONUCLEIDOS CON MATERIALES GRANÍTICOS. EL BERROCAL, ESPAÑA.
- 10 ESTUDIOS DE Desequilibrios isotópicos de series radiactivas naturales en un ambiente granítico: plutón de el Berrocal (Toledo).
- 11 RELACIÓN ENTRE PARÁMETROS GEOFÍSICOS E HIDROGEOLÓGICOS. Una revisión de literatura.
- 12 DISEÑO Y CONSTRUCCIÓN DE LA COBERTURA MULTICAPA DEL DIQUE DE ESTÉRILES DE LA FÁBRICA DE URANIO DE ANDÚJAR.

### Publicaciones no periódicas

SEGUNDO PLAN I+D 1991-1995. INFORME ANUAL 1993.

1995

- 01 DETERMINACIÓN DEL MÓDULO DE ELASTICIDAD DE FORMACIONES ARCILLOSAS PROFUNDAS.
- 02 UO LEACHING AND RADIONUCLIDE RELEASE MODELLING UNDER HIGH AND LOW IONIC STRENGTH SOLUTION AND OXIDATION CONDITIONS.
- 03 THERMO-HYDRO-MECHANICAL CHARACTERIZATION OF THE SPANISH REFERENCE CLAY MATERIAL FOR ENGINEERED BARRIER FOR GRANITE AND CLAY HLW REPOSITORY: LABORATORY AND SMALL MOCK UP TESTING.
- 04 DOCUMENTO DE SÍNTESIS DE LA ASISTENCIA GEOTÉCNICA AL DISEÑO AGP-ARCILLA. Concepto de referencia.
- 05 DETERMINACIÓN DE LA ENERGÍA ACUMULADA EN LAS ROCAS SALINAS FUERTEMENTE IRRADIADAS MEDIANTE TÉCNICAS DE TERMOLUMINISCENCIA. Aplicación al análisis de repositorios de residuos radiactivos de alta actividad.
- 06 PREDICCIÓN DE FENÓMENOS DE TRANSPORTE EN CAMPO PRÓXIMO Y LEJANO. Interacción en fases sólidas.
- 07 ASPECTOS RELACIONADOS CON LA PROTECCIÓN RADIOLÓGICA DURANTE EL DESMANTELAMIENTO Y CLAUSURA DE LA FÁBRICA DE ANDÚJAR.
- 08 ANALYSIS OF GAS GENERATION MECHANISMS IN UNDERGROUND RADIOACTIVE WASTE REPOSITORIES. (Pegase Project).
- 09 ENSAYOS DE LIXIVIACIÓN DE EMISORES BETA PUROS DE LARGA VIDA.
- 10 2º PLAN DE I+D. DESARROLLOS METODOLÓGICOS, TECNOLÓGICOS, INSTRUMENTALES Y NUMÉRICOS EN LA GESTIÓN DE RESIDUOS RADIACTIVOS.
- 11 PROYECTO AGP-ALMACENAMIENTO GEOLÓGICO PROFUNDO. FASE 2.
- 12 IN SITU INVESTIGATION OF THE LONG-TERM SEALING SYSTEM AS COMPONENT OF DAM CONSTRUCTION (DAM PROJECT). Numerical simulator: Code-Bright.

### Publicaciones no periódicas

TERCER PLAN DE I+D 1995-1999.  
SEGUNDAS JORNADAS DE I+D. EN LA GESTIÓN DE RESIDUOS RADIACTIVOS. TOMOS I Y II.

1996

- 01 DESARROLLO DE UN PROGRAMA INFORMÁTICO PARA EL ASESORAMIENTO DE LA OPERACIÓN DE FOCOS EMISORES DE CONTAMINANTES GASEOSOS.
- 02 FINAL REPORT OF PHYSICAL TEST PROGRAM CONCERNING SPANISH CLAYS (SAPONITES AND BENTONITES).
- 03 APORTACIONES AL CONOCIMIENTO DE LA EVOLUCIÓN PALEOCLIMÁTICA Y PALEOAMBIENTAL EN LA PENÍNSULA IBÉRICA DURANTE LOS DOS ÚLTIMOS MILLONES DE AÑOS A PARTIR DEL ESTUDIO DE TRAVERTINOS Y ESPELEOTEMAS.
- 04 MÉTODOS GEOESTADÍSTICOS PARA LA INTEGRACIÓN DE INFORMACIÓN.
- 05 ESTUDIO DE LONGEVIDAD EN BENTONITAS: ESTABILIDAD HIDROTÉRMAL DE SAPONITAS.
- 06 ALTERACIÓN HIDROTÉRMAL DE LAS BENTONITAS DE ALMERÍA.
- 07 MAYDAY. UN CÓDIGO PARA REALIZAR ANÁLISIS DE INCERTIDUMBRE Y SENSIBILIDAD. Manuales.

### Publicaciones no periódicas

EL BERROCAL PROJECT. VOLUME I. GEOLOGICAL STUDIES.  
EL BERROCAL PROJECT. VOLUME II. HYDROGEOCHEMISTRY.  
EL BERROCAL PROJECT. VOLUME III. LABORATORY MIGRATION TESTS AND IN SITU TRACER TEST.  
EL BERROCAL PROJECT. VOLUME IV. HYDROGEOLOGICAL MODELLING AND CODE DEVELOPMENT.

1997

- 01 CONSIDERACIÓN DEL CAMBIO MEDIOAMBIENTAL EN LA EVALUACIÓN DE LA SEGURIDAD. ESCENARIOS CLIMÁTICOS A LARGO PLAZO EN LA PENÍNSULA IBÉRICA.
- 02 METODOLOGÍA DE EVALUACIÓN DE RIESGO SÍSMICO EN SEGMENTOS DE FALLA.
- 03 DETERMINACIÓN DE RADIONUCLEIDOS PRESENTES EN EL INVENTARIO DE REFERENCIA DEL CENTRO DE ALMACENAMIENTO DE EL CABRIL.
- 04 ALMACENAMIENTO DEFINITIVO DE RESIDUOS DE RADIACTIVIDAD ALTA. Caracterización y comportamiento a largo plazo de los combustibles nucleares irradiados (I).
- 05 METODOLOGÍA DE ANÁLISIS DE LA BIOSFERA EN LA EVALUACIÓN DE ALMACENAMIENTOS GEOLÓGICOS PROFUNDOS DE RESIDUOS RADIACTIVOS DE ALTA ACTIVIDAD ESPECÍFICA.
- 06 EVALUACIÓN DEL COMPORTAMIENTO Y DE LA SEGURIDAD DE UN ALMACENAMIENTO GEOLÓGICO PROFUNDO EN GRANITO. Marzo 1997
- 07 SÍNTESIS TECTOESTRATIGRÁFICA DEL MACIZO HESPÉRICO. VOLUMEN I.
- 08 III JORNADAS DE I+D Y TECNOLOGÍAS DE GESTIÓN DE RESIDUOS RADIACTIVOS. Pósters descriptivos de los proyectos de I+D y evaluación de la seguridad a largo plazo.
- 09 FEBEX. ETAPA PREOPERACIONAL. INFORME DE SÍNTESIS.
- 10 METODOLOGÍA DE GENERACIÓN DE ESCENARIOS PARA LA EVALUACIÓN DEL COMPORTAMIENTO DE LOS ALMACENAMIENTOS DE RESIDUOS RADIACTIVOS.
- 11 MANUAL DE CESARR V.2. Código para la evaluación de seguridad de un almacenamiento superficial de residuos radiactivos de baja y media actividad.

1998

- 01 FEBEX. PRE-OPERATIONAL STAGE. SUMMARY REPORT.
- 02 PERFORMANCE ASSESSMENT OF A DEEP GEOLOGICAL REPOSITORY IN GRANITE. March 1997.
- 03 FEBEX. DISEÑO FINAL Y MONTAJE DEL ENSAYO "IN SITU" EN GRIMSEL.
- 04 FEBEX. BENTONITA: ORIGEN, PROPIEDADES Y FABRICACIÓN DE BLOQUES.
- 05 FEBEX. BENTONITE: ORIGIN, PROPERTIES AND FABRICATION OF BLOCKS.
- 06 TERCERAS JORNADAS DE I+D Y TECNOLOGÍAS DE GESTIÓN DE RESIDUOS RADIACTIVOS. 24-29 Noviembre, 1997. Volumen I
- 07 TERCERAS JORNADAS DE I+D Y TECNOLOGÍAS DE GESTIÓN DE RESIDUOS RADIACTIVOS. 24-29 Noviembre, 1997. Volumen II
- 08 MODELIZACIÓN Y SIMULACIÓN DE BARRERAS CAPILARES.
- 09 FEBEX. PREOPERATIONAL THERMO-HYDRO-MECHANICAL (THM) MODELLING OF THE "IN SITU" TEST.

## Títulos publicados

- 10 FEBEX. PREOPERATIONAL THERMO-HYDRO-MECHANICAL (THM) MODELLING OF THE "MOCK UP" TEST.
- 11 DISOLUCIÓN DEL UO (S) EN CONDICIONES REDUCTORAS Y OXIDANTES.
- 12 FEBEX. FINAL DESIGN AND INSTALLATION OF THE "IN SITU" TEST AT GRIMSEL.

### 1999

- 01 MATERIALES ALTERNATIVOS DE LA CÁPSULA DE ALMACENAMIENTO DE RESIDUOS RADIATIVOS DE ALTA ACTIVIDAD.
- 02 INTRAVAL PROJECT PHASE 2: STOCHASTIC ANALYSIS OF RADIONUCLIDES TRAVEL TIMES AT THE WASTE ISOLATION PILOT PLANT (WIPP), IN NEW MEXICO (U.S.A.).
- 03 EVALUACIÓN DEL COMPORTAMIENTO Y DE LA SEGURIDAD DE UN ALMACENAMIENTO PROFUNDO EN ARCILLA. Febrero 1999.
- 04 ESTUDIOS DE CORROSIÓN DE MATERIALES METÁLICOS PARA CÁPSULAS DE ALMACENAMIENTO DE RESIDUOS DE ALTA ACTIVIDAD.
- 05 MANUAL DEL USUARIO DEL PROGRAMA VISUAL BALAN V. 1.0. CÓDIGO INTERACTIVO PARA LA REALIZACIÓN DE BALANCES HIDROLÓGICOS Y LA ESTIMACIÓN DE LA RECARGA.
- 06 COMPORTAMIENTO FÍSICO DE LAS CÁPSULAS DE ALMACENAMIENTO.
- 07 PARTICIPACIÓN DEL CIEMAT EN ESTUDIOS DE RADIOECOLOGÍA EN ECOSISTEMAS MARINOS EUROPEOS.
- 08 PLAN DE INVESTIGACIÓN Y DESARROLLO TECNOLÓGICO PARA LA GESTIÓN DE RESIDUOS RADIATIVOS 1999-2003. OCTUBRE 1999.
- 09 ESTRATEGIA BIOMOLECULAR. LA RACEMIZACIÓN/EPIMERIZACIÓN DE AMINOÁCIDOS COMO HERRAMIENTA GEOCRONOLÓGICA Y PALEOTERMOMÉTRICA.
- 10 CATSIUS CLAY PROJECT. Calculation and testing of behaviour of unsaturated clay as barrier in radioactive waste repositories. STAGE 1: VERIFICATION EXERCISES.
- 11 CATSIUS CLAY PROJECT. Calculation and testing of behaviour of unsaturated clay as barrier in radioactive waste repositories. STAGE 2: VALIDATION EXERCISES AT LABORATORY SCALE.
- 12 CATSIUS CLAY PROJECT. Calculation and testing of behaviour of unsaturated clay as barrier in radioactive waste repositories. STAGE 3: VALIDATION EXERCISES AT LARGE "IN SITU" SCALE.

### 2000

- 01 FEBEX PROJECT. FULL-SCALE ENGINEERED BARRIERS EXPERIMENT FOR A DEEP GEOLOGICAL REPOSITORY FOR HIGH LEVEL RADIOACTIVE WASTE IN CRYSTALLINE HOST ROCK. FINAL REPORT.
- 02 CÁLCULO DE LA GENERACIÓN DE PRODUCTOS RADIOLÍTICOS EN AGUA POR RADIACIÓN  $\alpha$ . DETERMINACIÓN DE LA VELOCIDAD DE ALTERACIÓN DE LA MATRIZ DEL COMBUSTIBLE NUCLEAR GASTADO.
- 03 LIBERACIÓN DE RADIONUCLIDOS E ISÓTOPOS ESTABLES CONTENIDOS EN LA MATRIZ DEL COMBUSTIBLE. MODELO CONCEPTUAL Y MODELO MATEMÁTICO DEL COMPORTAMIENTO DEL RESIDUO.
- 04 DESARROLLO DE UN MODELO GEOQUÍMICO DE CAMPO PRÓXIMO.
- 05 ESTUDIOS DE DISOLUCIÓN DE ANÁLOGOS NATURALES DE COMBUSTIBLE NUCLEAR IRRADIADO Y DE FASES DE (U)VI-SILICIO REPRESENTATIVAS DE UN PROCESO DE ALTERACIÓN OXIDATIVA.
- 06 CORE2D. A CODE FOR NON-ISOTHERMAL WATER FLOW AND REACTIVE SOLUTE TRANSPORT. USERS MANUAL VERSION 2.
- 07 ANÁLOGOS ARQUEOLÓGICOS E INDUSTRIALES PARA ALMACENAMIENTOS PROFUNDOS: ESTUDIO DE PIEZAS ARQUEOLÓGICAS METÁLICAS.

- 08 PLAN DE INVESTIGACIÓN Y DESARROLLO TECNOLÓGICO PARA LA GESTIÓN DE RESIDUOS RADIATIVOS 1999-2003. REVISIÓN 2000.
- 09 IV JORNADAS DE INVESTIGACIÓN Y DESARROLLO TECNOLÓGICO EN GESTIÓN DE RESIDUOS RADIATIVOS. POSTERS DIVULGATIVOS.
- 10 IV JORNADAS DE INVESTIGACIÓN Y DESARROLLO TECNOLÓGICO EN GESTIÓN DE RESIDUOS RADIATIVOS. POSTERS TÉCNICOS.
- 11 PROGRAMA DE INVESTIGACIÓN PARA ESTUDIAR LOS EFECTOS DE LA RADIACIÓN GAMMA EN BENTONITAS CÁLCICAS ESPAÑOLAS.
- 12 CARACTERIZACIÓN Y LIXIVIACIÓN DE COMBUSTIBLES NUCLEARES IRRADIADOS Y DE SUS ANÁLOGOS QUÍMICOS.

### 2001

- 01 MODELOS DE FLUJO MULTIFÁSICO NO ISOTERMO Y DE TRANSPORTE REACTIVO MULTICOMPONENTE EN MEDIOS POROSOS.
- 02 IV JORNADAS DE INVESTIGACIÓN Y DESARROLLO TECNOLÓGICO EN GESTIÓN DE RESIDUOS RADIATIVOS. RESÚMENES Y ABSTRACTS.
- 03 ALMACENAMIENTO DEFINITIVO DE RESIDUOS DE RADIATIVIDAD ALTA. CARACTERIZACIÓN Y COMPORTAMIENTO A LARGO PLAZO DE LOS COMBUSTIBLES NUCLEARES IRRADIADOS (II).
- 04 CONSIDERATIONS ON POSSIBLE SPENT FUEL AND HIGH LEVEL WASTE MANAGEMENT OPTIONS.
- 05 LA PECHBLENDA DE LA MINA FE (CIUDAD RODRIGO, SALAMANCA), COMO ANÁLOGO NATURAL DEL COMPORTAMIENTO DEL COMBUSTIBLE GASTADO. Proyecto Matrix I.
- 06 TESTING AND VALIDATION OF NUMERICAL MODELS OF GROUNDWATER FLOW, SOLUTE TRANSPORT AND CHEMICAL REACTIONS IN FRACTURED GRANITES: A QUANTITATIVE STUDY OF THE HYDROGEOLOGICAL AND HYDROCHEMICAL IMPACT PRODUCED.
- 07 IV JORNADAS DE INVESTIGACIÓN Y DESARROLLO TECNOLÓGICO EN GESTIÓN DE RESIDUOS RADIATIVOS. Volumen I.
- 08 IV JORNADAS DE INVESTIGACIÓN Y DESARROLLO TECNOLÓGICO EN GESTIÓN DE RESIDUOS RADIATIVOS. Volumen II.
- 09 IV JORNADAS DE INVESTIGACIÓN Y DESARROLLO TECNOLÓGICO EN GESTIÓN DE RESIDUOS RADIATIVOS. Volumen III.
- 10 IV JORNADAS DE INVESTIGACIÓN Y DESARROLLO TECNOLÓGICO EN GESTIÓN DE RESIDUOS RADIATIVOS. Volumen IV.

### 2002

- 01 FABRICACIÓN DE BLANCOS PARA LA TRANSMUTACIÓN DE AMERICIO: SÍNTESIS DE MATRICES INERTES POR EL MÉTODO SOL-GEL. ESTUDIO DEL PROCEDIMIENTO DE INFILTRACIÓN DE DISOLUCIONES RADIATIVAS.
- 02 ESTUDIO GEOQUÍMICO DE LOS PROCESOS DE INTERACCIÓN AGUA-ROCA SOBRE SISTEMAS GEOTERMALES DE AGUAS ALCALINAS GRANITOIDES.
- 03 ALTERACIÓN ALCALINA HIDROTÉRMICA DE LA BARRERA DE BENTONITA POR AGUAS INTERESTICIALES DE CEMENTOS.
- 04 THERMO-HYDRO-MECHANICAL CHARACTERISATION OF A BENTONITE FROM CABO DE GATA. A study applied to the use of bentonite as sealing material in high level radioactive waste repositories.
- 05 ESTUDIOS GEOLÓGICO-ESTRUCTURALES Y GEOFÍSICOS EN MINA RATONES (PLUTÓN DE ALBALÁ).
- 06 IMPACTO DE LA MINA RATONES (ALBALÁ, CÁCERES) SOBRE LAS AGUAS SUPERFICIALES Y SUBTERRÁNEAS: MODELIZACIÓN HIDROGEOQUÍMICA.

- 07 CARACTERIZACIÓN PETROLÓGICA, MINERALÓGICA, GEOQUÍMICA Y EVALUACIÓN DEL COMPORTAMIENTO GEOQUÍMICO DE LAS REE EN LA FASE SÓLIDA (GRANITOIDES Y RELLENOS FISURALES) DEL SISTEMA DE INTERACCIÓN AGUA-ROCA DEL ENTORNO DE LA MINA RATONES.
- 08 MODELLING SPENT FUEL AND HLW BEHAVIOUR IN REPOSITORY CONDITIONS. A review of the state of the art.
- 09 UN MODELO NUMÉRICO PARA LA SIMULACIÓN DE TRANSPORTE DE CALOR Y LIBERACIÓN DE MATERIA EN UN ALMACENAMIENTO PROFUNDO DE RESIDUOS RADIATIVOS.
- 10 PROCESOS GEOQUÍMICOS Y MODIFICACIONES TEXTURALES EN BENTONITA FEBEX COMPACTADA SOMETIDA A UN GRADIENTE TERMOHIDRÁULICO.

### 2003

- 01 CONTRIBUCIÓN EXPERIMENTAL Y MODELIZACIÓN DE PROCESOS BÁSICOS PARA EL DESARROLLO DEL MODELO DE ALTERACIÓN DE LA MATRIZ DEL COMBUSTIBLE IRRADIADO.
- 02 URANIUM(VI) SORPTION ON GOETHITE AND MAGNETITE: EXPERIMENTAL STUDY AND SURFACE COMPLEXATION MODELLING.
- 03 ANÁLOGOS ARQUEOLÓGICOS E INDUSTRIALES PARA ALMACENAMIENTO DE RESIDUOS RADIATIVOS: ESTUDIO DE PIEZAS ARQUEOLÓGICAS METÁLICAS (ARCHEO-II).
- 04 EVOLUCIÓN PALEOAMBIENTAL DE LA MITAD SUR DE LA PENÍNSULA IBÉRICA. APLICACIÓN A LA EVALUACIÓN DEL COMPORTAMIENTO DE LOS REPOSITARIOS DE RESIDUOS RADIATIVOS.
- 05 THE ROLE OF COLLOIDS IN THE RADIONUCLIDE TRANSPORT IN A DEEP GEOLOGICAL REPOSITORY. Participation of CIEMAT in the CRR project.
- 06 V JORNADAS DE INVESTIGACIÓN Y DESARROLLO TECNOLÓGICO EN GESTIÓN DE RESIDUOS RADIATIVOS. Resúmenes de ponencias.
- 07 V JORNADAS DE INVESTIGACIÓN Y DESARROLLO TECNOLÓGICO EN GESTIÓN DE RESIDUOS RADIATIVOS. Sinopsis de pósters.
- 08 V JORNADAS DE INVESTIGACIÓN, DESARROLLO TECNOLÓGICO Y DEMOSTRACIÓN EN GESTIÓN DE RESIDUOS RADIATIVOS. Pósters técnicos.
- 09 DISMANTLING OF THE HEATER 1 AT THE FEBEX "IN SITU" TEST. Descriptions of operations
- 10 GEOQUÍMICA DE FORMACIONES ARCILLOSAS: ESTUDIO DE LA ARCILLA ESPAÑOLA DE REFERENCIA.
- 11 PETROPHYSICS AT THE ROCK MATRIX SCALE: HYDRAULIC PROPERTIES AND PETROGRAPHIC INTERPRETATION.

### 2004

- 01 PLAN DE INVESTIGACIÓN, DESARROLLO TECNOLÓGICO Y DEMOSTRACIÓN PARA LA GESTIÓN DE RESIDUOS RADIATIVOS 2004-2008.
- 02 ESTUDIO DE LOS PRODUCTOS DE CORROSIÓN DE LA CÁPSULA Y SU INTERACCIÓN CON LA BARRERA ARCILLOSA DE BENTONITA "CORROBEN".
- 03 EFECTO DE LA MAGNETITA EN LA RETENCIÓN DE LOS RADIONUCLIDOS EN EL CAMPO PRÓXIMO: CESIO, ESTRONCIO, MOLIBDENO Y SELENIO.
- 04 Vª JORNADAS DE INVESTIGACIÓN Y DESARROLLO TECNOLÓGICO EN GESTIÓN DE RESIDUOS RADIATIVOS. Volumen I.
- 05 Vª JORNADAS DE INVESTIGACIÓN Y DESARROLLO TECNOLÓGICO EN GESTIÓN DE RESIDUOS RADIATIVOS. Volumen II.
- 06 Vª JORNADAS DE INVESTIGACIÓN Y DESARROLLO TECNOLÓGICO EN GESTIÓN DE RESIDUOS RADIATIVOS. Volumen III.
- 07 Vª JORNADAS DE INVESTIGACIÓN Y DESARROLLO TECNOLÓGICO EN GESTIÓN DE RESIDUOS RADIATIVOS. Volumen IV.
- 08 FEBEX PROJECT. POST-MORTEM ANALYSIS: CORROSION STUDY.
- 09 FEBEX II PROJECT. THG LABORATORY EXPERIMENTS

This page blank

# FEBEX II Project Final report on thermo-hydro-mechanical laboratory tests

*PUBLICACIÓN TÉCNICA 10/2004*

Para más información, dirigirse a:



Dirección de Comunicación  
C/ Emilio Vargas, 7  
28043 MADRID

<http://www.enresa.es>

*Octubre 2004*